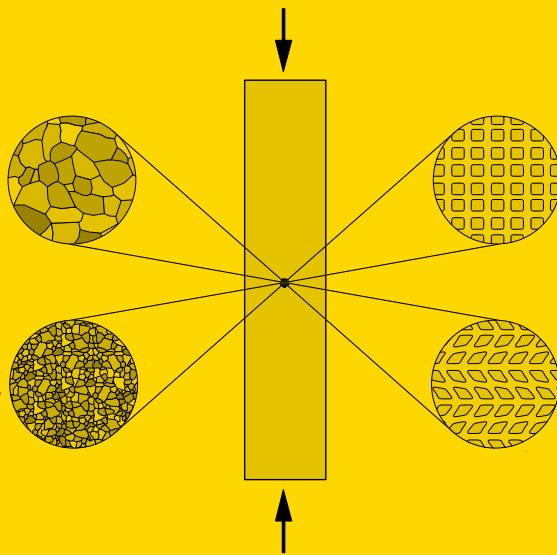


# Incompatibility and Instability Based Size Effects in Crystals and Composites at Finite Elastoplastic Strains

Martin Becker



$$\tau_r^\alpha = c\mu b \sqrt{G^{\alpha\beta} [\rho_{\text{SSD}}^\beta (\gamma^\beta) + \rho_{\text{GND}}^\beta (\nabla \gamma^\beta)]}$$

$$\bar{W} = \inf_{n_c} \left\{ \inf_{\varphi} \frac{1}{|V(n_c)|} \int_{\mathcal{B}(n_c)} W(\nabla \varphi, \mathbf{X}) dV \right\}$$

Bericht Nr.: I-18 (2006)  
Institut für Mechanik (Bauwesen), Lehrstuhl I  
Professor Dr.-Ing. C. Miehe  
Stuttgart 2006



# **Incompatibility and Instability Based Size Effects in Crystals and Composites at Finite Elastoplastic Strains**

Von der Fakultät Bau- und Umweltingenieurwissenschaften  
der Universität Stuttgart zur Erlangung der Würde  
eines Doktor-Ingenieurs (Dr.-Ing.)  
genehmigte Abhandlung

vorgelegt von

**Martin Becker**

aus Reutlingen

Hauptberichter: Prof. Dr.-Ing. C. Miede

Mitberichter : Prof. Dr. Ir. M.G.D. Geers

Tag der mündlichen Prüfung: 21. Februar 2006

Institut für Mechanik (Bauwesen) der Universität Stuttgart  
2006

**Herausgeber:**

Prof. Dr.-Ing. habil. C. Miehe

**Organisation und Verwaltung:**

Institut für Mechanik (Bauwesen)

Lehrstuhl I

Universität Stuttgart

Pfaffenwaldring 7

70550 Stuttgart

Tel.: ++49-(0)711/685-6378

Fax : ++49-(0)711/685-6347

© Martin Becker

Institut für Mechanik (Bauwesen)

Lehrstuhl I

Universität Stuttgart

Pfaffenwaldring 7

70550 Stuttgart

Tel.: ++49-(0)711/685-6326

Fax : ++49-(0)711/685-6347

Alle Rechte, insbesondere das der Übersetzung in fremde Sprachen, vorbehalten. Ohne Genehmigung des Autors ist es nicht gestattet, dieses Heft ganz oder teilweise auf fotomechanischem Wege (Fotokopie, Mikrokopie) zu vervielfältigen.

ISBN 3-937859-06-3 (D 93 Stuttgart)

## Zusammenfassung

Gegenstand dieser Arbeit ist die Beschreibung des skalenabhängigen Verhaltens von Kristallen im Zuge inhomogener Deformationen sowie die Entwicklung eines Homogenisierungszuganges für instabile, inelastische Komposite, bei dem Größenabhängigkeiten in klassischen Konzepten beseitigt werden. Hauptaugenmerk, im Bereich der Untersuchung von Größeneffekten bei Kristallen, liegt dabei auf einer umfassenden Darlegung der zugrunde liegenden mikromechanischen Interpretation, der zugehörigen Deformationsgeometrie und experimenteller Beobachtungen. Dies beinhaltet insbesondere detaillierte Betrachtungen zur Inkompatibilität, zum Versetzungsdichtetensor und zur Speicherung geometrisch notwendiger Versetzungen. Diese Untersuchungen münden in der Entwicklung eines gradientenerweiterten Kristallplastizitätsmodells basierend auf Versetzungsdichten. Für dieses Modell wird eine gemischte Finite Elemente Formulierung und alternativ eine effiziente erweiterte lokale Formulierung entwickelt. Diese Entwicklungen werden anhand verschiedener numerischer Beispiele validiert, die sowohl den Vergleich mit experimentellen Messungen als auch mit Vorhersagen anderer Formulierungen, beispielsweise diskreten Versetzungssimulationen, abdecken. Im Hinblick auf die Untersuchung von Größenabhängigkeiten bei der Homogenisierung instabiler inelastischer Komposite werden zunächst Kriterien für die Stabilitätsanalyse auf der Mikro- und der Makroskala entwickelt. Die zugrunde liegende Basis bildet eine inkrementelle Variationsformulierung des Homogenisierungsproblems. Diese ermöglicht die Herstellung des Zusammenhanges zwischen Mikro- und Makroinstabilitäten sowie die Entwicklung eines Zuganges für die nichtkonvexe Homogenisierung inelastischer Komposite. Abschließend wird das nichtkonvexe Homogenisierungsverfahren, das als wesentliche Größe zusätzlich die relevante Mikrostrukturabmessung liefert, anhand einiger Beispiele demonstriert.

## Abstract

The purpose of this work is the description of length scale dependencies in nonhomogeneously deforming crystals and the elimination of size dependencies in classical homogenization approaches for instable elastoplastically deforming composites. Key aspects, on the side of the investigation of size effects in crystals, are a comprehensive discussion of the underlying micromechanical interpretation, the deformation geometry and related experimental observations. These include a detailed incompatibility analysis and an extensive discussion of the dislocation density tensor and the storage of geometrically necessary dislocations. A dislocation density based strain gradient crystal plasticity model is developed as a main outcome of these investigations. This model is subsequently treated in the context of a mixed finite element formulation or alternatively in a more efficient manner through an extended standard local formulation. The developments are validated through various numerical examples which cover also a comparison with experimental observations or predictions obtained through alternative approaches such as discrete dislocation simulations. In view of an investigation of size dependencies in the homogenization analysis of instable inelastic composites, first criteria for an instability analysis on the micro- as well as the macro-scale are developed. The underlying basis is an incremental variational formulation of the homogenization problem. This allows for an investigation of the interaction between micro- and macro-instabilities and the development of a non-convex homogenization approach for inelastic composites at finite strains. The implications of the non-convex homogenization approach which, as a key point additionally determines the relevant microstructure size, are finally demonstrated for several examples.



## Preface

The work presented in the following was developed in the course of my occupation at the Institute of Applied Mechanics, Chair I at the University of Stuttgart. The support provided by the Deutsche Forschungsgemeinschaft (DFG) under grant SFB404/A8 „Mikro-Makro-Übergänge zur Beschreibung thermomechanischer Deformationsprozesse heterogener Materialien“ is gratefully acknowledged.

I would like to express my gratitude to Prof. Dr.-Ing. Christian Miehe. He opened my eyes to the intriguing world of mechanics, supported my application for an one-year stay at the University of Calgary and finally gave me the chance to work in his research group at the Institute of Applied Mechanics in Stuttgart. I would like to thank him for his support, his guidance and his inspirations for this work and for accepting the main referee position.

A sincere thank you goes to Prof. Dr. Ir. M.G.D. Geers. On one hand I am grateful for his interest in this work and for his acceptance to become correferree for this thesis. On the other hand I am also very thankful for the valuable scientific discussions we had and for his inspiring comments.

Furthermore I would like to thank Dominik Zimmermann for his friendship and his help in many scientific questions. This concerns additionally Jan Schotte, Daniele Rosato and Barish Gökce who provided me with significant support on the topic of crystal plasticity, also through the mastertheses of the latter two, whose supervision was a true pleasure.

My sincere gratitude goes to all my colleagues at the Institute of Applied Mechanics in Stuttgart for the pleasant working conditions and the excellent social atmosphere. In this respect I want to thank specifically my roommate Manuel Birkle, my colleagues Ercan Gürses and Serdar Göktepe and my former fellow student and colleague Joachim Dettmar.

Finally I am truly grateful for the everlasting support, the great basis and the chances my parents, Brita and Olaf Becker, provided me with wherever I was and whatever idea I had. This includes also my beloved sister, Karin Degler, and brother, Jan Becker, with whom I have shared so many happy years.

Stuttgart, March 2006

Martin Becker



---

## Contents

<b>1. Introduction</b> . . . . .	<b>1</b>
1.1. Motivation and State of the Art . . . . .	1
1.2. Objective and Overview . . . . .	4
<b>2. Foundations of Continuum Mechanics</b> . . . . .	<b>7</b>
2.1. Kinematics . . . . .	7
2.1.1. Material Bodies, Configurations, Base Systems and Metric Tensors .	7
2.1.2. The Deformation Gradient . . . . .	9
2.1.3. Convective Coordinates . . . . .	10
2.1.4. Pull-Back and Push-Forward Transformations, Strain Tensors . . . .	11
2.2. The Concept of Stresses and Heat Flux . . . . .	12
2.2.1. Representations of the Stress Tensor . . . . .	12
2.2.2. Heat Flux . . . . .	13
2.3. Balance Principles . . . . .	14
2.3.1. Reynold's Transport Theorem . . . . .	14
2.3.2. Conservation of Mass . . . . .	14
2.3.3. Momentum Balance Principles . . . . .	14
2.3.4. Balance of Energy . . . . .	15
2.3.5. Entropy Inequality Principle . . . . .	16
<b>3. Fundamentals of Metal Crystals</b> . . . . .	<b>17</b>
3.1. The Crystal Structure . . . . .	17
3.2. Miller Indices . . . . .	19
3.2.1. Indication of Crystal Planes . . . . .	19
3.2.2. Indication of Directions . . . . .	20
3.3. Closest Packed Crystal Planes . . . . .	21
3.4. Visualization of Crystallographic Directions . . . . .	21
3.5. Defects in Crystalline Materials . . . . .	22
3.6. Dislocations . . . . .	23
3.6.1. Theoretical Strength of a Crystal . . . . .	23
3.6.2. Dislocation Movement . . . . .	25
3.6.3. The Burgers Vector . . . . .	25

3.6.4.	Dislocation Loops . . . . .	26
3.6.5.	Dislocation Density . . . . .	26
3.6.6.	Plastic Deformation through Dislocation Movement . . . . .	26
3.6.7.	Dislocation Multiplication . . . . .	27
3.7.	Slip Systems . . . . .	28
3.8.	Schmid's Law . . . . .	28
3.9.	Work Hardening of Metal Crystals . . . . .	30
3.9.1.	The Three Stage Hardening Response . . . . .	30
3.9.2.	Latent Hardening - Dislocation Interactions . . . . .	31
3.9.3.	Work Hardening Theories . . . . .	32
<b>4.</b>	<b>Crystal Plasticity at Finite Strains . . . . .</b>	<b>37</b>
4.1.	The Continuum Slip Theory of Single Crystal Plasticity . . . . .	37
4.1.1.	Homogeneous Deformation of a Crystal . . . . .	37
4.1.2.	Free Energy Storage in Deforming Crystals . . . . .	38
4.1.3.	Elastic Stress Response of Single Crystals . . . . .	40
4.1.4.	Elastic Domain and Evolution of Plastic Deformation . . . . .	40
4.1.5.	Visco-Plastic Flow Response of Single Crystals . . . . .	41
4.2.	Algorithmic Formulation of Single Crystal Plasticity . . . . .	43
4.2.1.	Integration of the Flow Rule . . . . .	43
4.2.2.	Standard Stress Update Algorithm of Crystal Plasticity . . . . .	44
4.2.3.	Local Incremental Variational Problem . . . . .	45
4.2.4.	Algorithmic Expressions for Standard and Variational Formulation . . . . .	46
4.2.5.	Algorithmic Update of the Active Set . . . . .	48
4.2.6.	Stresses and Consistent Tangent Moduli . . . . .	49
<b>5.</b>	<b>Dislocation Density Based Strain Gradient Crystal Plasticity . . . . .</b>	<b>53</b>
5.1.	Introduction into Strain Gradient Crystal Plasticity . . . . .	53
5.2.	Geometrically Necessary Dislocations and Compatibility - Introduction . . . . .	56
5.3.	A Direct Approach to the Compatibility Analysis . . . . .	60
5.4.	Dislocation Density Tensors of Multiplicative Crystal Plasticity . . . . .	64
5.5.	Differential Geometric Compatibility Analysis . . . . .	70
5.5.1.	Compatibility Conditions at Small Strains . . . . .	71
5.5.2.	The Geometric Objects of Differential Geometry . . . . .	72

---

5.5.3.	Compatibility of the Total Deformation State . . . . .	81
5.5.4.	Incompatibility of Intermediate Configuration and GND Density . .	83
5.6.	Crystallographic Interpretation of the Dislocation Density Tensor . . . . .	89
5.6.1.	Nye's Dislocation Tensor . . . . .	89
5.6.2.	Slip Gradient Induced Dislocation Storage . . . . .	90
5.6.3.	Lattice Geometric Representation of the Dislocation Tensor . . . . .	93
5.6.4.	Incorporation of GND Density into Hardening Relations . . . . .	95
5.7.	Micromechanically Motivated Strain Gradient Crystal Plasticity . . . . .	97
<b>6.</b>	<b>Numerical Implementation of Gradient Crystal Plasticity . . . . .</b>	<b>99</b>
6.1.	Global Formulation for Fully Rate Dependent Gradient Plasticity . . . . .	100
6.1.1.	Strong Form of the Coupled Problem . . . . .	100
6.1.2.	Temporal Discretization and Weak Form of the Coupled Problem . .	100
6.1.3.	Algorithmic Linearization for Monolithic Solution Procedure . . . . .	101
6.1.4.	Finite Element Discretization of the Coupled Problem . . . . .	102
6.2.	Global Formulation for Gradient Crystal Viscoplasticity . . . . .	104
6.2.1.	Strong Form of the Coupled Problem . . . . .	104
6.2.2.	Temporal Discretization and Weak Form of the Coupled Problem . .	104
6.2.3.	Algorithmic Linearization for Monolithic Solution Procedure . . . . .	105
6.2.4.	Finite Element Discretization of the Coupled Problem . . . . .	106
6.2.5.	Active Set Search . . . . .	108
6.2.6.	Comparison of Discrete Global and Standard Local Formulation . . .	109
6.3.	Extended Local Formulation for Gradient Crystal Plasticity . . . . .	111
6.3.1.	The $L_2$ -Projection . . . . .	111
6.3.2.	The Patch Recovery . . . . .	112
<b>7.</b>	<b>Numerical Examples for Gradient Crystal Plasticity . . . . .</b>	<b>115</b>
7.1.	Numerical Example for Fully Rate Dependent Gradient Plasticity . . . . .	115
7.1.1.	Constrained Shear of a Strip in Double Slip . . . . .	115
7.2.	Numerical Examples for Gradient Crystal Viscoplasticity . . . . .	121
7.2.1.	Comparison of Global and Standard Local Plasticity Formulation . .	121
7.2.2.	Shear Test for a Composite Material . . . . .	123
7.2.3.	Bending Test for a Single Crystal . . . . .	129
7.2.4.	Tension Test for an FCC Polycrystal . . . . .	135

<b>8. Incremental Stability of Microheterogeneous Materials</b> . . . . .	<b>141</b>
8.1. Introduction . . . . .	141
8.2. Incremental Homogenization Analysis in Finite Inelasticity . . . . .	142
8.2.1. Microscopic Incremental Variational Formulation of Inelasticity . . .	142
8.2.2. Fluctuation Field on Heterogeneous Micro-structures . . . . .	143
8.2.3. Incremental Variational Formulation of Homogenization . . . . .	144
8.2.4. Macroscopic Incremental Variational Formulation of Inelasticity . . .	146
8.3. Non-Convex Homogenization for Standard Dissipative Materials . . . . .	146
8.3.1. Stability Analysis of Inelastic Microheterogeneous Solids . . . . .	147
8.3.2. Size of the Representative Micro-structure . . . . .	152
8.3.3. Micro-Macro-Interaction of Instability Phenomena . . . . .	153
8.4. Numerical Examples . . . . .	154
8.4.1. Buckling Analysis of a Fiber Reinforced Micro-Structure . . . . .	155
8.4.2. Buckling Analysis of a Cellular Micro-Structure . . . . .	160
<b>9. Conclusion</b> . . . . .	<b>165</b>
<b>A. A Model Problem of Single Crystal Viscoplasticity</b> . . . . .	<b>167</b>
A.1. Constitutive Functions . . . . .	167
A.2. Algorithmic Expressions of the Standard Formulation . . . . .	167
A.3. Stresses and Consistent Tangent Moduli . . . . .	168
<b>B. The Curl Operator</b> . . . . .	<b>168</b>
B.1. Definition of the Contravariant Lagrangian and Eulerian Curl Operators . .	168
B.2. Relation Between Eulerian and Lagrangian Curl Operator . . . . .	169
B.3. The Curl Operator in the Intermediate Configuration . . . . .	170
<b>C. Algorithmic Sensitivities</b> . . . . .	<b>170</b>
C.1. Sensitivities with respect to the Total Deformation Field . . . . .	170
C.2. Sensitivities with respect to the Plastic Slip . . . . .	171
<b>D. The Enhanced Strain Formulation</b> . . . . .	<b>172</b>
<b>References</b> . . . . .	<b>175</b>

## 1. Introduction

The overall objective of this work is the investigation of scale and size dependencies in nonhomogeneously deforming inelastic solids at finite strains. Thereby the main focus concerns the *length scale dependent* response of plastically *inhomogeneously deforming metal crystals*. Further emphasis is placed upon an investigation of possible *size dependencies* within the post-critical *homogenization analysis of instable microheterogeneous solids*. A schematic example of either task is depicted in figure 1.1.

### 1.1. Motivation and State of the Art

Experimentally *size effects* have been already observed in *nonhomogeneously deforming metals* for decades (HALL [53], PETCH [125], STOLKEN & EVANS [143], FLECK ET AL. [42], STELMASHENKO [142] among others). Maybe the most prominent description of such length scale dependent material behavior is given in terms of the Hall-Petch relation established upon experimental evidence in the 1950's by HALL and PETCH. According to their observations, the yield strength of a polycrystalline metal specimen scales linearly with the inverse square root of the grain size. This means that the yield strength of a fine-grained specimen with an average grain diameter of  $d_2$  exhibits a much higher yield strength than a corresponding coarse-grained specimen with  $d_1 > d_2$ , see figure 1.1 a). Hence the grain size represents an intrinsic length scale of the polycrystal which inevitably affects the overall material response. Further important examples for experiments which reveal a size effect in inelastically deforming metals are micro-bending, -torsion or

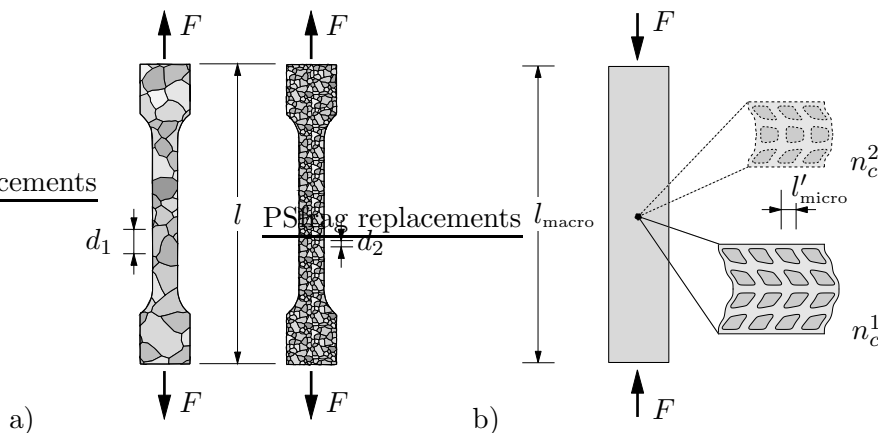


**Figure 1.1:** Schematic examples of scale and size dependencies. a) Experimentally polycrystalline materials exhibit a length scale dependent response governed by the grain size  $d$ , b) in classical homogenization approaches micro-buckling phenomena entail a dependency of the macroscopic material response upon the chosen size of the micro-structure  $n_c$ .

-indentation tests. Common to all of these experiments is the fact that they induce pronounced *elastic* or *plastic deformation inhomogeneities*. These are entailed by either the inhomogeneity of the specimen itself, the overall deformation geometry or the local boundary conditions. Any of these experiments reveals the observation that the overall material hardening increases as the length scale inherent to the inhomogeneity decreases.

With the underlying concept of dislocations, as introduced by OROWAN, POLANYI and TAYLOR, these size effects are attributed to an elevated level of the dislocation storage in connection with increasing deformation inhomogeneities and the associated strain gradi-

ents. The dislocations necessary in order to support such inhomogeneous deformation geometries were thus termed as *geometrically necessary dislocations*, *GNDs*, by COTTRELL [31] and ASHBY [12] in the 1960's. In contrast to the *statistically stored dislocations*, *SSDs*, which provide the underlying mechanism of homogeneous plastic deformations the GND population gives rise to an overall lattice curvature and guarantees lattice continuity under (superposed) non-uniform elastic-plastic deformations. Clearly, if the concern is with a separate dislocation it induces a local lattice curvature in any case and there is no difference between a GND and a SSD as far as a local cut-out part of a single dislocation line is considered. Both dislocation densities contribute to a growing total dislocation population and thus result in an overall hardening response.

The connection between a stress free lattice curvature and the storage of dislocations giving rise to such a curvature was already established in 1953 by NYE [119] which lead him to the definition of the *dislocation density tensor*. Integration of this dislocation density tensor over any cut surface of the body gives the resulting Burgers vector of all dislocations piercing that surface. A more general view of the theory of continuous distributions of defects was developed in the works of KONDO [71, 72], BILBY & SMITH [20], BILBY ET AL. [19], KRÖNER [77] and ANTHONY [4]. Therein, the fundamental relation between the state of a *continuously dislocated crystal* and a *non-Riemannian geometry* was established allowing to relate *Cartan's torsion* (CARTAN [24]) as an incompatibility measure to the aforementioned dislocation density tensor. This differential geometric point of view provided the basis for the computation of residual stresses induced by a continuous distribution of dislocations in the material for the geometrically linear case in KRÖNER [76] and the nonlinear setting in KRÖNER & SEEGER [80] and KRÖNER [77].

The commonly accepted kinematic assumption in the continuum mechanical description of finite strain single crystal plasticity is a *multiplicative split* of the *total deformation gradient*  $\mathbf{F}$  into an elastic part  $\mathbf{F}^e$  and a plastic part  $\mathbf{F}^p$  as proposed in the works of KRÖNER [77] and LEE [83]. This implies the definition of an *intermediate configuration* which, in contrast to the reference and the current configuration, is generally *incompatible*, i.e. broken up if viewed in an Euclidean representation. Consequently, in general neither  $\mathbf{F}^e$  nor  $\mathbf{F}^p$  are compatible, i.e. derivable from a continuous single valued deformation map. Following BILBY ET AL. [19] and KRÖNER [77], an access to the incompatibility analysis is provided through the previously mentioned objects of differential geometry. Accordingly, the setting of multiplicative plasticity is associated with a *flat non-Riemann geometry*. Alternatively the matter of incompatibility can be investigated with tools from calculus. Both approaches are adopted by STEINMANN [140] and ACHARYA & BASSANI [1].

The classical continuum slip theory of crystals (TEODOSIU [149], RICE [129], HILL & RICE [61], MANDEL [89], ASARO [11], HAVNER [56], CUITIÑO & ORTIZ [33], BASSANI [15], MIEHE [95] and MIEHE & SCHOTTE [102] among others) is equipped with a sound physical basis where the evolution of plastic flow arises from the movement of dislocations on certain crystallographic planes. Thereby the presence of dislocations is not modelled in an explicit manner, but their combined action enters the model in a phenomenological way through the constitutive equations that govern the evolution of crystallographic slip and the slip resistance. The accumulation of dislocation density with ongoing plastic deformation through self-interaction or other impeding obstacles most commonly results in work hardening which hinders further plastic flow (TAYLOR [148], KOITER [70], HILL [59], KOCKS [68, 69], HUTCHINSON [65], FRANCIOSI ET AL. [44], PEIRCE ET AL. [124],

ASARO [11], BASSANI & WU [17], CUITIÑO & ORTIZ [33]). The dislocations accounted for in this manner can all be termed as statistically stored dislocations in the aforementioned sense. The underlying assumption of this conventional local continuum theory of finite strain crystal plasticity is the existence of a compatible intermediate configuration with associated compatible elastic and plastic deformations throughout the material body. Hence, possible incompatibilities of the intermediate configuration in connection with inhomogeneous elastic or plastic deformations and the corresponding storage of geometrically necessary dislocations are neglected. Incompatibility measures do not enter the formulation and an influence of the GND storage on the hardening behavior is ignored although it has a significant impact for sufficiently small length scales (ASHBY [12], FLECK & HUTCHINSON [40], FLECK ET AL. [42]). Consequently the experimentally observed size effects are not predictable through a conventional local theory of crystal plasticity.

These deficiencies motivated a number of authors over the last few years to propose various strain gradient crystal plasticity models. Some of these shall be briefly mentioned. A more detailed discussion can be found in the introduction of chapter 5. All of these models include one or more *material length scales* which occasionally have less physical significance. In connection with such a length scale, a size dependent material response is induced through the inclusion of rotation gradients in the couple stress theory of FLECK & HUTCHINSON [40], FLECK ET AL. [42] or rotation and stretch gradients in the Toupin-Mindlin theory of FLECK & HUTCHINSON [41]. A more direct provision for possible incompatibilities relies on the inclusion of a corresponding incompatibility measure in the hardening relations (ACHARYA & BASSANI [1], ACHARYA & BEAUDOIN [2], BASSANI [16]) which preserves the standard structure of the boundary value problem. Alternatively, in the works of STEINMANN [140], SHIZAWA & ZBIB [133], MENZEL & STEINMANN [92], GURTIN [51], SVENDSEN [145], LIEBE [85], LEVKOVITCH ET AL. [84] the dislocation density tensor contributes, through a phenomenological dependence, to the energy storage and its conjugate force to the slip resistance. Such an extended dependence of the energy storage recently became of interest in the mathematical existence theory of incremental finite strain elastoplasticity (MIELKE & MÜLLER [110]). A further point of intense discussion concerns the requirement for higher order boundary conditions in several approaches (GURTIN [51], SHU & FLECK [135]). A more direct incorporation of the contribution of the GND storage to the hardening response is adopted e.g. in DAI & PARKS [35] and EVERS ET AL. [38]. Finally, the discrete dislocation plasticity framework (KUBIN ET AL. [82], VAN DER GIESSEN & NEEDLEMAN [154]) is inherently capable of predicting size effects and relies on a superposition of line discontinuities representative of the discrete dislocations and complementary fields which enforce the boundary conditions.

The scale dependencies discussed so far are physically well motivated and intrinsic to the real material response. This is not the case for the *size dependencies* observed for classical micro-to-macro transitions in the postcritical regime of instable solids. This problem is visualized in the schematic example of figure 1.1 b). The average-type *homogenization analysis* provides an efficient approach to describe microheterogeneous materials with a significant scale separation, i.e.  $l_{\text{micro}} \ll l_{\text{macro}}$ . Thereby a critical point is the choice of the *representative volume element (RVE)* size  $n_c$ . For classical micro-to-macro transitions this choice is solely limited by the size and distribution of the microheterogeneities. However this induces a dependency of the homogenized material response on the RVE size in the case of structural micro-instabilities such as buckling phenomena. This is indicated in figure 1.1 b) where the governing micro-instability mode can only be captured by a RVE of

size  $n_c^1$ . If a RVE size of  $n_c^2$  were used, the relevant buckling mode could not be captured implying a false estimation of the local macroscopic material response. Consequently classical micro-to-macro transitions induce a dependence of the homogenized response on the chosen size of the representative volume element.

The concept of homogenization is outlined in the works WILLIS [156], SUQUET [144], MÜLLER [114], NEMAT-NASSER & HORI [117], PONTE CASTAÑEDA & SUQUET [127] or MIEHE ET AL. [104] among others. Based on incremental minimization principles, an extension to standard dissipative materials is developed in the recent papers MIEHE [97, 98], MIEHE ET AL. [103] and MIEHE & SCHOTTE [101]. Existence results in nonlinear elasticity (BALL [13], DACOROGNA [34], MARSDEN & HUGHES [90]) are based on several (weak) convexity conditions for the stored energy function. A detailed discussion of criteria for the existence of sufficiently stable solutions on the macro- as well as the micro-scale in the context of a homogenization analysis in finite strain elasticity is given in MIEHE ET AL. [108]. Therein (see also GEYMONAT ET AL. [47], TRIANTAFYLIDIS & MAKER [151]) a connection between structural instabilities on the micro-scale and material instabilities on the macro-scale is established as well. Structural instabilities on the micro-scale imply a loss of ellipticity of the homogenization functional which in turn induces the above mentioned dependency of the homogenized response upon the chosen RVE size in classical homogenization approaches. In order to preclude such size dependencies in the postcritical non-convex regime, an extended homogenization principle is proposed for finite strain elasticity in MIEHE ET AL. [108] in line with the fundamental results on non-convex integral functionals of MÜLLER [114]. Through this non-convex homogenization approach the relevant RVE size is additionally determined. Mathematically this can be expressed in terms of the  $\Gamma$ -convergence of the solutions on the micro-structure.

## 1.2. Objective and Overview

Beyond the overall perspective to describe size effects in finite strain crystal plasticity and to eliminate size dependencies in the homogenization analysis of instable solids, major objectives and achievements of this work are the

- incompatibility analysis for nonhomogeneously deforming elastoplastic crystals
- discussion of several incompatibility measures and the dislocation density tensor
- micromechanical foundation through the incompatibility induced GND storage
- formulation of a dislocation density based strain gradient crystal plasticity model
- elaboration of a mixed finite element formulation for strain gradient plasticity
- development of an extended standard FE formulation for gradient plasticity
- incremental stability analysis of microheterogeneous standard dissipative solids
- non-convex homogenization analysis of unstable inelastic solids at finite strains
- analysis of the interaction between micro-instabilities and macro-instabilities

In **Chapter 3** some fundamentals of metal crystals are briefly reiterated in view of a sound micromechanical basis for the subsequent developments. Key elements are: the crystal structure which defines the slip system geometry employed in the continuum model as discussed in section 4; the concept of dislocations which provides the underlying basis of crystallographic slip and work hardening and which resolves the lattice incompatibili-

ties under inhomogeneous elastic or plastic deformations; furthermore a collection of the governing dislocation interactions and the dislocation density based hardening models.

**Chapter 4** is concerned with the constitutive modeling of purely local crystal plasticity at finite strains. The considerations are restricted to homogeneously deforming crystals with associated compatible elastic and plastic deformations. An extension to inhomogeneously deforming crystals is given in chapter 5. First the continuum slip theory is discussed with the key assumptions of a multiplicative split of the deformation gradient and a Schmid type flow response. Thereafter two alternative algorithms of local single crystal viscoplasticity are discussed: a classical fully implicit return mapping scheme and an implicit variational formulation which, in contrast to the standard scheme, results in a symmetric formulation and allows for an instability analysis as discussed in chapter 8.

In **Chapter 5**, a dislocation density based strain gradient crystal plasticity model is developed which accounts for possible incompatibilities in nonhomogeneously deforming metal crystals. The model is equipped with a sound mathematical, micromechanical and experimental foundation. To this end the chapter starts with a vast introduction giving an overview of recent developments, some experimental observations and the notion of geometrically necessary dislocations (GNDs). Subsequently the matter of incompatibility is approached with tools from calculus and alternatively from a differential geometric point of view. This defines the dislocation density tensor as a key incompatibility measure. The dislocation density tensor is discussed in its Lagrangian, intermediate, Eulerian and two field representations and a crystallographic interpretation in terms of the storage of dislocations is given. Finally, for the rate dependent as well as the rate independent case, a micromechanically motivated strain gradient crystal plasticity model is developed which directly incorporates the dislocation density tensor.

**Chapter 6** treats the numerical implementation of the developed strain gradient crystal plasticity model. The dependence on the plastic strain gradients implies a (weakly) nonlocal formulation which requires to supply in addition to the displacement field the slip distribution throughout the solution domain. In this respect two alternative solution strategies are proposed. First, a fully implicit monolithic formulation is considered in the context of a mixed finite element formulation for both the rate dependent and the rate independent case. Secondly, in view of an efficient algorithmic treatment, an extended local formulation for gradient plasticity is developed based on an operator split where the slip distribution is computed through an interpolation of the integration point values.

**Chapter 7** provides a validation of the theoretical and the algorithmic developments for several representative numerical examples. This includes a comparison with the responses of other continuum models of strain gradient crystal plasticity, discrete dislocation simulation results and experimental measurements. Furthermore, the alternative solution strategies developed in chapter 6 are compared with each other as well.

**Chapter 8** finally discusses the stability analysis of microheterogeneous standard dissipative materials at finite strains and the development of a non-convex homogenization approach which determines the relevant micro-structure size. After a brief introduction into the incremental variational formulation of homogenization the criteria for a stability analysis on the micro- and macro-scale are developed. Subsequently an extended homogenization principle for the postcritical non-convex regime is proposed and the interaction between micro- and macro-instabilities is investigated. The chapter closes with numerical examples for a homogenization analysis of unstable elastic and elastoplastic composites.



## 2. Foundations of Continuum Mechanics

Within the following chapter the key foundations of continuum mechanics are summarized, building the basis for the developments in this work and introducing the notation followed therein. Further details can be found in TRUESDELL & NOLL [153], MALVERN [88], MARSDEN & HUGHES [90], HOLZAPFEL [62] or HAUPT [55], to name a few among many other textbooks addressing this issue. In the subsequent discussion the underlying geometric picture is adopted from the modern representations in MIEHE [96].

### 2.1. Kinematics

As continuum mechanics generally relates to the description of the deformation processes of a physical body the starting point for the following developments will be the mathematical description of the motion and deformation of such a material body  $B$ .

**2.1.1. Material Bodies, Configurations, Base Systems and Metric Tensors.** The material body  $B$  (see figure 2.1) is a physical object with specific physical properties which specify the material behavior. The body  $B = \{P\}$  is a set of material points  $P$  which occupy at time  $t$  the domain  $\mathcal{B}_t$  which is defined by the one-to-one mapping

$$\chi_t : \begin{cases} B \rightarrow \mathcal{B}_t \subset \mathbb{R}^3 \\ P \mapsto \mathbf{x} = \chi_t(P) \end{cases} \quad (2.1)$$

Here it is assumed, like always in classical mechanics, that the location of the material body  $\mathcal{B}_t$  is a subset of the three-dimensional Euclidean space  $\mathbb{E}^3$  of physical observation which allows for the introduction of Cartesian coordinates. That this general assumption is strictly admissible only for the description of the overall deformation state of the material body will be elucidated in connection with the introduction of an intermediate configuration in section 5.5. Turning back to (2.1), the configuration defined by  $\chi_t$  uniquely maps the material point  $P$  to the coordinate triple  $\mathbf{x} \in \mathbb{E}^3$  with respect to the global Cartesian basis  $\{\mathbf{E}_i\}_{i=1,2,3}$ . By means of (2.1), the family of configurations  $\mathcal{B}_t$  describes the motion of the body (see figure 2.1) where typically the time dependent configuration  $\mathcal{B}_t$  is denoted as the *current*, the *spatial*, or the *Eulerian configuration*. As it is more convenient to

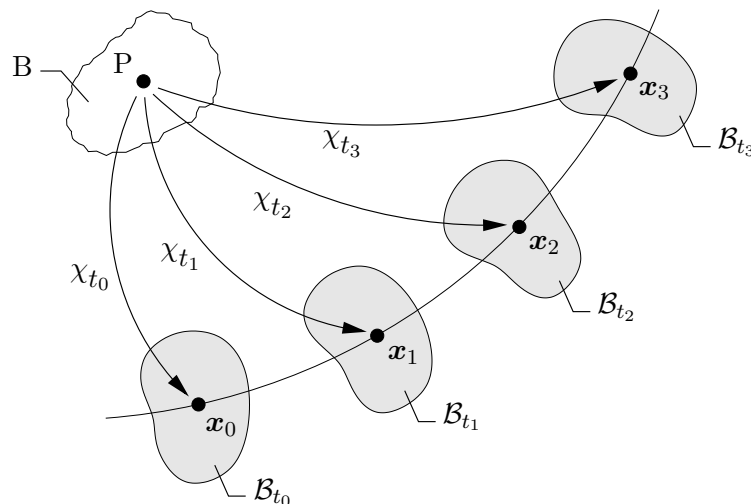


**Figure 2.1:** Motion of a material body  $B$ . The family of configurations  $\mathcal{B}_t$  parametrized in time  $t$  describes the motion of the material body.

describe the motion of the material body with respect to a fixed configuration a so-called *reference* or *material* or *Lagrangian configuration* is chosen at will defined by

$$\chi_0 : \begin{cases} B \rightarrow \mathcal{B} \subset \mathbb{R}^3 \\ P \mapsto \mathbf{X} = \chi_0(P) \end{cases} \quad (2.2)$$

Generally the initial undeformed configuration at time  $t = t_0$  is chosen as reference configuration as this stage of the material body is usually known. Now a relative description for the motion of the material body is obtained by considering the composition of the mappings  $\chi_t$  and  $\chi_0^{-1}$  which defines the nonlinear *deformation map*

$$\varphi_t := \chi_t \circ \chi_0^{-1} : \begin{cases} \mathcal{B} \rightarrow \mathcal{S} \subset \mathbb{R}^3 \\ \mathbf{X} \mapsto \mathbf{x} = \varphi_t(\mathbf{X}) \end{cases} \quad (2.3)$$

The *current configuration*  $\mathcal{S}$  represents the actual location  $\mathcal{B}_t$  of the material body evolving throughout the deformation process characterized by  $\varphi_t$  from the *reference configuration*  $\mathcal{B}$ . Apart from the global Cartesian coordinate system  $\{\mathbf{E}_i\}_{i=1,2,3}$ , Eulerian curvilinear coordinates  $\theta^i$  are introduced oriented along the *material lines* which deform with the body in the Eulerian configuration. The spatial position vectors then have the representations  $\mathbf{x} = x^i(\theta^1, \theta^2, \theta^3)\mathbf{E}_i$ . This results in the definition of two dual co- and contravariant bases  $\{\mathbf{g}_i\}$  and  $\{\mathbf{g}^i\}$  which are obtained as follows

$$\mathbf{g}_i := \partial_{\theta^i} \mathbf{x} = \partial_{\theta^i} x^j(\theta^1, \theta^2, \theta^3)\mathbf{E}_j \quad \text{and} \quad \mathbf{g}^i := \partial_{\mathbf{x}} \theta^i = \partial_{x^j} \theta^i(x^1, x^2, x^3)\mathbf{E}^j \quad (2.4)$$

where the *covariant basis*  $\{\mathbf{g}_i\}$  spans the so-called *tangent space*  $T_{\mathbf{x}}\mathcal{S}$  and the *contravariant basis*  $\{\mathbf{g}^i\}$  spans the *cotangent space*  $T_{\mathbf{x}}^*\mathcal{S}$  with the property  $\mathbf{g}^i \cdot \mathbf{g}_j = \delta_j^i$  for the bases. In connection with the tangent and cotangent space the associated co- and contravariant Eulerian *metric tensors* are defined as follows

$$\mathbf{g} = \mathbf{g}_i \cdot \mathbf{g}_j \mathbf{g}^i \otimes \mathbf{g}^j = g_{ij} \mathbf{g}^i \otimes \mathbf{g}^j \quad \text{and} \quad \mathbf{g}^{-1} = \mathbf{g}^i \cdot \mathbf{g}^j \mathbf{g}_i \otimes \mathbf{g}_j = g^{ij} \mathbf{g}_i \otimes \mathbf{g}_j \quad (2.5)$$

A similar development gives, after introduction of the Lagrangian curvilinear coordinates  $\Theta^I$ , the counterparts in the reference configuration, namely the *co-* and *contravariant Lagrangian bases*  $\{\mathbf{G}_I\}$  and  $\{\mathbf{G}^I\}$  and furthermore the respective *Lagrangian metric tensors*  $\mathbf{G}$  and  $\mathbf{G}^{-1}$ . The developed geometric setting is summarized in figure 2.2. Spaces equipped with metric tensors are called *metric spaces*. The metric tensors allow for the measurement of lengths, areas, volumes and angles (see section 5.5.2). For *Euclidean spaces*  $g_{ij}$  and  $g^{ij}$  need to be positive definite symmetric tensors, satisfying the *compatibility conditions*, (see section 5.5). The above explanations were presented for the case of general curvilinear coordinates, however, the relations simplify significantly for a choice of Cartesian bases for both the current and the reference configuration which results in

$$\{\mathbf{G}_I\} = \{\mathbf{g}_i\} = \{\mathbf{E}_i\} \quad (2.6)$$

For clarity a formal differentiation will be adopted in the following between the four Lagrangian and Eulerian tangent and cotangent spaces spanned by the bases  $\{\mathbf{E}_A\}, \{\mathbf{E}^A\}$  and  $\{\mathbf{e}_a\}, \{\mathbf{e}^a\}$ , respectively. This gives the following specific forms of the metric tensors

$$\begin{aligned} \mathbf{G} &= \delta_{AB} \mathbf{E}^A \otimes \mathbf{E}^B & \text{and} & & \mathbf{g} &= \delta_{ab} \mathbf{e}^a \otimes \mathbf{e}^b \\ \mathbf{G}^{-1} &= \delta^{AB} \mathbf{E}_A \otimes \mathbf{E}_B & & & \mathbf{g}^{-1} &= \delta^{ab} \mathbf{e}_a \otimes \mathbf{e}_b \end{aligned} \quad (2.7)$$

**2.1.2. The Deformation Gradient.** The key quantity in the description of finite strain kinematics is the *deformation gradient*. It is defined by the *Frechet-derivative* of the nonlinear deformation map  $\varphi_t(\mathbf{X})$  with respect to the material coordinates  $\mathbf{X}$

$$\mathbf{F}(\mathbf{X}) := \nabla_{\mathbf{X}} \varphi_t(\mathbf{X}) \quad (2.8)$$

Thus the deformation gradient is a second order tensor. It reads in base notation as

$$\mathbf{F} = F^a{}_A \mathbf{g}_a \otimes \mathbf{G}^A := \frac{\partial x^a}{\partial X^A} \mathbf{g}_a \otimes \mathbf{G}^A \quad (2.9)$$

The deformation gradient is a linear mapping from the Lagrangian tangent space to the Eulerian tangent space with mixed-variant basis. Its components  $F^a{}_A$  coincide with the elements of the *Jacobian matrix* of the nonlinear deformation map  $\varphi$ . The deformation gradient maps tangent vectors  $\mathbf{T}$  of Lagrangian material lines to tangent vectors  $\mathbf{t}$  of Eulerian material lines

$$\mathbf{F} : \begin{cases} T_{\mathbf{X}}\mathcal{B} \rightarrow T_{\mathbf{x}}\mathcal{S} \\ \mathbf{T} \mapsto \mathbf{t} = \mathbf{F} \cdot \mathbf{T} \end{cases} \quad (2.10)$$

Reversely, the inverse deformation gradient is defined as the spatial derivative of the inverse nonlinear deformation map

$$\mathbf{F}^{-1} := \nabla_{\mathbf{x}} \varphi_t^{-1}(\mathbf{x}) \quad \Leftrightarrow \quad \mathbf{F}^{-1} = F^{-1A}{}_a \mathbf{G}_A \otimes \mathbf{g}^a := \frac{\partial X^A}{\partial x^a} \mathbf{G}_A \otimes \mathbf{g}^a \quad (2.11)$$

Thus the inverse deformation gradient is also a mixed variant map mapping spatial tangent vectors  $\mathbf{t}$  to material tangent vectors  $\mathbf{T}$

$$\mathbf{F}^{-1} : \begin{cases} T_{\mathbf{x}}\mathcal{S} \rightarrow T_{\mathbf{X}}\mathcal{B} \\ \mathbf{t} \mapsto \mathbf{T} = \mathbf{F}^{-1} \cdot \mathbf{t} \end{cases} \quad (2.12)$$

Combining two infinitesimal Lagrangian line elements  $d\mathbf{X}_1$  and  $d\mathbf{X}_2$  by taking their cross product defines an area element  $d\mathbf{A} = d\mathbf{X}_1 \times d\mathbf{X}_2 = dA \mathbf{N}$  in terms of the normal  $\mathbf{N}$ . The mapping of the normal between the Lagrangian and the Eulerian cotangent space  $T_{\mathbf{X}}^*\mathcal{B}$  and  $T_{\mathbf{x}}^*\mathcal{S}$  is given by

$$\mathbf{F}^{-T} : \begin{cases} T_{\mathbf{X}}^*\mathcal{B} \rightarrow T_{\mathbf{x}}^*\mathcal{S} \\ \mathbf{N} \mapsto \mathbf{n} = \mathbf{F}^{-T} \cdot \mathbf{N} \end{cases} \quad (2.13)$$

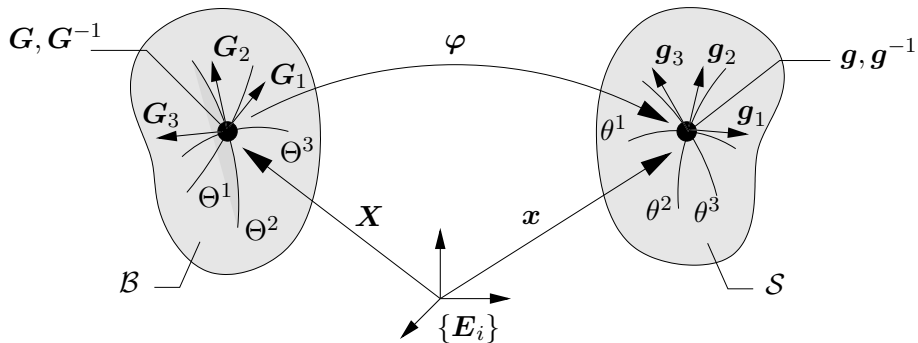


**Figure 2.2:** Reference and actual configuration  $\mathcal{B}$  and  $\mathcal{S}$ , covariant bases and metric tensors. The Lagrangian and Eulerian covariant base vectors  $\mathbf{G}_I$  and  $\mathbf{g}_i$  are tangential to the Lagrangian and Eulerian material lines along which the curvilinear coordinates  $\Theta^I$  and  $\theta^i$  are introduced (for the sake of clarity only the material lines are displayed).

and the infinitesimal area element  $dA$  is mapped by the *Jacobian determinant*  $J := \det \mathbf{F}$

$$J : \begin{cases} \mathbb{R} \rightarrow \mathbb{R} \\ dA \mapsto da = J dA \end{cases} \quad (2.14)$$

(Note: for general coordinates the definition  $J := \det |F^a_A| \sqrt{\frac{\det |g_{ab}|}{\det |G_{AB}|}}$  holds where the second term ensures that  $J$  is a scalar, invariant under coordinate transformations) Assembling (2.13) and (2.14) gives the Nanson formula

$$J \mathbf{F}^{-T} \cdot \mathbf{N} dA = \mathbf{n} da \quad (2.15)$$

Finally, combining three infinitesimal line elements defines the scalar infinitesimal volume  $dV = (d\mathbf{X}_1 \times d\mathbf{X}_2) \cdot d\mathbf{X}_3$  in the Lagrangian configuration. Its Eulerian counterpart is also determined by a transformation with the Jacobian determinant

$$J : \begin{cases} \mathbb{R} \rightarrow \mathbb{R} \\ dV \mapsto dv = J dV \end{cases} \quad (2.16)$$

The deformation gradient is representative of all quantities describing the local deformation state. Thus, the key mappings between the co- and contravariant tangent and cotangent spaces of a Lagrangian material point  $\mathbf{X}$  and its Eulerian counterpart  $\mathbf{x}$  have now been defined. They are visualized in figure 2.3.

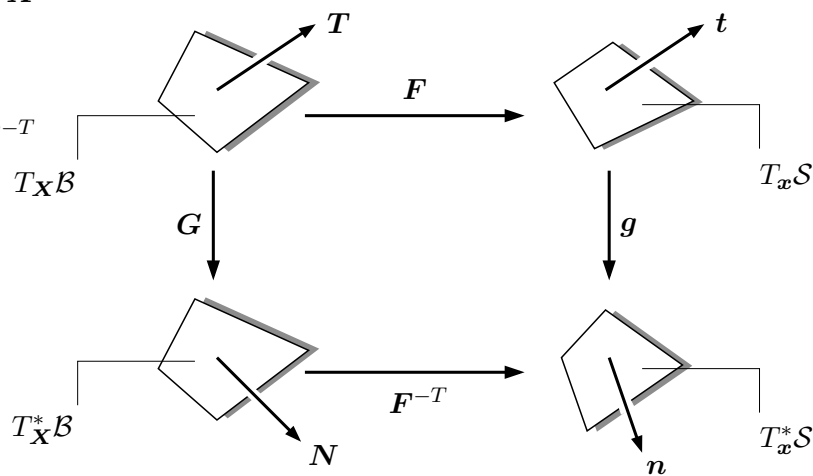


**Figure 2.3:** Mappings between Lagrangian and Eulerian tangent and cotangent spaces. The deformation gradient  $\mathbf{F}$  maps tangent vectors and the transpose of its inverse  $\mathbf{F}^{-T}$  maps normals between the Lagrangian and the Eulerian configuration.

**2.1.3. Convective Coordinates.** In general, any two independent systems of Cartesian or curvilinear coordinates may be chosen as material or spatial coordinate systems as introduced in section 2.1.1. A special choice are *convective coordinates* where the coordinate lines in the Lagrangian configuration are oriented along material lines and the spatial image of these same lines is then identified with the coordinate lines of the Eulerian configuration. This results in  $\theta^i = \Theta^I$  and gives with  $\mathbf{G}_I = \partial_{\Theta^I} \mathbf{X}$  and (2.4)

$$\mathbf{g}_I = \partial_{\theta^i} \mathbf{x} = \partial_{\Theta^I} \mathbf{x} = \nabla_{\mathbf{X}} \varphi_t(\mathbf{X}) \frac{\partial \mathbf{X}}{\partial \Theta^I} = \mathbf{F} \cdot \mathbf{G}_I \quad (2.17)$$

From this the following simple representation of the deformation gradient with respect to convective coordinates can be directly identified

$$\mathbf{F} = \delta^I_J \mathbf{g}_I \otimes \mathbf{G}^J = \mathbf{g}_J \otimes \mathbf{G}^J \quad (2.18)$$

Thus, with respect to the mixed base system  $\{\mathbf{g}_I \otimes \mathbf{G}^J\}$ , the components of the deformation gradient are given by the identity matrix while all information related to the deformation state is carried by the base system or rather the corresponding metric tensors themselves. This viewpoint is crucial for the understanding of finite strain kinematics, especially in connection with the developments of differential geometry in section 5.5. Although, throughout the rest of this work, Cartesian base systems as specified in connection with (2.7) will be utilized. Note that due to this specific choice the metric tensors no longer carry information about the actual deformation state of the material body. They solely serve as mappings between the respective tangent and cotangent space in the sense of 'rising' and 'lowering' tensor indices. Representing the convective base systems with respect to the Cartesian base systems specified in connection with (2.7) gives

$$\mathbf{g}_I = \bar{g}_I^a \mathbf{e}_a \quad \text{and} \quad \mathbf{G}^J = \bar{G}^J_A \mathbf{E}^A \quad (2.19)$$

Through insertion of (2.19) into (2.18) this finally results in the following identification for the deformation gradient

$$\mathbf{F} = \delta^I_J \bar{g}_I^a \bar{G}^J_A \mathbf{e}_a \otimes \mathbf{E}^A = \bar{g}_J^a \bar{G}^J_A \mathbf{e}_a \otimes \mathbf{E}^A = F^a_A \mathbf{e}_a \otimes \mathbf{E}^A \quad (2.20)$$

**2.1.4. Pull-Back and Push-Forward Transformations, Strain Tensors.** Denoting with  $[\cdot]$  and  $(\cdot)$  dual Lagrangian and Eulerian objects, the following abstract notation is introduced for the *pull-back* of an Eulerian object

$$[\cdot] = \varphi_t^*(\cdot) \quad (2.21)$$

and for the *push-forward* of a Lagrangian object

$$(\cdot) = \varphi_{t*}[\cdot] \quad (2.22)$$

For example the pull-back of the Eulerian metric reads

$$\mathbf{C} := \varphi_t^*(\mathbf{g}) = \mathbf{F}^T \cdot \mathbf{g} \cdot \mathbf{F} \quad (2.23)$$

where  $\mathbf{C}$  is the Lagrangian representation of the current metric  $\mathbf{g}$ , also denoted as *right Cauchy Green tensor*. In turn, the push-forward of the Lagrangian metric reads

$$\mathbf{c} := \varphi_{t*}(\mathbf{G}) = \mathbf{F}^{-T} \cdot \mathbf{G} \cdot \mathbf{F}^{-1} \quad (2.24)$$

where  $\mathbf{c}$  is the Eulerian representation of the reference metric  $\mathbf{G}$  defining the so-called *Finger tensor*  $\mathbf{b} := \mathbf{c}^{-1} = \mathbf{F} \cdot \mathbf{G}^{-1} \cdot \mathbf{F}^T$ .

To measure the extent of straining of an infinitesimal line element, the initial length of a material line element  $|\mathrm{d}\mathbf{X}|_{\mathbf{G}} = \sqrt{\mathrm{d}\mathbf{X} \cdot \mathbf{G} \cdot \mathrm{d}\mathbf{X}}$  is compared with its deformed length  $|\mathrm{d}\mathbf{x}|_{\mathbf{g}} = \sqrt{\mathrm{d}\mathbf{x} \cdot \mathbf{g} \cdot \mathrm{d}\mathbf{x}}$  defining the scalar *strain measure*  $\delta$  with

$$\delta := \frac{1}{2} \left[ |\mathrm{d}\mathbf{x}|_{\mathbf{g}}^2 - |\mathrm{d}\mathbf{X}|_{\mathbf{G}}^2 \right] = \frac{1}{2} \mathrm{d}\mathbf{X} \cdot \mathbf{E} \cdot \mathrm{d}\mathbf{X} = \frac{1}{2} \mathrm{d}\mathbf{x} \cdot \mathbf{e} \cdot \mathrm{d}\mathbf{x} \quad (2.25)$$

This implies the definitions of the positive definite symmetric *Green strain tensor*  $\mathbf{E} := \frac{1}{2}[\mathbf{C} - \mathbf{G}]$  and the *Almansi strain tensor*  $\mathbf{e} := \frac{1}{2}[\mathbf{g} - \mathbf{c}]$ .

## 2.2. The Concept of Stresses and Heat Flux

In order to introduce the notion of stresses and heat flux *Euler's cut principle* is applied. Therefore an arbitrary part  $\mathcal{P}_S \subset \mathcal{S}$  of the deformed body  $\mathcal{S}$  is cut out and the effects of the remaining body  $\mathcal{S} \setminus \mathcal{P}_S$  onto the part  $\mathcal{P}_S$  are replaced by a *surface traction vector*  $\mathbf{t}_S$  and a *heat flux*  $h$ , see figure 2.4 for a visualization.

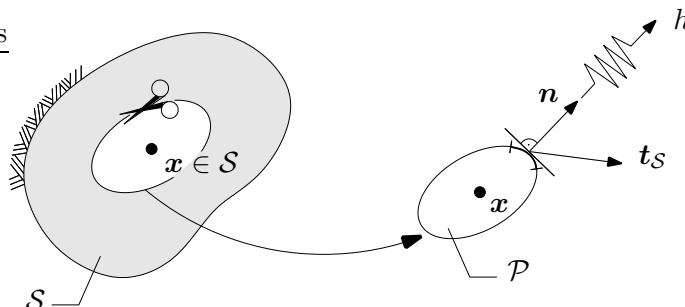


**Figure 2.4:** Euler's cut principle. The effects of the remaining part  $\mathcal{S} \setminus \mathcal{P}_S$  with respect to the cut out part  $\mathcal{P}_S$  are replaced by a surface traction vector  $\mathbf{t}_S$  and a heat flux  $h$

**2.2.1. Representations of the Stress Tensor.** Multiplication of the traction vector  $\mathbf{t}_S \in T_x\mathcal{S}$  with an infinitesimal surface element  $da$  gives the infinitesimal force vector

$$d\mathbf{f} = \mathbf{t}_S da \quad (2.26)$$

acting on the infinitesimal area  $da$  within the cut-surface  $\partial\mathcal{P}_S$ . According to *Cauchy's theorem*, the surface traction vector  $\mathbf{t}_S$  is a linear function of the *surface normal*  $\mathbf{n} \in T_x^*\mathcal{S}$

$$\mathbf{t}_S(\mathbf{x}, t, \mathbf{n}) =: \boldsymbol{\sigma}(\mathbf{x}, t) \cdot \mathbf{n} \quad (2.27)$$

where  $\boldsymbol{\sigma}$  is the *true Cauchy stress tensor* relating the actual force in the cut-surface to the actual deformed area. Thereby  $\boldsymbol{\sigma}$  is a fully covariant tensor mapping from the spatial cotangent space  $T_x^*\mathcal{S}$  to the tangent space  $T_x\mathcal{S}$

$$\boldsymbol{\sigma} : \begin{cases} T_x^*\mathcal{S} \rightarrow T_x\mathcal{S} \\ \mathbf{n} \mapsto \mathbf{t}_S = \boldsymbol{\sigma} \cdot \mathbf{n}, \quad t_S^a = \sigma^{ab} n_b \end{cases} \quad (2.28)$$

Weighting  $\boldsymbol{\sigma}$  with the Jacobian determinant  $J$  defines the *Kirchhoff stress tensor*  $\boldsymbol{\tau} = J\boldsymbol{\sigma}$ .

Relating the actual infinitesimal force vector  $d\mathbf{f}$  in analogy to (2.26) to a surface element  $dA$  of the corresponding undeformed (subscript  $\mathcal{B}$ ) cut-surface  $\partial\mathcal{P}_B$  defines the so-called *nominal surface traction vector*  $\mathbf{t}_B \in T_x\mathcal{S}$

$$d\mathbf{f} = \mathbf{t}_B dA \quad (2.29)$$

In analogy to (2.27),  $\mathbf{t}_B$  is a linear function of the *Lagrangian surface normal*  $\mathbf{N} \in T_X^*\mathcal{B}$

$$\mathbf{t}_B(\mathbf{X}, t, \mathbf{N}) =: \mathbf{P}(\mathbf{X}, t) \cdot \mathbf{N} \quad (2.30)$$

which implies the definition of the so-called *nominal stress tensor* or *first Piola Kirchhoff stress tensor*  $\mathbf{P}$  relating the actual force to an undeformed area element in the reference configuration. Thus  $\mathbf{P}$  maps normals from  $T_X^*\mathcal{B}$  to traction vectors in  $T_x\mathcal{S}$

$$\mathbf{P} : \begin{cases} T_X^*\mathcal{B} \rightarrow T_x\mathcal{S} \\ \mathbf{N} \mapsto \mathbf{t}_B = \mathbf{P} \cdot \mathbf{N}, \quad t_B^a = P^{aB} N_B \end{cases} \quad (2.31)$$

Insertion of (2.27) into (2.26) and of (2.30) into (2.29) gives with the Nanson formula (2.15) the following identification for the Kirchhoff/Cauchy stress tensor and  $\mathbf{P}$

$$\boldsymbol{\tau} \cdot \mathbf{F}^{-T} = J \boldsymbol{\sigma} \cdot \mathbf{F}^{-T} = \mathbf{P} \quad (2.32)$$

Finally, the formal introduction of the *Lagrangian surface traction vector*  $\mathbf{T}_B \in T_{\mathbf{X}}\mathcal{B}$ , obtained through formal transformation of  $\mathbf{t}_B$  to the Lagrangian tangent space  $T_{\mathbf{X}}\mathcal{B}$

$$\mathbf{T}_B := \mathbf{F}^{-1} \cdot \mathbf{t}_B \quad (2.33)$$

implies the definition of the fully Lagrangian *second Piola Kirchhoff stress tensor*  $\mathbf{S}$

$$\mathbf{S} : \begin{cases} T_{\mathbf{X}}^*\mathcal{B} \rightarrow T_{\mathbf{X}}\mathcal{B} \\ \mathbf{N} \mapsto \mathbf{T}_B = \mathbf{S} \cdot \mathbf{N}, \quad T_B^A = S^{AB} N_B \end{cases} \quad (2.34)$$

which is a purely geometric construct without any real physical meaning. The relation between  $\mathbf{S}$  and  $\mathbf{P}$  or  $\boldsymbol{\sigma}$  follows directly by insertion of (2.30) into (2.33) with (2.32) and (2.34) giving the result

$$\mathbf{S} = \mathbf{F}^{-1} \cdot \mathbf{P} = J \mathbf{F}^{-1} \cdot \boldsymbol{\sigma} \cdot \mathbf{F}^{-T} \quad (2.35)$$

Obviously  $\mathbf{S}$  is the pull-back of the Kirchhoff stresses  $\boldsymbol{\tau}$ . The commutative representations of the stress relations introduced in this section are visualized in figure 2.5.

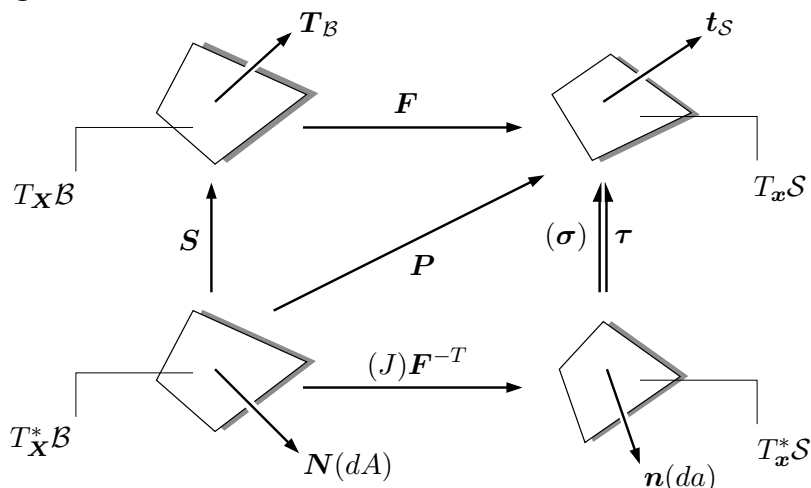


**Figure 2.5:** Definition of stress tensors. The four stress tensor representations  $\sigma$ ,  $\tau$ ,  $\mathbf{P}$  and  $\mathbf{S}$  are commutatively related through the tangent mapping  $\mathbf{F}$  and the normal mapping  $\mathbf{F}^{-T}$ .

**2.2.2. Heat Flux.** As visualized in figure 2.4, the thermal effects of the remaining part of the body  $\mathcal{S} \setminus \mathcal{P}_S$  onto the part  $\mathcal{P}_S$  are represented by the scalar heat flux  $h$  acting in outward normal direction  $\mathbf{n}$  on the cut-surface  $\partial\mathcal{P}_B$ . In analogy to Cauchy's stress theorem, *Stoke's heat flux theorem* postulates that  $h$  is a linear function of the unit normal vector

$$h(\mathbf{x}, t, \mathbf{n}) = \mathbf{q}(\mathbf{x}, t) \cdot \mathbf{n} \quad (2.36)$$

where  $\mathbf{q}$  is the *true* or *Cauchy heat flux vector* defined per unit deformed area. Relating the heat flux similarly to the undeformed area defines the *nominal heat flux vector*  $\mathbf{Q}$ . Through the identification  $\mathbf{q} \cdot \mathbf{n} da = \mathbf{Q} \cdot \mathbf{N} dA$  and with Nanson's formula (2.15), the nominal heat flux vector can be expressed in terms of the Cauchy heat flux vector by

$$\mathbf{Q} = J \mathbf{F}^{-1} \cdot \mathbf{q} \quad (2.37)$$

### 2.3. Balance Principles

In the following the classical *balance principles*, i.e. conservation of mass, the momentum balance principles and the balance of energy as well as the entropy *inequality principle* will be discussed. These principles apply to all materials and have to be satisfied at any time. They are formulated as *global* or *integral forms* valid for a cut-out part  $\mathcal{P}_S$  of the body. For sufficiently regular  $\varphi_t$ , *local* or *differential forms* of these principles, valid for any  $\mathbf{x} \in \mathcal{S}$ , can be derived from the global forms using the Gauss theorem for the transformation between surface and volume integrals and applying the localization theorem.

**2.3.1. Reynold's Transport Theorem.** In the following all balance equations will be formulated for the spatial configuration. The corresponding developments in the material configuration are straightforward and in complete analogy to the subsequent considerations. The *material time derivative*, i.e. the temporal change of a quantity  $(\bullet)$  at an arbitrary but fixed point of the reference configuration is denoted with  $d/dt(\bullet) = \overline{(\bullet)}$  and consists for Eulerian fields  $f(\mathbf{x}, t)$  of two parts, a local part and a convective part according to  $\dot{f}(\mathbf{x}, t) = \partial f / \partial t + \nabla_{\mathbf{x}} f \cdot \dot{\mathbf{x}}$ . A very useful relationship for spatial scalar fields is the following integral equation, often referred to as *Reynold's transport theorem*

$$\frac{d}{dt} \int_{\mathcal{P}_S} f(\mathbf{x}, t) dv = \int_{\mathcal{P}_S} \dot{f} + f \operatorname{div}[\dot{\mathbf{x}}] dv = \int_{\mathcal{P}_S} \dot{f} dv + \int_{\partial \mathcal{P}_S} f \dot{\mathbf{x}} \cdot \mathbf{n} da \quad (2.38)$$

This relation is obtained after some algebraic manipulations which take into account that in the Eulerian setting integration and time differentiation do not commute since  $\mathcal{P}_S$  is time dependent.

**2.3.2. Conservation of Mass.** Throughout this work, only *non-relativistic* physics for closed systems are considered. Hence the mass of a body or of any part of it is a *conserved quantity*, i.e.

$$M_{\mathcal{P}_B} = m_{\mathcal{P}_S} > 0 \quad \text{and} \quad \dot{M}_{\mathcal{P}_B} = \dot{m}_{\mathcal{P}_S} = 0 \quad (2.39)$$

where

$$M_{\mathcal{P}_B} = \int_{\mathcal{P}_B} \rho_0 dV \quad \text{and} \quad m_{\mathcal{P}_S} = \int_{\mathcal{P}_S} \rho dv \quad (2.40)$$

in terms of the *reference mass density*  $\rho_0$  and the *spatial mass density*  $\rho$ . Insertion of (2.40) into (2.39) gives after application of the localization theorem the two local forms

$$\rho_0 - J\rho = 0 \quad \text{and} \quad \dot{\rho} + \rho \operatorname{div}[\dot{\mathbf{x}}] = 0 \quad (2.41)$$

(2.41)<sub>1</sub> is obtained through insertion of (2.40)<sub>1</sub> and (2.40)<sub>2</sub> into (2.39)<sub>1</sub> together with (2.16) and (2.41)<sub>2</sub> follows by insertion of (2.40)<sub>2</sub> into (2.39)<sub>2</sub> in connection with (2.38).

**2.3.3. Momentum Balance Principles.** The *linear* and *angular momentum*  $\mathbf{I}_{\mathcal{P}_S}$  and  $\mathbf{D}_{\mathcal{P}_S}$  of a part  $\mathcal{P}_S$  of the body are defined by

$$\mathbf{I}_{\mathcal{P}_S} := \int_{\mathcal{P}_S} \rho \dot{\mathbf{x}} dv \quad \text{and} \quad \mathbf{D}_{\mathcal{P}_S} := \int_{\mathcal{P}_S} \mathbf{x} \times \rho \dot{\mathbf{x}} dv \quad (2.42)$$

The momentum balance principles postulate that the temporal change of the linear and the angular momentum respectively equal the *resultant force*  $\mathbf{F}_{\mathcal{P}_S}$  and the *resultant moment*  $\mathbf{M}_{\mathcal{P}_S}$  acting on the part  $\mathcal{P}_S$  of the body. Hence the *balance of linear momentum* and the *balance of angular momentum* read

$$\dot{\mathbf{I}}_{\mathcal{P}_S} = \mathbf{F}_{\mathcal{P}_S} \quad \text{and} \quad \dot{\mathbf{D}}_{\mathcal{P}_S} = \mathbf{M}_{\mathcal{P}_S} \quad (2.43)$$

The momentum balance principles are generalizations of Newton's first and second principle of motion within the context of continuum mechanics. The resultant force and moment developing due to the body forces  $\rho\mathbf{b}$  and surface tractions  $\mathbf{t}_S$  have the forms

$$\mathbf{F}_{\mathcal{P}_S} = \int_{\mathcal{P}_S} \rho\mathbf{b} dv + \int_{\partial\mathcal{P}_S} \mathbf{t}_S da \quad \text{and} \quad \mathbf{M}_{\mathcal{P}_S} = \int_{\mathcal{P}_S} \mathbf{x} \times \rho\mathbf{b} dv + \int_{\partial\mathcal{P}_S} \mathbf{x} \times \mathbf{t}_S da \quad (2.44)$$

Application of the Gauss theorem gives the local form of the balance of linear momentum

$$\operatorname{div}[\boldsymbol{\sigma}] + \rho(\mathbf{b} - \dot{\mathbf{x}}) = \mathbf{0} \quad (2.45)$$

Similarly the local form of the balance of angular momentum is obtained after some lengthy reformulations. It states the symmetry of the Cauchy stresses

$$\boldsymbol{\sigma} = \boldsymbol{\sigma}^T \quad (2.46)$$

which, with the relations (2.32) and (2.35), results also in symmetric Kirchhoff and second (but in general *not* first) Piola Kirchhoff stresses

$$\boldsymbol{\tau} = \boldsymbol{\tau}^T \quad \text{and} \quad \mathbf{S} = \mathbf{S}^T \quad (2.47)$$

**2.3.4. Balance of Energy.** In the present context the considerations are restricted to *thermodynamical* problems. Hence, besides the *mechanical* and *thermal* energy the effect of any other energy (e.g. electrical, chemical, nuclear) on the behavior of the continuum is neglected. The *first law of thermodynamics* governs, as a fundamental axiom in thermomechanics, the transformation of energy from one type into another. It demands that the rate of change of *total energy*  $E = K + U$  (*kinetic*  $K$  and *internal*  $U$ ) equals the *external mechanical power*  $P_{\text{ext}}$  plus the *thermal power*  $Q$ , i.e.

$$\overline{(K + U)} = P_{\text{ext}} + Q \quad (2.48)$$

associated with the cut-out part  $\mathcal{P}_S$ . The kinetic and internal energy are defined through

$$K := \int_{\mathcal{P}_S} \frac{1}{2} \rho \dot{\mathbf{x}} \cdot \dot{\mathbf{x}} dv \quad \text{and} \quad U := \int_{\mathcal{P}_S} \rho u dv \quad (2.49)$$

in terms of the *internal energy density*  $u$  per unit mass. The external mechanical power  $P_{\text{ext}}$  supplied by the surface tractions and body forces and the thermal power  $Q$  supplied by heat fluxes and heat sources read

$$P_{\text{ext}} := \int_{\mathcal{P}_S} \dot{\mathbf{x}} \cdot \rho\mathbf{b} dv + \int_{\partial\mathcal{P}_S} \dot{\mathbf{x}} \cdot \mathbf{t}_S da \quad \text{and} \quad Q := \int_{\mathcal{P}_S} \rho r dv - \int_{\partial\mathcal{P}_S} \mathbf{q} \cdot \mathbf{n} da \quad (2.50)$$

in terms of the *heat supply*  $r$  per unit time and unit mass. The balance of total energy (2.48) can be split up into two parts, the *balance of kinetic energy* and the *balance of internal energy* (note that independently  $K$  and  $U$  are *not* conserved quantities). The balance of kinetic energy is equivalent to the equilibrium condition and follows by multiplication of (2.43) with the velocity  $\dot{\mathbf{x}}$  and subsequent integration over the volume, i.e.

$$\dot{K} = P_{\text{ext}} - P_{\text{int}} \quad (2.51)$$

This implies the definition of the so-called *stress power*  $P_{\text{int}}$

$$P_{\text{int}} := \int_{\mathcal{P}_S} \boldsymbol{\sigma} : \mathbf{d} \, dv \quad (2.52)$$

in terms of the *rate of deformation tensor*  $\mathbf{d} := 1/2(\mathbf{g} \cdot \mathbf{l} + \mathbf{l}^T \cdot \mathbf{g})$  defined as the symmetric part of the covariant *spatial velocity gradient*  $\mathbf{g} \cdot \mathbf{l} := \mathbf{g} \cdot \partial_{\mathbf{x}} \dot{\mathbf{x}}$ . (2.48) together with (2.51) implies the following form of the *balance of internal energy*

$$\dot{U} = Q + P_{\text{int}} \quad (2.53)$$

which finally induces the *local form of the balance of internal energy*

$$\rho \dot{u} = \boldsymbol{\sigma} : \mathbf{d} - \text{div}[\mathbf{q}] + \rho r \quad (2.54)$$

**2.3.5. Entropy Inequality Principle.** The first law of thermodynamics governs the energy transfer but not its direction. Based on the *entropy* as a fundamental state variable which measures microscopic randomness and disorder, the direction of energy transfer can be described through the *second law of thermodynamics*. The second law demands that the entropy production is never negative, i.e.

$$\Gamma = \dot{H} - \tilde{Q} \geq 0 \quad (2.55)$$

where  $\Gamma$ ,  $H$  and  $\tilde{Q}$  denote the *entropy production*, the *entropy* and the *rate of entropy input* respectively. These quantities are defined through

$$\Gamma = \int_{\mathcal{P}_S} \rho \gamma \, dv, \quad H = \int_{\mathcal{P}_S} \rho \eta \, dv, \quad \tilde{Q} = \int_{\mathcal{P}_S} \rho \tilde{r} \, dv - \int_{\partial \mathcal{P}_S} \tilde{\mathbf{q}} \cdot \mathbf{n} \, da \quad (2.56)$$

in terms of the *local entropy production*  $\gamma(\mathbf{x}, t)$  and the *local entropy*  $\eta(\mathbf{x}, t)$  per unit mass and with the *entropy sources*  $\tilde{r}$  and the *entropy flux vector*  $\tilde{\mathbf{q}}$  per unit time and mass/surface area, respectively. A thermodynamic process which takes place without any entropy production ( $\Gamma = 0$ ) is called *reversible*. An *irreversible* process is always related to a dissipation of energy. A general assumption is to relate the entropy sources and fluxes to the heat sources and fluxes through  $\tilde{r} = r/\theta$  and  $\tilde{\mathbf{q}} = \mathbf{q}/\theta$  in terms of the absolute temperature  $\theta$ . Insertion of these relations and the definitions (2.56) into (2.55) gives with the localization theorem the local form of the so-called *Clausius-Duhem inequality*

$$\rho \gamma = \rho \dot{\eta} - \rho \frac{r}{\theta} + \frac{1}{\theta} \text{div}[\mathbf{q}] - \frac{1}{\theta^2} \mathbf{q} \cdot \nabla_{\mathbf{x}} \theta \geq 0 \quad (2.57)$$

Insertion of (2.54) into (2.57) gives, with the *Helmholtz free energy* per unit mass defined through the Legendre transformation  $\Psi = u - \theta \eta$ , the alternative representation of the Clausius-Duhem inequality

$$\theta \rho \gamma = \boldsymbol{\sigma} : \mathbf{d} - \rho \dot{\Psi} - \rho \dot{\theta} \eta - \frac{1}{\theta} \mathbf{q} \cdot \nabla_{\mathbf{x}} \theta \geq 0 \quad (2.58)$$

Introducing by definition the dissipation  $\mathcal{D} := \theta \rho \gamma$ , a stronger form of (2.58) is obtained for separate investigation of the *local dissipation*  $\mathcal{D}_{\text{loc}}$  through the so-called *Clausius-Planck inequality* and the *conductive dissipation*  $\mathcal{D}_{\text{con}}$  through the *Fourier inequality*, i.e.

$$\mathcal{D}_{\text{loc}} = \boldsymbol{\sigma} : \mathbf{d} - \rho \dot{\Psi} - \rho \dot{\theta} \eta \geq 0 \quad \text{and} \quad \mathcal{D}_{\text{con}} = -\frac{1}{\theta} \mathbf{q} \cdot \nabla_{\mathbf{x}} \theta \geq 0 \quad (2.59)$$

### 3. Fundamentals of Metal Crystals

Before starting with the continuum mechanical description of crystal plasticity in the next chapter, some fundamentals of metal crystals will be reviewed in the following. This brief summary is by no means complete. For a more detailed discussion see e.g. TROOST [152], HULL & BACON [64] or HONEYCOMBE [63] among others.

#### 3.1. The Crystal Structure

Metals and many other important solids possess a *crystalline structure*, i.e. the constituent atoms are arranged in a selfrepeating 3-dimensional structure, the so-called *space lattice*, see figure 3.1 a) for a visualization (constraining the considerations to metal crystals in the following each *lattice point* is assumed to reflect at least the *outer* lattice symmetry). Since the lattice exhibits several distinct directions the single crystalline material behavior is strongly direction dependent, i.e. anisotropic. Thus it is important to classify the respective lattices by their symmetry properties in order to gain insight into the type of anisotropy to be expected. The smallest unit, which by successive arrangement reproduces the space lattice, is the *unit cell*. The unit cell and consequently also the space lattice is uniquely described by the *grid vectors*  $\mathbf{a}$ ,  $\mathbf{b}$  and  $\mathbf{c}$ , or alternatively by the three *grid constants*  $a$ ,  $b$  and  $c$  and the corresponding angles  $\alpha$ ,  $\beta$  and  $\gamma$ , see figure 3.1 b). The spe-

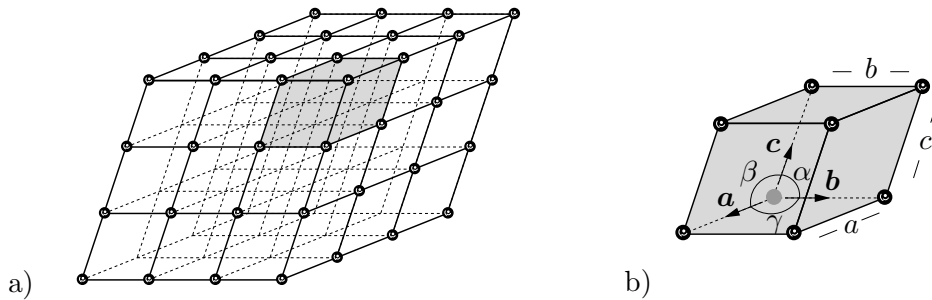


**Figure 3.1:** Space lattice, a), and primitive unit cell, b).

cific choice of the unit cell selected in order to represent the space lattice is not unique. A natural choice, however also not unique, is the *primitive unit cell* which contains in total one (eight times one eighth) lattice point, i.e. atom, as depicted in figure 3.1 b). Nevertheless, the symmetries and thus the anisotropy directions of the crystal structure are in many cases more easily visible through *non-primitive unit cells* like the *C*-, *B*- or *F*-centered unit cell containing in total 2, 2 or 4 atoms, respectively, see figure 3.2. Based

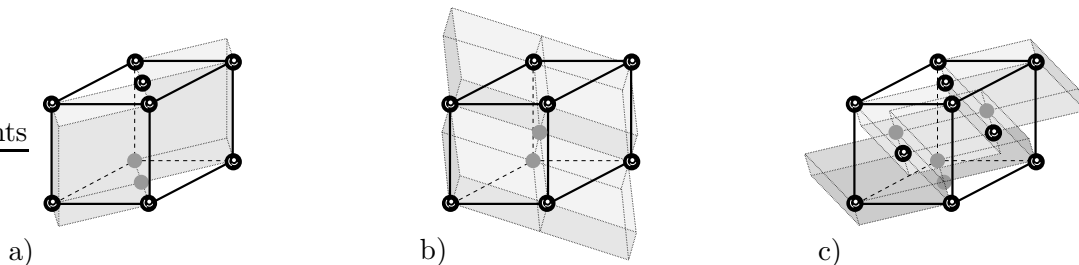


**Figure 3.2:** Non-primitive unit cells. a) C-, b) B- and c) F-centered unit cell.

on the inherent symmetry properties of the lattice, it is possible to differentiate in total 14 distinct *Bravais lattices* which comprise of 14 different primitive unit cells. To clarify the

**Table 3.1:** Bravais cells for the classification of the 14 Bravais lattices

Symmetry	Primitive	C-centered	B-centered	F-centered
triclinic: $a, b, c$ arbitrary, $\alpha, \beta, \gamma$ arbitrary				
monoclinic: $a, b, c$ arbitrary, $\alpha = \gamma = \frac{\pi}{2} \neq \beta$				
orthorhombic: $a, b, c$ arbitrary, $\alpha = \beta = \gamma = \frac{\pi}{2}$				
tetragonal: $a = b \neq c$ , $\alpha = \beta = \gamma = \frac{\pi}{2}$				
trigonal: $a = b = c$ , $\alpha = \beta = \gamma \neq \frac{\pi}{2}$				
hexagonal: $a = b \neq c$ , $\alpha = \beta = \frac{\pi}{2} = \frac{1}{3}\gamma$				
cubic: $a = b = c$ , $\alpha = \beta = \gamma = \frac{\pi}{2}$				

symmetry properties usually 14 *Bravais cells* are used to classify these Bravais lattices. 7 of the Bravais cells are primitive cells and, as stated above in order to point out the symmetries more directly, the remaining 7 cells are C-, B- and F-centered cells having the same shape as the corresponding primitive cell. See table 3.1 for a visualization. The most general unit cell with the least symmetry properties is the *primitive triclinic unit cell* with

$$a \neq b \neq c \quad \text{and} \quad \alpha \neq \beta \neq \gamma \quad (3.1)$$

The only possible symmetry operations for this cell are the identity and the inversion. In contrast, the unit cell with the highest symmetry is the *cubic unit cell* with

$$a = b = c \quad \text{and} \quad \alpha = \beta = \gamma \quad (3.2)$$

Further important lattice parameters are the *packing density*  $P$  and the *stacking sequence*. Thinking of the atoms as spheres contacting one another, the packing density is

$$P = \frac{V_s}{V} \quad (3.3)$$

where  $V_s$  is the part of the volume of the atoms which lies within the unit cell and  $V = a \cdot b \cdot c$  is the unit cell volume itself. Clearly among the cubic unit cells the *primitive cubic (pc) cell* has the lowest density ( $P = \frac{\pi}{6} \approx 0.524$ ) since the atoms are just arranged on top of one another and touch themselves along the cube edges. This results in a stacking sequence of *AAA...*. Consequently, a crystal structure comprised of this unit cell can be sheared off relatively easy. Arranging an atom on the spatial diagonal of the *body centered cubic (bcc) cell* results already in a stiffer structure with a density of  $P = \frac{\sqrt{3}}{8}\pi \approx 0.680$ . Thereby the atoms touch along the spatial diagonal and the layers have a stacking sequence of *ABAB...* (i.e. the atoms of every second layer are positioned axially on top of one another). Finally, the closest packing density ( $P = \frac{\pi}{6}\sqrt{2} \approx 0.74$ ) is obtained with the *face centered cubic (fcc) cell* (stacking sequence *ABCABC...*) and the more complicated *hexagonal closest packed (hcp) cell* (stacking sequence *ABAB...*). Some examples for the most important crystal lattices are the following metals

$$\begin{aligned} \text{bcc} &: \text{Li, Cr, Nb, Mo, Ta, W, } \alpha\text{-Fe, } \beta\text{-Ti} \\ \text{fcc} &: \text{Al, Ni, Cu, Ag, Pt, Au, Pb, } \gamma\text{-Fe} \\ \text{hcp} &: \text{Be, Mg, Co, Zr, } \alpha\text{-Ti} \end{aligned} \quad (3.4)$$

### 3.2. Miller Indices

As discussed above, the crystal structure induces a strongly direction dependent (i.e. anisotropic) behavior of a single crystalline material. Crystallographic directions can be indicated in a unique manner through the so-called *Miller indices*.

**3.2.1. Indication of Crystal Planes.** Any plane  $A'B'C'$  in figure 3.3 can be defined by the intercepts  $a' = ma, b' = nb, c' = pc$  with the three principal axis ( $a, b$  and  $c$  are the

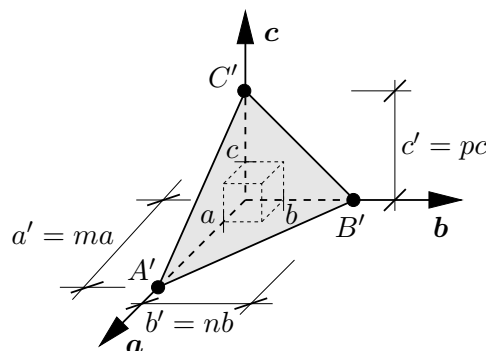


**Figure 3.3:** Intercepts of a plane with the grid triad, used in order to compute the Miller indices which specify the plane position.

grid constants of the underlying crystal lattice). The Miller indices  $(hkl)$  are computed from the intercepts by first taking the reciprocals of the coefficients  $\frac{1}{m}, \frac{1}{n}, \frac{1}{p}$  and subsequent multiplication with the common denominator  $N$  of the nonzero reciprocals

$$(hkl) = \left( \frac{N}{m} \frac{N}{n} \frac{N}{p} \right) \quad (3.5)$$

By definition, the Miller indices are written within parentheses. If several planes are of the same crystallographic type, they can be collectively described by writing the Miller indices of one representative plane in curly braces  $\{hkl\}$ . E.g. the planes  $(111)$ ,  $(11\bar{1})$ ,  $(\bar{1}11)$  and  $(1\bar{1}1)$  can be collectively described by  $\{111\}$  for cubic crystals. Thereby the bar indicates that the plane cuts the respective axis on the negative side of the origin. Some important crystallographic planes in the cubic lattice are depicted in figure 3.4 along with their Miller indices.

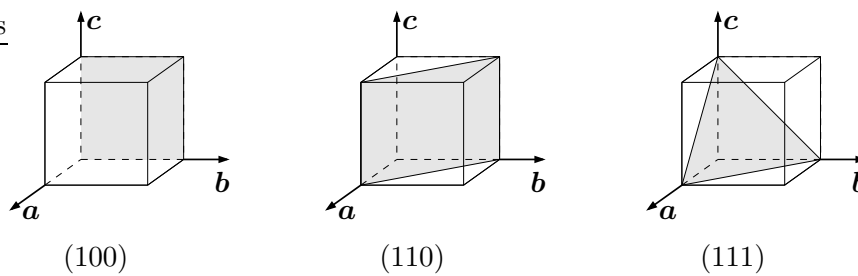


**Figure 3.4:** Selected crystallographic planes in the cubic lattice.

**3.2.2. Indication of Directions.** To describe a direction in terms of Miller indices, the direction is first represented by a parallel line through the origin of the crystallographic coordinate system, see figure 3.5. Then the Miller indices  $[uvw]$  are directly obtained by multiplication of the coefficients  $r, s, t$  with their common denominator  $N$

$$[uvw] = [Nr Ns Nt] \quad (3.6)$$

By definition, the Miller indices of a direction are written within square brackets. If several directions are of the same crystallographic type, they can be collectively described by putting the Miller indices of one representative direction in angular brackets. E.g. the directions  $[111]$ ,  $[\bar{1}11]$ ,  $[11\bar{1}]$  and  $[1\bar{1}1]$  can be represented by  $\langle 111 \rangle$  in a cubic crystal.

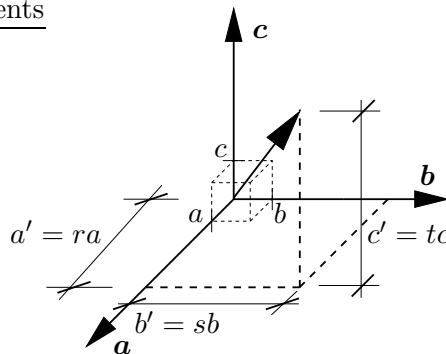


**Figure 3.5:** Description of a direction by Miller indices.

Note that in cubic crystals the Miller indices of a plane ( $hkl$ ) are the same as the indices of a direction  $[uvw]$  normal to that plane, i.e.  $h = u, k = v$  and  $l = w$ . A further extension of the Miller-Bravais indices for hexagonal systems will not be considered here.

### 3.3. Closest Packed Crystal Planes

The closest packed crystal planes of the three cubic lattices are visualized in figure 3.6 along with their in plane packing densities  $D_P$ . This packing density plays a crucial role in the deformability of the crystal lattice. As also explained below, plastic slip occurs mainly

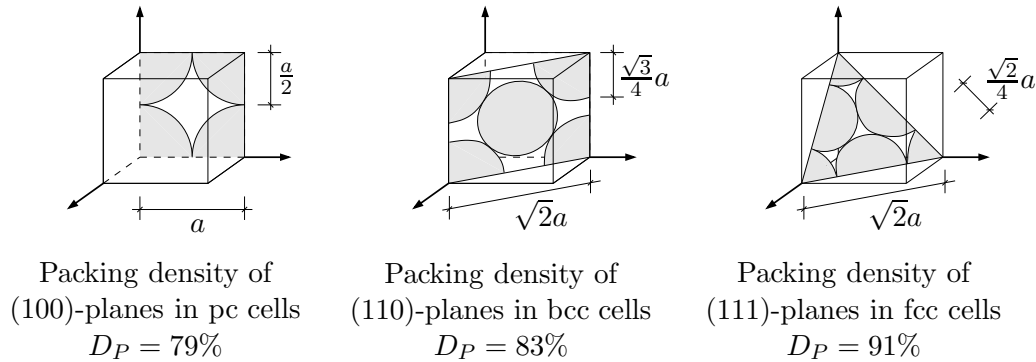


**Figure 3.6:** Packing density  $D_P$  in closest packed planes in the cubic lattices.

in the direction of highest packing density (*slip direction*) within the closest packed crystal planes (*slip plane*). These directions are for the pc cell the  $\langle 100 \rangle$ -, for the bcc cell the  $\langle 111 \rangle$ - and for the fcc cell the  $\langle 110 \rangle$ -directions.

### 3.4. Visualization of Crystallographic Directions

Crystal orientations, e.g. the spatial orientation of crystallographic planes, can be represented in an effective manner by means of a sphere. To this end, a reference sphere is chosen to circumscribe the crystal and the directions of interest are represented by their intercepts with this sphere. In order to finally get a two-dimensional visualization this three-dimensional point scatter needs to be projected onto a plane. This can be done in an effective manner through a *stereographic* or an *equal area projection*. In the following, the stereographic projection will be explained exemplarily for the representation of the spatial orientation of planes.

**Stereographic Projection.** Within the stereographic projection the equatorial plane is chosen as the plane of projection. The specific orientation of the equatorial plane can however be chosen arbitrarily. The south pole  $S$  is furthermore picked as the center of projection, see figure 3.7 a). The orientation of crystal planes is now obtained by simply connecting the intercept  $I$  of the plane normal with the center of projection  $S$  and subsequent determination of the intercept  $I'$  of this line with the plane of projection. Thereby only intercepts  $I$  of the northern hemisphere are taken into consideration. Selecting for example the  $[001]$ -direction of the crystal as plane normal for the equatorial plane gives the so-called standard projection which fully reveals the symmetry of the lattice. The standard projection of a cubic lattice is shown in figure 3.7 b) where the projection is divided, by intersecting great circles, into 24 unit stereographic triangles which are crystallographically identical. In each case the corners of the triangles represent the directions  $\langle 001 \rangle$ ,  $\langle 011 \rangle$  and  $\langle 111 \rangle$ . Thus a crystal orientation can be uniquely specified through only

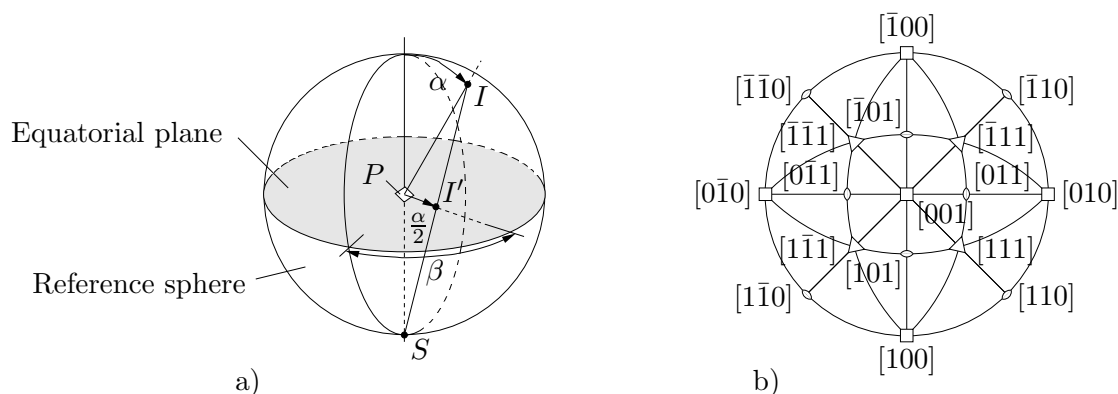


**Figure 3.7:** Stereographic projection. a) determination of the stereographic projection with  $P$  crystal plane,  $I$  intercept of the plane normal with the reference sphere and  $I'$  stereographic projection of the intercept  $I$ . b) standard cubic projection.

one triangle, customarily the position of the  $[001]$ ,  $[011]$ ,  $[\bar{1}11]$  triangle. On the other hand, the crystal orientation with respect to a macroscopic direction of the specimen (e.g. tensile axis, rolling direction or direction of the sheet normal) is also of interest. To this end,  $\langle uvw \rangle$ -pole figures are used where only the  $\langle uvw \rangle$ -poles of each plane of interest are visualized in a stereographic projection with respect to the designated specimen direction.

### 3.5. Defects in Crystalline Materials

In contrast to the *ideal crystals* considered so far, *real crystals* contain several *imperfections*. These can be differentiated into three groups. *Electrical defects* are concerned with e.g. local electric charge imperfections. *Chemical defects* are caused for example by *substitutional* or *interstitial impurity atoms* or *precipitates*. And finally *structural defects* are caused by deviations of the crystal lattice from its ideal structure. According to their spatial extension, these defects can be further differentiated into *point* (0-dimensional), *line* (1-dimensional), *surface* (2-dimensional) and *volume* (3-dimensional) defects. Some of these defects are visualized in figure 3.8 and are briefly explained in the following.

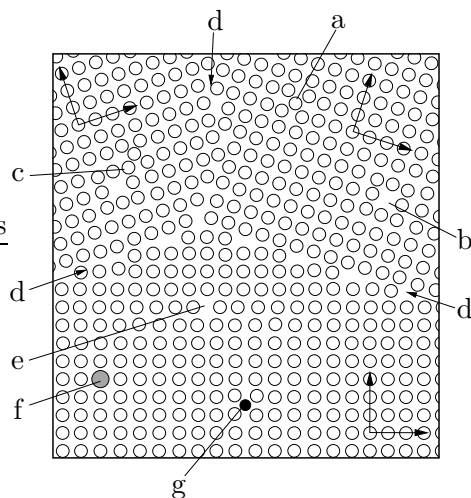


**Figure 3.8:** Two-dimensional cut through a crystalline structure with imperfections. (a) interstitial atom, (b) vacancy, (c) Frenkel pair, (d) grain boundary, (e) dislocation, (f) substitutional impurity atom, (g) interstitial impurity atom.

**Point Defects.** These can be either *intrinsic* zero-dimensional defects such as *vacancies*, *interstitial atoms* or the combination of both, so-called *Frenkel pairs*. Or they are caused by *extrinsic* defects such as *substitutional* or *interstitial impurity atoms*.

**Line Defects.** These are the most important defects in the context of the following crystal plasticity formulation and are denoted as *dislocations*. They are formed if e.g. half a lattice plane is missing or if a part of the lattice is displaced in opposite directions on either side of a two-dimensional surface, see section 3.6 for further details.

**Surface Defects.** The most important surface defects are *grain boundaries* which develop during *crystallization*. Thereby each grain is a single crystal of generally arbitrary orientation. If the misorientation between neighbouring grains is small, the boundary consists of an array of dislocations and is called *low angle grain boundary*. In contrast, the atomic arrangement at *high angle grain boundaries* is more complicated and varies significantly with the angle of misorientation. During crystallization impurities are also very likely to segregate at, or within the vicinity of, grain boundaries. Further examples of surface defects are *stacking faults* which occur e.g. in connection with *prismatic dislocation loops* (pure edge dislocation loops) or *partial dislocations*. And as a last example, *twin boundaries* also form surface defects, however these are not considered in further detail here.

**Volume Defects.** Examples for volume defects are precipitates and voids or bubbles which develop under certain circumstances.

### 3.6. Dislocations

One of the most important discoveries in metal physics certainly is the concept of *dislocations* introduced independently by OROWAN, POLANYI and TAYLOR in 1934. It was mainly the discrepancy between the strength of metals observed experimentally and the theoretical strength estimates for perfect crystals which led to the first purely theoretical introduction of the dislocation as a line defect. The subsequent experimental evidence of dislocations through *etch pits*, *transmission electron microscopy*, *X-ray diffraction*, *field ion microscopy* and other techniques greatly proved the validity of this concept in reality, significant not only in the process of plastic deformation itself but also in crystal growth, recovery and further phenomena.

**3.6.1. Theoretical Strength of a Crystal.** The *theoretical shear strength* of a perfect crystal was first estimated by FRENKEL in 1926. To this end, he considered as a simplified model two rows of atoms subjected to a shear stress. For convenience all considerations will be visualized for a primitive cubic crystal structure in the following. In their equilibrium positions, the atoms have a respective distance of  $a$ , see figure 3.9 a). In order to displace one atom-row (in 3D one atom-layer) by an amount  $\delta = \frac{x}{a}$  a deformation work  $W$  has to be performed for each atom, figure 3.9 b). Due to the periodicity of the lattice, this work and consequently the required shear stress  $\tau$  (figure 3.9 c)) derived from it is periodic and thus by assumption (with Hooke's law  $\tau = \frac{Gx}{a}$  for elastic deformations,  $x \ll a$ )

$$\tau(x) = \frac{G}{2\pi} \sin \frac{2\pi x}{a} \quad (3.7)$$

The maximum value of  $\tau$  occurs at  $x = \frac{a}{4}$  representing the theoretical critical shear stress

$$\tau_c^{th} = \frac{G}{2\pi} \approx 1,6 \cdot 10^{-1} G \quad (3.8)$$

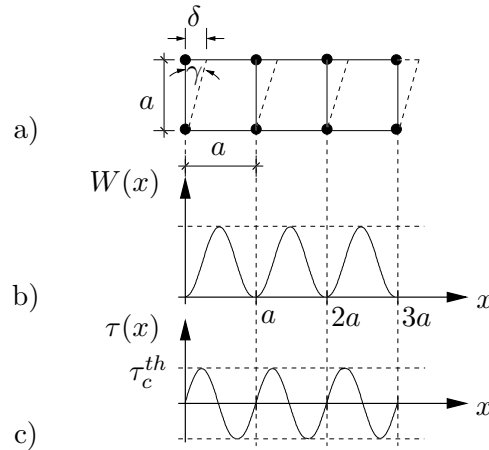


**Figure 3.9:** The theoretical shear strength of a primitive cubic lattice. a) simplified perfect crystal lattice, b) deformation work and c) required shear stress.

If the applied stress exceeds  $\tau_c^{th}$ , the lattice is rendered unstable and the top atom layer is likely to shear off and switch into the next stable equilibrium position. In contrast, the resolved shear stress for plastic slip measured in real well-annealed crystals  $\tau_c^{exp}$  is many orders of magnitude smaller and of the order  $\tau_c^{exp} \approx 10^{-4} G$ . Thus there is a significant difference of an order of 1000 between  $\tau_c^{th}$  and  $\tau_c^{exp}$ . This difference can be explained by accounting for an imperfect lattice structure of the real crystal which led OROWAN, POLANYI and TAYLOR in 1934 independently to the concept of *dislocations*.

Motivated by the considerations of FRENKEL, the theoretical strength of an imperfect crystal can be explained by the following *corrugated sheet model*. Consider first again an ideal crystal modeled by the corrugated sheet in figure 3.10. Thereby each of the  $Z$  sinks (= stable equilibrium positions) is occupied by an atom. Aiming at a plastic deformation,

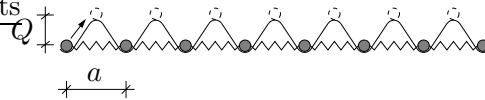


**Figure 3.10:** Corrugated sheet model. Representation of one atom row of a perfect crystal.

the first atom needs to be lifted to the top which requires an energy  $Q$  before it can fall into the next sink. Since each sink can always be occupied only by one atom, all subsequent atoms need to be displaced by an equal amount  $a$ , respectively, which is ensured through the interconnecting springs. This requires a relatively large amount of total energy  $Z \cdot Q$ ,

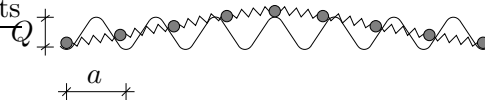


**Figure 3.11:** Corrugated sheet model. Representation of one atom row of a real crystal.

which can only be supplied through a very high shear stress  $\tau_c^{th}$  according to (3.8). If instead the real imperfect crystal is modeled with the corrugated sheet model, one gets the representation shown in figure 3.11. Due to the lattice defects in the real crystal, most of the atoms are now a priori in unstable positions which already facilitates plastic slip at small applied shear stresses. Particularly the middle atom in figure 3.11 is in an indifferent

equilibrium position where only a small amount of energy  $\Delta Q$  is sufficient to promote its displacement into the next sink. Such a defect is called *dislocation* and provides the key mechanism for plastic deformation.

**3.6.2. Dislocation Movement.** As can be deduced from figure 3.11, in a real crystal plastic deformation takes place through consecutive displacement of neighbouring atoms and not through shearing complete atom layers off like in the perfect crystal. Thus plastic deformation occurs by movement of the dislocation through the lattice. As soon as the dislocation reaches the crystal boundary, a slip step of one *Burgers vector length*  $b$  is produced. This is visualized for a 2-dimensional cut through a cubic lattice in figure 3.12.

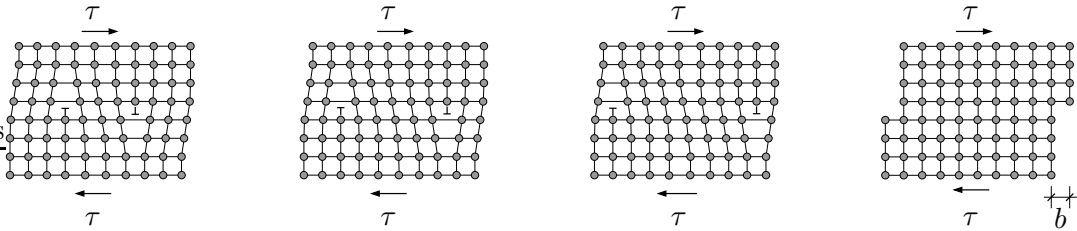


**Figure 3.12:** Glide of an edge-dislocation (symbol  $\perp$ ) under an applied shear stress  $\tau$ .

**3.6.3. The Burgers Vector.** A very effective definition of a dislocation is given in terms of the *Burgers circuit*. According to the definition given by FRANK [46], a Burgers circuit is any closed atom-to-atom path in the real crystal, figure 3.13 a). Taking the same path in a perfect dislocation free lattice, the circuit does not close if the real crystal contains dislocations, figure 3.13 b). The vector required to close the circuit in the perfect crystal is called the *Burgers vector*. Thereby it has been implied that the Burgers circuit is taken in the sense of a right hand rule looking in the direction of the dislocation line (e.g. within the two-dimensional cut through the dislocation line in figure 3.12, the dislocation line points paper-inward on the right-hand side ( $\perp$ ) and paper-outward on the left-hand side ( $\top$ )). If dislocations with the same line sense but opposite Burgers vector are brought together they annihilate and restore a perfect lattice. Dislocations whose Burgers

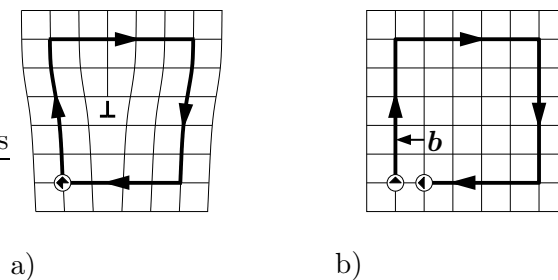


**Figure 3.13:** Determination of the Burgers vector of an edge dislocation. A closed Burgers circuit in the real crystal a) does not close in a corresponding perfect crystal b).

vector coincides with the shortest *crystallographic vector* (i.e. the shortest vector joining two adjacent lattice points) are called *perfect* or *unit dislocations* (in contrast to partial dislocations which will not be treated any further here). The Burgers vectors  $\mathbf{b}$  and their lengths  $b = |\mathbf{b}|$  for unit dislocations in the cubic lattices are given as follows (with the lattice parameter  $a$ )

$$\text{pc: } \mathbf{b} = \langle 100 \rangle, b = a; \quad \text{bcc: } \mathbf{b} = \frac{1}{2} \langle 111 \rangle, b = \frac{\sqrt{3}}{2} a; \quad \text{fcc: } \mathbf{b} = \frac{1}{2} \langle 110 \rangle, b = \frac{1}{\sqrt{2}} a \quad (3.9)$$

**3.6.4. Dislocation Loops.** Dislocations develop during crystallization from the melt and with ongoing plastic deformation. Generally they form a 3-dimensional *dislocation network* which comprises of *edge*, *screw* and *mixed dislocation* segments, see figure 3.14. Edge dislocations are characterized by the fact that the Burgers vector  $\mathbf{b}$  is always perpendicular to their line direction  $\mathbf{l}_\perp$  which defines a unique *slip plane* (shaded area in figure 3.14 a)). Thus the circumvention of obstacles within the slip plane requires climbing (*non-conservative motion*) of the dislocation or diffusion processes. This furthermore also induces a rather small annihilation distance between dislocations residing in parallel slip planes. In turn, screw dislocations are characterized by the fact that the Burgers vector  $\mathbf{b}$  is always parallel to their line direction  $\mathbf{l}_\odot$ , see figure 3.14 b). Thus  $\mathbf{b}$  and  $\mathbf{l}_\odot$  do not define a unique slip plane and consequently screw dislocations are not bounded to a specific slip plane. This facilitates the circumvention of obstacles and the annihilation of dislocation segments at large distances through cross slip. Any mixed dislocation can be resolved into pure edge and pure screw dislocations by splitting the Burgers vector into a part perpendicular and a part parallel to the line direction.

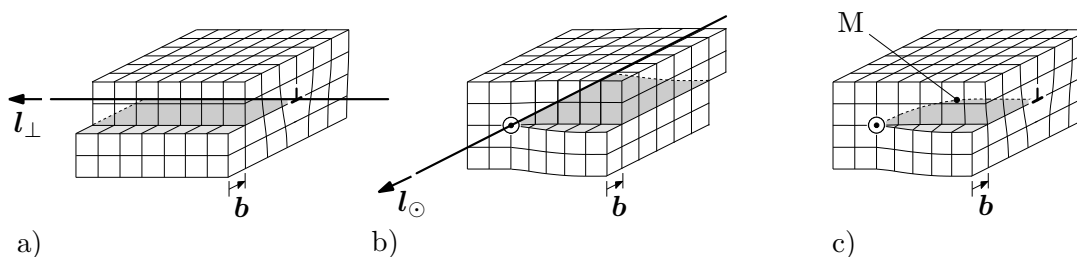


**Figure 3.14:** Geometry and movement of a) pure edge, b) pure screw and c) at M mixed dislocation segments. The dislocation line represents the boundary between slipped and unslipped crystal parts. A dislocation loop (c) comprises of all 3 kinds of dislocation segments.

**3.6.5. Dislocation Density.** A scalar measure for the number of dislocations which reside in a real crystal is given by the *dislocation density*  $\rho$  defined in terms of the total dislocation line length  $l$  per reference volume  $V$  or alternatively in terms of the number  $n$  of dislocations piercing a reference area  $A$

$$\rho = \frac{l}{V} \quad \text{or} \quad \rho' = \frac{n}{A} \quad (3.10)$$

In well-annealed metal crystals this density ranges typically between  $10^{10} \text{ m}^{-2}$  and  $10^{12} \text{ m}^{-2}$  which corresponds to a dislocation line length of  $10 \text{ m}$  to  $1 \text{ km}$  within a small crystal cube of  $1 \text{ mm}$  in width. This density rapidly increases with ongoing plastic deformation up to values of more than  $10^{15} \text{ m}^{-2}$ .

**3.6.6. Plastic Deformation through Dislocation Movement.** The main source of plastic deformation due to an applied shear stress is the expansion of *dislocation loops* (figure 3.15 a)) through *conservative dislocation movement* within the glide plane (figure 3.14). This is also denoted as *glide*. If a dislocation segment reaches the crystal boundary after moving over the slip plane (shaded areas in figure 3.14), a slip step equal to and in direction of the Burgers vector is produced. According to the simple visualization of a pure edge dislocation in figure 3.15 b), this results in a plastic shear strain  $\gamma$  of

$$\gamma = \frac{b}{h} \quad (3.11)$$

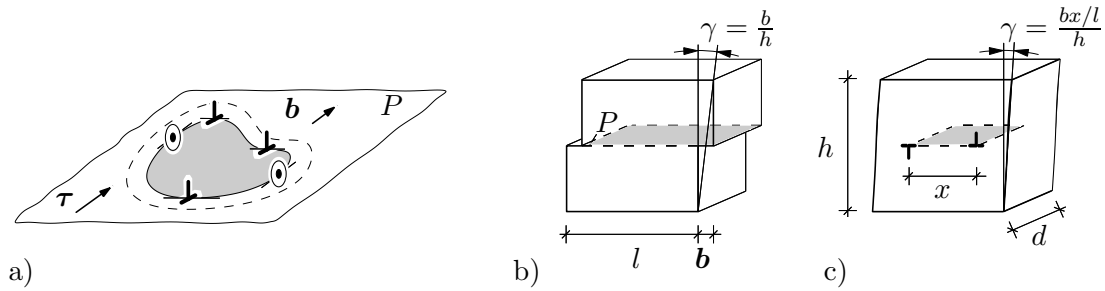


**Figure 3.15:** Plastic deformation through dislocation movement. a) expansion of a simple dislocation loop within the slip plane  $P$  due to a resolved shear stress  $\tau$ . Plastic shear strain  $\gamma$  induced by b) complete and c) partial sweep of an edge dislocation through the crystal.

However, if the dislocation did not fully traverse the crystal, the resulting shear strain is only a fraction of (3.11), according to the distance  $x$  covered so far, see figure 3.15 c)

$$\gamma = \frac{bx/l}{h} = \frac{bx}{lh} \quad (3.12)$$

The combined expansion of  $n$  mobile dislocations results in a total plastic shear strain

$$\gamma = \frac{b}{lh} \sum_{i=1}^n x_i \quad \Leftrightarrow \quad \gamma = b\rho \bar{x} \quad (3.13)$$

where the expansion  $x_i$  of each dislocation results in an average distance  $\bar{x} = \frac{1}{n} \sum_{i=1}^n x_i$  and the mobile dislocation density  $\rho$  follows according to (3.10)<sub>1</sub> as  $\rho = nd/lhd$ . Thus the strain rate follows with  $\rho = \text{const.}$  as

$$\dot{\gamma} = b\rho \dot{\bar{x}} \quad (3.14)$$

which is also known as Orowan-equation. In (3.14),  $\dot{\bar{x}}$  is the average dislocation velocity. Identical relations also hold for screw and mixed dislocations.

**3.6.7. Dislocation Multiplication.** As explained above dislocations develop during crystallization from the melt resulting in an initial density of  $\rho = 10^{10} \text{ m}^{-2} - 10^{12} \text{ m}^{-2}$  in well annealed metal crystals. With ongoing plastic deformation, this density rapidly increases through *dislocation multiplication* mainly by the action of *Frank-Read type sources* or other mechanisms such as the expansion of *prismatic loops*. The mechanism of the Frank-Read source is explained in figure 3.16. A dislocation segment of length  $l$  is pinned between two points  $A$  and  $B$ . The barriers  $A, B$  may be *intersections* with other dislocations, *nodes* of the dislocation network, *jogs* formed e.g. in the course of previous

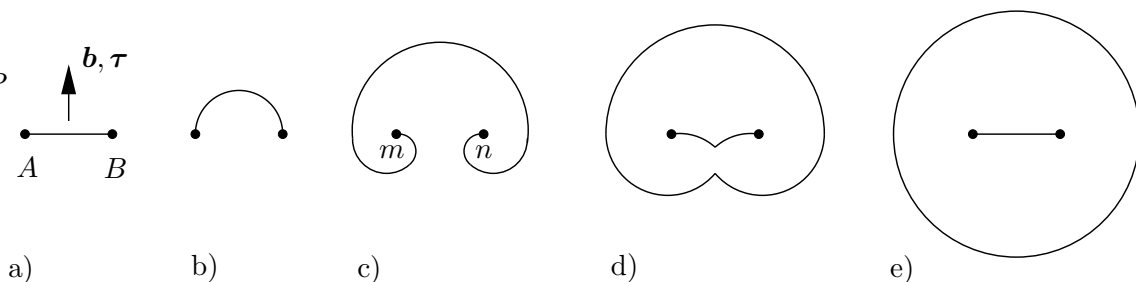


**Figure 3.16:** Illustration of the mechanism of dislocation multiplication through the action of a Frank-Read source.

dislocation intersections, *junctions* resulting from dislocation reactions, *fixed dislocation segments* of a non-planar dislocation loop resulting from *cross slip*, precipitates, etc. Upon the action of an applied shear stress, the dislocation bows out until the minimum radius of  $r = l/2$  is reached at the maximum shear stress  $\tau$ , figure 3.16 b). Thereby the dislocation becomes unstable and furthermore bows out with increasing radius  $r$ , figure 3.16 c), until the segments  $m$  and  $n$  mutually annihilate, figure 3.16 d). This results in a large outer loop which further expands and a new segment  $A-B$  which replicates the process, figure 3.16 e). In this manner up to 1000 dislocation loops can be emitted per source. This mechanism operates most effectively in combination with *multiple cross slip*. Thereby the screw section of a moving dislocation migrates through consecutive parallel planes, thus creating pairs of possibly immovable jogs.

### 3.7. Slip Systems

The strain energy per unit dislocation length, also denoted as *line energy*, is approximately

$$W_l = \alpha \mu b^2 \quad (3.15)$$

where  $\alpha \approx 0.5 - 1.0$  depending also on whether the dislocation is of screw, edge or mixed character. If the work performed per unit dislocation length by the applied shear stress within the slip plane exceeds this value, additional dislocation length is stored within the crystal through expansion, i.e. movement of the dislocation loop. This in turn results also in partial energy release through e.g. annihilation processes and eventually the formation of slip steps when the dislocation reaches the crystal boundary. Consequently, slip will preferably occur in the planes and directions of shortest Burgers vector  $b_{min}$ , thus minimizing the line energy  $W_{l_{min}} = \alpha \mu b_{min}^2$ . Since, according to the previous considerations, the Burgers vector is a crystallographic direction the *slip plane* is a closest packed crystallographic plane and the *slip direction* is the closest packed in plane direction, see section 3.3. Accordingly, the *slip systems* of an fcc crystal can be classified, following SCHMID & BOAS [130], by the slip plane (normal  $M^\alpha$ ) and the slip direction ( $S^\alpha$ ), see table 3.2 and figure 3.17. If, within a tension test, the stereographic projection of the tensile axis lies

**Table 3.2:** The 12 slip systems of an fcc lattice.

slip system	A2	A3	A6	B2	B4	B5	C1	C3	C5	D1	D4	D6
$M^\alpha$	( $\bar{1}11$ )	( $\bar{1}11$ )	( $\bar{1}11$ )	(111)	(111)	(111)	( $\bar{1}\bar{1}1$ )	( $\bar{1}\bar{1}1$ )	( $\bar{1}\bar{1}1$ )	(1 $\bar{1}1$ )	(1 $\bar{1}1$ )	(1 $\bar{1}1$ )
$S^\alpha$	[0 $\bar{1}1$ ]	[101]	[110]	[0 $\bar{1}1$ ]	[ $\bar{1}01$ ]	[ $\bar{1}10$ ]	[011]	[101]	[ $\bar{1}10$ ]	[011]	[ $\bar{1}01$ ]	[110]

within one of the designated stereographic triangles in figure 3.17 b), the indicated slip system will be activated since the resolved shear stress will have the highest value for this slip system.

### 3.8. Schmid's Law

If the orientation of the crystal is known, the slip system which will start to deform plastically under an applied load follows, according to the previous considerations, directly

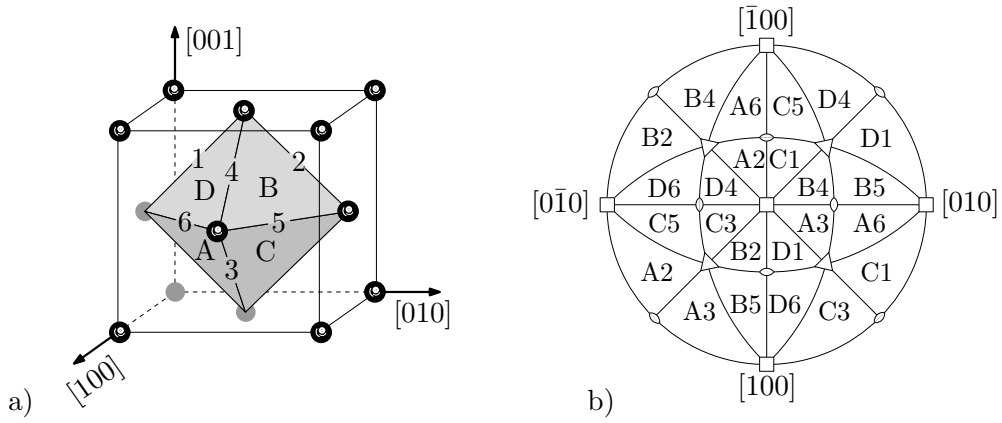


**Figure 3.17:** Slip Systems of fcc-crystals (after SCHMID & BOAS [130]). a) slip planes and slip directions defining 4 · 3 slip systems. b) standard stereographic projection showing the respective slip systems activated in a tension test.

from geometrical considerations. If the concern is e.g. with a tension test as depicted in figure 3.18 a), the *resolved or slip system projected shear stress*  $\tau^\alpha$  acting on system  $\alpha$  is readily verified as

$$\tau^\alpha = \sigma \mathbf{n} \otimes \mathbf{n} : \mathbf{S}^\alpha \otimes \mathbf{M}^\alpha = \frac{F}{A} \cos\phi^\alpha \cos\lambda^\alpha \quad \text{with} \quad \sigma = \frac{F}{A} \quad (3.16)$$

where  $A' = A/\cos\phi^\alpha$  is the area in a cut perpendicular to  $\mathbf{M}^\alpha$ , i.e. in the slip plane, and  $F\cos\lambda^\alpha$  is the force component in the slip direction  $\mathbf{S}^\alpha$ . Plastic slip commences if the resolved shear stress reaches a certain critical value, the so-called slip resistance  $\tau_r^\alpha$

$$\tau^\alpha = \tau_r^\alpha \quad (3.17)$$

The specific form of (3.17) at the initial yield point  $\tau_{r0}^\alpha$  is usually referred to as *Schmid's law* and analogously the resolved shear stress  $\tau^\alpha$  is also known as *Schmid stress*. However,  $\tau_r^\alpha$  changes significantly, especially for fcc crystals, with ongoing plastic deformation leading generally to a hardening response, see section 3.9. According to (3.16) and (3.17), slip

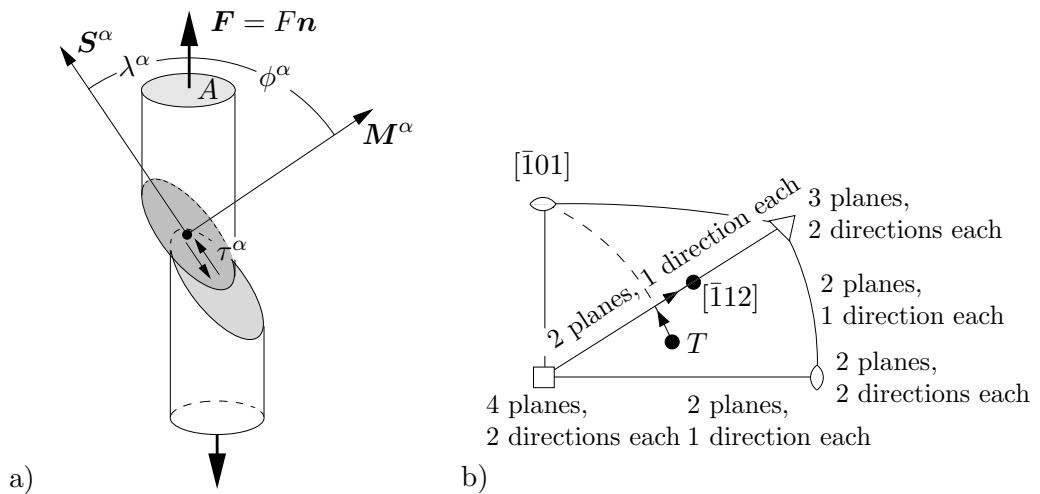


**Figure 3.18:** Schmid's law and operative slip systems. a) resolved shear stress in an uniaxial tension test. b) rotations during slip and activation of multislip.

will start on the slip system(s) with the highest *Schmid factor(s)*  $\cos\phi^\alpha\cos\lambda^\alpha \leq 0.5$ . I.e. if the tensile axis lies within one stereographic triangle in figure 3.17 b), slip commences on the corresponding slip system which is also denoted as *primary slip system*. However, with ongoing deformation the crystal rotates such that the slip direction tends to rotate towards the tensile axis. This is visualized vice versa in figure 3.18 b) for the standard stereographic triangle (B4) as a movement of the tensile axis  $T$  towards the  $[\bar{1}01]$  slip direction. As the tensile axis reaches the  $[001] - [\bar{1}11]$  boundary a second, so-called *conjugate*, slip system (C1) is activated resulting in double slip and a subsequent movement of the tensile axis along the  $[001] - [\bar{1}11]$  boundary up to the intersection with the great circle between the two operating slip directions at  $[\bar{1}12]$  where it stabilizes until failure of the specimen. (Thereby an *overshooting* due to latent hardening has been neglected.) In a compression test, the loading axis rotates similarly towards the  $[111]$  slip plane normal. Further cases in which the loading axis lies on the boundary or even in a corner of the stereographic triangle are depicted in figure 3.18 b). In the most complicated case, the  $[001]$ -orientation, 4 slip systems with 2 slip directions in each are equally favoured. This results in multislip and consequently a strong interaction between the dislocations on the various slip systems leading to high work hardening rates.

### 3.9. Work Hardening of Metal Crystals

Since the dislocations provide for the mechanism which induces a comparably low initial yield stress in real metal crystals, it is clear that any obstacle which hinders consecutive dislocation movement will suppress further plastic deformation unless the applied resolved shear stress is increased. This intriguing process by which the strength of the metal increases as it deforms is referred to as *work hardening*. Due to its complexity this is still a lively field of research which commences with the introduction of the dislocation concept itself. The following considerations will be restricted to *dislocation hardening* where the obstacles which impede the motion of a dislocation are provided by other dislocations. Further strengthening mechanisms which partially also have a main impact on the initial yield point are not considered here or are treated in chapter 5. Examples of such mechanisms are solid solution hardening, grain refinement or particle strengthening.

The earliest work hardening theory which based already on the idea that the strengthening results from mutual dislocation interactions was introduced by TAYLOR [147] in the form

$$\tau_r = c\mu b\sqrt{\rho} \quad (3.18)$$

where  $\tau_r$  is the specimen flow stress,  $\rho$  is the (total) dislocation density and  $c$  is a constant limited according to TAYLOR [147] by  $0.1 < c < \pi^{-1}$ . Within the proposed model, the hardening response is motivated by the stress required to force two edge dislocations on parallel slip planes past one another against their elastic stress fields. The resulting parabolic stress-strain relation was found to be fairly representative of experimental observations also for single crystals. However, by now it is known that such a response can only be viewed as a rough estimate since the barriers to dislocation motion evolve with ongoing deformation and the stress-strain curve of highly pure single crystals consequently exhibits a pronounced *three-stage* behaviour rather than a monotonous parabolic one.

**3.9.1. The Three Stage Hardening Response.** The three-stage behaviour is shown schematically for an fcc crystal, oriented initially for single slip, in figure 3.19 a). The three stages can be classified as follows

*Stage I: (easy glide)* slip occurs through operation of dislocation sources on *primary* slip system. Dislocations of predominantly edge character extend over large distances. Screw dislocations frequently annihilate by cross slip. The *secondary (forest)* dislocation density is only a small fraction of the primary one.

*Stage II: (rapid hardening)* dislocation multiplication and movement considerably increases on secondary system resulting in almost equal primary and secondary dislocation densities. The densities interact and form *glissile* and *sessile junctions* and *jogs* impeding dislocation motion on both systems.

*Stage III: (parabolic hardening)* *dynamic recovery processes* start through thermally activated cross slip and collapse of the previously developed barriers. Cell structures become more pronounced and heavy slip bands develop.

The specific extension and the slope of each of the three stages is highly dependent on various parameters, the most influential ones being the metal, its purity and orientation, the temperature and the crystal size and shape. A detailed discussion in this respect can be found for example in HONEYCOMBE [63].

**3.9.2. Latent Hardening - Dislocation Interactions.** With the previous considerations in mind, it is clear that a detailed insight into the mechanisms of dislocation interaction is necessary in order to understand the complex hardening process in multislip. An indirect measure of the interaction strength between distinct slip systems is obtained through *latent hardening* experiments, see figure 3.19 b). Thereby in a *primary test* a specimen is oriented for single slip on system  $\alpha$  and strained up to  $\gamma_p^\alpha$ . Then, in a successive *secondary test* on a part of the same specimen, another previously *latent* slip system  $\beta$  is activated. The amount of *latent hardening*, i.e. hardening of the secondary non-active system during primary slip, is directly observable through comparison of the backextrapolated initial yield stress  $\tau_{rs}^\beta$  in the secondary test with the stress level  $\tau_{rp}^\alpha$  at the prestrain  $\gamma_p^\alpha$  in the primary test. For sufficiently large  $\gamma_p^\alpha$ , where  $\gamma_p^\alpha < \gamma_p^\alpha$ , experiments generally reveal that  $\tau_{rs}^\beta > \tau_{rp}^\alpha$ . A quantitative measure for the amount of latent hardening

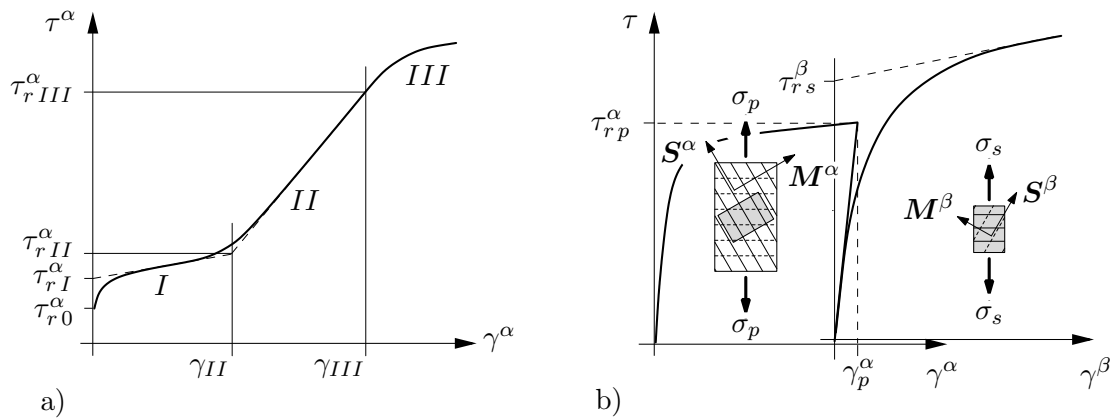


**Figure 3.19:** Work hardening of single crystals. a) typical relation between resolved shear stress  $\tau^\alpha$  vs. approximated shear strain  $\gamma^\alpha$  of primary system  $\alpha$  for a pure fcc single crystal initially oriented for single slip in uniaxial loading. b) Latent hardening experiment.

is defined through the *latent hardening ratio (LHR)*

$$\text{LHR} = \frac{\tau_{rs}^\beta}{\tau_{rp}^\alpha} \quad (3.19)$$

The (latent) hardening on the secondary system during prestraining results from the dislocation multiplication on the primary system during slip on that system. Thereby  $\tau_{rp}^\alpha$  increases at a low rate, which is characteristic of stage I hardening. During consecutive secondary slip, the dislocations on the primary system act as *forest dislocations* hindering dislocation motion on the secondary system and thus resulting in a high hardening rate, typical of stage II hardening. According to the experimental data (e.g. FRANCIOSI ET AL. [44]), the LHR depends on the metal, the prestrain  $\gamma_p^\alpha$  and the *interaction strength* between primary and secondary systems. The interaction strength depends on the type of *dislocation junction* formed between the gliding dislocation density on system  $\alpha$  and the forest density on system  $\beta$  and the number of *jogs* produced upon cutting one another. These interactions in turn depend on the geometric relation between both slip systems. Accordingly, the interaction strength  $G_i$  between system B4 and the 11 remaining systems of an fcc crystal can be classified into five groups (FRANCIOSI ET AL. [44], FRANCIOSI & ZAOUÏ [45], BASSANI & WU [17]), see table 3.3. For the interaction strengths generally

**Table 3.3:** Interaction with slip system B4 ( $b_{res}$  = resultant Burgers vector).

secondary system	name of system	# of jogs	reaction with system B4	strength coeff.
D4	cross-slip	0	no junction/annihilation: $b_{res} \parallel$ original ones	$G_1$
A3, C3	critical	2	Hirth lock: $b_{res}$ energetically not admissible	$G_2$
B2, B5	coplanar	0	junction/annihil.: $b_{res}$ and originals in plane	$G_3$
A2, C5, D1, D6	half -related	1	glissile junction: $b_{res}$ energetically admissible and on one of original slip planes	$G_4$
A6, C1	conjugate	2	Lomer-Cottrell lock: $b_{res}$ energetically admissible but on neither of original slip planes	$G_5$

the relations  $G_1 < G_2 < G_3 < G_4 < G_5$  hold. For example of the *sessile junctions* the *Hirth lock* is much weaker than the *Lomer-Cottrell lock*. Latent systems which exert the same interaction strength are in a symmetrical situation with respect to B4 in Thomson's tetrahedra, see figure 3.20 a).

**3.9.3. Work Hardening Theories.** As a consequence of the hardening response of the crystal, the slip resistance on system  $\alpha$  is strongly dependent on the strain state, thus  $\tau_r^\alpha = \hat{\tau}_r^\alpha(\gamma^1, \dots, \gamma^m)$ , where  $m$  is the number of slip systems. In accordance with the complexity and variety of the processes involved in the work hardening mechanisms, there exists a wide range of models proposed in order to describe the overall hardening response of the crystal. In classical continuum crystal plasticity formulations the following rate form is employed in order to describe the hardening response in multislip (HILL [59])

$$\dot{\tau}_r^\alpha = \sum_{\beta=1}^m h^{\alpha\beta} \dot{\gamma}^\beta \quad \text{with} \quad \tau_r^\alpha(0) = \tau_{r0} \quad (3.20)$$

where  $h^{\alpha\beta}$  governs the slip system interaction within the hardening process and  $\tau_{r0}$  is the initial value of the critical shear stress.

**3.9.3.1. Phenomenological Hardening Models.** Focussing first on purely phenomenological models, the simplest assumption introduced already by TAYLOR [148] bases on the supposition that slip on one system induces linear *isotropic hardening* on all other systems, thus  $h^{\alpha\beta} = h$ . In contrast, the assumption of *pure self-hardening* as considered by KOITER [70] induces a purely diagonal hardening matrix  $h^{\alpha\beta} = h\delta^{\alpha\beta}$ . As a very simple purely phenomenological approach towards the incorporation of the latent hardening effects described previously, a combination of the linear isotropic and the self-hardening model results in the following expression for the hardening matrix (HUTCHINSON [65], ASARO [11])

$$h^{\alpha\beta} = h[q + (1 - q)\delta^{\alpha\beta}] \quad (3.21)$$

Thereby  $1 \leq q \leq 1.4$  governs the extent of off-diagonal latent hardening. So far  $h$  has for simplicity been considered to be constant. To include active hardening PEIRCE ET AL. [124] extended the isotropic part of (3.21) to a saturation type response

$$h = \hat{h}(\gamma) = h_s + (h_0 - h_s) \operatorname{sech}^2 \left[ \frac{h_0 - h_s}{\tau_s - \tau_0} \gamma \right] \quad \text{with} \quad \gamma = \sum_{\alpha=1}^m \gamma^\alpha \quad (3.22)$$

where  $h_0$  is the initial and  $h_s$  the saturated amount of hardening. A phenomenological model capable of reproducing the three-stage hardening response was proposed by BASANI & WU [17] with the following expressions for the terms of the hardening matrix

$$h^{\alpha\alpha} = \left( (h_0 - h_s) \operatorname{sech}^2 \left[ h_s + \frac{h_0 - h_s}{\tau_I - \tau_0} \gamma^\alpha \right] \right) \left( 1 + \sum_{\beta \neq \alpha}^m G^{\alpha\beta} \tanh \left[ \frac{\gamma^\beta}{\gamma_0} \right] \right) \quad (3.23)$$

$$\text{and } h^{\alpha\beta} = \epsilon h^{\alpha\alpha}$$

Thereby the *interaction matrix*  $G^{\alpha\beta}$  quantifies the interaction strength between system  $\alpha$  and  $\beta$  according to the coefficients  $G_i$  given in table 3.3, see also the representation in figure 3.20 b). A specification of these coefficients for copper of at least 99.99% purity is

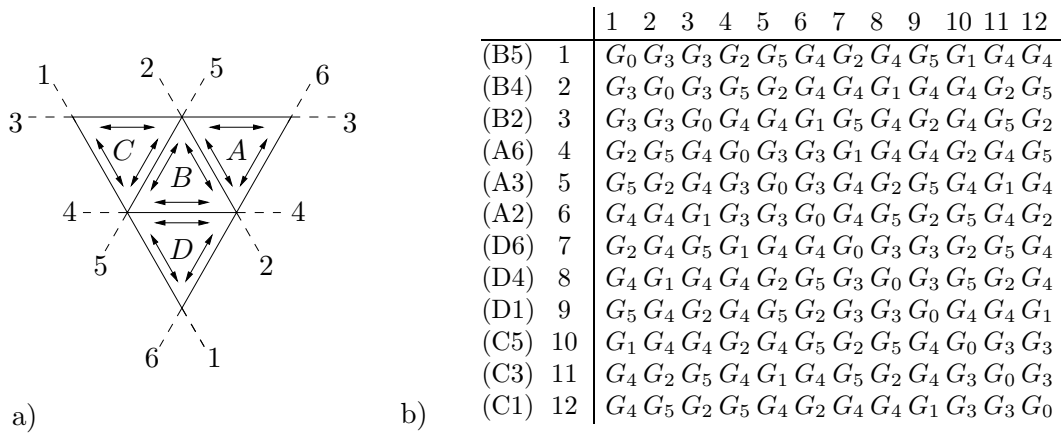


**Figure 3.20:** Latent hardening in single crystals. a) Thomson tetrahedra. b) specification of the strength-interaction matrix  $G^{\alpha\beta}$  in terms of the self interaction coefficient  $G_0$  and the strength coefficients  $G_{1-5}$  of table 3.3 for fcc crystals with Schmid type behavior.

given in BASSANI & WU [17] based on the experimental results of WU ET AL. [158] and FRANCIOSI ET AL. [44] with  $G_0 = 0$  (self-interaction),  $G_1 = G_2 = G_3 = 8$ ,  $G_4 = 15$  and  $G_5 = 20$ . A specification for aluminum is given in ARSENLIS & PARKS [7]. Further experimental quantifications of the interaction strength are given in FRANCIOSI & ZAOUÏ [45] for fcc and in FRANCIOSI [43] for bcc crystals. In (3.23)  $\tau_I$  denotes the critical shear stress of stage  $I$  and  $\epsilon$  is a small parameter which specifies the off-diagonal terms of  $h^{\alpha\beta}$ .

**3.9.3.2. Micromechanically Based Hardening Models.** In view of a rather micromechanically based hardening model, the slip resistance can, as a first simple approach, be directly related to the (total) dislocation density through the classical assumption of Taylor, see equation (3.18). Besides Taylor's observations, MITCHELL [111] also found that the experimental data was mimicked quite well with (3.18) for a value of  $c = 0.5$ . He collected data from several sources on dislocation densities determined from etch pits in copper crystals deformed in stage I. NABARRO ET AL. [115] proposed a range of  $0.2 - 0.3$  for the constant  $c$ . However, as also discussed at the beginning of this section, the simple assumption (3.18) leads to a monotonous parabolic stress-strain relation contrary to the one observed experimentally beyond stage I in single crystals of high purity. An improvement of (3.18) bases on the forest dislocation density  $n^\alpha$  hindering slip on system  $\alpha$  through

$$\tau_r^\alpha = c\mu b\sqrt{n^\alpha} \quad \text{with} \quad n^\alpha = \sum_{\beta} G^{\alpha\beta} \rho^\beta \quad (3.24)$$

where the absolute contribution of the dislocation density  $\rho^\beta$  on system  $\beta$  to the forest density  $n^\alpha$  on system  $\alpha$  is governed by the interaction strength between both systems represented by the previously introduced interaction matrix  $G^{\alpha\beta}$  in (3.24)<sub>2</sub>. Thereby, in contrast to the underlying micromechanical motivation of Taylor's classical model, dislocation hardening is primarily attributed to the interaction of gliding dislocations with the forest dislocations. However, an increase in the slip resistance due to interactions between glide dislocations and dislocations in parallel glide planes is also taken into account through  $G_0$ . The specific form of (3.24)<sub>1</sub> is motivated by line tension approximations used in order to estimate the energy needed in order to overcome an obstacle in form of a forest dislocation, see KOCKS [68, 69]. To complete the hardening model, an equation for the evolution of the dislocation density needs to be specified. Neglecting the production by fixed Frank-Read sources, the increase in dislocation density might be determined by contrasting the dislocation generation by breeding through cross glide with the dislocation attrition due to pair annihilation. This results in an evolution equation of the form (GILLIS & GILMAN [48], ESSMANN & RAPP [37])

$$\dot{\rho}^\alpha := \lambda/b(1 - \rho^\alpha/\rho^{\text{sat}})\dot{\gamma} \quad (3.25)$$

in terms of the saturation density  $\rho^{\text{sat}} := \lambda/y_c$  at which the rate of annihilation balances the rate of dislocation production. The coefficient  $\lambda$  characterizes the reciprocal mean free path between cross glide events and  $y_c$  the critical annihilation distance beneath which two dislocations of opposite sign cancel each other out. Solving the linear ordinary differential equation (3.25) for the dislocation density on glide system  $\alpha$  gives

$$\rho^\alpha = \rho^{\text{sat}}[1 - (1 - \rho^{0,\alpha}/\rho^{\text{sat}})\exp(-\gamma^\alpha/\gamma^{\text{sat}})] \quad (3.26)$$

where  $\gamma^{\text{sat}} := b\rho^{\text{sat}}/\lambda$  is the saturation slip strain and  $\rho^{0,\alpha}$  is the initial dislocation density on system  $\alpha$ . The resulting relation between the stored dislocation density and the accumulated plastic slip strain is visualized in figure 3.21. According to (3.26), only one scalar

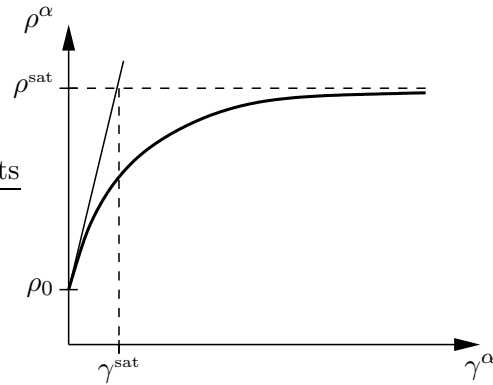


**Figure 3.21:** Dislocation accumulation due to cross glide breeding and pair annihilation.

density  $\rho^\alpha$  is considered for each slip system  $\alpha$  capturing mixed as well as pure screw and pure edge dislocation segments altogether. A more rigorous treatment based on internal variables which characterize the crystallographic dislocation density and evolve according to simple laws in dislocation mechanics, such as continuity of the dislocation line and conservation of the Burgers vector, was recently proposed by ARSENLIS & PARKS [7]. Furthermore, the storage of dislocations for compatibility reasons will be treated in chapter 5. The rate of (3.24)<sub>1</sub> gives together with (3.25) a rate form according to (3.20) where the hardening matrix takes the form

$$h^{\alpha\beta} = \frac{c\mu b}{2\sqrt{n^\alpha}} G^{\alpha\beta} \frac{\lambda}{b} \left( 1 - \frac{\rho^\alpha}{\rho^{\text{sat}}} \right) \quad (3.27)$$

A statistically based extension of this model which implicitly differentiates between mobile and immobile dislocations has been proposed by CUITIÑO & ORTIZ [33].



## 4. Crystal Plasticity at Finite Strains

Based on the considerations in the previous chapter, the classical continuum mechanical description of *homogeneous* plastic deformations in crystals will be reviewed in the first part of this chapter. Mathematical relations for the description of plastically deforming crystals have been developed by HILL [59] in the small strain context and consecutively in the finite strain setting by TEODOSIU [149], RICE [129], HILL & RICE [61], MANDEL [89], ASARO [10] and the reviews LIN [87], ASARO [11], HAVNER [56], BASSANI [15] and more recently MIEHE & SCHOTTE [102]. An extension to *plastically inhomogeneously* deforming crystals will be given in chapter 5. After the discussion of the continuum slip theory of finite strain single crystal plasticity, its algorithmic setting will be developed. Algorithmic representations of finite strain crystal plasticity suitable for an implementation in connection with the finite element method have been developed by PEIRCE ET AL. [124], NEEDLEMAN ET AL. [116], RASHID & NEMAT-NASSER [128], STEINMANN & STEIN [141] in the rate dependent context and for the rate independent case by BORJA & WREN [22], CUITIÑO & ORTIZ [33], MIEHE [95] and MIEHE ET AL. [109] among others. In view of a symmetric formulation and in order to be able to perform an incremental stability analysis also in elastoplastic crystals as discussed in chapter 8, a variational structure for the algorithmic setting of crystal plasticity will alternatively be considered.

### 4.1. The Continuum Slip Theory of Single Crystal Plasticity

In the following, the continuum slip theory will be discussed as a micromechanically well motivated framework of finite strain single crystal plasticity. Thereby the considerations are in line with the recent work MIEHE & SCHOTTE [102].

**4.1.1. Homogeneous Deformation of a Crystal.** The *total* deformation of a crystal consists of a *plastic part*, *elastic lattice distortions* and *rigid body rotations*. The plastic part of the deformation results from the simultaneous motion of dislocations on the *active slip systems* as discussed in the previous chapter. The *homogenization* of these combined dislocation actions induces a *continuous* plastic shear deformation on the macroscopic, i.e. *continuum*, length scale. Following KRÖNER [77] (although in different order) and LEE [83] this is suggestive of a multiplicative decomposition of the total deformation gradient

$$\mathbf{F} = \mathbf{F}^e \cdot \mathbf{F}^p \quad \text{with} \quad F^a_A = F^e{}^a_{\bar{A}} F^p{}^{\bar{A}}_A \quad (4.1)$$

into an *elastic part*  $\mathbf{F}^e$ , which describes the elastic distortion and rigid rotation of the lattice, and a *plastic part*  $\mathbf{F}^p$  representative of the combined dislocation movements. As will be seen in chapter 5, neither  $\mathbf{F}^e$  nor  $\mathbf{F}^p$  generally follows from an associated global vector field. Only in the special case of a homogeneous deformation  $\mathbf{F}^e$  and  $\mathbf{F}^p$  are gradient fields. Following TEODOSIU [149], RICE [129], HILL & RICE [61] and MANDEL [89] a common assumption is that  $\mathbf{F}^p$  leaves the lattice *undistorted* and *unrotated*. Thus, by choice of the rotation contained in  $\mathbf{F}^p$ , the lattice rotation is fully included in  $\mathbf{F}^e$ . Along with the multiplicative split, the fictitious *intermediate configuration*  $\bar{\mathcal{B}}$  is introduced, see figure 4.1 for a visualization. A common assumption of Schmid type crystal plasticity is that the plastic deformation is independent of volumetric deformations. This is manifested in the so-called *incompressibility constraint*

$$J^p := \det[\mathbf{F}^p] = 1 \Rightarrow \mathbf{F}^p \in SL(3) \quad (4.2)$$

A pull-back of the *spatial velocity gradient*  $\mathbf{l} := \nabla_{\mathbf{x}} \mathbf{v} = \dot{\mathbf{F}} \cdot \mathbf{F}^{-1}$  to the intermediate configuration  $\bar{\mathcal{B}}$  results in the following additive decomposition

$$\bar{\mathbf{L}} = \mathbf{F}^{e-1} \cdot \mathbf{l} \cdot \mathbf{F}^e = \underbrace{\mathbf{F}^{e-1} \cdot \dot{\mathbf{F}}^e}_{\bar{\mathbf{L}}^e} + \underbrace{\dot{\mathbf{F}}^p \cdot \mathbf{F}^{p-1}}_{\bar{\mathbf{L}}^p} = \bar{\mathbf{L}}^e + \bar{\mathbf{L}}^p \quad (4.3)$$

into its mixed variant elastic and plastic counterparts.

**4.1.2. Free Energy Storage in Deforming Crystals.** Under isothermal conditions, the elastic response of the deforming crystal is governed by global lattice distortions resulting in *macroscopic stress fields* and local small-scale lattice distortions inducing *microscopic stress fields*. The corresponding energy storage follows from the constitutive expression for the *free energy* storage

$$\psi = \hat{\psi}(\mathbf{F}, \mathbf{F}^p, \gamma^{1\dots m}) = \hat{\psi}^e(\mathbf{F}, \mathbf{F}^p) + \hat{\psi}^p(\gamma^{1\dots m}) \quad (4.4)$$

in terms of the *external state variable*  $\mathbf{F}$  and the *internal state variables*  $\mathbf{F}^p$  and  $\gamma^\alpha := \int_0^t \dot{\gamma}^\alpha dt$ . Thereby  $\mathbf{F}^p$  is only a *formal internal variable* depending on the accumulated plastic slip  $\gamma^\alpha$  on system  $\alpha$  as an effectively *independent internal variable*. The additive decomposition in (4.4) is representative of the observation that the microscopic and the macroscopic stress fields do not directly influence one another and thus independently contribute to the energy storage.

Before considering specific forms of the free energy function (4.4), two basic physical restrictions on  $\psi$  should be briefly mentioned. As discussed previously and also depicted in figure 4.1, the plastic deformation through dislocation motion leaves the lattice structure unchanged. Consequently the macroscopic free energy  $\psi^e$  should be *invariant* with respect to preceding plastic deformations  $\mathbf{F}_0^p$ , i.e.

$$\hat{\psi}^e(\mathbf{F} \cdot \mathbf{F}_0^p, \mathbf{F}^p \cdot \mathbf{F}_0^p) \stackrel{!}{=} \hat{\psi}^e(\mathbf{F}, \mathbf{F}^p) \quad \forall \quad \mathbf{F}_0^p \in SL(3) \quad (4.5)$$

With the specific choice  $\mathbf{F}_0^p = \mathbf{F}^{p-1}$ , this obviously induces that the free energy must be directly expressible in terms of  $\mathbf{F}^e$ , i.e.  $\psi^e = \hat{\psi}^e(\mathbf{F}^e)$ . As a second restriction,  $\psi^e$  has to

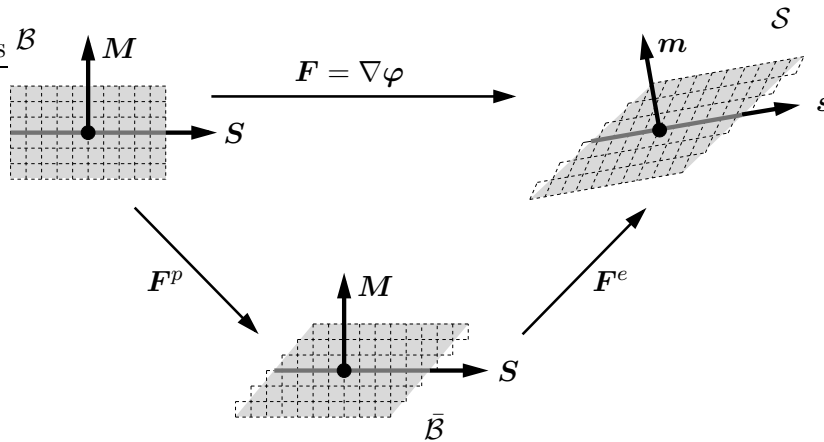


**Figure 4.1:** Geometric setting of multiplicative crystal plasticity. The total deformation gradient  $\mathbf{F}$  is split into a plastic part  $\mathbf{F}^p$  representative of the dislocation movements and an elastic part  $\mathbf{F}^e$  describing elastic lattice distortions and rigid rotations. For a homogeneous deformation state, the corresponding intermediate configuration  $\bar{\mathcal{B}}$  is compatible.

satisfy the principle of material objectivity which demands that the energy storage has to be independent of the chosen reference frame

$$\hat{\psi}^e(\mathbf{F}^e) \stackrel{!}{=} \hat{\psi}^e(\mathbf{Q} \cdot \mathbf{F}^e) \quad \forall \quad \mathbf{Q} \in SO(3) \quad (4.6)$$

where the rotation tensor  $\mathbf{Q}$  links two arbitrary Cartesian frames and is an element of the proper orthogonal group  $SO(3)$ . A choice which a priori satisfies this restriction is to assume that the macroscopic free energy depends on the symmetric and positive definite *elastic right Cauchy-Green tensor*  $\bar{\mathbf{C}}^e$

$$\psi^e = \hat{\psi}^e(\bar{\mathbf{C}}^e) \quad \text{with} \quad \bar{\mathbf{C}}^e := \mathbf{F}^{eT} \cdot \mathbf{g} \cdot \mathbf{F}^e \in \text{Sym}_+(3) \quad (4.7)$$

$\bar{\mathbf{C}}^e$  is the pull-back of the current metric to the intermediate configuration and obviously induces material frame invariance since  $(\mathbf{Q} \cdot \mathbf{F}^e)^T \cdot \mathbf{g} \cdot (\mathbf{Q} \cdot \mathbf{F}^e) = \mathbf{F}^{eT} \cdot (\mathbf{Q}^T \cdot \mathbf{g} \cdot \mathbf{Q}) \cdot \mathbf{F}^e = \bar{\mathbf{C}}^e$ .

As discussed in the previous chapter, metal crystals possess certain symmetry properties which result in a direction dependent, i.e. anisotropic, material behavior. Consequently, the material response is in general only *invariant* with respect to certain rotations superimposed onto the reference configuration, i.e.

$$\hat{\psi}^e(\bar{\mathbf{C}}^e) = \hat{\psi}^e(\mathbf{Q} \cdot \bar{\mathbf{C}}^e \cdot \mathbf{Q}^T) \quad \forall \quad \mathbf{Q} \in \mathcal{G} \subset SO(3) \quad (4.8)$$

The *material symmetry group*  $\mathcal{G} \subset SO(3)$ , i.e. the set of possible rotations, reflects the symmetry properties of the crystal structure, see e.g. table 3.1. The construction of such *anisotropic functions* (4.8) is frequently reduced to the problem of constructing an *isotropic tensor function* with an extended set of argument tensors. These additional  $\mathcal{G}$ -invariant tensors are called *structural tensors*. Accordingly, the macroscopic free energy function is a scalar valued function in terms of the coupled invariants of the argument tensor  $\bar{\mathbf{C}}^e$  and the structural tensors. The construction of such isotropic tensor functions is generally quite difficult. In crystal plasticity however, a rather simple quadratic form is usually sufficient since the plastic strains generally outweigh the elastic strains, i.e.

$$\|\bar{\mathbf{E}}^e\| < \delta \quad \text{with} \quad \bar{\mathbf{E}}^e := \frac{1}{2}[\bar{\mathbf{C}}^e - \bar{\mathbf{G}}] \quad (4.9)$$

with the elastic Green-Lagrange strain tensor  $\bar{\mathbf{E}}^e$  and the metric  $\bar{\mathbf{G}}$  of the intermediate configuration. Consequently, in the range of small elastic strains  $\bar{\mathbf{C}}^e$  is close to  $\bar{\mathbf{G}}$  and the comparison of several nonlinear models shows that it is sufficient to consider a *quadratic macroscopic free energy function* such as for the *St. Venant type material* with

$$\hat{\psi}^e = \frac{1}{2} \bar{\mathbf{E}}^e : \bar{\mathbb{C}} : \bar{\mathbf{E}}^e \quad (4.10)$$

in terms of the *fourth order structural tensor*  $\bar{\mathbb{C}}$  representative of the specific symmetry properties. (Note that (4.10) satisfies the *polyconvexity condition* (section 8.3.1) necessary for the existence of sufficiently regular minimizers of the boundary value problem only within a restricted range of *tensile* strains.) A further simplification results from completely disregarding the anisotropy in the elastic response by assuming a dependence of the macroscopic free energy on the Eulerian elastic *Finger tensor*  $\mathbf{b}^e$  in the sense

$$\psi^e = \hat{\psi}^e(\mathbf{b}^e) \quad \text{with} \quad \mathbf{b}^e := \mathbf{F}^e \cdot \bar{\mathbf{G}}^{-1} \cdot \mathbf{F}^{eT} \quad (4.11)$$

Some of the geometric quantities introduced so far are visualized in figure 4.2.

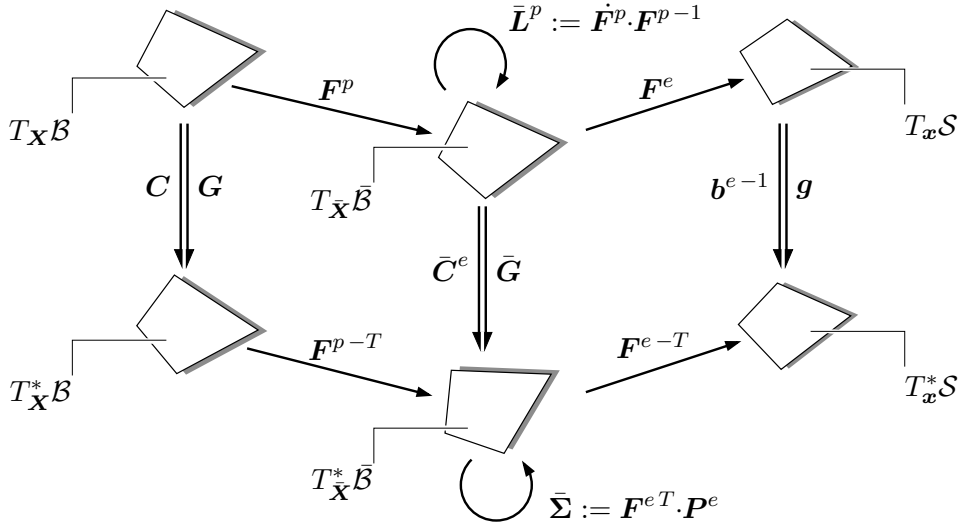


**Figure 4.2:** Geometry of multiplicative plasticity at finite strains. Definition of key objects as mappings between reference and actual tangent and cotangent spaces.

**4.1.3. Elastic Stress Response of Single Crystals.** The *Clausius-Planck* inequality postulates that the external stress power acting on a homogeneously deforming material always exceeds the evolution of the internal energy storage, i.e.

$$\mathcal{D}_{\text{loc}} := \bar{\Sigma} : \bar{\mathbf{L}} - \dot{\psi} \geq 0 \quad \text{with} \quad \bar{\Sigma} := \mathbf{F}^{eT} \cdot (\mathbf{g} \cdot \boldsymbol{\tau}) \cdot \mathbf{F}^{e-T} \quad (4.12)$$

in terms of the mixed variant stresses  $\bar{\Sigma}$  work-conjugate to the total intermediate velocity gradient  $\bar{\mathbf{L}}$  (4.3). Inserting the constitutive assumption for the free energy  $\psi$  of the previous section into (4.12) gives, following a standard argumentation often denoted as *Coleman's method*, the identifications for the stresses and the reduced dissipation  $\mathcal{D}_{\text{loc}}^{\text{red}}$

$$\bar{\Sigma} = \mathbf{F}^{eT} \cdot \mathbf{P}^e \quad \text{and} \quad \mathcal{D}_{\text{loc}}^{\text{red}} := \bar{\Sigma} : \bar{\mathbf{L}}^p - \sum_{\alpha=1}^m \tau_{r,s}^{\alpha} \dot{\gamma}^{\alpha} \geq 0 \quad \text{with} \quad \mathbf{P}^e := \partial_{\mathbf{F}^e} \hat{\psi}^e \quad (4.13)$$

Thereby, (4.13)<sub>1</sub> induces the expression  $\boldsymbol{\tau} = \mathbf{g}^{-1} \cdot \mathbf{P}^e \cdot \mathbf{F}^{eT}$  for the Kirchhoff stresses and  $\tau_{r,s}^{\alpha}$  represents the contribution to the *slip resistance*  $\tau_r^{\alpha}$  due to hardening mechanisms, i.e. the storage of dislocation line length on the micro-scale, where by definition

$$\tau_{r,s}^{\alpha} := \hat{\psi}_{,\gamma^{\alpha}}^p \quad (4.14)$$

Here the notation  $(\cdot)_{,\gamma^{\alpha}}$  indicates the sensitivity of the quantity  $(\cdot)$  with respect to the total slip  $\gamma^{\alpha}$  on system  $\alpha$ . Note that a potential structure for the hardening contribution in the sense of (4.14) cannot always be specified in a direct manner. This is especially true for the nonlinear micromechanically based hardening models considered e.g in section 3.9.3.2 or 5.6.4. Thereby an evaluation of the dissipation and consequently *thermodynamic consistency* in the sense of (4.12)<sub>1</sub> is not possible in a direct manner. However, in some cases, e.g. for the hardening model of section 3.9.3.2, an incremental approximation can be constructed.

**4.1.4. Elastic Domain and Evolution of Plastic Deformation.** The onset of plastic deformation described on the macro-level by  $\mathbf{F}^p$  is governed by the slip resistances  $\tau_r^{\alpha}$  which are assumed to act as thresholds leading to a discontinuous evolution of the plastic

slips  $\gamma^\alpha$  on systems  $\alpha$ . The threshold character is described by a non-smooth convex *elastic domain*  $\mathcal{E}$

$$\mathcal{E} = \{(\bar{\Sigma}, \tau_{r,s}^\alpha) \mid \hat{\Phi}^\alpha(\bar{\Sigma}, \tau_{r,s}^\alpha) \leq 0 \quad \text{for } \alpha = 1, 2, \dots, m\} \quad (4.15)$$

in the stress space in terms of the *yield criterion functions*  $\Phi^\alpha$  which for Schmid type single crystal plasticity take the form

$$\Phi^\alpha = \tau^\alpha - \tau_r^\alpha \quad \text{with} \quad \tau^\alpha := \bar{\Sigma} : \mathbf{S}^\alpha \otimes \mathbf{M}^\alpha \quad \text{and} \quad \tau_r^\alpha := \tau_{r,0} + \tau_{r,s}^\alpha \quad (4.16)$$

Here  $\tau^\alpha$  denotes the Schmid stress, and  $\tau_{r,0}$  the initial value of the critical shear stress. The evolution equations are derived from the classical *principle of maximum dissipation* in connection with (4.15). The resulting constrained optimization problem can be solved by a Lagrange multiplier method, i.e.

$$\mathcal{L}(\bar{\Sigma}, \tau_{r,s}^\alpha, \lambda^\alpha) = \bar{\Sigma} : \bar{\mathbf{L}}^p - \sum_{\alpha=1}^m \tau_{r,s}^\alpha \dot{\gamma}^\alpha - \sum_{\alpha=1}^m \lambda^\alpha \Phi^\alpha \rightarrow \text{stat.} \quad (4.17)$$

This gives the identification  $\dot{\gamma}^\alpha = \lambda^\alpha$ , the evolution equation

$$\bar{\mathbf{L}}^p = \dot{\mathbf{F}}^p \cdot \mathbf{F}^{p-1} = \sum_{\alpha=1}^m \dot{\gamma}^\alpha \mathbf{S}^\alpha \otimes \mathbf{M}^\alpha \quad (4.18)$$

and the *Karush-Kuhn-Tucker loading-unloading* conditions

$$\dot{\gamma}^\alpha \geq 0, \quad \Phi^\alpha \leq 0, \quad \dot{\gamma}^\alpha \Phi^\alpha = 0 \quad (4.19)$$

Observe that the flow rule (4.18) is purely deviatoric, i.e. it preserves the plastic volume  $J^p = \det[\mathbf{F}^p] = 1$ . Inserting the evolution equation (4.18) into (4.13) gives with the definition of the Schmid stress (4.16)<sub>2</sub> the following evaluation of the reduced dissipation

$$\mathcal{D}_{\text{loc}}^{\text{red}} = \sum_{\alpha=1}^m (\tau^\alpha - \tau_{r,s}^\alpha) \dot{\gamma}^\alpha \geq 0 \quad (4.20)$$

Accordingly, the Schmid stresses  $\tau^\alpha$  can be considered as the *driving force* conjugate to the plastic slip  $\gamma^\alpha$ . In view of a unified algorithmic treatment for both *standard* and *incremental variational* formulation in section 4.2, it is convenient to represent the Schmid stresses in terms of the macroscopic stresses  $\mathbf{P}^e$ , see (4.13)<sub>3</sub>, as follows

$$\tau^\alpha = -\mathbf{P}^e : \mathbf{F}_{,\gamma^\alpha}^e = -\hat{\psi}_{,\gamma^\alpha}^e \quad \text{with} \quad \mathbf{F}_{,\gamma^\alpha}^e := \mathbf{F} \cdot \mathbf{F}_{,\gamma^\alpha}^{p-1} = -\mathbf{F}^e \cdot \mathbf{S}^\alpha \otimes \mathbf{M}^\alpha \quad (4.21)$$

where (4.21)<sub>2</sub> follows directly from (4.18). What remains to be determined is the evolution of plastic slip  $\dot{\gamma}^\alpha$ .

**4.1.5. Visco-Plastic Flow Response of Single Crystals.** The evolution of the plastic deformation on the macro-scale (4.18) might be related to the dislocation movement through the classical Orowan equation (3.14)

$$\dot{\gamma}^\alpha = b\rho^\alpha \dot{x}^\alpha \quad (4.22)$$

which is considered to be the key link between *discrete dislocation mechanics* and the *continuum slip theory of crystal plasticity*. Turning back again to the latter theory, the

evolution of plastic slip  $\dot{\gamma}^\alpha$  is, in the *rate-independent* case, implicitly specified through the loading-unloading conditions (4.19). The *active slip systems* with currently nonzero slip evolution are collected in an *active set*

$$\mathcal{A} := \{\alpha \mid \dot{\gamma}^\alpha > 0\} \quad \text{with} \quad \alpha \in \{1, \dots, m\} \quad (4.23)$$

In a *rate-dependent* setting, the thresholds  $\tau_r^\alpha$  are exceeded by viscous overstresses

$$\tau_v^\alpha = \tau_{v0} \left( \frac{\dot{\gamma}^\alpha}{\dot{\gamma}_0} \right)^{1/\epsilon} \quad (4.24)$$

resulting in the *modified* yield criterion functions for *crystal viscoplasticity*

$$\Phi^\alpha = \tau^\alpha - \tau_r^\alpha - \tau_v^\alpha \quad (4.25)$$

For plastic loading with  $\dot{\gamma}^\alpha > 0$ , (4.25) and (4.24) result together with (4.19)<sub>3</sub> in the following constitutive relations for the evolution of plastic slip

$$\dot{\gamma}^\alpha = \dot{\gamma}_0 \left[ \frac{\tau^\alpha - \tau_r^\alpha}{\tau_{v0}} \right]^\epsilon \quad \forall \quad \alpha \in \mathcal{A} \quad (4.26)$$

which corresponds to the classical Norton-Bayley-type creep law for an overstress  $\tau^\alpha - \tau_r^\alpha$ .  $\dot{\gamma}_0$ ,  $\tau_{v0}$  and  $\epsilon$  are positive material parameters which characterize the viscosity of the plastic flow response. This basic model of local crystal viscoplasticity is summarized in table 4.1 and will be further discussed in the algorithmic formulations.

**Table 4.1:** Basic constitutive model of local single crystal plasticity.

Free energy	$\psi = \hat{\psi}^e(\mathbf{F}^e) + \hat{\psi}^p(\gamma^{1\dots m})$	with $\mathbf{F}^e := \mathbf{F} \cdot \mathbf{F}^{p-1}$
Kirchhoff stresses	$\boldsymbol{\tau} = \mathbf{g}^{-1} \cdot \mathbf{P}^e \cdot \mathbf{F}^{eT}$	
Schmid stresses	$\tau^\alpha = -\mathbf{P}^e : \mathbf{F}_{,\gamma^\alpha}^e$	with $\mathbf{F}_{,\gamma^\alpha}^e := -\mathbf{F}^e \cdot \mathbf{S}^\alpha \otimes \mathbf{M}^\alpha$
Slip resistance	$\tau_r^\alpha = \hat{\tau}_r^\alpha(\gamma^{1\dots m})$	
Overstresses	$\tau_v^\alpha = \tau_{v0} (\dot{\gamma}^\alpha / \dot{\gamma}_0)^{1/\epsilon}$	
Flow criterion	$\Phi^\alpha = \tau^\alpha - \tau_r^\alpha - \tau_v^\alpha$	
Slip evolution	$\dot{\gamma}^\alpha \geq 0, \quad \Phi^\alpha \leq 0, \quad \dot{\gamma}^\alpha \Phi^\alpha = 0$	with $\gamma^\alpha(0) = 0$
Flow rule	$\dot{\mathbf{F}}^p \cdot \mathbf{F}^{p-1} = \sum_{\alpha=1}^m \dot{\gamma}^\alpha \mathbf{S}^\alpha \otimes \mathbf{M}^\alpha$	with $\mathbf{F}^p(0) = \mathbf{1}$

An alternative formulation for the rate-dependent setting might be based directly on the following slip evolution equations (HUTCHINSON [66], PEIRCE ET AL. [124])

$$\dot{\gamma}^\alpha = \dot{\gamma}_0 \left[ \frac{|\tau^\alpha|}{\tau_r^\alpha} \right]^{1/\epsilon} \text{sign}[\tau^\alpha] \quad \forall \quad \alpha \quad (4.27)$$

in connection with the evolution equation (4.18). Thereby no discontinuous loading conditions are considered so that the plastic slips are continuously evolving with increasing resolved shear stress  $\tau^\alpha$ . This results in a *viscous formulation* where the rate-independent case is recovered in the limit of small values,  $\epsilon \rightarrow 0$ , of the rate sensitivity exponent.  $\tau_r^\alpha$  can be regarded as the slip resistance on system  $\alpha$  if the slip rate on that system is  $\dot{\gamma}_0$  throughout the deformation process.

## 4.2. Algorithmic Formulation of Single Crystal Plasticity

Within this section two alternative stress update algorithms for the constitutive model of crystal viscoplasticity will be discussed, following conceptually the recent publication MIEHE & SCHOTTE [102]. Therefore a typical time step  $[t_n, t_{n+1}]$  is considered where all quantities are known at time  $t_n$ . Furthermore, within a *deformation driven* context the actual total deformation gradient  $\mathbf{F}_{n+1}$  is also known at time  $t_{n+1}$ . In the following all variables evaluated at time  $t_{n+1}$  are represented without a subscript.

**4.2.1. Integration of the Flow Rule.** A crucial point for the robustness of the algorithm with underlying Schmid type isochoric flow is the geometrically exact integration of the flow rule. The flow rule (4.18) is integrated using a backward Euler-type fully implicit integration scheme based on an exponential map as follows

$$\mathbf{F}^p = \mathbf{e}^{-1} \cdot \mathbf{F}_n^p \quad \text{with} \quad \mathbf{e} := \exp[-\mathbf{N}] \quad \text{and} \quad \mathbf{N} = \sum_{\alpha=1}^m (\gamma^\alpha - \gamma_n^\alpha) \mathbf{S}^\alpha \otimes \mathbf{M}^\alpha \quad (4.28)$$

in terms of the *inverse incremental exponential map*  $\mathbf{e}$  and the current *accumulated plastic slips*  $\gamma^\alpha := \int_0^t \dot{\gamma}^\alpha dt$  which are required to lie in the plastic loading cs  $\mathcal{K}^\alpha := \{\gamma^\alpha \in \mathcal{R} | \gamma^\alpha \geq \gamma_n^\alpha\}$ . The algorithm (4.28) is a priori volume preserving, i.e. it satisfies the incompressibility constraint (4.2) and was introduced in the context of crystal plasticity by WEBER & ANAND [155].

A highly accurate but rather costly evaluation of the exponential map can be based on a *Taylor series expansion* (MIEHE [94], MIEHE ET AL. [103]) or on *spectral decomposition formulae* (ORTIZ ET AL. [120]). Thereby the spectral decomposition based approach is computationally advantageous but its accuracy and thus its applicability significantly decreases when corresponding left and right eigenvectors are orthogonal. Alternatively, following MIEHE [95] and MIEHE & SCHOTTE [102], a computationally very efficient evaluation bases on an *approximation* of the exponential algorithm (4.28) in the form

$$\check{\mathbf{F}}^p := [\mathbf{1} - \xi \mathbf{N}]^{-1} \cdot [\mathbf{1} + (1 - \xi) \mathbf{N}] \cdot \mathbf{F}_n^p = \check{\mathbf{e}}^{-1} \cdot \mathbf{F}_n^p \quad (4.29)$$

This represents a whole family of algorithms parametrized by the integration constant  $\xi \in [0, 1]$ . Thereby  $\xi = 0$  corresponds to a *fully explicit* and  $\xi = 1$  to a *fully implicit* update of  $\mathbf{F}^p$ .  $\xi = 1/2$  represents the trapezoidal rule and can also be considered as a Padé approximation of the exponential map (4.28). Clearly the approximation (4.29) does not preserve the group structure  $SL(3)$ . Consequently, the incompressibility constraint (4.2) is enforced in a *postprocessing step* as follows

$$\mathbf{F}^p = (\det[\check{\mathbf{F}}^p])^{-1/3} \check{\mathbf{F}}^p = (\det[\check{\mathbf{e}}^{-1}])^{-1/3} \check{\mathbf{e}}^{-1} \cdot \mathbf{F}_n^p \quad (4.30)$$

A comparison with the Taylor series or spectral decomposition based approaches proves the efficiency and robustness of the latter algorithm (4.29) and (4.30).

The update (4.28) induces the following update expression for the elastic part of the deformation gradient needed within the stress computation

$$\mathbf{F}^e = \mathbf{F}^{e*} \cdot \mathbf{e} \quad \text{with} \quad \mathbf{F}^{e*} := \mathbf{F} \cdot \mathbf{F}_n^{p-1} \quad (4.31)$$

where the *trial elastic deformation map*  $\mathbf{F}^{e*}$  is known at time  $t_{n+1}$  within the local deformation driven stress update algorithm. The compositions (4.28)<sub>1</sub> and (4.31) are visualized in figure 4.3. Within the algorithmic formulations discussed in the following the first and second order sensitivities of the elastic part of the deformation gradient  $\mathbf{F}^e$  with respect to the active slips  $\gamma^\alpha$  are needed. These sensitivities follow as

$$\mathbf{F}^e_{,\gamma^{\hat{\alpha}}} = \mathbf{F}^{e*} \cdot \mathbf{e}_{,\gamma^\alpha} \quad \text{and} \quad \mathbf{F}^e_{,\gamma^{\hat{\alpha}}\gamma^{\hat{\beta}}} = \mathbf{F}^{e*} \cdot \mathbf{e}_{,\gamma^\alpha\gamma^\beta} \quad (4.32)$$

where the derivatives  $\mathbf{e}_{,\gamma^\alpha}$  and  $\mathbf{e}_{,\gamma^\alpha\gamma^\beta}$  of the exponential map can be computed in a straightforward manner for the approximative algorithms (4.29) and (4.30), see MIEHE & SCHOTTE [102] for further details. For the a priori geometrically consistent evaluation of the exponential map by means of a spectral decomposition or a Taylor series expansion, the derivations are slightly more tedious and base in the latter case, like the evaluation of the exponential map itself, on a recursive formula, see MIEHE ET AL. [103] in this respect. In order to differentiate between the *algorithmic sensitivities*  $\mathbf{F}^e_{,\gamma^{\hat{\alpha}}}$  and  $\mathbf{F}^e_{,\gamma^{\hat{\alpha}}\gamma^{\hat{\beta}}}$  determined for the actual time step  $[t_n, t_{n+1}]$  and the *derivative of the continuous formulation*  $\mathbf{F}^e_{,\gamma^\alpha}$  specified in (4.21)<sub>2</sub>, the sensitivities in (4.32) are furnished with an overset symbol in the following sense  $\gamma^{\hat{\alpha}}$ . For ease of reference, the first and second order sensitivities of the elastic deformation map needed in the subsequent developments are summarized below

$$\begin{aligned} \mathbf{F}^e_{,\gamma^\alpha} &= -\mathbf{F}^e \cdot \mathbf{S}^\alpha \otimes \mathbf{M}^\alpha & \text{and} & \quad \mathbf{F}^e_{,\gamma^\alpha\gamma^\beta} = -\mathbf{F}^e \cdot \mathbf{e}_{,\gamma^\beta} \cdot \mathbf{S}^\alpha \otimes \mathbf{M}^\alpha \\ \mathbf{F}^e_{,\gamma^{\hat{\alpha}}} &= \mathbf{F}^{e*} \cdot \mathbf{e}_{,\gamma^\alpha} & \text{and} & \quad \mathbf{F}^e_{,\gamma^{\hat{\alpha}}\gamma^{\hat{\beta}}} = \mathbf{F}^{e*} \cdot \mathbf{e}_{,\gamma^\alpha\gamma^\beta} \end{aligned} \quad (4.33)$$

**4.2.2. Standard Stress Update Algorithm of Crystal Plasticity.** In order to obtain an updated stress expression at the end of the current time step for the nonlinear constitutive model, summarized in table 4.1, first the plastic slips  $\gamma^\alpha$  need to be determined in a local iteration. Borrowing strategies from the solution procedures in constraint optimization problems, the set of *active slip systems*  $\mathcal{A}$  will first be assumed to be known during the iterative update of the slip parameters. Following conceptually MIEHE [95], MIEHE & SCHRÖDER [106] and more precisely MIEHE ET AL. [103] and MIEHE & SCHOTTE [102], this *active set strategy* will be discussed in section 4.2.5. An alternative strategy which circumvents the difficulties arising in connection with a possible non-uniqueness of the active set and bases on an augmented Lagrangian formulation was proposed by SCHMIDT-BALDASSARI [131].

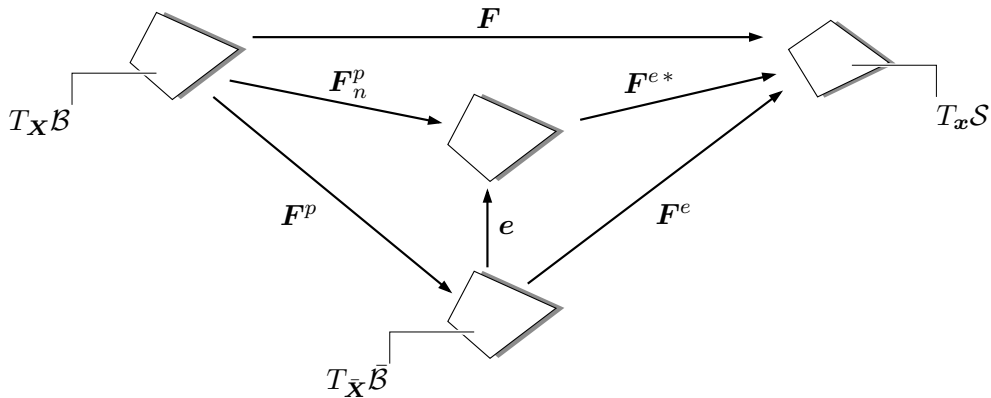


**Figure 4.3:** Algorithmic update of the intermediate configuration. The inverse incremental exponential map  $\mathbf{e}$  governs the update of both the elastic map  $\mathbf{F}^e$  and the plastic map  $\mathbf{F}^p$ .

For a known active set  $\mathcal{A}$ , the current slips  $\{\gamma^\alpha\}_{\alpha \in \mathcal{A}}$  are computed from the pseudo-consistency conditions

$$r^\alpha := -\Phi^\alpha = -\tau^\alpha + \tau_r^\alpha + \tau_v^\alpha = 0 \quad \forall \quad \alpha \in \mathcal{A} \quad (4.34)$$

This system of nonlinear equations is solved by means of a local Newton iteration resulting in the following update equations for the accumulated plastic slips

$$\gamma^\alpha \leftarrow \gamma^\alpha + \Delta\Delta\gamma^\alpha \quad \text{with} \quad \Delta\Delta\gamma^\alpha = - \sum_{\beta \in \mathcal{A}} [H^{\alpha\beta}]^{-1} r^\beta \quad \forall \quad \alpha \in \mathcal{A} \quad (4.35)$$

where the iteration matrix  $H^{\alpha\beta}$  contains the stress sensitivities

$$H^{\alpha\beta} := -[\tau^\alpha]_{,\gamma^\beta} + [\tau_r^\alpha]_{,\gamma^\beta} + [\tau_v^\alpha]_{,\gamma^\beta} \quad \forall \quad (\alpha, \beta) \in \mathcal{A} \quad (4.36)$$

The Newton iteration is terminated if the residual norm is smaller than a certain tolerance

$$\sqrt{\sum_{\alpha \in \mathcal{A}} [r^\alpha]^2} \leq \text{tol} \quad (4.37)$$

As will be seen in section 4.2.4, the iteration matrix  $H^{\alpha\beta}$  in (4.36) is *unsymmetric*. Clearly in terms of efficiency of the implicit algorithm, *symmetry* of  $H^{\alpha\beta}$  would be highly desirable. This however requires the existence of a *potential structure* which by derivation leads to expressions corresponding to (4.34) and (4.36). The construction of such a *variational problem* for the determination of the plastic slips  $\gamma^\alpha$  will be considered in the next section.

**4.2.3. Local Incremental Variational Problem.** Following MIEHE [97], MIEHE ET AL. [103] and conceptually also ORTIZ & REPETTO [121], a consistent *incremental potential function*  $W$  for the stresses can be constructed for *standard dissipative materials* within the actual finite time step  $[t_n, t_{n+1}]$  through a *variational problem* in terms of the two basic constitutive functions

$$W(\mathbf{g}; \mathbf{F}) = \inf_{\mathcal{I} \in \mathcal{G}} \int_{t_n}^{t_{n+1}} [\dot{\psi} + \phi] dt \quad \text{with} \quad \mathcal{I}(t_n) = \mathcal{I}_n \quad (4.38)$$

For prescribed deformation  $\mathbf{F}$  and given initial condition  $\mathcal{I}(t_n) = \mathcal{I}_n$ , the *incremental minimization problem* (4.38) defines an optimal path for the *generic internal variables*  $\mathcal{I}$  and provides an *incremental stress potential*  $W$  which allows for a quasi-hyperelastic stress evaluation

$$\boldsymbol{\tau} = 2\partial_{\mathbf{g}}W(\mathbf{g}; \mathbf{F}) \quad \text{or} \quad \mathbf{P} = \partial_{\mathbf{F}}W(\mathbf{F}) \quad (4.39)$$

in terms of the energy storage function  $\psi = \hat{\psi}(\mathbf{g}; \mathbf{F}, \mathcal{I})$  (as a generalized form of (4.4)) and the *dissipation function*  $\phi = \hat{\phi}(\dot{\mathcal{I}}, \mathcal{I})$ .

The incremental variational formulation also gives, within a typical time step, the desired potential structure for the determination of the plastic slips. The specification of (4.38) to the current setting of single crystal plasticity reads

$$W(\mathbf{F}) = \inf_{\gamma^\alpha \in \mathcal{K}^\alpha} \hat{W}(\mathbf{F}, \gamma^{1\dots m}) \quad (4.40)$$

Again, the plastic slips are constrained to lie in the plastic loading cones  $\mathcal{K}^\alpha := \{\gamma^\alpha \in \mathcal{R} \mid \gamma^\alpha \geq \gamma_n^\alpha\}$ . Thereby, the local incremental variational problem specifies the plastic slips by minimization of the incremental potential function

$$\hat{W}(\mathbf{F}, \gamma^{1\dots m}) = \hat{\psi}^e(\mathbf{F} \cdot \mathbf{F}^{p-1}(\gamma^{1\dots m})) + \hat{\psi}^p(\gamma^{1\dots m}) - \psi_n^e - \psi_n^p + \Delta t \hat{\phi}^r(\gamma^{1\dots m}) + \Delta t \hat{\phi}^v(\gamma^{1\dots m}) \quad (4.41)$$

based on a fully implicit algorithmic approximation of the integral of the dissipation function. With these considerations, an alternative stress update algorithm will be developed in the following where its key feature is the resulting symmetric formulation. According to (4.34) and (4.36), the residual expression and the tangent matrix for the local Newton iteration are now defined by

$$r^\alpha := \hat{W}_{,\gamma^\alpha} \quad \text{and} \quad H^{\alpha\beta} := \hat{W}_{,\gamma^\alpha\gamma^\beta} \quad (4.42)$$

as the derivatives of the incremental potential function (4.41) with respect to the plastic slips. The necessary Karush-Kuhn-Tucker optimization conditions of the constrained minimization problem (4.40) read

$$r^\alpha \geq 0 \quad , \quad \gamma^\alpha \geq \gamma_n^\alpha \quad , \quad r^\alpha(\gamma^\alpha - \gamma_n^\alpha) = 0 \quad (4.43)$$

These relations represent the algorithmic counterparts to the loading-unloading conditions (4.19) of the continuous setting. If some violations of (4.43) occur, the active set  $\mathcal{A}$  will be updated and a new iterate is computed. The specific form of the active set update will be discussed in section (4.2.5).

**4.2.4. Algorithmic Expressions for Standard and Variational Formulation.** After setting up the general outline of the stress update algorithms for both the *standard* (SF) and the *variational formulation* (VF) in the previous two sections, the respective contributions to the residual expressions (4.34) or (4.42)<sub>1</sub> and the iteration matrices (4.36) or (4.42)<sub>2</sub> will be discussed in the following. Thereby a focus is also put on a possible symmetry of  $H^{\alpha\beta}$ . The residual expressions are given by

$$\begin{aligned} \text{(SF)} \quad r^\alpha &:= -\Phi^\alpha = -\tau^\alpha + \tau_r^\alpha + \tau_v^\alpha \\ \text{(VF)} \quad r^\alpha &:= \hat{W}_{,\gamma^\alpha} = \hat{\psi}_{,\gamma^\alpha}^e + \hat{\psi}_{,\gamma^\alpha}^p + \Delta t \hat{\phi}_{,\gamma^\alpha}^r + \Delta t \hat{\phi}_{,\gamma^\alpha}^v \end{aligned} \quad (4.44)$$

And the corresponding iteration matrices read

$$\begin{aligned} \text{(SF)} \quad H^{\alpha\beta} &:= -\Phi_{,\gamma^\alpha\gamma^\beta} = [-\tau^\alpha]_{,\gamma^\beta} + [\tau_r^\alpha]_{,\gamma^\beta} + [\tau_v^\alpha]_{,\gamma^\beta} \\ \text{(VF)} \quad H^{\alpha\beta} &:= \hat{W}_{,\gamma^\alpha\gamma^\beta} = \hat{\psi}_{,\gamma^\alpha\gamma^\beta}^e + \hat{\psi}_{,\gamma^\alpha\gamma^\beta}^p + \Delta t \hat{\phi}_{,\gamma^\alpha\gamma^\beta}^r + \Delta t \hat{\phi}_{,\gamma^\alpha\gamma^\beta}^v \end{aligned} \quad (4.45)$$

Obviously the variational formulation results in a tangent matrix which is symmetric in the indices  $\alpha$  and  $\beta$ . In turn, the standard formulation induces a nonsymmetric tangent matrix as will be seen in the following section.

**4.2.4.1. Algorithmic Schmid Stresses.** The Schmid stresses  $\tau^\alpha$  of the standard update are given in terms of the sensitivity of the macroscopic free energy  $\hat{\psi}^e$  with respect to the plastic slips in the *continuous* setting, see (4.21). In turn, the algorithmic Schmid stresses of the variational formulation (1<sup>st</sup> residual term in (4.44)<sub>2</sub>) are derived within the *incremental* setting. Thus the respective Schmid stresses of both formulations read

$$\begin{aligned} \text{(SF)} \quad -\tau^\alpha &= \mathbf{P}^e : \mathbf{F}_{,\gamma^\alpha}^e \\ \text{(VF)} \quad \hat{\psi}_{,\gamma^\alpha}^e &= \mathbf{P}^e : \mathbf{F}_{,\gamma^\alpha}^e \end{aligned} \quad (4.46)$$

in terms of the respective sensitivities of  $\mathbf{F}^e$ , see (4.33)<sub>1</sub> or (4.33)<sub>3</sub>, and the stresses  $\mathbf{P}^e := \partial_{\mathbf{F}^e} \hat{\psi}^e$ . With the definition of the *nominal elastic moduli*  $\mathcal{A}^e := \partial_{\mathbf{F}^e}^2 \hat{\psi}^e$ , the sensitivities of (4.46) which enter the expressions for the tangent matrices are derived as follows

$$\begin{aligned} \text{(SF)} \quad [-\tau^\alpha]_{,\gamma\beta} &= \mathbf{F}_{,\gamma\alpha}^e : \mathcal{A}^e : \mathbf{F}_{,\gamma\beta}^e + \mathbf{P}^e : \mathbf{F}_{,\gamma^\alpha\gamma\beta}^e \\ \text{(VF)} \quad \hat{\psi}_{,\gamma^\alpha\gamma\beta}^e &= \mathbf{F}_{,\gamma^\alpha}^e : \mathcal{A}^e : \mathbf{F}_{,\gamma\beta}^e + \mathbf{P}^e : \mathbf{F}_{,\gamma^\alpha\gamma\beta}^e \end{aligned} \quad (4.47)$$

in terms of the second order sensitivities specified in (4.33). The algorithmic sensitivity of the standard formulation obviously becomes *nonsymmetric* since it contains both sensitivities of the *continuous* formulation with infinitely small time steps and *algorithmic* sensitivities of the finite-step-sized setting. In contrast, the algorithmic sensitivity of the variational update is obviously symmetric. However, its evaluation requires first and second order derivatives of the exponential map, see (4.33) as a drawback of this formulation.

**4.2.4.2. Algorithmic Slip Resistance.** The possibility to construct *potential functions*  $\hat{\psi}^p$  and  $\hat{\phi}^r$  is crucial for the formulation of an incremental variational update algorithm and for the symmetry of the sensitivity  $[\tau_r^\alpha]_{,\gamma\beta}$  of the slip resistance.  $\hat{\psi}^p$  and  $\hat{\phi}^r$  are representative of storage and dissipative mechanisms related to the plastic slip and govern the hardening response of the crystal. For most micromechanically based hardening laws, especially the ones including hardening effects due to geometrically necessary dislocations (chapter 5), such potential functions cannot be constructed. In many cases however, e.g. hardening laws with a rate form, such as specified in (3.20), and symmetric hardening matrix  $h^{\alpha\beta}$ , incremental quadratic potentials can be specified as follows (with  $\dot{\gamma}^\alpha = (\gamma^\alpha - \gamma_n^\alpha)/\Delta t$ )

$$\begin{aligned} \hat{\psi}^p(\gamma^{1\dots m}) &= \sum_{\alpha \in \mathcal{A}} (\tau_{r,n}^\alpha - \tau_{r,0}^\alpha) (\gamma^\alpha - \gamma_n^\alpha) + \frac{1}{2} \sum_{\alpha \in \mathcal{A}} \sum_{\beta \in \mathcal{A}} (\gamma^\alpha - \gamma_n^\alpha) h_n^{\alpha\beta} (\gamma^\beta - \gamma_n^\beta) \\ \text{and} \quad \hat{\phi}^r(\gamma^{1\dots m}) &= \sum_{\alpha \in \mathcal{A}} \tau_{r,0}^\alpha \dot{\gamma}^\alpha \end{aligned} \quad (4.48)$$

which bases on a standard assumption for the split into storage and dissipative mechanisms. Here  $\tau_{r,n}^\alpha$  and  $h_n^{\alpha\beta}$  are the slip resistance and hardening modulus evaluated at time  $t_n$  and  $\tau_{r,0}^\alpha$  is the slip resistance evaluated at  $t = t_0$ . Thus (4.48) provides in some cases a potential structure for the sensitivities needed in (4.44) and (4.45) through

$$\tau_r^\alpha = \hat{\psi}_{,\gamma^\alpha}^p + \Delta t \hat{\phi}_{,\gamma^\alpha}^r = \tau_{r,n}^\alpha + \sum_{\beta \in \mathcal{A}} h_n^{\alpha\beta} (\gamma^\beta - \gamma_n^\beta) \quad \text{and} \quad [\tau_r^\alpha]_{,\gamma\beta} = h_n^{\alpha\beta} \quad (4.49)$$

**4.2.4.3. Algorithmic Viscous Overstresses.** A potential function  $\hat{\phi}^v$  for the contribution of the viscous effects to the dissipation potential can, e.g. for a Norton-Bayley-type overstress (4.26), be constructed in the following manner

$$\hat{\phi}^v(\gamma^{1\dots m}) = \tau_{v,0} \dot{\gamma}_0 \frac{\epsilon}{1 + \epsilon} \sum_{\alpha \in \mathcal{A}} \left[ \frac{\gamma^\alpha - \gamma_n^\alpha}{\dot{\gamma}_0 \Delta t} \right]^{(1+\epsilon)/\epsilon} \quad (4.50)$$

which provides a potential structure for the sensitivities needed in (4.44) and (4.45), i.e.

$$\begin{aligned} \tau_v^\alpha &= \Delta t \hat{\phi}_{,\gamma^\alpha}^v = \tau_{v,0} \left( \frac{\gamma^\alpha - \gamma_n^\alpha}{\dot{\gamma}_0 \Delta t} \right)^{1/\epsilon} \\ \text{and} \quad [\tau_v^\alpha]_{,\gamma\beta} &= \Delta t \hat{\phi}_{,\gamma^\alpha\gamma\beta}^v = \frac{\tau_{v,0}}{\epsilon \dot{\gamma}_0 \Delta t} \left( \frac{\gamma^\alpha - \gamma_n^\alpha}{\dot{\gamma}_0 \Delta t} \right)^{(1-\epsilon)/\epsilon} \delta^{\alpha\beta} \end{aligned} \quad (4.51)$$

**4.2.5. Algorithmic Update of the Active Set.** Now that all quantities required within the local projected Newton iteration have been specified, the last key ingredient for the local stress update algorithm will be discussed: the *active set search*. The following considerations are essentially in line with the active-set strategy introduced in ORTIZ & STAINIER [123] (Algorithm 1), and are adopted within both standard and variational update. Therefore, the set of all possible slip systems  $\mathcal{S} := \{1, \dots, m\}$  is separated into two sets, a *working set*  $\mathcal{W}$  containing the slip systems subjected to active equality constraints

$$\mathcal{W} := \{\alpha \mid \Delta\gamma^\alpha = 0\} \quad \text{with} \quad \alpha \in \mathcal{S} \quad (4.52)$$

and a complementary set, the so-called *active set*, containing all active slip systems

$$\mathcal{A} := \mathcal{S} \setminus \mathcal{W} \quad (4.53)$$

Thereby  $\Delta\gamma^\alpha$  denotes the actual *incremental slip parameters*  $\Delta\gamma^\alpha := \gamma^\alpha - \gamma_n^\alpha$ .

To start, the active  $\mathcal{A}$  is initialized at the beginning of each time step with the one at the end of the last time step, i.e.  $\mathcal{A} = \mathcal{A}_n$ . Then, an improved solution for the accumulated plastic slips is obtained through the local Newton update (4.35) with fixed active set. If some violations of (4.43)<sub>2</sub> occur in the sense of  $\Delta\gamma^\alpha < 0$  for  $\alpha \in \mathcal{A}$ , the most violated system (index  $\alpha^-$ ) is identified and a corresponding scaling parameter  $\xi$  is computed by

$$\alpha^- := \arg \left[ \min_{\substack{\alpha \in \mathcal{A} \\ \Delta\gamma^\alpha < 0}} \left( 1 - \frac{\Delta\gamma^\alpha}{\Delta\Delta\gamma^\alpha} \right) \right] \quad \text{and} \quad \xi := \min_{\substack{\alpha \in \mathcal{A} \\ \Delta\gamma^\alpha < 0}} \left( 1 - \frac{\Delta\gamma^\alpha}{\Delta\Delta\gamma^\alpha} \right) \quad (4.54)$$

Subsequently all incremental slip parameters  $\Delta\gamma^\alpha$  are scaled by

$$\Delta\gamma^\alpha \Leftarrow \Delta\gamma^\alpha - (1 - \xi)\Delta\Delta\gamma^\alpha \quad \forall \quad \alpha \in \mathcal{A} \quad (4.55)$$

such that they are admissible in the sense of (4.43)<sub>2</sub>. Thereby  $\Delta\gamma^{\alpha^-} = 0$  holds for the initially most violated system  $\alpha^-$ . Whether system  $\alpha^-$  needs to be removed from the active set  $\mathcal{A}$  or not is decided on basis of the sensitivity  $\Delta W$  of the incremental potential  $W$  with respect to the slip increment  $\Delta\Delta\gamma$  in the solution point (4.55)

$$\Delta W := \sum_{\alpha \in \mathcal{A}} r^\alpha \Delta\Delta\gamma^\alpha \quad (4.56)$$

For  $\Delta W < 0$ , the Newton iteration is on a minimization path, but in the nonadmissible range of negative incremental slip. Consequently, the most violated system  $\alpha^-$  is removed from the active set by the *system dropping update*

$$\mathcal{A} \Leftarrow \{\mathcal{A} \setminus (\alpha^- \in \mathcal{A})\} \quad (4.57)$$

and a further iteration loop is launched.

If the Newton iteration has converged in the sense of (4.37) and no further changes of the active set according to (4.57) are necessary, the actual solution point is a local minimum in the admissible space of incremental plastic slips  $\Delta\gamma^\alpha \in \mathcal{A}$ . Then the condition (4.43)<sub>1</sub> is checked. If some violation in the sense  $r^\alpha < 0$  for one of the currently non-active systems occurs, i.e.  $\alpha \in \mathcal{S} \setminus \mathcal{A}$ , the most violated system  $\alpha^+$  is identified through

$$\alpha^+ := \arg \left[ \min_{\substack{\alpha \in \mathcal{S} \setminus \mathcal{A} \\ r^\alpha < 0}} (r_\alpha) \right] \quad (4.58)$$

and consequently added to the active set by the *system adding update*

$$\mathcal{A} \Leftarrow \{\mathcal{A} \cup (\alpha^+ \in \mathcal{S} \setminus \mathcal{A})\} \quad (4.59)$$

Subsequently a new local iteration loop is started and if finally upon convergence no further active set updates (4.59) are required, the minimizing solution is found and the local iteration is terminated. Employing a small tolerance in (4.54) and (4.58) allows to drop or add a set of most violated systems at the same time. The complete algorithm outlined so far is summarized in table 4.2 together with the computation of the stresses and consistent tangent moduli required for the treatment of the global boundary value problem within the context of a finite element formulation. A comparison of the standard and the variational stress update algorithm is presented in MIEHE & SCHOTTE [102].

**4.2.6. Stresses and Consistent Tangent Moduli.** Having a converged solution for the plastic slips  $\{\gamma^\alpha\}_{\alpha \in \mathcal{A}}$  at hand, the stresses and the consistent tangent moduli can be directly computed. In an Eulerian representation, the Kirchhoff stresses are given by the

**Table 4.2:** Standard (SF) and variational (VF) update algorithm of crystal plasticity.

- 
1. Given Database:  $\{\mathbf{F}, \mathbf{F}_n^{p-1}, \mathcal{A}_n\}$ , Initialization:  $\Delta\gamma^\alpha = 0 \forall \alpha \in \mathcal{S}$ ,  $\mathcal{A} = \mathcal{A}_n$
  2. Compute  $\mathbf{F}^e$ ,  $\mathbf{F}^{p-1}$  and sensitivities
 

(SF)	$\mathbf{F}_{,\gamma^\alpha}^e, \mathbf{F}_{,\gamma^\alpha\gamma^\beta}^e$
(VF)	$\mathbf{F}_{,\gamma^{\hat{\alpha}}}^e, \mathbf{F}_{,\gamma^{\hat{\alpha}}\gamma^{\hat{\beta}}}^e$
  3. For  $\alpha, \beta \in \mathcal{A}$  evaluate residual and iteration matrix for local Newton iteration
 

(SF)	$r^\alpha := \mathbf{P}^e : \mathbf{F}_{,\gamma^\alpha}^e + \tau_r^\alpha + \tau_v^\alpha, \quad H^{\alpha\beta} := \mathbf{F}_{,\gamma^\alpha}^e : \mathcal{A}^e : \mathbf{F}_{,\gamma^\beta}^e + \mathbf{P}^e : \mathbf{F}_{,\gamma^\alpha\gamma^\beta}^e + [\tau_r^\alpha]_{,\gamma^\beta} + [\tau_v^\alpha]_{,\gamma^\beta}$
(VF)	$r^\alpha := \mathbf{P}^e : \mathbf{F}_{,\gamma^{\hat{\alpha}}}^e + \tau_r^\alpha + \tau_v^\alpha, \quad H^{\alpha\beta} := \mathbf{F}_{,\gamma^{\hat{\alpha}}}^e : \mathcal{A}^e : \mathbf{F}_{,\gamma^{\hat{\beta}}}^e + \mathbf{P}^e : \mathbf{F}_{,\gamma^{\hat{\alpha}}\gamma^{\hat{\beta}}}^e + [\tau_r^\alpha]_{,\gamma^{\hat{\beta}}} + [\tau_v^\alpha]_{,\gamma^{\hat{\beta}}}$
  4. Convergence check: If  $(\sqrt{\sum_{\alpha \in \mathcal{A}} [r^\alpha]^2} \leq \text{tol})$  go to 8
  5. Newton update:  $\Delta\gamma^\alpha \Leftarrow \Delta\gamma^\alpha + \Delta\Delta\gamma^\alpha$  with  $\Delta\Delta\gamma^\alpha := -\sum_{\beta \in \mathcal{A}} [H^{\alpha\beta}]^{-1} [r^\beta]$
  6. System scaling/dropping update: If  $\Delta\gamma^\alpha < 0$  for any  $\alpha \in \mathcal{A}$ 
    - identify most violated system  $\alpha^- := \arg[\xi]$  with  $\xi := \min_{\alpha \in \mathcal{A}} (1 - \frac{\Delta\gamma^\alpha}{\Delta\Delta\gamma^\alpha})$
    - perform scaling update  $\Delta\gamma^\alpha \Leftarrow \Delta\gamma^\alpha - (1 - \xi)\Delta\Delta\gamma^\alpha \quad \forall \alpha \in \mathcal{A}$
    - If  $\Delta W := \sum_{\alpha \in \mathcal{A}} r^\alpha \Delta\Delta\gamma^\alpha < 0$  drop system  $\alpha^-$ ,  $\mathcal{A} \Leftarrow \{\mathcal{A} \setminus (\alpha^- \in \mathcal{A})\}$
  7. Go to 2
  8. System adding update: If  $r^\alpha < 0$  for any  $\alpha \in \mathcal{S} \setminus \mathcal{A}$ 
    - identify most violated system  $\alpha^+ := \arg[\min_{\alpha \in \mathcal{S} \setminus \mathcal{A}} (r^\alpha)]$
    - add system  $\alpha^+$  to active set  $\mathcal{A} \Leftarrow \{\mathcal{A} \cup (\alpha^+ \in \mathcal{S} \setminus \mathcal{A})\}$
    - go to 2
  9. Compute stresses and tangent moduli

---


$$\boldsymbol{\tau} = 2\hat{\psi}_{,\mathbf{g}}^e \quad \text{and} \quad \begin{array}{l} \text{(SF)} \quad \mathfrak{c}^{ep} = 4\hat{\psi}_{,\mathbf{g}\mathbf{g}}^e - \sum_{\alpha \in \mathcal{A}} \sum_{\beta \in \mathcal{A}} H^{\alpha\beta-1} 2\hat{\psi}_{,\mathbf{g}\gamma^\alpha}^e \otimes 2\partial_{\mathbf{g}}\tau^\beta \\ \text{(VF)} \quad \mathfrak{c}^{ep} = 4\hat{\psi}_{,\mathbf{g}\mathbf{g}}^e - \sum_{\alpha \in \mathcal{A}} \sum_{\beta \in \mathcal{A}} H^{\alpha\beta-1} 2\hat{\psi}_{,\mathbf{g}\gamma^\alpha}^e \otimes 2\hat{\psi}_{,\gamma^\beta\mathbf{g}}^e \end{array}$$


---

(quasi-) hyperelastic function evaluations

$$\begin{aligned} \text{(SF)} \quad \boldsymbol{\tau} &= 2\partial_{\mathbf{g}}\hat{\psi}^e(\mathbf{g}; \mathbf{F}^e) = 2\hat{\psi}_{,\mathbf{g}}^e \\ \text{(VF)} \quad \boldsymbol{\tau} &= 2\partial_{\mathbf{g}}W(\mathbf{g}; \mathbf{F}) = 2\psi_{,\mathbf{g}}^e \end{aligned} \quad (4.60)$$

The Oldroyd-type incremental stress rate  $\mathcal{L}_{\Delta\varphi}\boldsymbol{\tau}$  is governed by the sensitivity of the algorithmic stress expression with respect to the spatial metric  $\mathbf{g}$  as follows

$$\mathcal{L}_{\Delta\varphi}\boldsymbol{\tau} = \mathfrak{c}^{ep} : \frac{1}{2}\mathcal{L}_{\Delta\varphi}\mathbf{g} = \mathfrak{c}^{ep} : \text{sym}[\nabla_{\mathbf{x}}\Delta\varphi] \quad \text{with} \quad \mathfrak{c}^{ep} := 2\partial_{\mathbf{g}}\boldsymbol{\tau}(\mathbf{g}; \mathbf{F}^e) \quad (4.61)$$

where  $\nabla_{\mathbf{x}}\Delta\varphi$  is the spatial gradient of the incremental deformation field  $\Delta\varphi$  determined during the global iteration procedure. The *algorithmic Eulerian elastic-plastic moduli*  $\mathfrak{c}^{ep}$  defined in (4.61) comprise of an *elastic part*  $\mathfrak{c}^e$  and a *plastic softening part*  $\mathfrak{c}^p$

$$\mathfrak{c}^{ep} = \mathfrak{c}^e - \mathfrak{c}^p \quad (4.62)$$

The elastic part is obtained for both standard and variational formulation by a fictitious freezing of the plastic slips, i.e

$$\mathfrak{c}^e := 2\partial_{\mathbf{g}}\boldsymbol{\tau} \big|_{\gamma^\alpha} = 4\hat{\psi}_{,\mathbf{g}\mathbf{g}}^e \quad (4.63)$$

The plastic softening part is defined as

$$\mathfrak{c}^p := - \sum_{\alpha \in \mathcal{A}} \partial_{\gamma^\alpha}\boldsymbol{\tau} \otimes 2\partial_{\mathbf{g}}\gamma^\alpha \quad (4.64)$$

where the first sensitivity is again identical for both standard and variational formulation and is computed in terms of the algorithmic sensitivities  $\mathbf{F}_{,\gamma^{\hat{\alpha}}}^e$

$$\partial_{\gamma^\alpha}\boldsymbol{\tau} = 2\hat{\psi}_{,\mathbf{g}\gamma^\alpha}^e \quad (4.65)$$

The second sensitivity  $\partial_{\mathbf{g}}\gamma^\alpha$  in (4.64) can be expressed in terms of the sensitivity of the Schmid stresses with respect to the Eulerian metric by use of the implicit function theorem

$$\begin{aligned} \frac{dr^\alpha}{d\mathbf{g}} &= \frac{\partial r^\alpha}{\partial \mathbf{g}} \bigg|_{\gamma^\alpha} + \sum_{\beta \in \mathcal{A}} \underbrace{\frac{\partial r^\alpha}{\partial \gamma^\beta}}_{=H^{\alpha\beta}} \frac{\partial \gamma^\beta}{\partial \mathbf{g}} = 0 \\ \text{thus} \quad \frac{\partial \gamma^\alpha}{\partial \mathbf{g}} &= - \sum_{\beta \in \mathcal{A}} H^{\alpha\beta-1} \frac{\partial r^\beta}{\partial \mathbf{g}} \bigg|_{\gamma^\beta} \end{aligned} \quad (4.66)$$

which depends on the algorithmic expression for the Schmid stresses in terms of the continuous sensitivity  $\mathbf{F}_{,\gamma^\beta}^e$  for the standard and  $\mathbf{F}_{,\gamma^{\hat{\beta}}}^e$  for the variational update, i.e.

$$\begin{aligned} \text{(SF)} \quad \frac{\partial \gamma^\alpha}{\partial \mathbf{g}} &= + \sum_{\beta \in \mathcal{A}} H^{\alpha\beta-1} \partial_{\mathbf{g}}\tau^\beta \\ \text{(VF)} \quad \frac{\partial \gamma^\alpha}{\partial \mathbf{g}} &= - \sum_{\beta \in \mathcal{A}} H^{\alpha\beta-1} \hat{\psi}_{,\gamma^\beta \mathbf{g}}^e \end{aligned} \quad (4.67)$$

Thus the complete elastic-plastic fourth-order tangent moduli read, respectively

$$\begin{aligned} \text{(SF)} \quad \mathfrak{c}^{ep} &= 4\hat{\psi}_{,gg}^e - \sum_{\alpha \in \mathcal{A}} \sum_{\beta \in \mathcal{A}} H^{\alpha\beta-1} 2\hat{\psi}_{,g\gamma^\alpha}^e \otimes 2\partial_{\mathbf{g}}\tau^\beta \\ \text{(VF)} \quad \mathfrak{c}^{ep} &= 4\hat{\psi}_{,gg}^e - \sum_{\alpha \in \mathcal{A}} \sum_{\beta \in \mathcal{A}} H^{\alpha\beta-1} 2\hat{\psi}_{,g\gamma^\alpha}^e \otimes 2\hat{\psi}_{,\gamma^\beta g}^e \end{aligned} \quad (4.68)$$

Obviously the consistent moduli of the variational formulation are *symmetric* which might also be represented by the potential structure of this formulation

$$\boldsymbol{\tau} = 2\partial_{\mathbf{g}}W(\mathbf{g}; \mathbf{F}) \quad \text{and} \quad \mathfrak{c}^{ep} = 4\partial_{\mathbf{g}\mathbf{g}}^2W(\mathbf{g}; \mathbf{F}) \quad (4.69)$$

An evaluation of the elastic-plastic moduli of the standard formulation is given for a specific model problem in chapter A in the Appendix. As can be also seen from (4.68)<sub>1</sub>, these moduli are generally *unsymmetric*.

Alternatively, the sensitivity of the nominal stresses with respect to the total deformation defines the nominal tangent moduli

$$\Delta_{\varphi}\mathbf{P} = \mathbf{P}_{,\mathbf{F}} : \Delta_{\varphi}\mathbf{F} + \sum_{\alpha \in \mathcal{A}} \mathbf{P}_{,\gamma^\alpha} \Delta_{\varphi}\gamma^\alpha = \mathcal{A}^{ep} : \Delta_{\varphi}\mathbf{F} \quad (4.70)$$

where the sensitivities  $\{\Delta_{\varphi}\gamma^\alpha\}_{\alpha \in \mathcal{A}}$  can be expressed in terms of the sensitivity  $\Delta_{\varphi}\mathbf{F}$  via the implicit function theorem in a similar way to the above considerations. This results in the following expressions for the nominal elastic-plastic moduli of the standard and the variational formulation, respectively

$$\begin{aligned} \text{(SF)} \quad \mathcal{A}^{ep} &= \left\{ \mathcal{A}^e - \sum_{\alpha \in \mathcal{A}} \sum_{\beta \in \mathcal{A}} H^{\alpha\beta-1} (\mathcal{A}^e : \mathbf{F}_{,\gamma^{\hat{\alpha}}}^e) \otimes (\mathbf{F}_{,\gamma^\beta}^e : \mathcal{A}^e) \right\} \overset{2}{\circ} \mathbf{F}^{p-T} \overset{4}{\circ} \mathbf{F}^{p-T} \\ \text{(VF)} \quad \mathcal{A}^{ep} &= \left\{ \mathcal{A}^e - \sum_{\alpha \in \mathcal{A}} \sum_{\beta \in \mathcal{A}} H^{\alpha\beta-1} (\mathcal{A}^e : \mathbf{F}_{,\gamma^{\hat{\alpha}}}^e) \otimes (\mathbf{F}_{,\gamma^{\hat{\beta}}}^e : \mathcal{A}^e) \right\} \overset{2}{\circ} \mathbf{F}^{p-T} \overset{4}{\circ} \mathbf{F}^{p-T} \end{aligned} \quad (4.71)$$

in terms of the nominal elastic moduli  $\mathcal{A}^e := \partial_{\mathbf{F}^e \mathbf{F}^e}^2 \hat{\psi}^e$  and the notation  $(\bullet) \overset{i}{\circ} \mathbf{F}^{p-T}$  indicating the composition of the  $i$ th slot of  $(\bullet)$  with  $\mathbf{F}^{p-T}$ . Again, the moduli of the variational formulation are obviously symmetric and may be defined in terms of the algorithmic stress potential  $W$  within the time step under consideration

$$\mathbf{P} = \partial_{\mathbf{F}}W(\mathbf{F}) \quad \text{and} \quad \mathcal{A}^{ep} = \partial_{\mathbf{F}\mathbf{F}}^2W(\mathbf{F}) \quad (4.72)$$



## 5. Dislocation Density Based Strain Gradient Crystal Plasticity

Classical local continuum crystal plasticity formulations as discussed in chapter 4 base on the assumption of a locally homogeneous and compatible elastic-plastic deformation state. This corresponds to the existence of a compatible intermediate configuration. Compatibility of the intermediate configuration and local deformation homogeneity are however greatly violated in the presence of specific gradients of the plastic or the elastic deformation. Under these circumstances lattice continuity can only be maintained through the storage of specific dislocation arrangements. The density of these dislocations is thus directly related to the deformation geometry or equivalently the corresponding strain gradients. The combined presence of these dislocations and the dislocations necessary to support the plastic deformation results in an overall hardening response of the crystal. Within this chapter, a detailed discussion of the incompatibility analysis will be given resulting in measures for the storage of dislocations as a consequence of an underlying deformation inhomogeneity. This provides for a micromechanically motivated nonlocal extension of existing crystal plasticity formulations in the context of a continuum theory of dislocations. Thereby the above mentioned implications which result most prominently in a size effect of the material behavior can be captured.

### 5.1. Introduction into Strain Gradient Crystal Plasticity

The observation of *size effects* through various experiments involving plastically *inhomogeneous deformations* is a well known fact. Classical mathematical continuum descriptions of elastic-plastic deformations in crystals (HILL & RICE [61], MANDEL [89], KRÖNER & TEODOSIU [81], ASARO [10], HAVNER [56] and more recently CUITIÑO & ORTIZ [33], ORTIZ & STAINIER [123], MIEHE [95], MIEHE ET AL. [103], MIEHE & SCHOTTE [102]) however lack the capability of describing such *length scale dependent* material behavior.

The goal of the developments in this and the following chapter is to quantify the source of such scale dependent behavior in crystal plasticity and to develop an extension of the above mentioned conventional continuum theories, settled on a sound physical and mathematical basis, to account for lattice incompatibilities and the resulting size effects. The key aim thereby is to maintain the classical structures which, as will be seen, is possible through inclusion of the incompatibility measures into the hardening relations.

Among the experiments which reveal a size effect even for high-purity single crystals are plastic bending (e.g. STOLKEN & EVANS [143]), torsion (e.g. FLECK ET AL. [42]) and indentation tests (e.g. STELMASHENKO [142]). A well known observation in the experimental analysis of polycrystals is the Hall-Petch effect (HALL [53], PETCH [125]). Common to all of these experiments is the observation that the stress level obtained for a certain overall strain level tends to increase with decreasing micro-structural length scale (i.e. beam thickness, wire diameter, indent size or grain size) - that is to say the smaller, the stronger. The underlying physical cause is attributed to the storage of so-called *Geometrically Necessary Dislocations*, GNDs, (COTTRELL [31], ASHBY [12]) arising in connection with a curvature of the crystal lattice (NYE [119]) and the associated *incompatibility* of the elastic and plastic strain field (KONDO [71, 72], BILBY ET AL. [19], KRÖNER [77], ANTHONY [4]). Through the work of the latter authors, the geometrically non-linear *continuum theory of dislocations* was identified with a *non-Riemannian* geometry implying a relation between *Cartan's torsion* (CARTAN [24]) and the *dislocation density tensor* originally introduced by NYE [119]. Thereby the storage of GNDs directly implies

a non-vanishing torsion tensor also at the continuum length scale and thus the density of these dislocations is directly related to the deformation geometry. This is in contrast to the so-called *Statistically Stored Dislocations*, SSDs, which accumulate through randomly trapping each other. Since the signs of the SSD population cancel each other at the continuum level, they do not contribute to plastically inhomogeneous deformations, i.e. lattice curvatures or equivalently the dislocation density tensor at that scale, unlike the GND arrays which are comprised of equally signed dislocations. Clearly such a distinction is only possible at the continuum level since, if the concern is with a single dislocation, any dislocation causes a local lattice curvature.

Various strain gradient continuum models have been proposed by many authors for the small strain as well as the large strain regime in order to capture size effects and thus to be able to model the material behavior more accurately also in the presence of large strain gradients. It is this motivation which the focus is put on throughout this chapter. Nonlocal formulations developed in view of a regularization technique for e.g. strain softening solids are not the key interest in the present strain gradient theory.

In a first class of models, a size dependent material response is initiated through the phenomenological inclusion of an *intrinsic (material) length scale* along with a functional strain gradient dependence within the constitutive model. Consequently, the effects caused by the GND storage are indirectly included into the theory. The generalized small strain couple stress theory by FLECK & HUTCHINSON [40] and FLECK ET AL. [42] represents such a model. Thereby the gradients of the continuum rotations are incorporated in order to account for higher order displacement gradients. However the size effect predicted for indentation tests on polycrystals using this theory (SHU & FLECK [134]) revealed that the restriction to rotation gradients is insufficient. In turn, all second order gradients of the displacements are taken into account in the strain gradient theory of FLECK & HUTCHINSON [41] which fits into the general framework of the Toupin-Mindlin theory. Common to these theories and also the formulation by GURTIN [50] is the fact that they don't fit within the classical structure of the boundary value problem since they involve higher order stresses and additional boundary conditions.

Alternatively, a more direct incorporation of the underlying physics is provided through inclusion of an *incompatibility measure* or equivalently the *dislocation density tensor* in a still rather phenomenological fashion into the (per slip system) *isotropic hardening* relations (ACHARYA & BASSANI [1], ACHARYA & BEAUDOIN [2], BASSANI [16]). Thereby the standard structure of the boundary value problem is preserved. In turn, aiming at a thermodynamically justified *kinematical hardening* theory, the dislocation density tensor is included as an argument of the free energy function and the (*thermodynamically* or alternatively *work*) *conjugate forces* contribute as kinematic hardening measures to the slip resistance (STEINMANN [140], SHIZAWA & ZBIB [133], MENZEL & STEINMANN [92], GURTIN [51], the “continuum model” in SVENDSEN [145], LIEBE [85], LEVKOVITCH ET AL. [84]). These and the following models can be further classified based on the fact whether a global incompatibility measure (e.g. based on the incompatibility of the plastic part of the total deformation gradient  $\mathbf{F}^p$  in STEINMANN [140], DAI & PARKS [35], ORTIZ & REPETTO [121], ORTIZ ET AL. [122], the “continuum model” in SVENDSEN [145]) or a slip system specific incompatibility measure is used (e.g. based on the glide system specific slip gradient  $\nabla\gamma^\alpha$  in the original model of ASHBY [12] (eqns. (1.1) and (3.1)), SHIZAWA & ZBIB [133], the “glide-system-based” model in SVENDSEN [145]).

Furthermore, a constitutive dependence upon the dislocation density tensor has recently also become of particular interest in the mathematical existence theory of incremental finite strain elastoplasticity (MIELKE & MÜLLER [110]). Accordingly, the inclusion of a convex dependence upon the dislocation density tensor within the energetic expressions allows, under certain coercivity requirements, to prove the existence of sufficiently regular minimizers of the incremental variational problem. In this respect refer also to chapter 8.

The goal in this chapter is the development of a continuum strain gradient crystal plasticity formulation which closely reproduces the underlying physics of plastically inhomogeneous deformations and the associated incompatibilities. To this end, the formulation will, in contrast to the previous two model classes, directly incorporate the continuum theory of dislocations as a unified framework with a sound lattice geometric interpretation for both, plastic or elastic incompatibilities and the plastic deformation itself. This is in line with the model outlined by ASHBY [12] and the more recent dislocation density based developments of DAI & PARKS [35] and EVERS ET AL. [38]. However the key differences between these approaches and the model developed throughout this chapter are as follows. In contrast to the approach of DAI & PARKS [35], a slip system specific incompatibility measure will be employed and instead of a strength based coupling between the SSD- and GND-contribution the respective densities themselves will be assumed to supplement one another. In comparison to the treatment of EVERS ET AL. [38], the GND-contribution to the slip resistance will here be restricted to an isotropic hardening response since at this point only monotonic loading processes are considered. Thereby a sound mathematical and physical basis for this isotropic hardening response will be presented. As shown in the examples in chapter 7, the response obtained through the presented approach fits well within the basic outline of ASHBY [12] where, accordingly, a size effect can be expected if the GND density exceeds the SSD density. Further differences with respect to the treatment of EVERS ET AL. [38] are revealed within the numerical treatment in chapter 6 where the approach presented in this work relies on a discretization of the plastic slip while the latter one resorts to a discretization of the GND density. Furthermore, the aim here is to develop a numerically efficient approach for the rate-dependent as well as the rate-independent case, based on an extension of existing local formulations (e.g. MIEHE [95], MIEHE ET AL. [103], MIEHE & SCHOTTE [102]) in combination with an operator split and a smoothing algorithm. To this end, it is crucial to provide the (inhomogeneous) spatial slip distribution throughout the solution domain within the numerical treatment.

As a last modeling approach also capable of predicting size effects, the *discrete dislocation* simulations of VAN DER GIESSEN & NEEDLEMAN [154], CLEVERINGA ET AL. [27, 29, 28], BITTENCOURT ET AL. [21] and SHU ET AL. [136] should be mentioned. Thereby the dislocations are modeled as line defects in a linear elastic solid. The solution in terms of stress, strain and displacement fields is obtained by superposition of the singular fields due to the discrete dislocations and complementary fields that enforce the boundary and continuity conditions. Therein considerations are restricted to the small strain setting. Some of the problems treated by the above mentioned authors will as well be considered in the numerical examples in chapter 7 where a comparison to the formulation developed in this work will also be given.

This chapter is organized as follows. As a starting point, the notion and physical interpretation of geometrically necessary dislocations and their relation to size effects and incompatibilities will be introduced in section 5.2. Thereby a rather descriptive motiva-

tion is chosen which will be equipped with a sound mathematical basis in sections 5.3 – 5.5. The matter of compatibility in its relation to continuously distributed defects will first be approached in a direct manner in sections 5.3 and 5.4 by application of the tools of linear algebra and calculus as also pointed out by STEINMANN [140] and ACHARYA & BASSANI [1]. This results already in the definition of the dislocation density tensor as an incompatibility measure in its various representations in the spatial, intermediate and material configuration. Thereafter, in section 5.5, the incompatibility analysis will be presented from a differential geometric point of view in order to get a much deeper insight into the topic, for historical reasons and in order to pave the way for future extensions established on a sound mathematical basis. Basically, it is this viewpoint, initiated already more than 50 years ago by KONDO and developed further by BILBY, KRÖNER and coworkers and ANTHONY, which led to the present understanding of *lattice incompatibility* and the storage of *geometrically necessary dislocations*. Then in section 5.6 the connection between the dislocation density tensor as the key incompatibility measure and its lattice geometric interpretation in the context of crystal plasticity will be given. Thereby the relation between incompatibilities and the storage of GNDs will become evident. Finally, in section 5.7 a micromechanically motivated strain gradient crystal plasticity formulation will be summarized based on the developments of the previous sections. The numerical implementation of the proposed model and representative numerical examples will then be presented in the following chapters 6 and 7.

## 5.2. Geometrically Necessary Dislocations and Compatibility - Introduction

As already stated within conventional plasticity formulations, a length scale is not included in the constitutive laws. Consequently, size effects, i.e. length scale dependent material behavior, can not be predicted by such theories. However, several experiments show that the real material behavior exhibits under certain circumstances a significant size dependence. Typical examples of such experiments are depicted in figure 5.1. Each of these experiments results in a plastically inhomogeneous deformation and consequently plastic strain gradients induced by one of the following three underlying mechanisms

- i) Based on the *deformation geometry*, a homogeneous specimen can exert deformation-inhomogeneities. E.g. in the bending and torsion specimens (figures 5.1 a) and 5.1 b)) the plastic slip remains zero ( $\gamma = 0$ ) on the neutral or the central axis and increases ( $\gamma \gg 0$ ) towards the compressive/tensile fiber or the wire surface, respectively.
- ii) The *local boundary conditions* may induce a locally inhomogeneous deformation. E.g. in the indentation test (figure 5.1 c)) and in the cracked specimen (figure 5.1 d)) a plastic zone with maximum plastic slip ( $\gamma \gg 0$ ) develops beneath the indenter or at the crack tip, respectively, while the remaining part of the specimen exhibits only elastic deformations ( $\gamma = 0$ ).
- iii) The *heterogeneity of the specimen* results in an inhomogeneous deformation. E.g. in the shear test of a heterogeneous composite (figure 5.1 e)) the stiff particles deform only elastically ( $\gamma = 0$ ) while the matrix material exhibits an inhomogeneous elastic-plastic deformation ( $\gamma \gg 0$ ). In the shear test of a polycrystal (figure 5.1 f)) neighbouring grains undergo different amounts of plastic slip in varying directions resulting in a possible mismatch of slip at the grain boundaries.

In either of the three cases, the inhomogeneous deformations induce gradients of plastic slip between plastically non-deforming zones ( $\gamma = 0$ ) and plastic zones ( $\gamma \gg 0$ ). These gradients are inversely proportional to the *local length scale*  $\lambda$  and require, as will be seen

later, for compatibility reasons the storage of dislocations. Thus, since these dislocations are *necessary* in order to accommodate non-uniform strains, they are denoted as *Geometrically Necessary Dislocation* (GNDs) in contrast to the *redundant* or *Statistically Stored Dislocations* (SSDs) which accumulate during uniform straining of the crystal. This precise distinction owes to COTTRELL [31], p. 277, and ASHBY [12], p. 400. Thus, for the continuum level where the concern is with distributions of large numbers of dislocations, one can adopt the following important distinction. Dislocations are stored for two reasons

- i) SSDs accumulate due to random trapping and subsequent dislocation multiplication with ongoing plastic deformation, also in absolutely *homogeneous*, i.e. *uniform*, deformations (e.g. simple tension or simple shear of a pure single crystal in Stage I and II). The precise density of these dislocations is not predictable through geometric arguments and thus can currently only be described in a phenomenological fashion.
- ii) The storage of GNDs is a direct consequence of the inhomogeneity of the deformation state. The arrangement of these dislocations is responsible for a remaining inhomogeneous plastic deformation upon load removal. Thus through geometric arguments the specific density of this dislocation population can be related to the gradients of plastic slip or the corresponding lattice curvature. The derivation of these relations is the main focus of this chapter. Accordingly, a homogeneous deformation does not induce any GND storage.

Clearly, if the concern is with a single discrete dislocation, there is no difference between SSDs and GNDs. The geometrical relation between a stress-free lattice curvature  $\kappa$  and the storage of dislocations was first established in the pioneering work of NYE [119]. Following

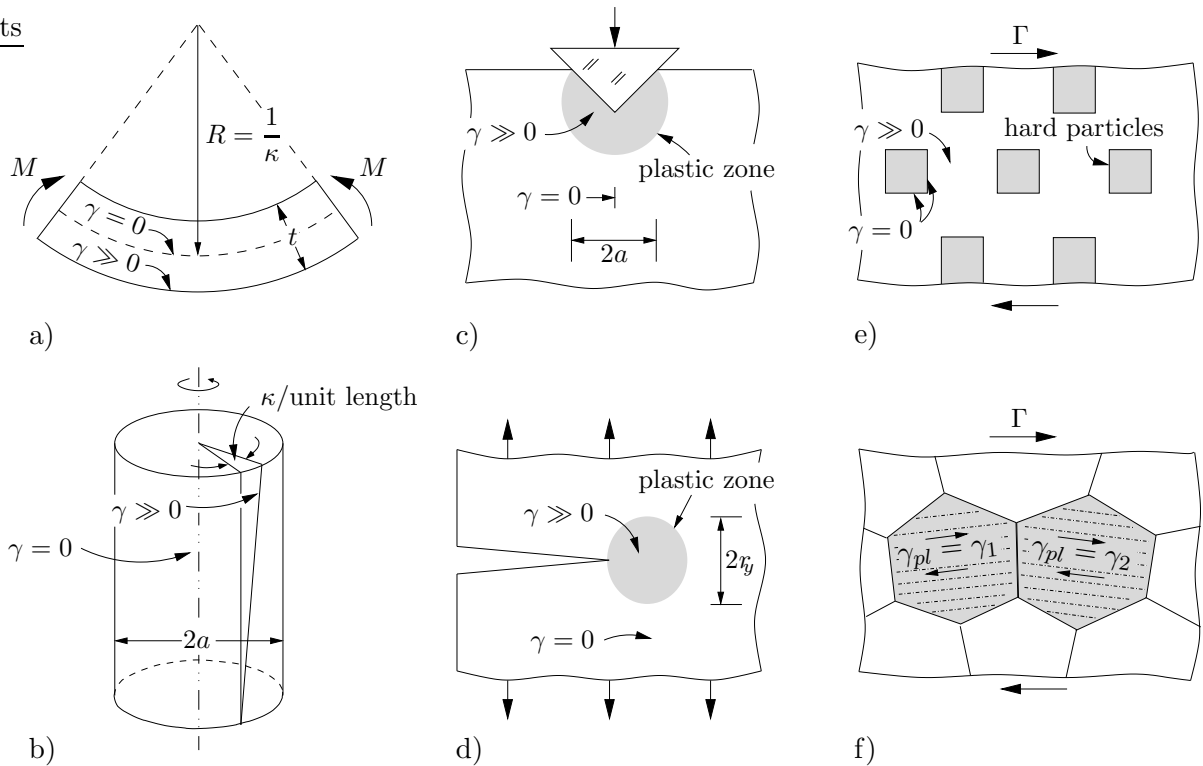


**Figure 5.1:** Experiments inducing plastically inhomogeneous deformations and thus plastic strain gradients, FLECK ET AL. [42]. a) bending and b) torsion test of a homogeneous specimen, c) and d) indentation test and cracking of a specimen with a zone of concentrated plastic deformation, e) shear test of a heterogeneous composite and f) of a polycrystal.

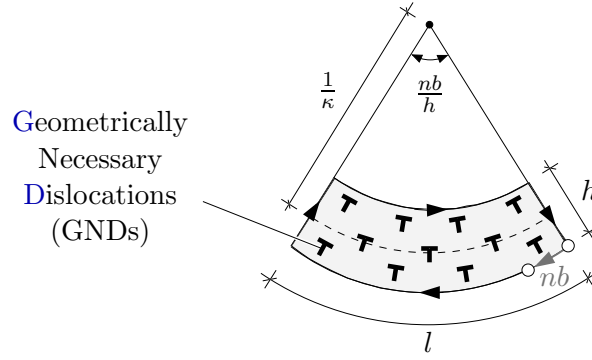


**Figure 5.2:** Storage of Geometrically Necessary Dislocations induced by a lattice curvature.

his argumentation, the density of geometrically necessary edge dislocations  $\rho_{\text{GND}\perp}$  stored in connection with a purely plastic bending test of an initially straight single crystal as depicted in figure 5.1 a) follows as

$$\rho_{\text{GND}\perp} = \frac{\kappa}{b} \quad \text{with} \quad \rho_{\text{GND}\perp} := \frac{n}{lh} \quad (5.1)$$

see figure 5.2 for a visualization. In (5.1),  $b$  denotes the length of the Burgers vector  $\mathbf{b}$ . As explained in detail in section 5.6.2, ASHBY [12] related the storage of geometrically necessary edge dislocations to a gradient of plastic slip through

$$\rho_{\text{GND}\perp} = \frac{1}{b} \frac{\partial \gamma}{\partial X_1} \quad (5.2)$$

where  $X_1$  is the coordinate in slip direction, perpendicular to the line direction of the edge dislocations. With the non-uniform slip distribution  $\gamma = \kappa X_1$  which leads to a constant lattice curvature  $\kappa$ , as depicted in figure 5.2, this directly gives relation (5.1). These considerations were extended by ASHBY [12] to more general setups inducing plastically inhomogeneous deformations as discussed e.g. in figures 5.1 e) and f). Thereby the average GND density stored in connection with a plastically inhomogeneous deformation can be written approximately as

$$\rho_{\text{GND}} \approx \frac{4\gamma}{b\lambda} \quad (5.3)$$

Here the local length scale  $\lambda$ , also denoted as *geometric slip distance*, is representative of the micro-structure or equivalently the induced deformation geometry. For heterogeneous composites containing more or less spherical stiff inclusions as depicted in figure 5.1 e), one gets  $\lambda = r/f$ , where  $r$  is the particle radius and  $f$  the volume fraction. In turn for plate like inclusions with a high aspect ratio  $\lambda$  equals the particle spacing. For pure polycrystals  $\lambda$  is proportional to the grain size. Furthermore, as pointed out by FLECK ET AL. [42],  $\lambda$  represents half the beam thickness in bending, the wire radius in torsion, the plastic zone size at the crack tip or it can be related to the indent size in the hardness test.

Following ASHBY [12], the GND density  $\rho_{\text{GND}}$  is plotted against the shear strain according to relation (5.3) in figure 5.3 for various values of the micro-structural length scale  $\lambda$ . For comparison, the SSD density evolution with ongoing shear is also depicted for pure single crystalline copper and polycrystalline copper by shaded bands. The SSD density evolution for the single crystal is adopted from measurements by BASINSKI & BASINSKI [14] and

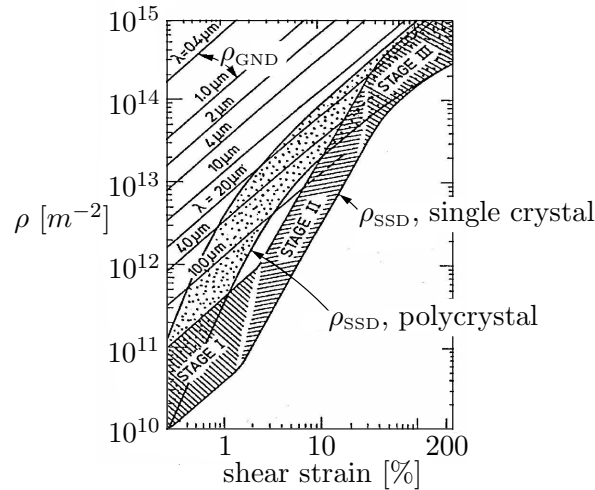


**Figure 5.3:** Comparison of the relative magnitudes of the SSD- and GND density for various values of microstructural length scale  $\lambda$ . Adopted from FLECK ET AL. [42] (ASHBY [12]).

corresponds to a pronounced three stage hardening response (Stage I: easy glide, Stage II: rapid hardening, Stage III: parabolic hardening). The  $\rho_{\text{SSD}}$  evolution for the polycrystal was added to the diagram by FLECK ET AL. [42] and follows by assumption from the polycrystalline stress strain response, which does not show a Stage I and II hardening. As suggested through relations (5.1) to (5.3) the GND density starts to play a predominant role at sufficiently small length scales, i.e. below  $100 \mu\text{m}$  where it might largely exceed the SSD density. As can be seen also from figure 5.3, this is especially pronounced at small up to moderate strains. However at larger strains the GND density might again be exceeded by the SSD density. Thus, the storage of GNDs clearly induces a scale dependent material behavior since they supplement to the *forest dislocation* density impeding the motion of gliding dislocations and they induce residual stresses within the crystal. Both effects are more pronounced for smaller governing length scales accompanied by higher GND densities and thus stronger incompatibilities.

The experimental observation of such scale dependent behavior is a well known fact. Already in the 1950's HALL [53] and PETCH [125] published independently the first experimental evidence of such behavior, where they studied different effects but arrived essentially at the same conclusion. HALL [53] analyzed the relation between the lower yield point and the grain size in polycrystalline mild steel. PETCH [125] in turn focused on the analysis of cleavage strength in brittle failure of steels. In both cases the observations obeyed the following empirical relationship for the yield (or cleavage) strength  $\sigma$

$$\sigma = \sigma_0 + \frac{k}{\sqrt{d}} \quad (5.4)$$

consequently known as the *Hall-Petch relationship*. Here  $\sigma_0$  denotes the yield strength of a single crystal, the slope  $k$  characterizes the transfer of slip over the grain boundaries and  $d$  is (related to) the grain size. Accordingly the yield strength scales linearly with the inverse square root of the grain size. An extension of (5.4) to the full work hardening regime was proposed by ARMSTRONG ET AL. [5]. Thereby the flow stress depends also on the strain level  $\epsilon$  as follows

$$\sigma(\epsilon) = \sigma_0(\epsilon) + k(\epsilon)d^{-n} \quad (5.5)$$

with  $n = \frac{1}{2}$ . A further extension concerns the exponent  $n$  where a variety of measurements for metals and alloys is covered by a range of  $n = \frac{1}{3}$  to  $n = 1$ .

The goal of this chapter is the development of an extended crystal plasticity formulation which is able to capture size effects attributed to incompatibilities and the corresponding storage of geometrically necessary dislocations. For a locally absolutely homogeneous deformation, a purely local description in terms of the elastic part  $\mathbf{F}^e$  and the plastic part  $\mathbf{F}^p$  of the total deformation gradient is sufficient since the corresponding intermediate configuration  $\tilde{\mathcal{B}}$  is compatible, see figure 4.1. Such a local description of crystal plasticity at finite strains has been considered in detail in chapter 4. Now if it comes to plastically inhomogeneous deformations, such as considered in connection with figure 5.1, a purely local description is insufficient since the corresponding intermediate configuration  $\tilde{\mathcal{B}}$  would be incompatible while the total deformation state remained compatible, see figure 5.4 for

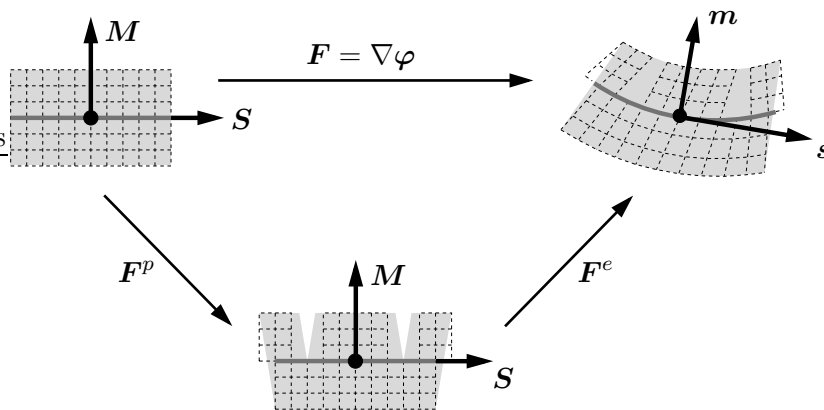


**Figure 5.4:** Geometric setting of multiplicative crystal plasticity for the case of an inhomogeneous plastic deformation. The corresponding intermediate configuration is characterized by incompatibilities. A standard local theory disregards the incompatibilities and describes a discontinuous body within an Euclidean setting for the fictitious intermediate configuration.

a schematic visualization. Thereby the elastic-plastic deformation in a macroscopic material point is described by the generally non-integrable parts  $\mathbf{F}^e$  and  $\mathbf{F}^p$  of the total deformation gradient  $\mathbf{F}$ . The incompatibility of  $\tilde{\mathcal{B}}$  however would not be captured. Note that the concern in the present theory is still with the macroscopic continuum, the lattice in figure 5.4 is just visualized for clarity which is also indicated by the dashed lines.

From these considerations, it is clear that the *storage of GNDs*, *incompatibilities* of the fictitious intermediate configuration and *size effects* in the material response are inextricably related. To elucidate their precise coherence is the main aim within the remaining sections of this chapter.

### 5.3. A Direct Approach to the Compatibility Analysis

To start the compatibility analysis one might directly look at the integrability conditions

$$F^a_{A,B} = F^a_{B,A} \quad \text{and} \quad F^{A-1}_{a,b} = F^{A-1}_{b,a} \quad (5.6)$$

which are the well known integrability conditions for an arbitrary sufficiently smooth invertible second-order tensor field, rewritten here for the deformation gradient  $\mathbf{F}$  and its inverse  $\mathbf{F}^{-1}$  in Cartesian components. These conditions are *necessary* and on *simply connected* domains also *sufficient* for the existence of a continuous single valued primitive,

i.e. deformation map  $\mathbf{x} = \boldsymbol{\varphi}(\mathbf{X})$  and inverse deformation map  $\mathbf{X} = \boldsymbol{\varphi}^{-1}(\mathbf{x})$ , respectively. Thus conditions (5.6) are the requirements for *global compatibility* of the spatial and the material configuration defined by  $\mathbf{x} = \boldsymbol{\varphi}(\mathbf{X})$  and  $\mathbf{X} = \boldsymbol{\varphi}^{-1}(\mathbf{x})$ , respectively. If conditions (5.6) are satisfied, the deformation gradient and its inverse are derivable in the sense of

$$F^a_{\ A} = \partial_{X^A} x^a \quad \text{and} \quad F^{A-1}_{\ a} = \partial_{x^a} X^A \quad (5.7)$$

An equivalent representation of the conditions (5.6) is given in Cartesian components by

$$F^a_{\ A,B} \epsilon^{ABC} = 0 \quad \text{and} \quad F^{A-1}_{\ a,b} \epsilon^{abc} = 0 \quad (5.8)$$

or in direct notation with the Curl-operators specified in the definitions (B.15) and (B.17) in section B.1 in the Appendix

$$\text{Curl}^T \mathbf{F} = \mathbf{0} \quad \text{and} \quad \text{curl}^T \mathbf{F}^{-1} = \mathbf{0} \quad (5.9)$$

A clear picture of the continuum mechanical meaning of the integrability conditions (5.6) can be obtained through reference to the fact that integrability of  $\mathbf{F}$  (or  $\mathbf{F}^{-1}$ ) also ensures path independence of a line integral formed with  $\mathbf{F}$  (or  $\mathbf{F}^{-1}$ ). Therefore, (5.9) is first integrated over an area  $\mathcal{A}_B$  (or  $\mathcal{A}_S$ ) surrounded by a closed curve  $\mathcal{C}_B$  (or  $\mathcal{C}_S$ ) and equipped with a surface normal  $\mathbf{N}$  (or  $\mathbf{n}$ ). A subsequent application of Stoke's theorem then gives

$$\int_{\mathcal{A}_B} \text{Curl}^T \mathbf{F} \cdot \mathbf{N} dA = \oint_{\mathcal{C}_B} \mathbf{F} \cdot d\mathbf{X} = \mathbf{0} \quad \text{and} \quad \int_{\mathcal{A}_S} \text{curl}^T \mathbf{F}^{-1} \cdot \mathbf{n} da = \oint_{\mathcal{C}_S} \mathbf{F}^{-1} \cdot d\mathbf{x} = \mathbf{0} \quad (5.10)$$

which, with the definition of the deformation gradient, finally transforms into

$$\int_{\mathcal{A}_B} \text{Curl}^T \mathbf{F} \cdot \mathbf{N} dA = \oint_{\mathcal{C}_S} d\mathbf{x} = \mathbf{0} \quad \text{and} \quad \int_{\mathcal{A}_S} \text{curl}^T \mathbf{F}^{-1} \cdot \mathbf{n} da = \oint_{\mathcal{C}_B} d\mathbf{X} = \mathbf{0} \quad (5.11)$$

Thus if the integrability conditions (5.6) are satisfied, the line integrals (5.11) are path independent (however since (5.11) are weaker conditions, the reverse is in general not true). Especially if (5.6)<sub>1</sub> is satisfied, according to (5.11)<sub>1</sub>, the *spatial closure failure* of a line integral of  $d\mathbf{x}$  over an arbitrary closed curve  $\mathcal{C}_S$  vanishes identically and compatibility of the Eulerian configuration is guaranteed. Analogously, the *material closure failure* of a line integral of  $d\mathbf{X}$  over any closed curve  $\mathcal{C}_B$  vanishes if the integrability condition (5.6)<sub>2</sub> is satisfied, guaranteeing compatibility of the Lagrangian configuration, see figure 5.5.

In turn, if the Eulerian or the Lagrangian configuration is incompatible, the closure failure of the corresponding line integral will not vanish, the integrability conditions (5.6) are

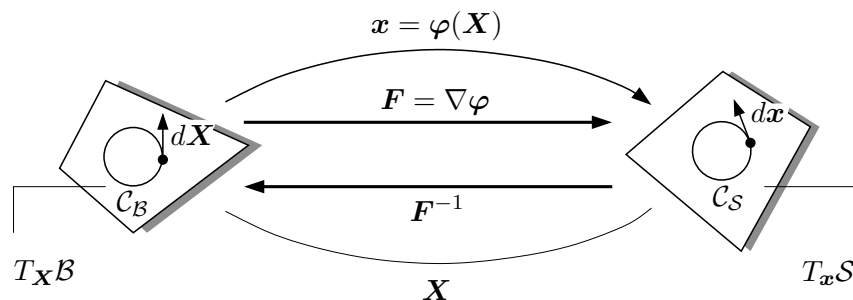


**Figure 5.5:** Line integrals in case of compatible configurations. If the integrability conditions are satisfied the closure failure vanishes and a continuous one-to-one deformation map exists.

violated, and consequently (5.9)<sub>1</sub> and (5.9)<sub>2</sub> represent the corresponding incompatibility measures. Before starting with the compatibility analysis for multiplicative elastoplasticity, the geometrical picture associated with the compatibility analysis of a general total deformation state, as visualized in figure 5.5, will be clarified. Thereby the closure failures will be identified with the *Burgers vector* and the incompatibility measures (5.9) with the *dislocation density tensor*. These notions are now introduced for the ease of reference, although at this point the considerations are not restricted to crystal plasticity. The specific meaning of these expressions will become self-evident in the following sections. To begin, the spatial closure failure according to (5.11)<sub>1</sub> will be analyzed and identified with the *macroscopic spatial Burgers vector*  $\beta^S$

$$\beta^S := \int_{\mathcal{A}_B} \text{Curl}^T \mathbf{F} \cdot \mathbf{N} \, dA = \int_{\mathcal{A}_B} \mathbf{A}_P^T \cdot \mathbf{N} \, dA = \int_{\mathcal{A}_B} \mathbf{b}_B \, dA \quad (5.12)$$

Thereby the macroscopic Burgers vector  $\beta^S$  results from the integral of the *local spatial Burgers vector*  $\mathbf{b}_B$  over an area  $\mathcal{A}_B$ . In turn,  $\mathbf{b}_B$  follows from the two field representation  $\mathbf{A}_P^T$  of the dislocation density tensor according to  $\mathbf{b}_B = \mathbf{A}_P^T \cdot \mathbf{N}$ . This is in full analogy to a material representation of the Cauchy theorem (2.27). In order to point out this formal coincidence between the stress measures and the dislocation density tensors, the dislocation density tensors will be equipped with a subscript indicating the corresponding stress analogon. Thus, in analogy to the first Piola Kirchhoff stress tensor  $\mathbf{P}$ , the contravariant dislocation density tensor  $\mathbf{A}_P := \text{Curl} \mathbf{F}$  is defined according to

$$\mathbf{A}_P^T / \mathbf{P} : \begin{cases} T_x^* \mathcal{B} \rightarrow T_x \mathcal{S} \\ \mathbf{N} \mapsto \mathbf{t}_B = \mathbf{P} \cdot \mathbf{N}, & t_B^a = P^{aA} N_A \\ \mathbf{N} \mapsto \mathbf{b}_B = \mathbf{A}_P^T \cdot \mathbf{N}, & b_B^a = A_P^{Aa} N_A \end{cases} \quad (5.13)$$

Next, reformulation of (5.12) with Nanson's formula  $J \mathbf{F}^{-T} \cdot \mathbf{N} \, dA = \mathbf{n} \, da$  gives

$$\beta^S = \int_{\mathcal{A}_S} \text{Curl}^T \mathbf{F} \cdot \frac{1}{J} \mathbf{F}^T \cdot \mathbf{n} \, da = \int_{\mathcal{A}_S} \mathbf{A}_\sigma^T \cdot \mathbf{n} \, da = \int_{\mathcal{A}_S} \mathbf{b}_S \, da \quad (5.14)$$

which implies  $\mathbf{b}_S = \mathbf{A}_\sigma^T \cdot \mathbf{n}$  as the counterpart to the spatial form of the Cauchy theorem. Furthermore, from (5.14) the definition of the spatial dislocation density tensor  $\mathbf{A}_\sigma := J^{-1} \mathbf{F} \cdot \text{Curl} \mathbf{F} = J^{-1} \mathbf{F} \cdot \mathbf{A}_P$  is deduced in analogy to the Cauchy stress tensor  $\boldsymbol{\sigma}$

$$\mathbf{A}_\sigma^T / \boldsymbol{\sigma} : \begin{cases} T_x^* \mathcal{S} \rightarrow T_x \mathcal{S} \\ \mathbf{n} \mapsto \mathbf{t}_S = \boldsymbol{\sigma} \cdot \mathbf{n}, & t_S^a = \sigma^{ab} n_b \\ \mathbf{n} \mapsto \mathbf{b}_S = \mathbf{A}_\sigma^T \cdot \mathbf{n}, & b_S^a = A_\sigma^{ba} n_b \end{cases} \quad (5.15)$$

In analogy to the Kirchhoff stresses  $\boldsymbol{\tau}$ , the spatial dislocation density tensor

$$\mathbf{A}_\tau := J \mathbf{A}_\sigma = \mathbf{F} \cdot \text{Curl} \mathbf{F} = \mathbf{F} \cdot \mathbf{A}_P \quad (5.16)$$

is introduced by weighting  $\mathbf{A}_\sigma$  with the Jacobian determinant  $J$ . Moreover the fully material dislocation density tensor  $\mathbf{A}_S$  is formally introduced as the pull-back of the spatial dislocation density tensor  $\mathbf{A}_\tau$  which obviously has no direct physical interpretation

$$\mathbf{A}_S := \mathbf{F}^{-1} \cdot \mathbf{A}_\tau \cdot \mathbf{F}^{-T} = \mathbf{A}_P \cdot \mathbf{F}^{-T} \quad (5.17)$$

After analyzing the spatial closure failure, the material closure failure according to (5.11)<sub>2</sub> is identified with the *macroscopic material Burgers vector*  $\beta^{\mathcal{B}}$

$$\beta^{\mathcal{B}} := \int_{\mathcal{A}_S} \text{curl}^T \mathbf{F}^{-1} \cdot \mathbf{n} \, da = \int_{\mathcal{A}_S} \mathbf{A}_{sm}^T \cdot \mathbf{n} \, da = \int_{\mathcal{A}_S} \mathbf{B}_S \, da \quad (5.18)$$

Thereby the macroscopic Burgers vector  $\beta^{\mathcal{B}}$  of the total inverse deformation state results from the integration of the *local material Burgers vector*  $\mathbf{B}_S$  over an area  $\mathcal{A}_S$ . Moreover, (5.18) renders the definition of the two-field dislocation density tensor  $A_{sm} := \text{curl} \mathbf{F}^{-1}$

$$\mathbf{A}_{sm}^T : \begin{cases} T_{\mathbf{x}}^* \mathcal{S} \rightarrow T_{\mathbf{X}} \mathcal{B} \\ \mathbf{n} \mapsto \mathbf{B}_S = \mathbf{A}_{sm}^T \cdot \mathbf{n}, \quad \mathbf{B}_S^A = A_{sm}^{aA} n_a \end{cases} \quad (5.19)$$

which maps between the  $s$ -patial cotangent and the  $m$ -aterial tangent space. However it has no direct analogon within the existing stress measures. With the relation between the spatial curl-operator and the material Curl-operator (see section B.2 in the Appendix), the dislocation density tensors introduced above can also be expressed in terms of  $A_{sm}$

$$\mathbf{A}_P^T = -J \mathbf{F} \cdot \mathbf{A}_{sm}^T \cdot \mathbf{F}^{-T} \quad \text{and} \quad \mathbf{A}_\tau^T = -J \mathbf{F} \cdot \mathbf{A}_{sm}^T \quad \text{and} \quad \mathbf{A}_S^T = -J \mathbf{A}_{sm}^T \cdot \mathbf{F}^{-T} \quad (5.20)$$

The pull-back and push-forward operations for the different representations of the dislocation density tensor are summarized in figure 5.6. From there, the formal correspondence

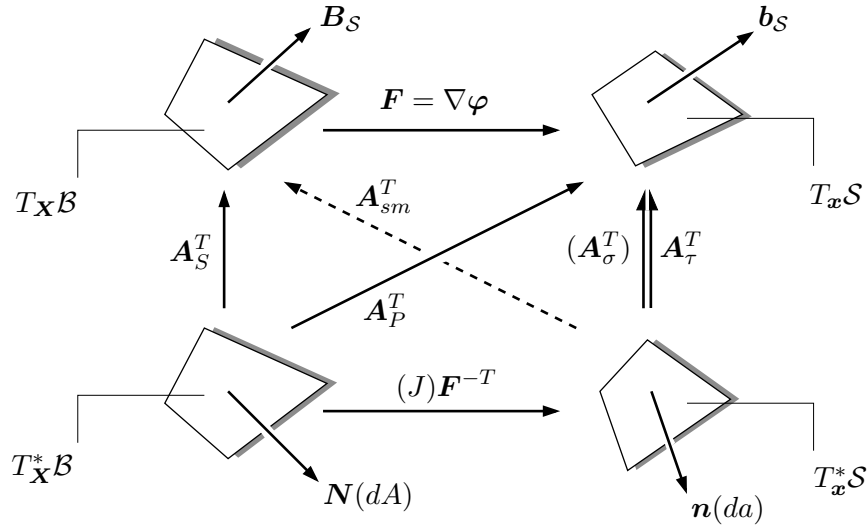


**Figure 5.6:** Burgers Vectors and dislocation density tensors of the total deformation state.

between the dislocation density tensors and the known stress measures is clearly visible. Recall that  $A_{sm}$  has no analogon among the stress measures and its transformation rule with regard to the remaining dislocation density tensors is given by (B.24).

Further evidence for the analogy between the stresses and the dislocation density tensors is given by the continuity conditions which state that a dislocation line can never end inside the crystal. Thereby, in analogy to the homogeneous equilibrium conditions, the divergence of the dislocation density tensors has to vanish identically. Compliance of these conditions in  $\mathcal{S}$  and  $\mathcal{B}$  is directly obvious from the definitions of  $\mathbf{A}_P$  and  $\mathbf{A}_{sm}$  in terms of the material and spatial curl-operators, respectively

$$\text{Div} \mathbf{A}_P^T = \mathbf{0} \quad \text{and} \quad \text{div} \mathbf{A}_{sm}^T = \mathbf{0} \quad (5.21)$$

Finally through (5.6) and (5.9) it is obvious that on simply connected domains integrability, global compatibility, vanishing closure failure, i.e. vanishing macroscopic Burgers vector and thus a vanishing dislocation density tensor are all equivalent assertions

$$\mathbf{A}_P = \mathbf{0} \Rightarrow \boldsymbol{\beta}^S = \mathbf{0} \quad \text{and} \quad \mathbf{A}_{sm} = \mathbf{0} \Rightarrow \boldsymbol{\beta}^B = \mathbf{0} \quad (5.22)$$

#### 5.4. Dislocation Density Tensors of Multiplicative Crystal Plasticity

As pointed out already in figure 5.4, the intermediate configuration introduced in connection with the multiplicative split of the deformation gradient  $\mathbf{F}$  in finite strain plasticity is in general incompatible. This is especially true for plastically inhomogeneous deformations. As already stated by KRÖNER [76] almost, any inhomogeneous plastic deformation  $\mathbf{F}^p$  which is not followed by a subsequent inhomogeneous elastic deformation  $\mathbf{F}^e$  would destroy the continuity of the body. This is, in analogy to figure 5.4, visualized from a purely macroscopic point of view in figure 5.7. Thus in general neither the plastic part

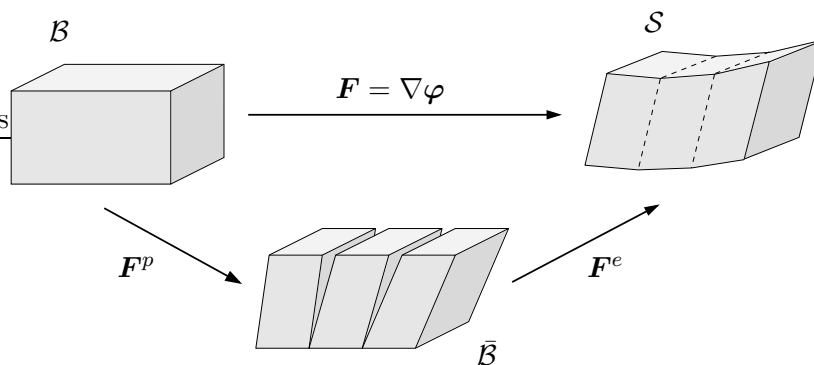


**Figure 5.7:** Almost any inhomogeneous plastic deformation which is not followed by an inhomogeneous elastic deformation destroys the continuity of the deformed body. (Applying a similar gradient to the plastic deformation in vertical direction would however maintain compatibility without a subsequent inhomogeneous elastic deformation.)

$\mathbf{F}^p$  nor the elastic part  $\mathbf{F}^e$  of the total deformation gradient  $\mathbf{F}$  is derivable from an associated global deformation field. In particular neither part,  $\mathbf{F}^e$  or  $\mathbf{F}^p$ , is in general a gradient field. Hence, only for the special case of a compatible intermediate configuration  $\bar{\mathbf{B}}$  the terms *elastic deformation gradient* and *plastic deformation gradient* are applicable.

After performing the compatibility analysis for the total deformation state in a direct manner as discussed in the previous section, the fictitious intermediate configuration will now be analyzed for compatibility in a similar way. Thereby, the closure failure of a line integral in the intermediate configuration  $\bar{\mathbf{B}}$  now has the substantial interpretation of a *real* Burgers vector representative of stored dislocations. Analogously, the corresponding dislocation density tensors now exhibit the real physical interpretation as a measure for the density of excess dislocations of one sign which did not fully traverse the crystal, giving rise to an incompatibility of the intermediate configuration. It will be proven in the following that the various dislocation density tensors proposed in literature are all related to each other through appropriate configurational mappings. Most of these relations were already derived by STEINMANN [140]. However the following interpretation of the dislocation density tensors as mappings between the tangent and cotangent spaces provides an extended view and contributes, at least in the opinion of the author, greatly to the understanding of the subject. Specifically, all of the following relations are directly obvious from the visualizations in figures 5.9 and 5.10.

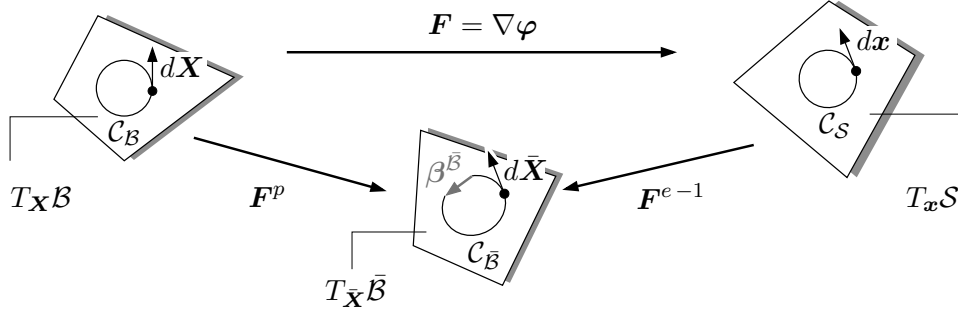


**Figure 5.8:** Incompatibility of the intermediate configuration. The closure failure of a line integral in the intermediate configuration corresponds to the real Burgers vector.

To start recall that the integrability conditions (5.6) are generally not fulfilled neither for the plastic part  $\mathbf{F}^p$  nor for the elastic part  $\mathbf{F}^e$  of the total deformation gradient. Thus a line integral in the intermediate configuration is generally not path independent

$$\oint_{C_{\bar{\mathbf{B}}}} d\bar{\mathbf{X}} \neq \mathbf{0} \quad (5.23)$$

Consequently  $\mathbf{F}^p$  is interpreted as a *Pfaffian anholonomic transformation*  $d\bar{\mathbf{X}} = \mathbf{F}^p \cdot d\mathbf{X}$ , (section 5.5.2) and the *intermediate* closure failure is identified with the macroscopic *real* Burgers vector in the intermediate configuration  $\beta^{\bar{\mathbf{B}}}$ , see figure 5.8 for a visualization,

$$\beta^{\bar{\mathbf{B}}} := \oint_{C_{\bar{\mathbf{B}}}} \mathbf{F}^p \cdot d\mathbf{X} = \int_{A_{\bar{\mathbf{B}}}} \text{Curl}^T \mathbf{F}^p \cdot \mathbf{N} \, dA \quad (5.24)$$

With the anholonomic transformation  $d\bar{\mathbf{X}} = \mathbf{F}^{e-1} \cdot d\mathbf{x}$  the intermediate closure failure  $\beta^{\bar{\mathbf{B}}}$  can alternatively be expressed solely in terms of  $\mathbf{F}^{e-1}$ . Reformulation of (5.24) gives

$$\beta^{\bar{\mathbf{B}}} = \oint_{C_{\bar{\mathbf{B}}}} \mathbf{F}^p \cdot d\mathbf{X} = \oint_{C_{\bar{\mathbf{B}}}} \mathbf{F}^p \cdot \mathbf{F}^{-1} \cdot \mathbf{F} \cdot d\mathbf{X} = \oint_{C_S} \mathbf{F}^{e-1} \cdot d\mathbf{x} = \int_{A_S} \text{curl}^T \mathbf{F}^{e-1} \cdot \mathbf{n} \, da \quad (5.25)$$

Based on these considerations, the fundamental plastic  $\mathbf{A}_P^p$  and elastic  $\mathbf{A}_{si}^e$  dislocation density tensors are introduced as follows

$$\mathbf{A}_P^p := \text{Curl} \mathbf{F}^p \quad \text{and} \quad \mathbf{A}_{si}^e := \text{curl} \mathbf{F}^{e-1} \quad (5.26)$$

For example, DAI & PARKS [35] used  $\mathbf{A}^{(DP)} = \mathbf{A}_P^p$  while e.g. ACHARYA & BASSANI [1] proposed  $\mathbf{A}^{(AB)} = \mathbf{A}_{si}^e$ . The plastic dislocation tensor  $\mathbf{A}_P^p$  determines in formal analogy to the Cauchy theorem the *real* local Burgers vector  $\bar{\mathbf{B}}_B$  in the intermediate configuration

$$\mathbf{A}_P^p : \begin{cases} T_{\mathbf{X}}^* \mathcal{B} \rightarrow T_{\bar{\mathbf{X}}} \bar{\mathcal{B}} \\ \mathbf{N} \mapsto \bar{\mathbf{B}}_B = \mathbf{A}_P^p \cdot \mathbf{N}, \quad \bar{B}_B^{\bar{A}} = A_P^{pA\bar{A}} N_A \end{cases} \quad (5.27)$$

Unlike  $\mathbf{A}_P^p$ , the elastic dislocation tensor  $\mathbf{A}_{si}^e$  does not correlate with a stress analogon and maps between the *s*-patial cotangent space and the *i*-ntermediate tangent space

$$\mathbf{A}_{si}^e : \begin{cases} T_{\mathbf{x}}^* \mathcal{S} \rightarrow T_{\bar{\mathbf{X}}} \bar{\mathcal{B}} \\ \mathbf{n} \mapsto \bar{\mathbf{B}}_S = \mathbf{A}_{si}^e \cdot \mathbf{n}, \quad \bar{B}_S^{\bar{A}} = A_{si}^{eA\bar{A}} n_a \end{cases} \quad (5.28)$$

Thus the macroscopic Burgers vector  $\boldsymbol{\beta}^{\bar{\mathcal{B}}}$  results from integration of the local counterparts

$$\boldsymbol{\beta}^{\bar{\mathcal{B}}} = \int_{\mathcal{A}_{\bar{\mathcal{B}}}} \bar{\mathbf{B}}_{\bar{\mathcal{B}}} dA = \int_{\mathcal{A}_{\mathcal{S}}} \bar{\mathbf{B}}_{\mathcal{S}} da \quad (5.29)$$

Obviously  $\mathbf{B}_{\bar{\mathcal{B}}}$  lies in the intermediate configuration (as indicated by the capital  $\bar{\mathbf{B}}$ ) but, as can be seen from (5.29), it relates to a surface element  $dA$  in the reference configuration (as indicated by the subscript  $\bar{\mathcal{B}}$ ). This is in full analogy to the contact stress vector  $\mathbf{T}$  measured by the first Piola Kirchhoff stress tensor  $\mathbf{P}$  (see (5.13)). Analogously,  $\bar{\mathbf{B}}_{\mathcal{S}}$  is also an element of the intermediate configuration (capital  $\bar{\mathbf{B}}$ ) but relates to a spatial surface element  $da$  (subscript  $\mathcal{S}$ ). Following the argumentation of CERMELLI & GURTIN [25], the *true* dislocation density tensor should measure the local Burgers vector in the intermediate configuration, per unit area in that configuration. In order to derive such a representation, (5.24) is reformulated with  $J^p \mathbf{F}^{p-T} \cdot \mathbf{N} dA = \bar{\mathbf{N}} d\bar{A}$  in the sense of Nanson's formula based on the anholonomic plastic transformation. This gives

$$\boldsymbol{\beta}^{\bar{\mathcal{B}}} := \int_{\mathcal{A}_{\bar{\mathcal{B}}}} \text{Curl}^T \mathbf{F}^p \cdot \mathbf{N} dA = \int_{\mathcal{A}_{\bar{\mathcal{B}}}} \text{Curl}^T \mathbf{F}^p \cdot \frac{1}{J^p} \mathbf{F}^{pT} \cdot \bar{\mathbf{N}} d\bar{A} \quad (5.30)$$

Analogous reformulation of (5.25) based on  $J^e \mathbf{F}^{e-T} \cdot \bar{\mathbf{N}} d\bar{a} = \mathbf{n} da$  gives

$$\boldsymbol{\beta}^{\bar{\mathcal{B}}} = \int_{\mathcal{A}_{\bar{\mathcal{B}}}} \text{curl}^T \mathbf{F}^{e-1} \cdot \mathbf{n} da = \int_{\mathcal{A}_{\bar{\mathcal{B}}}} \text{curl}^T \mathbf{F}^{e-1} \cdot J^e \mathbf{F}^{e-T} \cdot \bar{\mathbf{N}} d\bar{A} \quad (5.31)$$

Thus (5.30) and (5.31) induce two alternative representations of the *true* dislocation density tensor  $\mathbf{A}$  purely in terms of the plastic  $\mathbf{F}^p$  or the inverse elastic  $\mathbf{F}^{e-1}$  gradient part

$$\mathbf{A} := \frac{1}{J^p} \mathbf{F}^p \cdot \text{Curl} \mathbf{F}^p = J^e \mathbf{F}^{e-1} \cdot \text{curl} \mathbf{F}^{e-1} \quad (5.32)$$

This representation of the dislocation density tensor is used by e.g. CERMELLI & GURTIN [25].  $\mathbf{A}$  measures the *real* Burgers vector  $\bar{\mathbf{B}}_{\bar{\mathcal{B}}}$  in the intermediate configuration (upper case  $\bar{\mathbf{B}}$ ) with respect to a unit area in that configuration (subscript  $\bar{\mathcal{B}}$ )

$$\mathbf{A}^T : \begin{cases} T_{\bar{\mathbf{X}}}^* \bar{\mathcal{B}} \rightarrow T_{\bar{\mathbf{X}}} \bar{\mathcal{B}} \\ \bar{\mathbf{N}} \mapsto \bar{\mathbf{B}}_{\bar{\mathcal{B}}} = \mathbf{A}^T \cdot \bar{\mathbf{N}}, \quad \bar{B}_{\bar{\mathcal{B}}}^{\bar{A}} = A^{\bar{B}\bar{A}} \bar{N}_{\bar{\mathcal{B}}} \end{cases} \quad (5.33)$$

Thereby the macroscopic Burgers vector  $\boldsymbol{\beta}^{\bar{\mathcal{B}}}$  follows now by integration of  $\bar{\mathbf{B}}_{\bar{\mathcal{B}}}$  over  $\bar{\mathcal{A}}_{\bar{\mathcal{B}}}$

$$\boldsymbol{\beta}^{\bar{\mathcal{B}}} = \int_{\bar{\mathcal{A}}_{\bar{\mathcal{B}}}} \bar{\mathbf{B}}_{\bar{\mathcal{B}}} d\bar{A} \quad (5.34)$$

Out of the two representations of the true dislocation density tensor  $\mathbf{A}$  in (5.32), the first one, in terms of  $\mathbf{F}^p$ , is favorable within the development of a dislocation density based constitutive model, since  $\mathbf{F}^p$  itself is representative of the defects. Thereby the plastic slip strain and its gradient directly establish the mathematical basis for the explanation of the storage of geometrically necessary dislocations based on Nye's idea. See section 5.6 for a detailed discussion. On the other hand, as stated by CERMELLI & GURTIN [25] the representation in terms of  $\mathbf{F}^{e-1}$  allows, at least at moderate strains, for experimental validations since  $\mathbf{F}^e$  then reduces to a rotation. Thus through (5.32) a relation between GNDs and measured lattice rotations could be established.

Through (5.32) the relation between the mixed variant fundamental plastic and elastic dislocation density tensors  $\mathbf{A}_P^p$  and  $\mathbf{A}_{si}^e$  can now be established as follows

$$\mathbf{A}_P^p = J\mathbf{F}^{-1} \cdot \mathbf{A}_{si}^e \quad (5.35)$$

Furthermore, in line with (5.16),  $\mathbf{A}_P^p$  can be interpreted as the Piola transformed two field representation in  $(\mathcal{B}, \bar{\mathcal{B}})$  of the true dislocation density tensor  $\mathbf{A}$  according to

$$\mathbf{A}_\Sigma^p = \mathbf{A} = \frac{1}{J^p} \mathbf{F}^p \cdot \mathbf{A}_P^p \quad (5.36)$$

In addition, the pull-back of the *weighted* true dislocation tensor  $J^p \mathbf{A}$  results in the fully Lagrangian representation  $\mathbf{A}_S^p$  in analogy to (5.17)

$$\mathbf{A}_S^p := \mathbf{F}^{p-1} \cdot \mathbf{A} \cdot J^p \mathbf{F}^{p-T} = \mathbf{A}_P^p \cdot \mathbf{F}^{p-T} \quad (5.37)$$

Equivalently  $\mathbf{A}_{si}^e$  is the Piola transformed two field representation in  $(\bar{\mathcal{B}}, \mathcal{S})$  of  $\mathbf{A}$

$$\mathbf{A} = J^e \mathbf{F}^{e-1} \cdot \mathbf{A}_{si}^e \quad (5.38)$$

and the formal push-forward of  $\frac{1}{J^e} \mathbf{A}$  gives the fully Eulerian representation  $\mathbf{A}_{ss}^e$

$$\mathbf{A}_{ss}^e := \mathbf{F}^e \cdot \mathbf{A} \cdot \frac{1}{J^e} \mathbf{F}^{eT} \quad (5.39)$$

The dislocation density tensors introduced so far are all directly related to the *true* dislocation density in the intermediate configuration and are summarized in figure 5.9. Note that again  $\mathbf{A}_{si}^e$  and  $\mathbf{A}_{ss}^e$  do not correspond to a known stress measure.

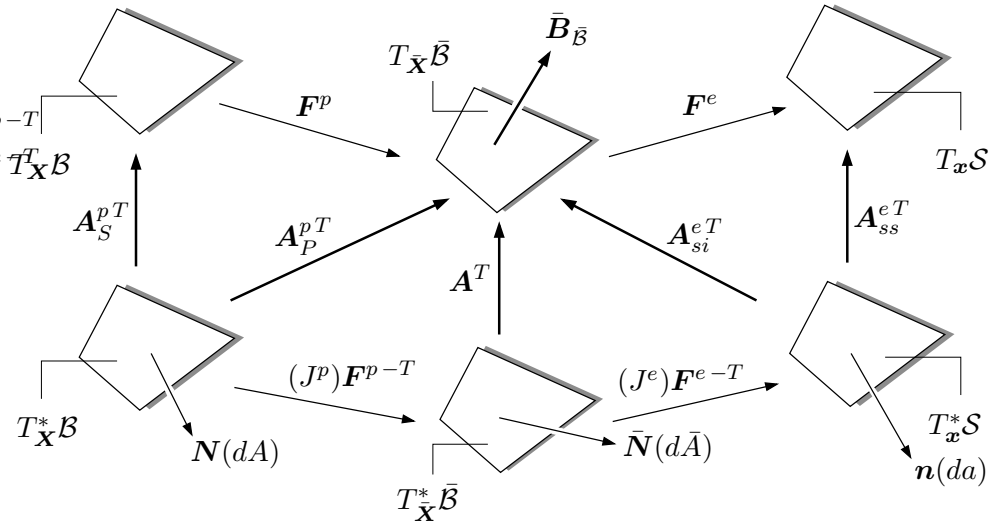


**Figure 5.9:** Incompatibility of the intermediate configuration. Burgers vector and dislocation density tensors as incompatibility measures. The true dislocation density tensor  $\mathbf{A}$  measures  $\bar{\mathbf{B}}_{\bar{\mathcal{B}}}$  in the intermediate configuration per unit area in that configuration.

The direct compatibility analysis is completed by the formal introduction of the two-field dislocation density tensors  $\mathbf{A}_{im}^p$  and  $\mathbf{A}_P^e$  (for the definition of  $\overline{\text{Curl}}$  see section B.3)

$$\mathbf{A}_{im}^p := \overline{\text{Curl}} \mathbf{F}^{p-1} \quad \text{and} \quad \mathbf{A}_P^e := \overline{\text{Curl}} \mathbf{F}^e \quad (5.40)$$

where  $\mathbf{A}_{im}^p$  measures the local material Burgers vector  $\mathbf{B}_{\bar{\mathcal{B}}}^p$  and  $\mathbf{A}_P^e$  the local spatial Burgers vector  $\mathbf{b}_{\bar{\mathcal{B}}}^e$  with respect to a surface element  $d\bar{A}$  in the intermediate configuration.  $\mathbf{A}_{im}^p$  maps between the  $i$ -intermediate cotangent and the  $m$ -aterial tangent space

$$\mathbf{A}_{im}^{pT} : \begin{cases} T_{\bar{\mathbf{X}}}\bar{\mathcal{B}} \rightarrow T_{\mathbf{X}}\mathcal{B} \\ \bar{\mathbf{N}} \mapsto \mathbf{B}_{\bar{\mathcal{B}}}^p = \mathbf{A}_{im}^{pT} \cdot \bar{\mathbf{N}}, \quad \mathbf{B}_{\bar{\mathcal{B}}}^{pA} = A_{im}^{p\bar{A}A} \bar{\mathbf{N}}_{\bar{A}} \end{cases} \quad (5.41)$$

Note that  $\mathbf{B}_{\bar{\mathcal{B}}}^p$  can be interpreted in the sense of the original definition of the Burgers vector given by FRANK [46].  $\mathbf{A}_P^e$  maps in analogy to the elastic first Piola Kirchoff stress tensor  $\mathbf{P}^e$  from the intermediate cotangent space to the spatial tangent space

$$\mathbf{A}_P^{eT} : \begin{cases} T_{\bar{\mathbf{X}}}\bar{\mathcal{B}} \rightarrow T_{\mathbf{x}}\mathcal{S} \\ \bar{\mathbf{N}} \mapsto \mathbf{b}_{\bar{\mathcal{B}}}^e = \mathbf{A}_P^{eT} \cdot \bar{\mathbf{N}}, \quad \mathbf{b}_{\bar{\mathcal{B}}}^{ea} = A_P^{e\bar{A}a} \bar{\mathbf{N}}_{\bar{A}} \end{cases} \quad (5.42)$$

As already pointed out  $\mathbf{A}_P^e$  possesses, unlike  $\mathbf{A}_{im}^p$ , a stress analogon. Thus in analogy to the Cauchy stresses and the Kirchoff stresses, the fully spatial dislocation density tensor  $\mathbf{A}_\sigma^e$  and its weighted counterpart  $\mathbf{A}_\tau^e$  associated with  $\mathbf{A}_P^e$  are defined through

$$\mathbf{A}_\sigma^e := \frac{1}{J^e} \mathbf{F}^e \cdot \mathbf{A}_P^e \quad \text{and} \quad \mathbf{A}_\tau^e := J^e \mathbf{A}_\sigma^e = \mathbf{F}^e \cdot \mathbf{A}_P^e \quad (5.43)$$

Moreover, the formal pull-back of  $\mathbf{A}_\tau^e$  results in the dislocation density tensor  $\mathbf{A}_S^e$  which fully lies in the intermediate configuration and has again no direct physical interpretation

$$\mathbf{A}_S^e := \mathbf{F}^{e-1} \cdot \mathbf{A}_\tau^e \cdot \mathbf{F}^{e-T} = \mathbf{A}_P^e \cdot \mathbf{F}^{e-T} \quad (5.44)$$

The relations between the  $\overline{\text{Curl}}$ -operator in the intermediate configuration and the material Curl- and the spatial curl-operators applied to  $\mathbf{F}^p$  and  $\mathbf{F}^e$  are given in the equations (B.28) and (B.29) in section B.3 of the Appendix. With these relations the connection between the dislocation density tensors (5.40)-(5.43) and the previously introduced dislocation tensors, summarized in figure 5.9, can now be established as follows

$$\begin{aligned} \mathbf{A}_{im}^{pT} &= -\frac{1}{J^p} \mathbf{F}^{p-1} \cdot \mathbf{A}_P^{pT} \cdot \mathbf{F}^{pT} \\ \mathbf{A}_P^{eT} &= -J^e \mathbf{F}^e \cdot \mathbf{A}_{si}^{eT} \cdot \mathbf{F}^{e-T} \\ \mathbf{A}_\tau^{eT} &= J^e \mathbf{A}_\sigma^{eT} = -J^e \mathbf{F}^e \cdot \mathbf{A}_{si}^{eT} \quad \text{and} \quad \mathbf{A}_S^{eT} = -J^e \mathbf{A}_{si}^{eT} \cdot \mathbf{F}^{e-T} = -\mathbf{A}^T \end{aligned} \quad (5.45)$$

Thereby taking gradients with respect to the generally anholonomic intermediate configuration is circumvented.

Now, in order to relate the dislocation density tensors of multiplicative crystal plasticity introduced in this section to the dislocation density tensors of the overall deformation state introduced in the previous section 5.3, the material gradient of the total deformation gradient is first evaluated by application of the chain rule as follows

$$\begin{aligned} \nabla_{\mathbf{X}} \mathbf{F} &= \nabla_{\mathbf{X}} (\mathbf{F}^e \cdot \mathbf{F}^p) = \nabla_{\mathbf{X}} \mathbf{F}^e : (\mathbf{F}^p \odot \mathbf{1}) + \mathbf{F}^e \cdot \nabla_{\mathbf{X}} \mathbf{F}^p \\ &= \bar{\nabla} \mathbf{F}^e : (\mathbf{F}^p \odot \mathbf{F}^p) + \mathbf{F}^e \cdot \nabla_{\mathbf{X}} \mathbf{F}^p \end{aligned} \quad (5.46)$$

Then contraction of (5.46) with  $\overset{3}{\mathbf{E}}$  gives with the relation between  $\overset{3}{\mathbf{E}}$  and  $\overset{3}{\mathbf{E}}$ , the fundamental tensors in the material and the intermediate configuration, (see (B.27) in the

Appendix) the following additive decomposition of the mixed variant dislocation density tensor  $\mathbf{A}_P^T$  of the total deformation into its elastic  $\mathbf{A}_P^{eT}$  and plastic  $\mathbf{A}_P^{pT}$  counterparts

$$\begin{aligned}\mathbf{A}_P^T &= -\nabla_{\mathbf{X}}\mathbf{F} : \overset{3}{\mathbf{E}} = -\bar{\nabla}\mathbf{F}^e : (\mathbf{F}^p \odot \mathbf{F}^p) : \overset{3}{\mathbf{E}} - \mathbf{F}^e \cdot \nabla_{\mathbf{X}}\mathbf{F}^p : \overset{3}{\mathbf{E}} \\ &= \mathbf{A}_P^{eT} \cdot J^p \mathbf{F}^{p-T} + \mathbf{F}^e \cdot \mathbf{A}_P^{pT}\end{aligned}\quad (5.47)$$

Equivalently, the additive decomposition of the spatial dislocation density tensor  $\mathbf{A}_\sigma^T$  of the total deformation state into its elastic  $\mathbf{A}_\sigma^{eT}$  and plastic  $\mathbf{A}_\Sigma^{pT} = \mathbf{A}^T$  counterparts is obtained by contraction of (5.47) with  $J^{-1}\mathbf{F}^T$ , according to the transformation (5.16)

$$\mathbf{A}_\sigma^T = \mathbf{A}_\sigma^{eT} + \mathbf{F}^e \cdot \mathbf{A}_\Sigma^{pT} \cdot \frac{1}{J^e} \mathbf{F}^{eT} \quad (5.48)$$

And finally the additive decomposition of the material dislocation density tensor  $\mathbf{A}_S^T$  into its elastic  $\mathbf{A}_S^{eT}$  and plastic  $\mathbf{A}_S^{pT}$  counterpart follows from (5.47) by contraction with  $\mathbf{F}^{-1}$

$$\mathbf{A}_S^T = \mathbf{F}^{p-1} \cdot \mathbf{A}_S^{eT} \cdot J^p \mathbf{F}^{p-T} + \mathbf{A}_S^{pT} \quad (5.49)$$

The elastic and the plastic contributions to each of the additive decompositions (5.47), (5.48) and (5.49) are also quite evident from the visualization in figure 5.10. From there it is obvious that e.g. the (*plastic*) pull-back of  $\mathbf{A}_S^{eT}$  and  $\mathbf{A}_S^{pT}$  itself render the contributions

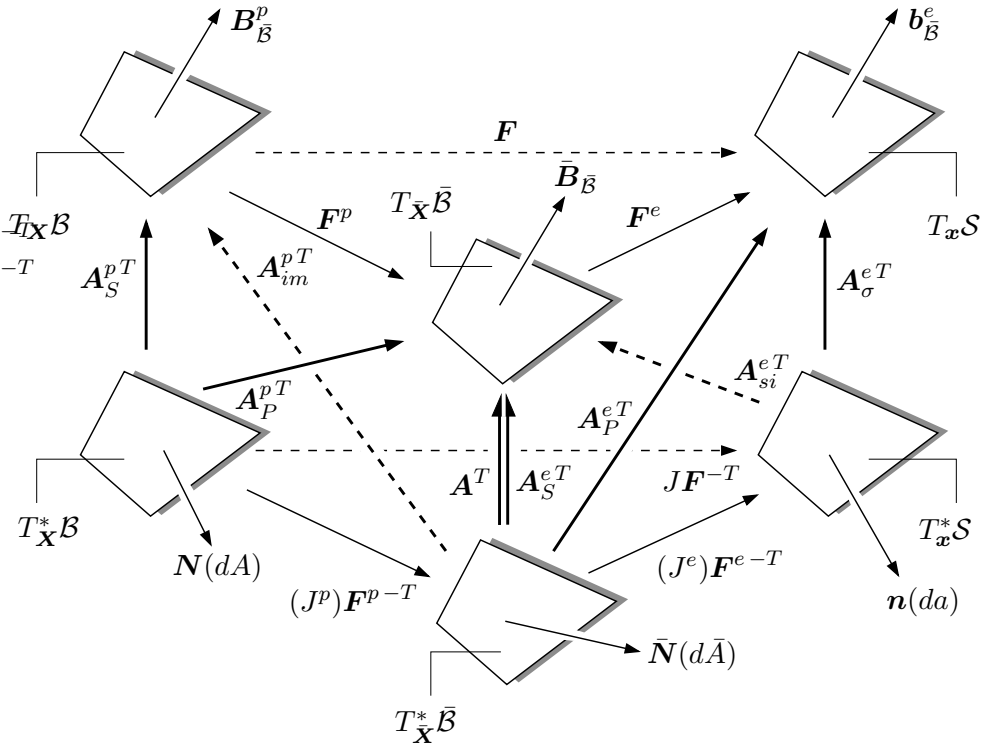


Figure 5.10: Dislocation density tensors of multiplicative plasticity.

to the material dislocation density tensor  $\mathbf{A}_S^T$  of the total deformation. Furthermore, as discussed in section 5.3, for a continuous deformed body characterized by a compatible overall deformation gradient  $\mathbf{F}$ , clearly the corresponding *total* dislocation density tensors  $\mathbf{A}_P$ ,  $\mathbf{A}_\sigma$  and  $\mathbf{A}_S$  have to vanish identically. Thus e.g. also the (*plastic*) push-forward of  $\mathbf{A}_S$  to the intermediate configuration has to vanish. Reformulation of (5.49) gives

$$\mathbf{F}^p \cdot \mathbf{A}_S \cdot \frac{1}{J^p} \mathbf{F}^{pT} = \mathbf{A}_S^e + \mathbf{F}^p \cdot \mathbf{A}_S^p \cdot \frac{1}{J^p} \mathbf{F}^{pT} \stackrel{!}{=} \mathbf{0} \quad (5.50)$$

which by insertion of the explicit forms of  $\mathbf{A}_S^e$  through (5.45)<sub>4</sub> in combination with (5.26)<sub>2</sub> and of  $\mathbf{A}_S^p$  through (5.37) with (5.26)<sub>1</sub> results in the expression

$$-J^e \mathbf{F}^{e-1} \cdot \text{curl} \mathbf{F}^{e-1} + \frac{1}{J^p} \mathbf{F}^p \cdot \text{Curl} \mathbf{F}^p \stackrel{!}{=} \mathbf{0} \quad (5.51)$$

This is obviously satisfied since it implies the definition of the true dislocation density tensor  $\mathbf{A}$  according to (5.32). The dislocation density tensors of multiplicative crystal plasticity introduced in this section are summarized in figure 5.10. Therein a special focus is put on the dislocation density tensors which are equipped with a stress analogon.

Finally, the following relation between the material and the spatial continuity equations for the dislocation density in the intermediate configuration is established

$$\text{Div}[\mathbf{A}_P^{pT}] = J \text{div}[\mathbf{A}_{si}^{eT}] \quad (5.52)$$

This follows directly from (5.35) with  $\text{Div}(J\mathbf{F}^{-T}) = \mathbf{0}$ , which for example results from  $\int_{\partial S} \mathbf{n} da = \mathbf{0}$  in the case of a compatible total deformation state.

To summarize, within this section the dislocation density tensor has been introduced in a direct manner as a measure of the incompatibility of the intermediate configuration. Thereby a clear understanding of the *true* dislocation density in the intermediate configuration was achieved, measured either through the spatial curl of the inverse elastic part of the deformation gradient or alternatively through the material Curl of the plastic gradient part. Furthermore, relations between the corresponding elastic and plastic dislocation density tensors have been established including also the relations to the vanishing ‘dislocation’ density tensors of the compatible total deformation state. These relations are apparent in a quite intriguing manner from their visualizations in figures 5.9 and 5.10.

In order to get a deeper insight into the aspects of incompatibility and also for the sake of a historical perspective, the topic of incompatibility will be approached in the following section from a differential geometric point of view. This will also equip further developments with a sound mathematical bases and provide several starting points for an extension of the model proposed in the subsequent sections.

## 5.5. Differential Geometric Compatibility Analysis

The key objective of this section is to analyze the incompatibility of the intermediate configuration based on a differential geometric point of view. Thereby the dislocation density tensor introduced in the previous section will be identified with the non-vanishing *Cartan torsion*, a key geometric object of the *non-Riemannian* geometry. This owes mainly to the description of continuous static defect distributions by objects of differential geometry in the works of KONDO [71, 72, 73], BILBY ET AL. [19], GÜNTHER [49], KRÖNER & SEEGER [80] and KRÖNER [77] which led to an identification of the continuum-mechanical theory of dislocations with a *Cartan geometry*. Based on this analogy, the latter authors developed a continuum theory relating internal stresses and dislocation distributions in the geometrically nonlinear setting. Extending the Cartan geometry to a more abstract differential geometry allows for the treatment of more general defects such as *vacancies* or *interstitial atoms*, e.g. ANTHONY [3, 4] or KRÖNER [78]. However, the present treatment is concerned solely with defects in the form of dislocations resulting in an identification of the geometry of the continuously dislocated crystal in the most general case with a *flat non-Riemannian* geometry characterized by a single asymmetric

*connection*. As will be seen, in the general case the *compatibility conditions* are violated in the context of multiplicative elastoplasticity, characterizing the *incompatibility* of the intermediate configuration. A connection to the elaborations by TRUESDELL & NOLL [153] can be made by understanding the incompatibility as the *inhomogeneity* of a what they call *materially uniform body*.

The outline of this section is as follows, in order to access in an easily accessible manner the implications of an incompatibility of the state of deformation, first the formulation of the incompatibility conditions will be discussed for the small strain setting. Next, before extending them to the finite strain setting, the definition of the key quantities of the non-Euclidean geometry needed in the further developments will be given. Then the compatibility conditions will be formulated for the overall state of deformation. Finally, compatibility of the plastic intermediate configuration will be analyzed and the corresponding incompatibility measures will be related to the previously introduced dislocation density tensors. Besides the classical works mentioned above, further literature related to the field of incompatible deformation states and differential geometry can be found in SCHOUTEN [132], MALVERN [88], ERINGEN [36], KLINGBEIL [67], STEINMANN [140], ACHARYA & BASSANI [1] and HAUPT [55] to name a few of the works underlying the following elaborations.

**5.5.1. Compatibility Conditions at Small Strains.** In the small strain context, the strains  $\boldsymbol{\varepsilon}$  are derived from the displacements  $\mathbf{u}$  in the following linearized format

$$\boldsymbol{\varepsilon} = \text{sym}[\nabla \mathbf{u}] \quad \text{or} \quad \varepsilon_{ij} = \frac{1}{2}(\partial_{x_j} u_i + \partial_{x_i} u_j) \quad (5.53)$$

Assuming a sufficiently differentiable displacement field  $\mathbf{u}$  the six, partial differential equations (5.53) uniquely define the strain field  $\boldsymbol{\varepsilon}$ . On the other hand, posing the inverse problem, i.e. attempting to determine the displacement field  $\mathbf{u}$  from a given strain field  $\boldsymbol{\varepsilon}$ , rises the mathematical difficulty that the system of equations (5.53) is overdetermined since it specifies six partial differential equations for only three unknowns. Thus certain *integrability* or *compatibility* conditions need to be imposed onto the strain field in order to obtain a continuous and single-valued displacement field solution. Within the present small strain context these conditions can be derived as follows. Taking the second order derivatives of  $\varepsilon_{yy}$  to  $z$ ,  $\varepsilon_{zz}$  to  $y$  and  $\varepsilon_{yz}$  to  $y$  and  $z$ , respectively, gives

$$\frac{\partial^2 \varepsilon_{yy}}{\partial z^2} = \frac{\partial^3 u_y}{\partial z^2 \partial y}, \quad \frac{\partial^2 \varepsilon_{zz}}{\partial y^2} = \frac{\partial^3 u_z}{\partial y^2 \partial z}, \quad 2 \frac{\partial^2 \varepsilon_{yz}}{\partial y \partial z} = \frac{\partial^3 u_y}{\partial z^2 \partial y} + \frac{\partial^3 u_z}{\partial y^2 \partial y} \quad (5.54)$$

Now insertion of (5.54)<sub>1</sub> and (5.54)<sub>2</sub> into (5.54)<sub>3</sub> gives the first compatibility condition

$$S_{11} = + \frac{\partial^2 \varepsilon_{yy}}{\partial z^2} + \frac{\partial^2 \varepsilon_{zz}}{\partial y^2} - 2 \frac{\partial^2 \varepsilon_{yz}}{\partial y \partial z} = 0 \quad (5.55)$$

In a similar manner, one can derive five more such necessary integrability conditions. This gives in total a set of six equations, known as *St.-Venant's compatibility equations* (B. de Saint-Venant, 1864, see Love [1944]). These can be written in the compact form

$$\mathbf{S} = \nabla \times \boldsymbol{\varepsilon} \times \nabla = \mathbf{0} \quad \text{or} \quad S_{ij} = \epsilon_{ikl} \varepsilon_{km,ln} \epsilon_{jmn} = 0 \quad (5.56)$$

These compatibility conditions are necessary and sufficient conditions for the existence of a continuous single-valued displacement field  $\mathbf{u}$  in a simply connected body (the proof for

sufficiency can be found e.g. in SOKOLNIKOFF [139]). However the six conditions (5.56) are not independent as they can be related to each other in accordance with the *Bianchi identities* of the *Riemannian geometry*, thus representing in total 3 independent equations. So these three compatibility conditions together with the three equilibrium differential equations and the six stress-strain relations form a system of 12 equations to solve for the 12 unknown functions in a classical boundary value problem of the small strain setting, i. e. the six independent stresses and the six independent strains. It is important to note that the compatibility conditions are not needed at all when the displacement field is explicitly included within the field of unknowns, since any continuous solution of the field equations in terms of these unknowns will automatically be compatible. Then one has 15 equations (six equations (5.53), three equilibrium equations and six stress-strain relations) to solve for the 15 unknown functions (three displacements, six stresses and six strains).

**5.5.2. The Geometric Objects of Differential Geometry.** In the context of the multiplicative split of the total deformation gradient  $\mathbf{F}$  in finite strain plasticity, the intermediate configuration  $\bar{\mathcal{B}}$  is specified solely by the plastic part  $\mathbf{F}^p$  or the elastic part  $\mathbf{F}^e$  which are generally not derivable from a deformation field. According to the previous section, this rises the question what integrability or compatibility conditions have to be posed for  $\mathbf{F}^p$  or  $\mathbf{F}^e$  (or the right Cauchy-Green or the inverse Finger tensor formed from them) such that they correspond to a continuous single-valued displacement field describing a compatible intermediate configuration. Vice versa one is tempted to ask for the physical interpretation of possible incompatibilities since in general the intermediate configuration is incompatible. In order to arrive at the compatibility conditions for the finite strain setting, more general non-Euclidean geometries will be considered in the following. Therefore first the definitions for some related geometric objects needed in the further developments will be given. The definitions of section 2.1 will not be repeated here, but they are crucial for the understanding of the following elaborations.

**Holonomic and Anholonomic Base Systems.** Assume two global base systems  $\{\mathbf{e}_i\}_{i=1,2,3}$  and  $\{\bar{\mathbf{e}}_i\}_{i=1,2,3}$  with the associated coordinates  $x^i$  and  $\bar{x}^i$ . Then, due to  $x^i = x^i(\bar{x}^i)$ , the base transformation reads

$$\bar{\mathbf{e}}_j = \partial_{\bar{x}^j} x^i \mathbf{e}_i \quad (5.57)$$

So the *Jacobian* of this transformation specifies the corresponding transformation matrix

$$A^i_j = \partial_{\bar{x}^j} x^i \quad (5.58)$$

which obviously has to satisfy the following *integrability* conditions, see equation (5.6)

$$\partial_{[k} A^i_{j]} := \frac{1}{2}(\partial_k A^i_j - \partial_j A^i_k) = 0 \quad (5.59)$$

or also SCHOUTEN [132], p. 99. Here, for the sake of a compact notation and the ease of reference to classical literature, square brackets  $[\bullet]$  are used to denote skewsymmetric permutation in the enclosed indices as defined in (5.59). Equations (5.57) to (5.59) define a base system  $\bar{\mathbf{e}}_i$  which is *holonomic with respect to system  $\mathbf{e}_i$* . The base systems introduced in section 2.1.1 and 2.1.3 can all be understood as holonomic base systems, furthermore as stated already in section 2.1.2 the deformation gradient can be identified with the transformation matrix (5.58). One can also define an *anholonomic base system*

$\bar{\mathbf{a}}_i$  (SCHOUTEN [132], p. 99 f.) which is not connected with any system of allowable coordinates  $\bar{x}^i$ . For such a system the transformation matrix  $A^i_j$  cannot be computed in the sense of (5.58). One can only specify the *Pfaffian anholonomic transformation*

$$\bar{\mathbf{a}}_j := A^i_j \mathbf{e}_i \quad (5.60)$$

Since coordinates  $\bar{x}^i$  do not exist, the partial derivative of any quantity  $(\bullet)$  cannot be computed in the sense of  $\frac{\partial(\bullet)}{\partial \bar{x}^i}$ . They are defined through the *anholonomic derivative*

$$\partial_k(\bullet) := A^i_k \partial_i(\bullet) \quad (5.61)$$

Moreover the matrices  $A^i_j$  do not satisfy the integrability conditions (5.59), i.e.

$$\partial_{[k} A^i_{j]} \neq 0 \quad (5.62)$$

As will be seen later, the intermediate configuration introduced in the context of the multiplicative split in finite strain plasticity defines in general an anholonomic configuration.

**Metric Tensor.** The co- and contravariant metric tensors  $g_{ij}$  and  $g^{ij}$  were already introduced in section 2.1.1. They allow for the determination of lengths of vectors and angles between vectors, e.g.

$$\|d\mathbf{x}\| = (dx^i g_{ij} dx^j)^{1/2} \quad \text{and} \quad \cos \alpha = \frac{dx^i g_{ij} dy^j}{(dx^k g_{kl} dx^l)^{1/2} (dy^m g_{mn} dy^n)^{1/2}} \quad (5.63)$$

which is defined of course only for a positive definite metric  $g_{ij}$ . Thus within the multidimensional space they also serve for the measurement of areas and volumes. Here it should just be emphasized that it is also possible to define the metric tensors for an anholonomic base system, e.g. the covariant metric  $\bar{g}_{kl}$  of the possibly anholonomic configuration

$$\bar{g}_{kl} := A^i_k A^j_l g_{ij} \quad (5.64)$$

which allows for the measurement of lengths and angles also in the anholonomic configuration, even if  $\bar{x}^i$  does not exist. In Euclidean systems the metric tensors can always be reduced to the simple diagonal form  $g_{ij} = \delta_{ij}$  and  $g^{ij} = \delta^{ij}$  by means of a coordinate transformation. In the case of non-Euclidean systems with non-vanishing *torsion*, the metric tensors will have the simple diagonal form only in an anholonomic base system.

**Affine Connection.** Besides being able to measure lengths and angles between vectors, it is also important to be able to determine the *parallelism* of vectors. In the Euclidean space, the parallelism of two vectors is trivially understood in terms of e.g. the angle between them. In the general non-Euclidean space, two vectors  $\mathbf{u}$  and  $\mathbf{u}'$  being a distance  $d\mathbf{x}$  apart from each other are said to be parallel if they satisfy

$$du^i = u'^i - u^i = -\Gamma^i_{jk} u^k dx^j \quad (5.65)$$

with the coefficients of the *linear* or *affine connection*  $\Gamma^i_{jk}$  (A more accurate way of writing would be  $\Gamma^i_{\cdot jk}$  for the connection. Nevertheless the notation  $\Gamma^i_{jk}$  will be used in the following implying the same meaning). The connection is the key geometric object of differential geometry in the following elaborations. According to (5.65), the connection describes how the components  $u^i$  of a vector change if it is displaced by a distance  $dx^j$  along a path

within the generally curved space. This is also known as *parallel transport*. The connection itself is not a tensor since it transforms according to

$$\Gamma_{mn}^l = A_m^j A_n^k A_i^l \Gamma_{jk}^i + A_k^l \partial_m A_n^k \quad (5.66)$$

which also contains derivatives of the transformation  $\mathbf{A}$ . Consequently the connection might vanish in one coordinate system while it is non-zero in another, in contrast to a tensor, which, once it vanishes in one system, vanishes identically in any other system as well. The connection transforms tensorially only when the term containing the derivative vanishes, i.e. in a Cartesian base system. The *affinity*  $\Gamma_{jk}^i$  also plays an important role in *covariant differentiation*. For a general *non-Riemannian* space which is not necessarily equipped with a metric, the covariant derivative  $D_j(\cdot)$  with respect to the connection  $\mathbf{\Gamma}$  of a contravariant vector is by definition

$$D_j u^i := \partial_j u^i + \Gamma_{jk}^i u^k \quad (5.67)$$

Since for the covariant differentiation the product rules are valid and moreover the covariant derivative of an absolute invariant must coincide with its partial derivative, one gets

$$D_j (u^i v_i) = \partial_j (u^i v_i) \quad (5.68)$$

From this the covariant derivative of a covariant vector follows by insertion of (5.67) as

$$D_j v_i = \partial_j v_i - \Gamma_{ji}^k v_k \quad (5.69)$$

Contrary to the partial derivative, the covariant derivative transforms like a tensor. With (5.67) and (5.69) the covariant derivative of a tensor of arbitrary order reads

$$D_l T_{ij\dots}^{mn\dots} = \partial_l T_{ij\dots}^{mn\dots} + \Gamma_{lk}^m T_{ij\dots}^{kn\dots} + \Gamma_{lk}^n T_{ij\dots}^{mk\dots} + \dots - \Gamma_{li}^k T_{kj\dots}^{mn\dots} - \Gamma_{lj}^k T_{ik\dots}^{mn\dots} - \dots \quad (5.70)$$

The notion of covariant differentiation and consequently the significance of the connection  $\mathbf{\Gamma}$  might be easier to understand in the less general *Riemannian space* which is equipped with a metric and a vanishing *torsion* (see below). There, the second term in (5.67) follows directly by keeping in mind that in addition to the partial derivatives  $\partial_j u^i$  of the components, the co- and contravariant base vectors  $\mathbf{g}_i$  and  $\mathbf{g}^i$  of general curvilinear coordinates  $\theta^i$  also possess non-vanishing partial derivatives. Thus writing the covariant derivative  $D_j(\cdot)$  of a contravariant vector  $u^i$  in base notation gives

$$D_j u^i \mathbf{g}_i = \partial_j u^i \mathbf{g}_i + u^i \partial_j \mathbf{g}_i \quad (5.71)$$

Through the connection one can express the partial derivative of the covariant base vectors  $\mathbf{g}_i$  with respect to the coordinates  $\theta^j$  as linear combinations of the base vectors themselves

$$\frac{\partial \mathbf{g}_i}{\partial \theta^j} = \Gamma_{ji}^k \mathbf{g}_k \quad (5.72)$$

Multiplication of both sides with a contravariant base vector  $\mathbf{g}^i$  (recall  $\mathbf{g}^i \cdot \mathbf{g}_j = \delta^i_j$ ) and insertion of (2.4) gives the following identification for the coefficients of the affine connection

$$\Gamma_{ji}^k = \mathbf{g}^k \cdot \frac{\partial \mathbf{g}_i}{\partial \theta^j} = \frac{\partial \theta^k}{\partial \mathbf{x}} \cdot \frac{\partial^2 \mathbf{x}}{\partial \theta^i \partial \theta^j} \quad (5.73)$$

Taking the partial derivative of  $\mathbf{g}^i \cdot \mathbf{g}_j = \delta^i_j$  in connection with (5.72), one can furthermore identify the partial derivatives of the contravariant basis as

$$\frac{\partial \mathbf{g}^i}{\partial \theta^j} = -\Gamma_{jk}^i \mathbf{g}^k \quad (5.74)$$

Insertion of (5.72) into (5.71) and (5.74) into the corresponding form for the covariant derivative of a covariant vector  $u_i$  gives the representations (5.67) and (5.69) for the Riemannian space. Obviously (5.73) induces that for the Riemannian space under consideration the connection is symmetric in the lower two indices

$$\Gamma_{ij}^k = \Gamma_{ji}^k \quad (5.75)$$

this in turn implies *global compatibility* since symmetry of the connection  $\Gamma$  ensures through (5.73) the existence of holonomic twice continuously differentiable coordinates  $\mathbf{x}$ . Within the Riemannian space, the connection can be derived from the metric coefficients allowing for a representation in terms of the *Christoffel symbols* (see below). Finally, note that the connection  $\Gamma_{jk}^i$  has generally 27 functional degrees of freedom, which reduces to 15 for metric spaces, i.e. spaces which are equipped with a metric.

**Metric Connections.** The connection is called a *metric connection* if it is consistent with the metric, such that the covariant derivatives of the metric tensor vanish. With (5.70) this demands for the covariant derivative of e.g. the covariant metric

$$D_l g_{ij} = \partial_l g_{ij} - \Gamma_{li}^k g_{kj} - \Gamma_{lj}^k g_{ik} = 0 \quad (5.76)$$

This requirement is also known as the *Ricci theorem*.

**Christoffel Symbols.** As mentioned above, in the Riemannian space the coefficients of the affine connection  $\Gamma_{ij}^k$  can be derived from the metric coefficients. To this end, differentiation of the covariant metric coefficients  $g_{ij}$  gives in analogy to condition (5.76)

$$\frac{\partial g_{ij}}{\partial \theta^n} = \frac{\partial(\mathbf{g}_i \cdot \mathbf{g}_j)}{\partial \theta^n} = \Gamma_{ni}^p \mathbf{g}_p \cdot \mathbf{g}_j + \Gamma_{nj}^p \mathbf{g}_i \cdot \mathbf{g}_p = \Gamma_{ni}^p g_{pj} + \Gamma_{nj}^p g_{ip} \quad (5.77)$$

Cyclic permutation of the indices  $i, n, j$  in (5.77) results in two more equations

$$\frac{\partial g_{ni}}{\partial \theta^j} = \Gamma_{jn}^p g_{pi} + \Gamma_{ji}^p g_{np} \quad (5.78)$$

$$\frac{\partial g_{jn}}{\partial \theta^i} = \Gamma_{ij}^p g_{pn} + \Gamma_{in}^p g_{jp} \quad (5.79)$$

Next, multiplication of (5.77) with  $-1/2$  and (5.78) and (5.79) with  $+1/2$  gives after summation and consideration of the respective symmetries for the Riemannian space

$$\Gamma_{ij}^p g_{pn} = \frac{1}{2} \left( \frac{\partial g_{jn}}{\partial \theta^i} + \frac{\partial g_{ni}}{\partial \theta^j} - \frac{\partial g_{ij}}{\partial \theta^n} \right) \quad (5.80)$$

This gives finally after contraction with the contravariant metric coefficients  $g^{kn}$

$$\Gamma_{ij}^k = \frac{1}{2} g^{kn} \left( \frac{\partial g_{jn}}{\partial \theta^i} + \frac{\partial g_{ni}}{\partial \theta^j} - \frac{\partial g_{ij}}{\partial \theta^n} \right) =: \left\{ \begin{matrix} k \\ ij \end{matrix} \right\} \quad (5.81)$$

which defines the so-called *Christoffel symbols of the second kind*  $\{\overset{k}{\Gamma}_{ij}\}$ . An equivalent definition of the Christoffel symbols is given by (5.73). Thus in the Riemannian space the connection can be derived from the metric coefficients and only in this space and its special cases (e.g. Euclidean space) it always coincides with the Christoffel symbols

$$\text{in Riemannian space: } \Gamma_{ij}^k = \left\{ \begin{matrix} k \\ ij \end{matrix} \right\} \quad (5.82)$$

A further simplification follows for Cartesian base systems. In this case  $g_{ij} = \delta_{ij}$  and obviously the partial derivatives of the metric coefficients vanish in (5.81) inducing

$$\Gamma_{ij}^k = 0 \quad (5.83)$$

which recovers in connection with (5.65) the trivial understanding of the parallel transport. By means of a base transformation it is indeed always possible in an Euclidean space to transform the connection such that it satisfies (5.83). For non-Euclidean spaces this transformation along with a metric representation in terms of the identity tensor is in general only possible within an anholonomic base system and if the corresponding *Riemann-Christoffel Curvature Tensor* (see below) vanishes.

**Cartan Torsion.** For *non-Riemannian* geometries the connection  $\Gamma$  does generally not satisfy (5.75), i.e. it is in general unsymmetric in the lower two indices. The skewsymmetric part of the connection forms a tensor, the so-called *torsion tensor* (CARTAN [24])

$$\mathcal{T}_{ij}^k := \Gamma_{[ij]}^k \quad (5.84)$$

Obviously, the torsion vanishes if the connection is symmetric. In turn a non-vanishing torsion induces that the inner geometry becomes non-Riemannian and the associated

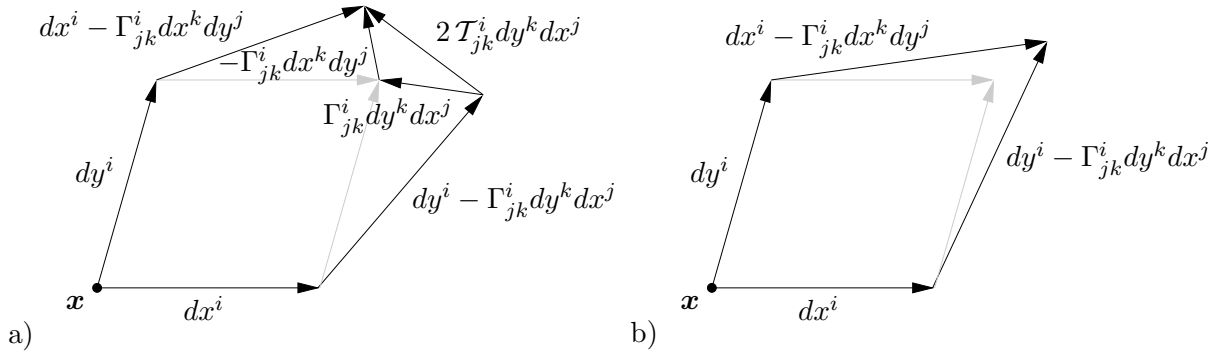


**Figure 5.11:** Geometrical significance of the torsion tensor  $\mathcal{T}$ . a) For a non-vanishing torsion the infinitesimal parallelogram has a closure failure. b) The torsion tensor vanishes for Riemannian spaces and any two vectors  $d\mathbf{x}$  and  $d\mathbf{y}$  define a closed infinitesimal *parallelogram*.

configuration is anholonomic, or *incompatible* (The definition of the torsion tensor with respect to an anholonomic base system would require to add the so-called *anholonomic object*  $\Omega_{ij}^k := A^o_i A^p_j \partial_{[o} A^k_{p]}$  to the right hand side of definition (5.84)). Thus the torsion tensor is a natural *incompatibility measure*. The geometrical significance of the torsion tensor can be explained as follows. Consider two infinitesimal vectors  $d\mathbf{x}$  and  $d\mathbf{y}$  at  $\mathbf{x}$ . Displacing  $d\mathbf{x}$  parallel along  $d\mathbf{y}$  gives through (5.65)

$$dx'^i = dx^i - \Gamma_{jk}^i dx^k dy^j \quad (5.85)$$

Similarly, displacing  $d\mathbf{y}$  parallel along  $d\mathbf{x}$  gives

$$dy'^i = dy^i - \Gamma_{jk}^i dy^k dx^j \quad (5.86)$$

As can be seen from figure 5.11, the closure failure of the polygon formed by the four vectors  $d\mathbf{x}$ ,  $d\mathbf{x}'$ ,  $d\mathbf{y}$  and  $d\mathbf{y}'$  follows in terms of the torsion tensor as

$$2\mathcal{T}_{jk}^i dy^k dx^j = \Gamma_{jk}^i dy^k dx^j - \Gamma_{kj}^i dy^k dx^j \quad (5.87)$$

Hence, any two vectors  $d\mathbf{x}$  and  $d\mathbf{y}$  define a closed infinitesimal *generalized parallelogram* only for geometries with vanishing torsion, i.e. a symmetric connection.

**Riemann Connection and Contortion.** The most general form of a metric connection in the non-Riemannian space is given by the following decomposition

$$\Gamma_{ij}^k = \mathcal{G}_{ij}^k + \mathcal{Q}_{ij}^k \quad (5.88)$$

in terms of the *Riemannian connection*  $\mathcal{G}$  which is specified entirely through the Riemannian metric  $\mathbf{g}$ , i.e. it is given by the the Christoffel symbols of the second kind corresponding to the metric  $\mathbf{g}$ , and in terms of the so-called *contortion tensor*  $\mathcal{Q}$ . The contortion can be expressed entirely through the torsion tensor  $\mathcal{T}$  which has been introduced above. In order to derive this representation one starts in the same way as in deriving the Christoffel symbols, i.e. one multiplies (5.77) with  $-1/2$  and (5.78) and (5.79) with  $+1/2$  and sums up, where this time for the non-Riemannian space the connection is generally unsymmetric, and hence one gets

$$\frac{1}{2} \left( \frac{\partial g_{jn}}{\partial \theta^i} + \frac{\partial g_{ni}}{\partial \theta^j} - \frac{\partial g_{ij}}{\partial \theta^n} \right) = \frac{1}{2} (\Gamma_{ij}^p + \Gamma_{ji}^p) g_{pn} + \frac{1}{2} (\Gamma_{jn}^p - \Gamma_{nj}^p) g_{pi} - \frac{1}{2} (\Gamma_{ni}^p - \Gamma_{in}^p) g_{pj} \quad (5.89)$$

From this one obtains after reformulation and insertion of the definition of the Christoffel symbols of the second kind (5.81)

$$\Gamma_{ij}^k g_{kn} = \left\{ \begin{matrix} k \\ ij \end{matrix} \right\} g_{pn} + \Gamma_{[ij]}^k g_{kn} + \Gamma_{[ni]}^k g_{kj} - \Gamma_{[jn]}^k g_{ki} \quad (5.90)$$

This renders the definition of the contortion tensor  $\mathcal{Q}$  in terms of the torsion tensor  $\mathcal{T}$

$$\mathcal{Q}_{ij}^k g_{kn} = \mathcal{T}_{[ij]}^k g_{kn} + \mathcal{T}_{[ni]}^k g_{kj} - \mathcal{T}_{[jn]}^k g_{ki} \quad (5.91)$$

Obviously the fully covariant representation of the contortion  $\mathcal{Q}_{ij}^k g_{kn}$  is antisymmetric in the indices  $j$  and  $n$ , and thus describes a pure rotation of a vector.

**Riemann-Christoffel Curvature Tensor.** Besides the torsion tensor the *Riemann-Christoffel curvature tensor*  $\mathbf{R}$  will now be introduced as a second incompatibility measure. It occurs in the second order covariant derivative, with respect to the generally holonomic coordinates and is defined as

$$R_{ljk}^i := \Gamma_{jk,l}^i - \Gamma_{lk,j}^i + \Gamma_{lo}^i \Gamma_{jk}^o - \Gamma_{jo}^i \Gamma_{lk}^o \quad (5.92)$$

(Again the most accurate way of writing would be  $R_{.ljk}^i$ ) If the curvature tensor vanishes, the connection is said to be integrable and the corresponding geometry is called *flat* or it is said to possess *distant parallelism* or *teleparallelism*. Vice versa, if the curvature tensor

is distinct from zero, the associated configuration is again anholonomic or *incompatible*. However, this compatibility criterion is only of local nature in contrast to a vanishing torsion or condition (5.75). Furthermore, it requires that the connection is continuously differentiable or equivalently that the overall coordinates are differentiable of third order in the case of global compatibility with a holonomic base system in the sense of (5.73). It is also important to note that in general the definition of the curvature tensor does not require the definition of a metric consistent with it, nor is the connection from which it is formed in general symmetric. In order to give again a geometrical interpretation of the meaning of the curvature tensor, consider the transplantation of a vector  $\mathbf{u}$  along a closed

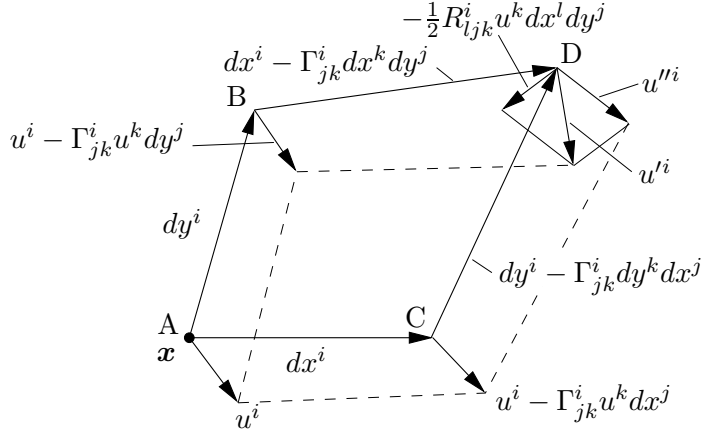


**Figure 5.12:** Geometrical significance of the Riemann-Christoffel curvature tensor  $\mathbf{R}$ .

parallelogram. Assuming a torsion free, i.e. Riemannian space any two vectors  $d\mathbf{x}$  and  $d\mathbf{y}$  define a closed infinitesimal *generalized parallelogram*  $ABCD$  at  $\mathbf{x}$ , see figure 5.12. In analogy to figure 5.11 b), the four sides of the parallelogram are given by  $d\mathbf{x}$ ,  $d\mathbf{y}$  and the parallel transplantations  $\overline{BD}$  of  $d\mathbf{x}$  along  $d\mathbf{y}$  and  $\overline{CD}$  of  $d\mathbf{y}$  along  $d\mathbf{x}$  respectively, where one gets with (5.65)

$$\begin{aligned}\overline{BD} &: dx^i - \Gamma_{jk}^i dx^k dy^j \\ \overline{CD} &: dy^i - \Gamma_{jk}^i dy^k dx^j\end{aligned}\quad (5.93)$$

Now, displacing the vector  $\mathbf{u}$  along  $\overline{AB}$  gives in B

$$u^i - \Gamma_{jk}^i u^k dy^j \quad (5.94)$$

Furthermore along  $\overline{AB}$  the connection changes, such that it is in B

$$\Gamma_{jk}^i + \Gamma_{jk,l}^i dy^l \quad (5.95)$$

Thus, transplanting the vector  $\mathbf{u}$  from A via B to  $\mathbf{u}'$  in D, gives in total

$$\begin{aligned}u'^i &= u^i - \Gamma_{jk}^i u^k dy^j - (\Gamma_{jk}^i + \Gamma_{jk,l}^i dy^l)(u^k - \Gamma_{mn}^k u^n dy^m)(dx^j - \Gamma_{or}^j dx^r dy^o) \\ &= u^i - \Gamma_{jk}^i u^k dy^j - \Gamma_{jk}^i u^k dx^j + (\Gamma_{jo}^i \Gamma_{lk}^o + \Gamma_{ok}^i \Gamma_{lj}^o - \Gamma_{jk,l}^i) u^k dx^j dy^l\end{aligned}\quad (5.96)$$

where all third-order terms are neglected. In a similar way, one obtains the transplantation of  $\mathbf{u}$  from A via C to  $\mathbf{u}''$  in D by interchanging  $d\mathbf{x}$  and  $d\mathbf{y}$  in (5.96) as

$$u''^i = u^i - \Gamma_{jk}^i u^k dx^j - \Gamma_{jk}^i u^k dy^j + (\Gamma_{lo}^i \Gamma_{jk}^o + \Gamma_{ok}^i \Gamma_{jl}^o - \Gamma_{lk,j}^i) u^k dx^j dy^l \quad (5.97)$$

Finally, since it is assumed that the generalized parallelogram ABCD is closed and thus the corresponding torsion vanishes identically (i.e.  $\Gamma_{jl}^o = \Gamma_{lj}^o$ ), the difference between the transplanted vectors  $\mathbf{u}'$  and  $\mathbf{u}''$  at D is

$$u'^i - u''^i = -(\Gamma_{jk,l}^i - \Gamma_{lk,j}^i + \Gamma_{lo}^i \Gamma_{jk}^o - \Gamma_{jo}^i \Gamma_{lk}^o) u^k dx^j dy^l = -\frac{1}{2} R_{ljk}^i u^k dx^j dy^l \quad (5.98)$$

where the antisymmetry in the indices  $j$  and  $l$  on the right hand side of equation (5.98) reflects the fact that one obtains the converse difference in the transplanted vectors if one computes  $u''^i - u'^i$ . Thus the parallel displacement of any quantity is path independent only if the corresponding geometry is flat and hence the curvature tensor  $\mathbf{R}$  vanishes.

If the space is equipped with a metric, the fully covariant curvature tensor  $R_{ljki} = R_{ljk}^n g_{ni}$  corresponding to a metric connection has the following antisymmetry properties

$$\begin{aligned} R_{ljki} &= -R_{jlk i} \\ R_{ljki} &= -R_{ljik} \end{aligned} \quad (5.99)$$

Note that the curvature tensor is symmetric with respect to an exchange of the first and second index pair only if the corresponding connection is symmetric, in general one has

$$R_{ljki} \neq -R_{kilj} \quad (5.100)$$

Thus in the three-dimensional space the covariant fourth order curvature tensor  $R_{ljki}$  is equivalent to the second order contravariant *Einstein tensor*  $R^{mn}$  (which is not valid for general-dimensional spaces where the Einstein tensor is defined through the Ricci-tensor)

$$R^{mn} = \frac{1}{4} \epsilon^{njl} \epsilon^{mki} R_{ljki} \quad (5.101)$$

Computing the covariant *axial vector*  $\omega$  of the Einstein tensor gives

$$\omega_i = -\frac{1}{2} \epsilon_{mni} R^{mn} = \frac{1}{4} \epsilon^{ljk} R_{ljki} \quad (5.102)$$

which is equivalent to the (*first*) *Bianchi identity*. Insertion of (5.92) into (5.102) gives

$$\begin{aligned} \omega_n &= \frac{1}{4} \epsilon^{ljk} g_{ni} \{ \Gamma_{jk,l}^i - \Gamma_{lk,j}^i + \Gamma_{lo}^i \Gamma_{jk}^o - \Gamma_{jo}^i \Gamma_{lk}^o \} \\ &= \frac{1}{2} g_{ni} \{ [\frac{1}{2}(\Gamma_{jk}^i - \Gamma_{kj}^i) \epsilon^{jkl}]_{,l} + \Gamma_{lo}^i [\frac{1}{2}(\Gamma_{jk}^o - \Gamma_{kj}^o) \epsilon^{jkl}] \} \end{aligned} \quad (5.103)$$

which finally gives with the definition of the torsion tensor (5.84)

$$\omega_n = \frac{1}{2} g_{ni} \{ [\mathcal{T}_{jk}^i \epsilon^{jkl}]_{,l} + \Gamma_{lo}^i [\mathcal{T}_{jk}^o \epsilon^{jkl}] \} \quad (5.104)$$

Thus, obviously for a vanishing torsion with  $\mathcal{T}_{jk}^i \epsilon^{jkl} = 0$  the axial vector  $\omega$  also vanishes and consequently the Einstein tensor is symmetric. In this case the corresponding geometry is called *symmetric*.

**Classification of Affine Geometries.** To summarize the significance of the introduced geometric objects of differential geometry, a classification of the different spaces through these quantities is visualized in figure 5.13 (vanishing curvature tensor:  $\mathbf{R} = \mathbf{0}$ , vanishing torsion tensor:  $\mathcal{T} = \mathbf{0}$ , metric connection:  $\mathbf{\Gamma} = \text{MC}$ ). A geometry which is torsion free but not necessarily flat defines a *Riemannian geometry*. On the other hand, a flat but

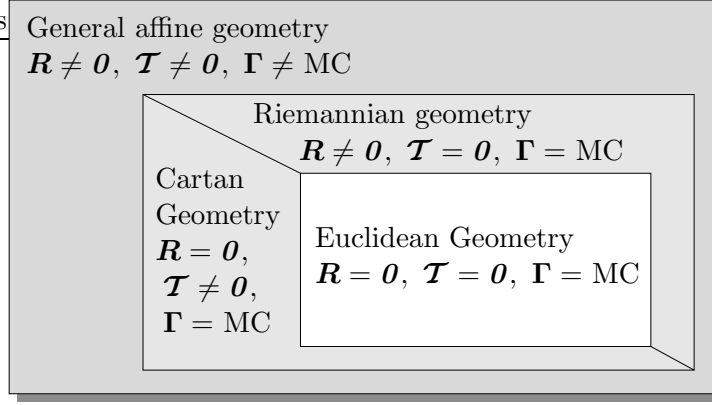


**Figure 5.13:** The special cases of a general affine geometry.

not necessarily torsion free geometry is denoted as a *Cartan geometry*. Obviously, in the general case, neither does the global demand for vanishing torsion induce vanishing curvature nor does the converse relation hold. However, if both compatibility conditions are satisfied, the geometry boils down to an *Euclidean geometry* being both globally and locally compatible.

**Connection for Geometries with Teleparallelism.** Before starting with the compatibility analysis for the setting of multiplicative plasticity, a specific form of the connection will finally be given which is metric and induces a flat geometry. Based on the definition of the deformation gradient according to e.g. (2.9) such a connection has the form

$$\Gamma_{bc}^a = F^a{}_A F^{-1A}{}_{c,b} \quad (5.105)$$

In order to prove that this form of the connection corresponds to a vanishing curvature tensor, one can proceed as follows. Clearly any solution  $\mathbf{F}^{-1}$  of the set of differential equations (5.105) has to satisfy

$$F^{-1A}{}_{c,bd} = F^{-1A}{}_{c,db} \quad (5.106)$$

Evaluating first the left hand side of (5.106) gives by insertion of (5.105)

$$\begin{aligned} (F^{-1A}{}_{c,b})_{,d} &= (F^{-1A}{}_a \Gamma_{bc}^a)_{,d} = F^{-1A}{}_{a,d} \Gamma_{bc}^a + F^{-1A}{}_a \Gamma_{bc,d}^a \\ &= F^{-1A}{}_a \{ \Gamma_{bc,d}^a + \Gamma_{do}^a \Gamma_{bc}^o \} \end{aligned} \quad (5.107)$$

Computing similarly the right hand side of (5.106) gives

$$F^{-1A}{}_{c,bd} - F^{-1A}{}_{c,db} = F^{-1A}{}_a \{ \Gamma_{bc,d}^a - \Gamma_{dc,b}^a + \Gamma_{do}^a \Gamma_{bc}^o - \Gamma_{bo}^a \Gamma_{dc}^o \} = 0 \quad (5.108)$$

This obviously implies that the Riemann-Christoffel curvature tensor which is contained in the right hand side of (5.108) has to vanish identically

$$R_{dbc}^a = \Gamma_{bc,d}^a - \Gamma_{dc,b}^a + \Gamma_{do}^a \Gamma_{bc}^o - \Gamma_{bo}^a \Gamma_{dc}^o = 0 \quad (5.109)$$

Thus a connection of the form (5.105) implies that the corresponding geometry is equipped with a teleparallelism, i.e. vanishing curvature  $\mathbf{R} = \mathbf{0}$ .

**5.5.3. Compatibility of the Total Deformation State.** Now that all objects of differential geometry needed for an incompatibility analysis are at hand, one can start with an examination of the compatibility of the overall deformation state. Therefore an overall deformation state of a material body will be considered which can be described by a deformation *gradient*  $\mathbf{F}$  possibly compatible with a deformation map  $\mathbf{x} = \varphi_t(\mathbf{X})$ . Furthermore, the *right Cauchy-Green tensor*  $\mathbf{C}$  is introduced as the material representation of the spatial metric and analogously the inverse *Finger tensor*  $\mathbf{b}^{-1}$  is defined as the spatial representation of the material metric tensor. Thus at this point it is not necessary to consider the introduction of an intermediate configuration. The general setting looked at for now is depicted in figure 5.14. The question whether or not the deformation *gradient*

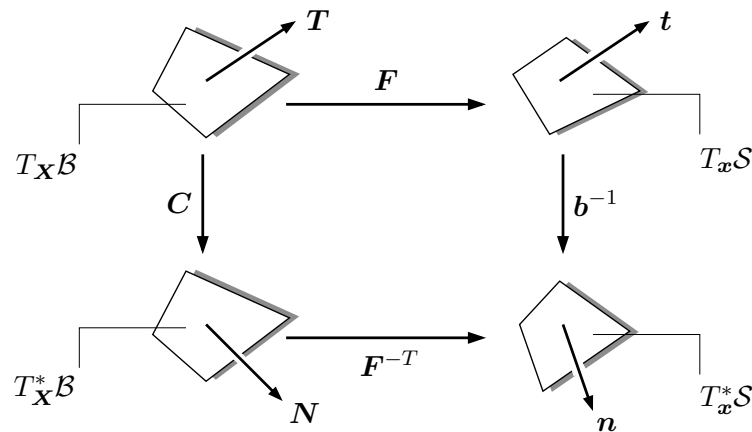


**Figure 5.14:** General geometric setting of the overall deformation state. The right Cauchy-Green tensor  $\mathbf{C}$  defines the Lagrangian representation of the Eulerian metric and analogously the inverse Finger tensor  $\mathbf{b}^{-1}$  is the Eulerian representation of the Lagrangian metric.

$\mathbf{F}$  is really a gradient field in the sense that it is derivable from a compatible deformation map  $\varphi$  is to be analyzed in the following. Consequently, the demand for the existence of a *compatible* initial or deformed configuration  $\mathcal{B}$  or  $\mathcal{S}$  requires that both incompatibility measures, the corresponding torsion tensor  $\mathcal{T}$  and the corresponding Riemann-Christoffel curvature tensor  $\mathcal{R}$  vanish.

First the compatibility analysis for the reference configuration  $\mathcal{B}$  is considered, based on the inverse deformation gradient  $\mathbf{F}^{-1}$ , the spatial metric representation  $\mathbf{g} = \mathbf{b}^{-1}$ , the connection  $\mathbf{\Gamma}$  and consequently the Cartan torsion tensor  $\mathcal{T}$  and the Riemann-Christoffel curvature tensor  $\mathcal{R}$  defined over the spatial configuration.

The demand for a torsion free, i.e. symmetric, connection corresponds to the existence of a globally compatible configuration as explained in the context of (5.73) and (5.75). This in turn is equivalent to global (and hence local) compatibility of the deformation gradient

$$F^{-1A}{}_{c,b} = F^{-1A}{}_{b,c} \quad (5.110)$$

To prove this assertion, assume that there exists a continuously differentiable deformation map  $\mathbf{X} = \varphi_t^{-1}(\mathbf{x})$  and a continuously differentiable inverse deformation gradient  $\mathbf{F}^{-1} = \nabla_{\mathbf{x}}\varphi_t^{-1}(\mathbf{x})$  compatible with it. The differentiability of  $\mathbf{F}^{-1}$  implies that  $\mathbf{X} = \varphi_t^{-1}(\mathbf{x})$  is twice continuously differentiable. Now in convective coordinates ( $\Theta^A = \theta^a$ ) one writes

with  $\mathbf{g}_a = \partial_{\theta^a} \mathbf{x}$  and  $\mathbf{G}_a = \partial_{\Theta^A} \mathbf{X} = \partial_{\theta^a} \mathbf{X}$  and (5.73)

$$\begin{aligned} \Gamma_{bc}^a &= \mathbf{G}^a \cdot \frac{\partial \mathbf{G}_c}{\partial \theta^b} = \mathbf{G}^a \cdot \frac{\partial^2 \mathbf{X}}{\partial \theta^c \partial \theta^b} = \mathbf{G}^a \cdot \frac{\partial}{\partial \theta^b} \left( \frac{\partial \mathbf{X}}{\partial \mathbf{x}} \frac{\partial \mathbf{x}}{\partial \theta^c} \right) = \mathbf{G}^a \cdot \frac{\partial}{\partial \theta^b} (\mathbf{F}^{-1} \mathbf{g}_c) \\ &= \mathbf{G}^a \cdot \frac{\partial}{\partial \mathbf{x}} (\mathbf{F}^{-1} \mathbf{g}_c) \frac{\partial \mathbf{x}}{\partial \theta^b} = \mathbf{G}^a \cdot \left\{ \left( \frac{\partial \mathbf{F}^{-1}}{\partial \mathbf{x}} \mathbf{g}_c \right) \mathbf{g}_b + \mathbf{F}^{-1} \frac{\partial^2 \mathbf{x}}{\partial \theta^c \partial \theta^b} \right\} \end{aligned} \quad (5.111)$$

Computing  $\Gamma_{bc}^a$  similarly, symmetry of the connection demands  $\Gamma_{bc}^a - \Gamma_{cb}^a = 0$ , thus

$$\Gamma_{bc}^a - \Gamma_{cb}^a = \mathbf{G}^a \cdot \left\{ \left( \frac{\partial \mathbf{F}^{-1}}{\partial \mathbf{x}} \mathbf{g}_c \right) \mathbf{g}_b - \left( \frac{\partial \mathbf{F}^{-1}}{\partial \mathbf{x}} \mathbf{g}_b \right) \mathbf{g}_c + \mathbf{F}^{-1} \left( \frac{\partial^2 \mathbf{x}}{\partial \theta^c \partial \theta^b} - \frac{\partial^2 \mathbf{x}}{\partial \theta^b \partial \theta^c} \right) \right\} = 0 \quad (5.112)$$

Assuming sufficient differentiability of  $\mathbf{x}$ , i.e.  $\mathbf{x}_{,cb} = \mathbf{x}_{,bc}$ , (5.112) implies

$$\mathbf{G}^a \cdot \left( \frac{\partial \mathbf{F}^{-1}}{\partial \mathbf{x}} \mathbf{g}_c \right) \mathbf{g}_b = \mathbf{G}^a \cdot \left( \frac{\partial \mathbf{F}^{-1}}{\partial \mathbf{x}} \mathbf{g}_b \right) \mathbf{g}_c \quad (5.113)$$

which after transformation back to Cartesian coordinates obviously implies (5.110). Thus it is proven that symmetry of the connection implies  $F^{-1A}_{c,b} = F^{-1A}_{b,c}$ . This motivates the definition of

$$\mathcal{K}_{bc}^A := F^{-1A}_{[c,b]} = \frac{1}{2} (F^{-1A}_{c,b} - F^{-1A}_{b,c}) \quad (5.114)$$

as a direct measure of the incompatibility of the inverse deformation gradient  $\mathbf{F}^{-1}$  or equivalently the alternative definition

$$-A_{sm}{}^{aA} := \mathcal{K}_{bc}^A \epsilon^{cba} = F^{-1A}_{c,b} \epsilon^{cba} \Leftrightarrow \mathbf{A}_{sm} := \text{curl} \mathbf{F}^{-1} \quad (5.115)$$

Here  $\mathcal{K}$  and  $\mathbf{A}_{sm}$  are both equivalent representations for the torsion tensor  $\mathcal{T}$  which in turn simply is a push-forward of the incompatibility tensor  $\mathcal{K}$  to the actual configuration

$$\mathcal{T}_{bc}^a = F^a{}_A \mathcal{K}_{bc}^A \quad (5.116)$$

This follows directly by representing  $\mathcal{K}$  in analogy to (5.113) again in convective coordinates and a subsequent transformation to a fully Eulerian representation (recall  $\mathbf{F} = \mathbf{g}_a \otimes \mathbf{G}^a$ ).

The above considerations induce the conclusion that the torsion tensor  $\mathcal{T}$ , or equivalently the incompatibility measures  $\mathcal{K}$  or  $\mathbf{A}_{sm}$ , have to vanish identically

$$\mathcal{T}_{bc}^a = 0 \Leftrightarrow \mathcal{K}_{bc}^A = 0 \Leftrightarrow A_{sm}{}^{aA} = 0 \quad (5.117)$$

in order to guarantee compatibility of the inverse deformation gradient  $\mathbf{F}^{-1}$ . Supposing that this condition is satisfied directly induces that the connection has to be a Riemannian connection, i.e. it coincides with the Christoffel symbols of the second kind  $\Gamma_{bc}^a = \{^a_{bc}\}$  associated with the spatial metric representation  $\mathbf{g} = \mathbf{b}^{-1}$ . Hence the connection is torsion free and metric. This directly leads to the second compatibility condition, the demand for a vanishing curvature tensor, which then corresponds to compatibility of the metric. Thus, a holonomic reference configuration  $\mathcal{B}$  exists only if the fourth order Riemann-Christoffel

curvature tensor corresponding to the Riemannian connection  $\mathbf{\Gamma}$ , or equivalently the second order symmetric Einstein tensor, vanishes identically

$$R_{dbc}^a = \Gamma_{bc,d}^a - \Gamma_{dc,b}^a + \Gamma_{do}^a \Gamma_{bc}^o - \Gamma_{bo}^a \Gamma_{dc}^o = 0 \quad \Leftrightarrow \quad R^{mn} = \frac{1}{4} \epsilon^{nbd} \epsilon^{mck} R_{dbc}^a g_{ak} = 0 \quad (5.118)$$

These compatibility conditions represent the extension of St.-Venant's compatibility conditions (5.56) to the geometrically nonlinear setting. A vanishing curvature ensures, in connection with (5.117), that the inverse Finger tensor  $\mathbf{b}^{-1}$  is derivable from a continuous vector valued deformation map  $\mathbf{X} = \boldsymbol{\varphi}_t^{-1}(\mathbf{x})$ . Obviously conditions (5.117) and (5.118) imply that for a compatible reference configuration the geometry reduces to an Euclidean geometry defined over the spatial configuration. Conversely, for a violation of either of these two conditions the associated geometry becomes non-Euclidean, the reference configuration  $\mathcal{B}$  is defined by an anholonomic configuration and  $\mathbf{F}^{-1}$  and/or  $\mathbf{b}^{-1}$  are characterized by incompatibilities measured by the torsion and the curvature tensor  $\mathcal{T}$  and  $\mathcal{R}$ , respectively.

The compatibility analysis of the deformed configuration proceeds in the same manner based on the deformation gradient  $\mathbf{F}$ , the material metric representation  $\mathbf{G} = \mathbf{C}$  and the associated torsion and curvature tensors  $\mathcal{T}$  and  $\mathcal{R}$  (the difference of these quantities to their spatial counterparts is indicated by employing upper case letters for the indices). Thereby symmetry of the connection  $\mathbf{\Gamma}$  implies compatibility of the deformation gradient

$$F^a_{C,B} = F^a_{B,C} \quad (5.119)$$

Thus a direct measure for the incompatibility of the deformation gradient is given by

$$\mathcal{K}_{BC}^a := F^a_{[C,B]} \quad \Leftrightarrow \quad A_P^{Aa} := -F^a_{C,B} \epsilon^{CBA} \quad \Leftrightarrow \quad \mathbf{A}_P := \text{Curl} \mathbf{F} \quad (5.120)$$

Where the torsion tensor is now the pull-back of the incompatibility measure  $\mathcal{K}$

$$\mathcal{T}_{BC}^A = F^{-1A}{}_a \mathcal{K}_{BC}^a \quad (5.121)$$

Consequently, equivalent compatibility conditions for the deformation gradient  $\mathbf{F}$  in terms of these incompatibility measures are again given through

$$\mathcal{T}_{BC}^A = 0 \quad \Leftrightarrow \quad \mathcal{K}_{BC}^a = 0 \quad \Leftrightarrow \quad A_P^{Aa} = 0 \quad (5.122)$$

Finally, if these conditions are satisfied the connection is a Riemannian connection, metric with respect to the right Cauchy-Green tensor. If additionally the curvature tensor vanishes

$$R_{DBC}^A = \Gamma_{BC,D}^A - \Gamma_{DC,B}^A + \Gamma_{DO}^A \Gamma_{BC}^O - \Gamma_{BO}^A \Gamma_{DC}^O = 0 \quad (5.123)$$

the existence of a holonomic spatial configuration  $\mathcal{S}$  is guaranteed.

**5.5.4. Incompatibility of Intermediate Configuration and GND Density.** Finally, the intermediate configuration, generally introduced in connection with the multiplicative split in finite strain plasticity, will now be examined for compatibility. The geometric setup with the intermediate configuration  $\mathcal{B}$  is visualized in figure 5.15.

To begin with the compatibility analysis, the corresponding geometry is defined over the spatial configuration  $\mathcal{S}$  based on the inverse elastic part of the deformation gradient  $\mathbf{F}^{e-1}$  and the spatial representation of the metric, i.e. the metric tensor is identified

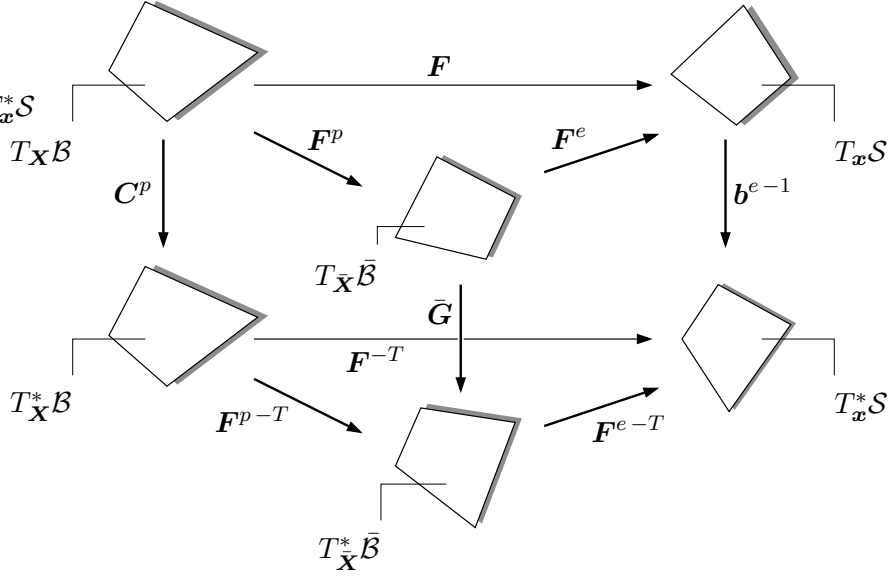


**Figure 5.15:** Geometric setting of multiplicative plasticity. The right plastic Cauchy-Green tensor  $\mathbf{C}^p$  defines the Lagrangian representation and analogously the inverse elastic Finger tensor  $\mathbf{b}^{e-1}$  the Eulerian representation of the metric of the intermediate configuration.

with the inverse *elastic Finger tensor*  $\mathbf{g} = \mathbf{b}^{e-1} = \mathbf{F}^{e-T} \cdot \mathbf{F}^{e-1}$ . If the real crystal deviates from the ideal crystal only by the inclusion of defects in the form of dislocations, i.e. no general defects such as *disclinations* or elementary point defects like *interstitial atoms* or *vacancies* are considered - and exclusively such a theory is treated in this work - then the corresponding geometry is equipped with a distant parallelism and a metric connection. Consequently the curvature tensor  $\mathbf{R}$  has to vanish and the connection  $\mathbf{\Gamma}$  has to be of the form (5.105) in terms of the elastic part  $\mathbf{F}^e$  and the spatial gradient of its inverse  $\mathbf{F}^{e-1}$

$$\Gamma_{bc}^a = F^{e a}{}_{\bar{A}} F^{e-1 \bar{A}}{}_{c,b} \quad (5.124)$$

which is metric but not necessarily symmetric. As pointed out already in the context of equations (5.105) to (5.109), this specific form of the connection ensures that the Riemann-Christoffel tensor formed from it vanishes identically. To prove that the connection (5.124) is also metric with respect to the metric tensor  $\mathbf{g} = \mathbf{b}^{e-1} = \mathbf{F}^{e-T} \cdot \mathbf{F}^{e-1}$ , evaluation of Ricci's theorem (5.76) for this specific case gives

$$\begin{aligned} D_c g_{ab} &= \partial_c g_{ab} - \Gamma_{ca}^d g_{db} - \Gamma_{cb}^d g_{ad} \\ &= F^{e-1 \bar{A}}{}_{a,c} \delta_{\bar{A}\bar{B}} F^{e-1 \bar{B}}{}_b + F^{e-1 \bar{A}}{}_a \delta_{\bar{A}\bar{B}} F^{e-1 \bar{B}}{}_{b,c} \\ &\quad - F^{e d}{}_{\bar{C}} F^{e-1 \bar{C}}{}_{a,c} F^{e-1 \bar{A}}{}_d \delta_{\bar{A}\bar{B}} F^{e-1 \bar{B}}{}_b - F^{e d}{}_{\bar{C}} F^{e-1 \bar{C}}{}_{b,c} F^{e-1 \bar{A}}{}_d \delta_{\bar{A}\bar{B}} F^{e-1 \bar{B}}{}_a \\ &= 0 \end{aligned} \quad (5.125)$$

where in the contractions for  $\mathbf{b}^{e-1}$  the metric of the embedding Euclidean space has been employed. Thus the covariant derivative of the metric vanishes, indicating that the connection is compatible with the metric. As in the general case, the inverse elastic part  $\mathbf{F}^{e-1}$  of the total deformation gradient is not derivable from a compatible continuous vector-valued deformation map, the connection is in general unsymmetric, i.e. the corresponding

torsion tensor does not vanish. This motivates in analogy to (5.114) the introduction of

$$\mathcal{K}_{bc}^{e\bar{A}} := F^{e-1\bar{A}}_{[c,b]} = \frac{1}{2} \left( F^{e-1\bar{A}}_{c,b} - F^{e-1\bar{A}}_{b,c} \right) \quad (5.126)$$

as a direct measure of the incompatibility of the inverse elastic gradient part  $\mathbf{F}^{e-1}$ . The incompatibility of the elastic gradient part can also be measured directly in terms of the the torsion tensor which is again a push-forward of the incompatibility measure  $\mathcal{K}$

$$\mathcal{T}_{bc}^a = \Gamma_{[bc]}^a = F^{ea}{}_{\bar{A}} F^{e-1\bar{A}}_{[c,b]} = F^{ea}{}_{\bar{A}} \mathcal{K}_{bc}^{e\bar{A}} \quad (5.127)$$

Obviously the dislocation density tensor  $\mathbf{A}_{si}^{eT}$  is an equivalent representation of (5.126)

$$-A_{si}^{e\ a\bar{A}} := \mathcal{K}_{bc}^{e\bar{A}} \epsilon^{cba} = F^{e-1\bar{A}}_{c,b} \epsilon^{cba} \quad \Leftrightarrow \quad \mathbf{A}_{si}^e := \text{curl} \mathbf{F}^{e-1} \quad (5.128)$$

and analogously the negative push-forward of its transpose  $\mathbf{A}_{\sigma}^{eT}$  measures the incompatibility of  $\mathbf{F}^{e-1}$  equivalent to the torsion tensor  $\mathcal{T}$

$$A_{\sigma}^{e\ da} = -F^{ed}{}_{\bar{A}} A_{si}^{e\ a\bar{A}} = F^{ed}{}_{\bar{A}} F^{e-1\bar{A}}_{c,b} \epsilon^{cba} = \mathcal{T}_{bc}^d \epsilon^{cba} \quad \text{with} \quad \mathbf{A}_{\sigma}^{eT} := -\mathbf{F}^e \cdot \mathbf{A}_{si}^{eT} \quad (5.129)$$

Thus the important relation between the spatial elastic dislocation tensor  $\mathbf{A}_{\sigma}^{eT}$  and the generally non-vanishing Cartan torsion  $\mathcal{T}$  has been found (see also STEINMANN [140])

$$-\mathbf{A}_{\sigma}^{eT} = \mathcal{T} : \overset{\circ}{\mathbf{e}} = \mathcal{Q} : \overset{\circ}{\mathbf{e}} = \Gamma : \overset{\circ}{\mathbf{e}} \quad (5.130)$$

For the definition of the fundamental tensor  $\overset{\circ}{\mathbf{e}}$  see (B.18). The result (5.130) is mainly due to KONDO [71], BILBY ET AL. [19] and also KRÖNER [77] and BILBY [18], who identified the Burgers circuit introduced in the definition of a dislocation by FRANK [46] with the Cartan-circuit of differential geometry.

Turning back to the analysis of the Riemann-Christoffel curvature tensor  $R_{dbc}^a$  it is first decomposed additively, in line with (5.88), into a contribution  $G_{dbc}^a$  corresponding to the Riemannian connection  $\mathcal{G}_{bc}^a$  and a remaining contribution  $Q_{dbc}^a$

$$R_{dbc}^a = G_{dbc}^a + Q_{dbc}^a \quad (5.131)$$

where the contributions  $G_{dbc}^a$  and  $Q_{dbc}^a$  follow as

$$\begin{aligned} G_{dbc}^a &:= 2 \partial_{[d} \mathcal{G}_{b]c}^a + 2 \mathcal{G}_{[d|o|}^a \mathcal{G}_{b]c}^o \\ Q_{dbc}^a &:= 2 \partial_{[d} \mathcal{Q}_{b]c}^a + 2 \mathcal{Q}_{[d|o|}^a \mathcal{Q}_{b]c}^o + 2 \mathcal{G}_{[d|o|}^a \mathcal{Q}_{b]c}^o + 2 \mathcal{Q}_{[d|o|}^a \mathcal{G}_{b]c}^o \end{aligned} \quad (5.132)$$

Here indices between vertical bars  $|\cdot|$  are excluded from the skewsymmetric permutation. As explained already for the general case, the Riemannian connection  $\mathcal{G}$  is defined through the Christoffel symbols of the second kind corresponding to the metric tensor, here  $\mathbf{g} = \mathbf{b}^{e-1}$ , and the contortion  $\mathcal{Q}$  is related to the torsion tensor  $\mathcal{T}$  through (5.91). In analogy to (5.101) the second order contravariant curvature contributions  $G^{mn}$  and  $Q^{mn}$  corresponding to  $G_{dbca} = G_{dbc}^n g_{na}$  and  $Q_{dbca} = Q_{dbc}^n g_{na}$ , respectively, are defined as follows

$$G^{mn} = \frac{1}{4} \epsilon^{nbd} \epsilon^{mca} G_{dbca} \quad \text{and} \quad Q^{mn} = \frac{1}{4} \epsilon^{nbd} \epsilon^{mca} Q_{dbca} \quad (5.133)$$

Obviously the contribution  $G^{mn}$  corresponding to the torsion free Riemannian connection  $\mathcal{G}_{bc}^a$  is symmetric. Consequently the axial vector  $\omega_a^Q$  of the remaining curvature contribution  $Q^{mn}$  coincides with the axial vector  $\omega_a$  of the corresponding total curvature tensor  $R^{mn}$

$$\omega_a^Q = -\frac{1}{2}\epsilon_{mna}Q^{mn} = -\frac{1}{2}\epsilon_{mna}R^{mn} = \omega_a \quad (5.134)$$

Thus in the analysis of the Riemann-Christoffel curvature tensor  $R_{dbc}^a$  or equivalently the Einstein tensor  $R^{mn}$ , the symmetric part  $R^{(mn)}$  and the skewsymmetric part  $R^{[mn]}$  are examined separately (round brackets  $(\cdot)$  indicate symmetric permutation of the enclosed indices). As explained already at the beginning of this subsection, the curvature tensor  $R_{dbc}^a$ , or equivalently  $R^{mn}$ , corresponding to  $\Gamma_{bc}^a$  is required to vanish identically

$$R_{dbc}^a = 0 \quad \Leftrightarrow \quad R^{mn} = 0 \quad (5.135)$$

This is also expressed by BILBY & SMITH [20] as a physical demand which ensures that a unique lattice orientation can be assigned to each point of the crystal. Analogously, ANTHONY [3] relates the requirement for a vanishing curvature to the existence of an anholonomic intermediate configuration equipped with a Pfaffian transformation  $\tilde{\mathbf{G}}_I = \mathbf{F}^{e-1} \cdot \mathbf{g}_i$  in the sense of (5.60). Now, as pointed out already by KRÖNER [77], p. 294, equations (49) and (50), the disappearance of the symmetric part  $R^{(mn)}$  of the Einstein tensor renders the relation between the storage of geometrically necessary dislocations and (macroscopic) residual stresses, while the skewsymmetric part  $R^{[mn]}$  constitutes the divergence condition for the dislocation density. In order to further elucidate these statements, first the symmetric part  $R^{(mn)}$  of the Einstein tensor is examined. Its disappearance relates the dislocation density associated with  $Q_{dbc}^a$ , or similarly  $Q^{mn}$ , to residual stresses associated with the part  $G_{dbc}^a$ , or equivalently  $G^{mn}$ , through

$$R^{(mn)} = G^{(mn)} + Q^{(mn)} = 0 \quad \Leftrightarrow \quad -Q^{(mn)} = G^{(mn)} \equiv G^{mn} \quad (5.136)$$

This relation generally ensures that the storage of dislocations associated with a non-vanishing torsion induces (macroscopic) residual stresses. This also includes the special case of a stress-free lattice curvature as examined by NYE [119]. In this case,  $\mathbf{b}^{e-1}$  vanishes identically resulting in  $G^{mn} = 0$  and consequently  $Q^{(mn)} \doteq 0$  while  $\mathbf{F}^e$  reduces to a non-constant rotation resulting in a non-vanishing torsion and thus the storage of dislocations inducing a (macroscopic) lattice curvature. Turning next to the skewsymmetric part  $R^{[mn]}$  of the Einstein tensor it is also required that this part or equivalently the corresponding axial vector vanishes identically

$$R^{[mn]} = 0 \quad \Leftrightarrow \quad \omega_k = \omega_k^Q = 0 \quad (5.137)$$

in analogy to the (first) Bianchi identity. Rewriting (5.137)<sub>2</sub> by insertion of (5.130) into (5.104) results in the following continuity equation for the spatial dislocation density  $\mathbf{A}_\sigma^e$

$$\omega_k = -\frac{1}{2}g_{kd} \{ [A_\sigma^{e da}]_{,a} + \Gamma_{ao}^d A_\sigma^{e oa} \} = 0 \quad \Leftrightarrow \quad \text{div} \mathbf{A}_\sigma^{eT} + \mathbf{\Gamma} : \mathbf{A}_\sigma^{eT} = \mathbf{0} \quad (5.138)$$

In order to get more insight into the implications of this divergence condition (5.138) is rewritten in terms of  $\mathbf{A}_{si}^e$ . Therefore first insert (5.124) and (5.129) into (5.138) yielding

$$\begin{aligned} & [(F^{e d} \bar{A} F^{e-1} \bar{A}_{c,b} - F^{e d} \bar{A} F^{e-1} \bar{A}_{b,c}) \epsilon^{cba}]_{,a} \\ & + F^{e d} \bar{B} F^{e-1} \bar{B}_{o,a} (F^{e o} \bar{A} F^{e-1} \bar{A}_{c,b} - F^{e o} \bar{A} F^{e-1} \bar{A}_{b,c}) \epsilon^{cba} = 0 \end{aligned} \quad (5.139)$$

From this one gets after contraction with  $F^{e-1}\bar{C}_d$  and subsequent insertion of  $F^{e-1}\bar{C}_{d,a}F^{ed}\bar{A} = -F^{e-1}\bar{C}_dF^{ed}\bar{A}_{,a}$  (which follows directly from  $[F^{e-1}\bar{C}_dF^{ed}\bar{A}]_{,a} = 0$ )

$$[(F^{e-1}\bar{C}_{c,b} - F^{e-1}\bar{C}_{b,c})\epsilon^{cba}]_{,a} = 0 \quad \Leftrightarrow \quad \text{div}\mathbf{A}_{si}^{eT} = \mathbf{0} \quad (5.140)$$

This is the continuity equation for the dislocation density tensor  $\mathbf{A}_{si}^e$ , consistent with the findings of NYE [119], page 159, equation (9). The divergence condition (5.140) states that dislocations can never end within the continuum.

To summarize, the geometry defined over the spatial configuration  $\mathcal{S}$  is identified by a Cartan geometry with a metric but generally unsymmetric connection  $\mathbf{\Gamma}$  where the nonvanishing Cartan torsion  $\mathbf{T}$  corresponds to incompatibilities of the elastic part  $\mathbf{F}^e$  of the total deformation gradient and measures, equivalent to the spatial elastic dislocation density tensor  $\mathbf{A}_\sigma^{eT}$ , the density of geometrically necessary dislocations stored due to the resulting incompatibility of the intermediate configuration. As a physical demand, the Riemann-Christoffel curvature tensor  $\mathbf{R}$  has to vanish as long as exclusively defects in the form of dislocations are considered. Its symmetric part relates the storage of dislocation arrays of equal sign to (macroscopic) residual stresses resulting from the incompatibility of the corresponding metric  $\mathbf{b}^{e-1}$ . Finally, the disappearance of the skewsymmetric part renders the continuity condition for the geometrically necessary dislocation density.

These considerations are also the starting point for further extensions of the theory. Thereby general defects might be taken into account by considering more general affine geometries ANTHONY [3, 4], KRÖNER [78, 79]. Referring to the classification of KONDO [72] besides dislocations, which might be interpreted as *torsion defects*, also *curvature defects*, which are related to a non-vanishing curvature tensor and thus a more general form of the connection, might be considered. Then the non-vanishing curvature tensor measures the density of these defects. Examples of such defects are *disclinations* or *quasi-dislocations* in the form of *interstitial atoms*, *vacancies*, significant *dislocation pile-ups* in a glide plane or inhomogeneous lattice distortions induced by temperature, electrical or magnetic fields. However, the considerations in this work are restricted to a dislocation based plasticity theory related to the differential geometric setting of a Cartan geometry.

Finally, the compatibility analysis of the intermediate configuration  $\bar{\mathcal{B}}$  is briefly outlined on basis of a Cartan geometry defined through the material configuration  $\mathcal{B}$ . With reference to figure 5.15, the analysis is now based on the plastic part  $\mathbf{F}^p$  of the deformation gradient, the material representation of the metric, i.e.  $\mathbf{G} = \mathbf{C}^p = \mathbf{F}^{pT} \cdot \mathbf{F}^p$ , and the connection

$$\Gamma_{BC}^A = F^{p-1A}\bar{A}F^{p\bar{A}}_{C,B} \quad (5.141)$$

which is metric and ensures that the geometry possesses a distant parallelism. As the connection (5.141) is in general unsymmetric, the corresponding torsion tensor  $\mathbf{T}$  does not vanish and measures in analogy to the material plastic dislocation density tensor  $\mathbf{A}_S^{pT} = \mathbf{F}^{p-1} \cdot \text{Curl}^T \mathbf{F}^p$  the density of geometrically necessary dislocations stored due to the incompatibility of the plastic part  $\mathbf{F}^p$  of the deformation gradient

$$A_S^{pAD} = -F^{p-1A}\bar{A}F^{p\bar{A}}_{C,B}\epsilon^{CBD} = -\mathcal{T}_{BC}^A\epsilon^{CBD} \quad \Leftrightarrow \quad \mathbf{A}_S^{pT} = \mathbf{T} : \overset{3}{\mathbf{E}} \quad (5.142)$$

In analogy to the previous elaborations, one demands again that the Riemann-Christoffel curvature tensor  $R_{DBC}^A$ , or equivalently the corresponding Einstein Tensor  $R^{MN}$  vanishes identically, where the disappearance of the symmetric part renders the relation between

the storage of dislocations due to the incompatibility of  $\mathbf{F}^p$  and the (macroscopic) residual stresses corresponding to an incompatibility of  $\mathbf{C}^p$ . Finally the disappearance of the skewsymmetric part in analogy to the (first) Bianchi identity constitutes the continuity equations for the dislocation density tensors  $\mathbf{A}_S^p$  and  $\mathbf{A}_P^p$ .

To close this section, the vision of finite strain multiplicative crystal plasticity obtained so far is summarized in figure 5.16. As discussed in detail, the fictitious intermediate configuration is in general characterized by incompatibilities which are measured by a non-vanishing (Cartan) torsion  $\mathcal{T}$  or equivalently the so-called dislocation density tensor defined in terms of  $\text{Curl}\mathbf{F}^p$  or alternatively in terms of  $\text{curl}\mathbf{F}^{e-1}$ . Thus in order to correctly account for the incompatibilities within a continuum theory, the classical local plasticity theory needs to be extended by an inclusion of these incompatibility measures as indicated in figure 5.16. The specific form of this extension will be addressed within the considerations in sections 5.6 and 5.7. As discussed also in sections 5.2, 5.4 and further quantified in the following section 5.6, the micromechanical interpretation of the incompatibilities within a crystal plasticity theory is the storage of so-called geometrically necessary dislocations, which is again illustrated in figure 5.16. Thereby it is important to note that a

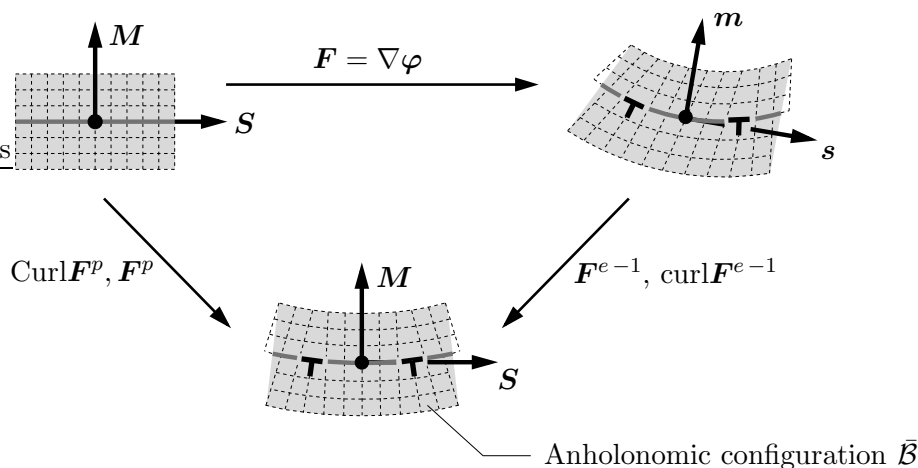


**Figure 5.16:** Extended geometric setting of multiplicative crystal plasticity. The incompatibility of the intermediate configuration  $\bar{\mathcal{B}}$  is measured by  $\text{Curl}\mathbf{F}^p$  or  $\text{curl}\mathbf{F}^{e-1}$ . A continuous intermediate configuration can only be described within an **anholonomic** coordinate system. An **Euclidean** representation of  $\bar{\mathcal{B}}$  is generally **broken up**, see figure 5.4.

continuously connected representation of the crystal in the intermediate configuration is only possible within an anholonomic, i.e. incompatible, coordinate system. Furthermore a direct visualization of the corresponding anholonomic intermediate configuration  $\bar{\mathcal{B}}$  is only possible in special cases. Figure 5.16 obviously represents such a special case. This is in particular clear if one thinks of a stress-free Nye lattice curvature. In this case,  $\mathbf{F}^e$  degenerates to a pure rotation and consequently the visualization of the crystal within an anholonomic coordinate system in the intermediate configuration would coincide with its spatial visualization within an Euclidean representation. In turn, from these considerations it is clear that the visualization of a continuously connected polycrystal in its anholonomic intermediate configuration is not possible (at least as long as the visualization is restricted to the n-dimensional Euclidean space, as such as is the paper which this work is written on).

## 5.6. Crystallographic Interpretation of the Dislocation Density Tensor

In order to arrive at a clear interpretation of the dislocation density tensor in the context of crystal plasticity, the aim is now to obtain a direct representation of the dislocation density tensor in terms of crystallographic slip. Therefore, firstly the definition of the dislocation tensor as introduced by NYE [119] is reiterated. Subsequently the specific form of the *true* dislocation density tensor  $\mathbf{A}$  introduced in connection with the incompatibility analysis in the previous sections is discussed for the assumption of separate single slip.

**5.6.1. Nye's Dislocation Tensor.** The first instance of a tensorial measure for the "state of dislocation" in a crystal was given by NYE [119]. He quantified the net Burgers vector  $B_i$  of a continuously distributed dislocation density piercing a unit area perpendicular to the unit normal  $l_j$  through

$$B_i = \alpha_{ij} l_j \quad (5.143)$$

where the components  $\alpha_{ij}$  of Nye's tensor follow for a given set of dislocations from

$$\alpha_{ij} := n b_i r_j \quad (5.144)$$

This implies the assumption of a continuous distribution of  $n$  dislocations of unit length with a Burgers vector  $b_i$  and a corresponding constant unit tangent vector  $r_j$ . Furthermore, if several sets of dislocations with different values of  $n$ ,  $\mathbf{b}$  and  $\mathbf{r}$  reside in the same unit volume, the total dislocation tensor  $\alpha_{ij}$  is obtained by summation over these contributions. Consequently, Nye's tensor quantifies only these dislocation populations which do not cancel one another within the volume element. In turn, the dislocations which cancel each other if summed over the control volume, like dislocation dipoles or selfterminating dislocation loops, but do not in reality annihilate, make up the so-called statistically stored dislocation (SSD) density which in contrast to the GND density does not give any net contribution to Nye's tensor. A simple example of such a dislocation distribution is visualized in figure 5.17 a). Through (5.144) any state of dislocations, and consequently

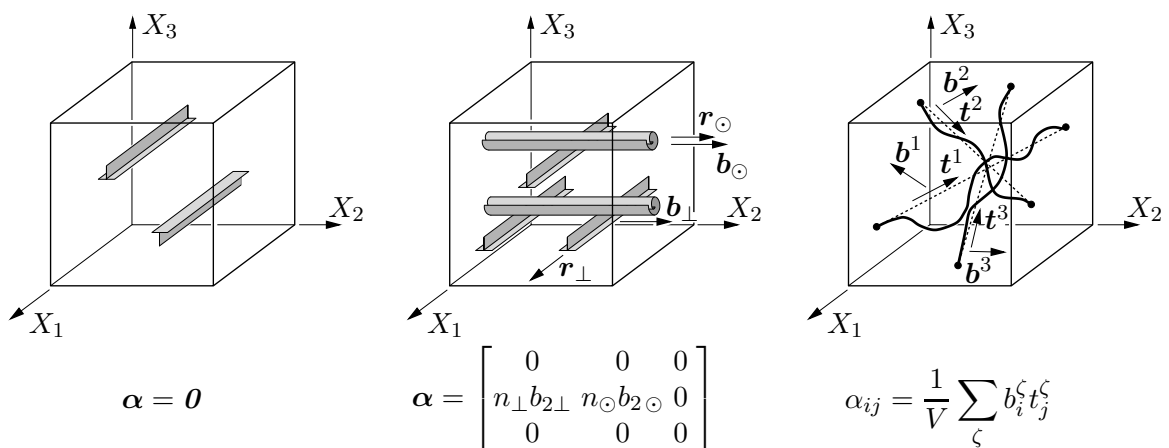


**Figure 5.17:** Nye's dislocation tensor  $\alpha$ . a) An edge dislocation dipole gives no net contribution to Nye's tensor. b) Example distribution of  $n_{\perp}$  edge and  $n_{\circ}$  screw dislocations resulting in a nonvanishing  $\alpha$ . c) Extension to a discrete dislocation structure.

any form of a curved glide plane, resulting from an inhomogeneous plastic deformation can be constructed by combination of nine sets of dislocations of unit length with their line

directions and Burgers vectors arranged parallel and perpendicular to the coordinate axis. Thereby the three terms on the main diagonal of  $\alpha_{ij}$  represent pure screw dislocations ( $\mathbf{b} \parallel \mathbf{r}$ ) and the six off-diagonal terms describe the six possible types of pure edge dislocations ( $\mathbf{b} \perp \mathbf{r}$ ). A visualization for the simple case of one set of screw and one set of edge dislocations within a unit volume is given in figure 5.17 b). Carefully note that the discrete dislocation structures in figure 5.17 a) and b) are only depicted for the sake of clarity. Specifically, the original definition of Nye's tensor as explained above bases on continuous dislocation distributions where each set has a constant tangent vector and the exact location of the respective dislocations is not of interest. However, the extension to discrete dislocation arrangements, as also discussed by ARSENLIS & PARKS [6], is straightforward and results in the expression

$$\alpha_{ij} = \frac{1}{V} \sum_{\zeta} b_i^{\zeta} t_j^{\zeta} \quad (5.145)$$

where  $V$  is the size of the reference volume element,  $\mathbf{b}^{\zeta}$  is the resulting Burgers vector of the  $\zeta$ -th discrete dislocation segment and  $\mathbf{t}^{\zeta}$  is the corresponding average line direction vector. In contrast to  $\mathbf{r}$  in (5.144),  $\mathbf{t}^{\zeta}$  now clearly is no longer a unit vector but also contains the resulting path length of the dislocation segment threading the reference volume element, see figure 5.17 c) for a visualization. From the explanations in connection with figure 5.17 a), it is clear that only the direct connection of the start and end point of the dislocation segment in the volume element (dashed line in figure 5.17 c)) results in a net contribution to Nye's tensor, while the remaining segment length has no geometric consequences and thus contributes only to the SSD density. With the interpretation of the dislocation density

$$\rho_{\text{GND}}^{\zeta} := \frac{|\mathbf{t}^{\zeta}|}{V} = \frac{l^{\zeta}}{V} \quad (5.146)$$

as line length  $l^{\zeta} = |\mathbf{t}^{\zeta}|$  per reference volume  $V$ , (5.145) can be rewritten with  $\mathbf{r}^{\zeta} = \frac{\mathbf{t}^{\zeta}}{|\mathbf{t}^{\zeta}|}$  as

$$\alpha_{ij} = \sum_{\zeta} \rho_{\text{GND}}^{\zeta} b_i^{\zeta} r_j^{\zeta} \quad (5.147)$$

where, as pointed out above, the GND density (dashed lines in figure 5.17 c)) constitutes a part of the total density (solid lines in figure 5.17 c)) defined by

$$\rho^{\zeta} := \frac{1}{V} \int_l ds^{\zeta} = \rho_{\text{SSD}}^{\zeta} + \rho_{\text{GND}}^{\zeta} \quad (5.148)$$

Recalling that any mixed dislocation density can be split up into corresponding edge and screw densities, it is evident that (5.147) closely resembles Nye's representation (5.144).

**5.6.2. Slip Gradient Induced Dislocation Storage.** Any storage of polar dislocation density, i.e. arrays of dislocations with equal signs, leads to a lattice curvature and is a direct consequence of the demand to maintain continuity in the presence of gradients of plastic slip. The mathematical implications of this statement have been elaborated in sections 5.4 and 5.5. In order to understand the crystallographic consequences of this assertion consider the schematic picture of a single crystal with one single slip system  $\alpha$  as depicted in figure 5.18 a). Here  $\mathbf{M}^{\alpha}$  denotes the slip plane unit normal,  $\mathbf{S}^{\alpha}$  is a unit

vector in the slip direction and  $\mathbf{T}^\alpha = \mathbf{S}^\alpha \times \mathbf{M}^\alpha$  lies in the slip plane and is perpendicular to  $\mathbf{S}^\alpha$ , such that  $(\mathbf{S}^\alpha, \mathbf{M}^\alpha, \mathbf{T}^\alpha)$  form a right handed triad. Following conceptually ARSENIS & PARKS [6], who extended the two-dimensional construction of ASHBY [12] to the three-dimensional setting, first imagine that the material is separated into three sections in figure 5.18 b). Each section is then deformed separately through crystallographic slip. Thereby a plastically inhomogeneous deformation is assumed such that the plastic slip increases linearly in the slip direction  $\mathbf{S}^\alpha$ . Consequently, in the left-most section the expansion of two dislocation loops leads to a total slip step of two Burgers vector lengths  $b = |\mathbf{b}|$  in figure 5.18 c), while the middle section is deformed through the expansion of four dislocation loops and the right-most section experiences a total slip step of 6 Burgers vector lengths in figure 5.18 c). When the sections are now forced again together in figure 5.18 d), the opposite slip steps cancel out but a portion of negative edge dislocations remains at each section boundary in figure 5.18 e) leading to a lattice curvature.

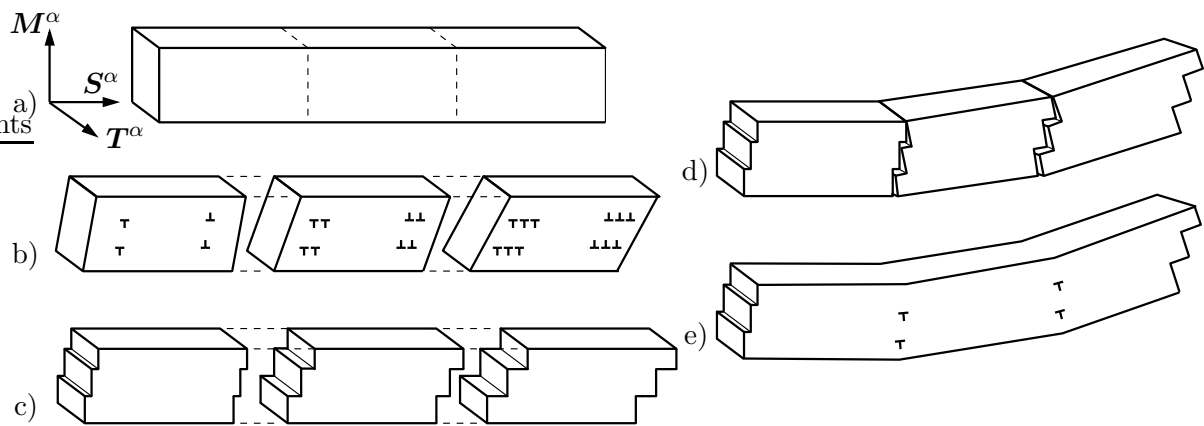


**Figure 5.18:** Plastically inhomogeneous deformation with a gradient of plastic slip in the direction  $\mathbf{S}^\alpha$ , leading to the storage of geometrically necessary edge dislocations.

To understand the crystallographic consequences of a gradient of plastic slip in the  $\mathbf{T}^\alpha$  direction, consider the schematic description in figure 5.19. In analogy to the previous considerations, the material is separated into three sections in figure 5.19 b) and subjected to a plastically inhomogeneous deformation, now in the  $\mathbf{T}^\alpha$  direction. Consequently, the uppermost section experiences a total slip step of two Burgers vector lengths while the bottom one undergoes a total step of six Burgers vector lengths in figure 5.19 c). Since a screw dislocation does not result in a slip step, when it reaches the free boundary here it is assumed that the screw parts of the dislocation loops are stopped by a fictitious boundary right before they would leave the crystal. This assumption is just adopted in order to have a clear visualization in figure 5.19. The sections are then again forced together in figure 5.19 d). Thereby the screw dislocations of opposite sign to the left and right of the fictitious boundaries annihilate and a portion of excess positive screw dislocations remains at the boundaries causing the lattice to warp.

In order to derive the specific relation between the density of stored geometrically necessary dislocations and the inhomogeneous plastic deformation, consider a lattice sample of size  $dX_1 \cdot dX_2$  on the micro-scale as depicted in figure 5.20 a). A plastically homogeneous deformation results in the slip pattern depicted in figure 5.20 b) which is homogeneous throughout the entire specimen. The plastic deformation occurs by expanding dipoles which leave the lattice at the left and right free boundaries resulting in slip steps, each

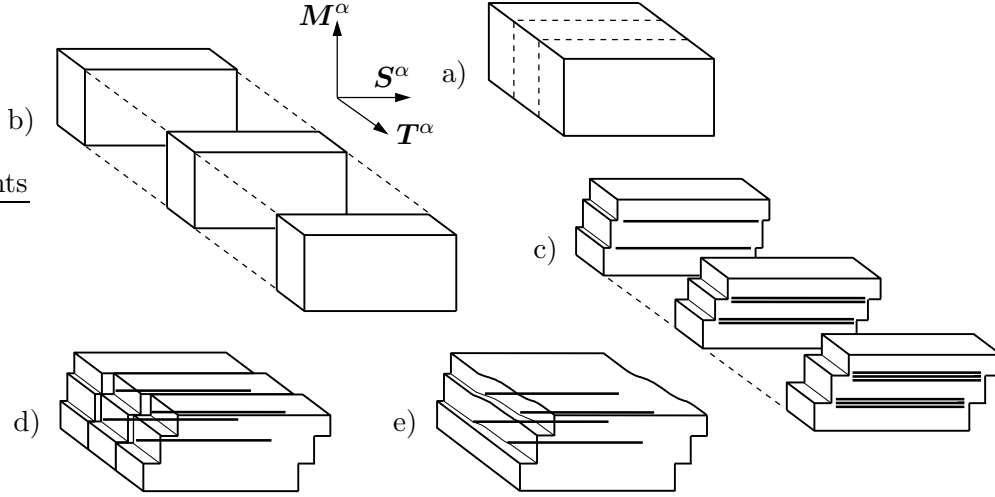


**Figure 5.19:** Plastically inhomogeneous deformation with a slip gradient in direction  $T^\alpha$ , leading to a storage of geometrically necessary screw dislocations (ARSENIS & PARKS [6]).

of a width of one Burgers vector length  $b$ . Thus dislocations do not need to be stored in the crystal in order to accommodate such a homogeneous deformation. Now, for a plastically inhomogeneous deformation the lattice sample is subdivided, in analogy to figure 5.18, into two sections which, by assumption, deform homogeneously. Thus in the left section in figure 5.21 a) the expansion of  $n$  dipoles results in a plastic deformation  $u_1$  or equivalently a plastic shear  $\gamma^\alpha$  related through

$$u_1 = nb = \gamma^\alpha dX_2 \quad (5.149)$$

Through the inhomogeneity of the deformation the plastic slip in the right section of figure 5.21 a) differs from the one in the left section by  $d\gamma^\alpha$  resulting in a total slip step

$$u_1 + du_1 = (n + dn)b = (\gamma^\alpha + d\gamma^\alpha)dX_2 \quad (5.150)$$

Now, upon rejoining of the cells, which at this point requires an (elastic) rotation, the opposite slip steps cancel out at the intersection and a certain density of edge dislocations remains in the crystal, see figure 5.21 b) for a visualization. This density follows from the simple consideration that at the left boundary of the reassembled lattice a number of  $n$  dislocations left the crystal resulting in a total slip step  $u_1$  while the slip steps at the right boundary were formed by  $n + dn$  dislocations which left the crystal. Thus, obviously a certain dislocation density remained in the crystal which follows after subtraction of (5.149) from (5.150) as

$$dnb = d\gamma^\alpha dX_2 = \frac{\partial \gamma^\alpha}{\partial X_1} dX_1 dX_2 \quad (5.151)$$

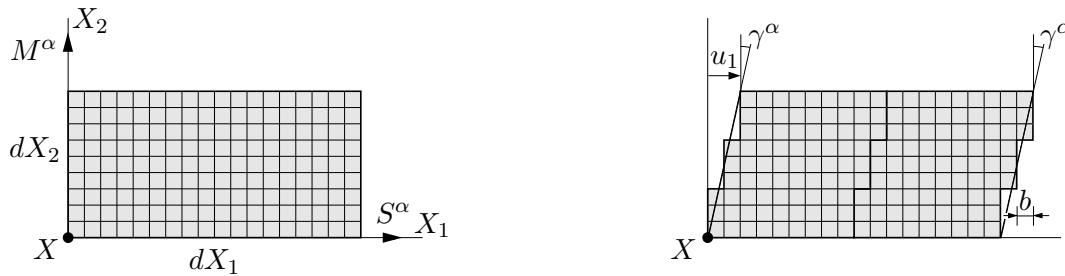


**Figure 5.20:** Schematic representation of a plastically homogeneous deformation of a lattice.

This finally gives, with the definition of dislocation density as dislocation line length per unit reference volume or piercing number density per unit area, the density of geometrically necessary edge dislocations stored due to a gradient of plastic slip in  $X_1$ -direction

$$\rho_{\text{GND}\perp}^{\alpha} = \frac{dn}{dX_1 dX_2} = \frac{1}{b} \frac{\partial \gamma^{\alpha}}{\partial X_1} \quad (5.152)$$

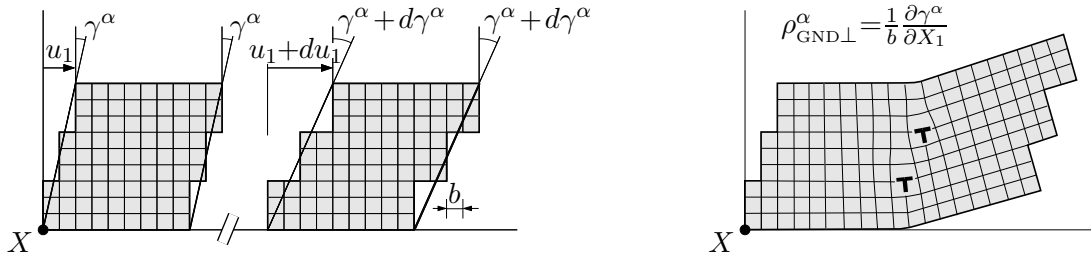


**Figure 5.21:** Plastically inhomogeneous deformation of a sample lattice. Relation between the slip gradient in  $X_1$ -direction and the density of geometrically necessary edge dislocations.

Similar considerations relate the density of geometrically necessary stored screw (subscript  $\odot$ ) dislocations  $\rho_{\text{GND}\odot}^{\alpha}$  to a gradient of plastic slip in the  $X_2$  direction through

$$\rho_{\text{GND}\odot}^{\alpha} = \frac{1}{b} \frac{\partial \gamma^{\alpha}}{\partial X_3} \quad (5.153)$$

Thus, through (5.152) and (5.153) now a plastically inhomogeneous deformation associated with plastic slip gradients is clearly related to the storage of dislocations on the micro-scale. Relation (5.152) was already established by ASHBY [12] and together with (5.153) also by FLECK ET AL. [42] and ARSENLIS & PARKS [6]. Rewriting (5.152) in terms of the slip system geometry immediately reveals that the geometrically necessary edge (subscript  $\perp$ ) dislocation density  $\rho_{\text{GND}\perp}^{\alpha}$  directly follows by projection of the slip gradient  $\nabla_{\mathbf{X}} \gamma^{\alpha}$  onto the slip direction  $\mathbf{S}^{\alpha}$  of the single slip system under consideration

$$\rho_{\text{GND}\perp}^{\alpha} = \frac{1}{b} \nabla_{\mathbf{X}} \gamma^{\alpha} \cdot \mathbf{S}^{\alpha} \quad (5.154)$$

Analogously, the screw dislocation density follows through reformulation of (5.153) by projection of the slip gradient onto  $\mathbf{T}^{\alpha} = \mathbf{S}^{\alpha} \times \mathbf{M}^{\alpha}$ , see figure 5.22 for a visualization

$$\rho_{\text{GND}\odot}^{\alpha} = \frac{1}{b} \nabla_{\mathbf{X}} \gamma^{\alpha} \cdot \mathbf{T}^{\alpha} \quad (5.155)$$

Note that a slip gradient perpendicular to the slip plane, i.e. in the normal direction  $\mathbf{M}^{\alpha}$  does not contribute to the storage of geometrically necessary dislocations.

**5.6.3. Lattice Geometric Representation of the Dislocation Tensor.** Carrying the definition of Nye's dislocation density tensor and the previously derived relations between a slip gradient and the storage of GNDs in mind, the *true* dislocation density tensor  $\mathbf{A}$  will now be related to the storage of geometrically necessary dislocations. The true dislocation tensor  $\mathbf{A}$  was introduced in (5.32) and motivated through the incompatibility analysis in sections 5.4 and 5.5. In contrast to the previous section and with regard to the

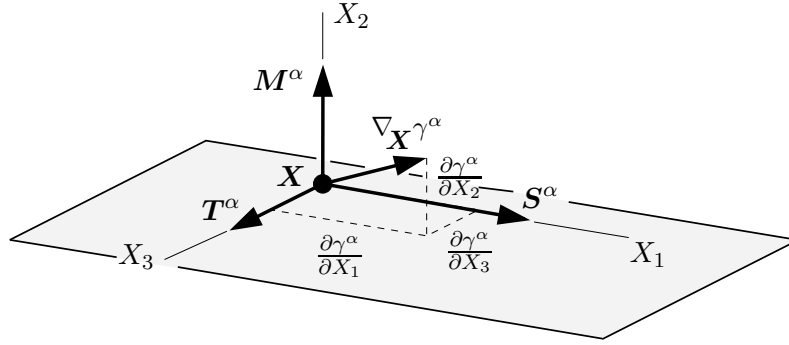


**Figure 5.22:** Slip gradient and slip system geometry for a single slip system.

model proposed in the following sections, the considerations are now constrained to the macro- (or meso-) scale. More precisely, the concern is not with individual, i.e. discrete, dislocations. Here, only the average characteristics of a distribution of large numbers of dislocations ( $\rho > 10^{10} \frac{1}{m^2}$ ) are considered. The plastic part  $\mathbf{F}^{p\alpha}$  of the macroscopic deformation gradient is, for a separate single slip system  $\alpha$ , given by

$$\mathbf{F}^{p\alpha} = \mathbf{1} + \gamma^\alpha \mathbf{S}^\alpha \otimes \mathbf{M}^\alpha \quad (5.156)$$

This directly results in the following evaluation of the true dislocation density tensor  $\mathbf{A}^\alpha$  for a separate single slip system ( $J^{p\alpha} \equiv 1$ ) as depicted in figure 5.23

$$\begin{aligned} \mathbf{A}^\alpha &= \frac{1}{J^{p\alpha}} \mathbf{F}^{p\alpha} \cdot \text{Curl} \mathbf{F}^{p\alpha} = (\nabla_{\mathbf{X}} \gamma^\alpha \times \mathbf{M}^\alpha) \otimes \mathbf{S}^\alpha \\ &= \frac{\partial \gamma^\alpha}{\partial X_1} \mathbf{T}^\alpha \otimes \mathbf{S}^\alpha - \frac{\partial \gamma^\alpha}{\partial X_3} \mathbf{S}^\alpha \otimes \mathbf{S}^\alpha \\ &= (\nabla_{\mathbf{X}} \gamma^\alpha \cdot \mathbf{S}^\alpha) \mathbf{T}^\alpha \otimes \mathbf{S}^\alpha - (\nabla_{\mathbf{X}} \gamma^\alpha \cdot \mathbf{T}^\alpha) \mathbf{S}^\alpha \otimes \mathbf{S}^\alpha \end{aligned} \quad (5.157)$$

where the definition of the Lagrangian Curl operator as specified in (B.15) in the Appendix has been applied. Obviously a slip gradient perpendicular to the slip plane does not give a contribution to the dislocation density tensor. This is also visualized in figure 5.23. Now by insertion of (5.154) and (5.155) into (5.157), the incompatibility measure  $\mathbf{A}^\alpha$  can finally be identified with the transpose of Nye's dislocation density tensor  $\boldsymbol{\alpha}$

$$\mathbf{A}^\alpha = b \rho_{\text{GND}\perp}^\alpha \mathbf{T}^\alpha \otimes \mathbf{S}^\alpha - b \rho_{\text{GND}\odot}^\alpha \mathbf{S}^\alpha \otimes \mathbf{S}^\alpha \quad (5.158)$$

(compare with (5.144) or (5.147)). Thus a direct relation between plastic slip gradients, incompatibilities and the storage of geometrically necessary dislocations has been obtained. Expressions similar to the right hand side of (5.157) were also found by FLECK ET AL. [42], SHIZAWA & ZBIB [133], ARSENLIS & PARKS [6] and CERMELLI & GURTIN [25] in the small strain context. The representations found in the first three publications are the transpose of the dislocation density tensor established in this thesis while the dislocation tensor found in the latter work is the negative of the present one (5.158) and is also known as Kröner's dislocation density tensor  $\boldsymbol{\alpha}_K$  related to Nye's tensor by  $\boldsymbol{\alpha}_K = -\boldsymbol{\alpha}^T$ .

For the case of single slip, as considered so far, relation (5.158) seems to be unambiguous such that for given edge and screw dislocation densities Nye's dislocation tensor can be uniquely determined and vice-versa. The latter is generally not true for multiple slip in crystals with a high degree of symmetry. Here a description of the dislocation state in

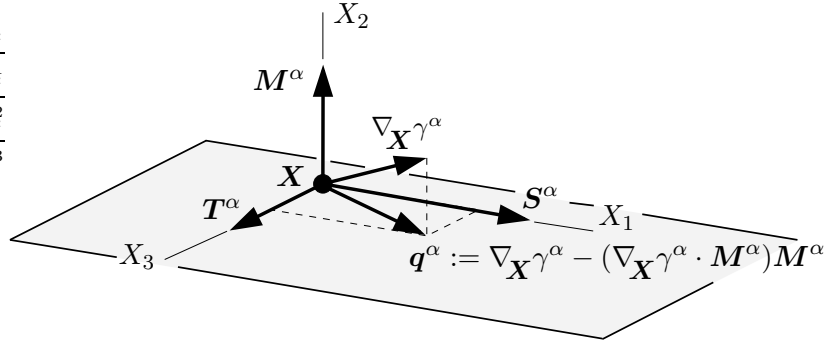


**Figure 5.23:** Crystallographic representation of the dislocation density tensor for a single slip system. Projection of the slip gradient onto the slip plane.

terms of crystallographic dislocation densities would be largely underdetermined. This is in analogy to the ambiguity of a specific apportion of crystallographic slip to the different slip planes in the case of a given overall plastic deformation. For example, in the case of an fcc crystal, a natural choice for a crystallographic dislocation basis is the limitation to only pure screw and edge dislocations such as employed in the dislocation simulations of KUBIN ET AL. [82]. This results in a total of 18 distinct dislocation types, 12 edge and 6 screw dislocations. In turn, the total dislocation density tensor, corresponding to the combined incompatibility measure of all slip systems together, is only comprised of 9 independent components. To overcome this redundancy ARSENLIS & PARKS [6] proposed two alternative minimization techniques resulting in crystallographic GND and higher order self-terminating SSD structures.

**5.6.4. Incorporation of GND Density into Hardening Relations.** In the present dislocation density based crystal plasticity model, the single crystal hardening response is based on the fundamental relation

$$\tau_r = c\mu b\sqrt{\rho} \quad (5.159)$$

where  $\rho$  is the (total) dislocation density,  $\tau_r$  the (specimen) flow stress,  $b$  the Burgers vector length and  $c$  is a constant. Based on the notion of *geometrically necessary dislocations* (COTTRELL [31], ASHBY [12]), the total dislocation density  $\rho$  was considered to be comprised of two distinct parts by ASHBY [12] in the following simple additive format

$$\rho = \rho_{\text{SSD}} + \rho_{\text{GND}} \quad (5.160)$$

Here,  $\rho_{\text{SSD}}$  again accumulates due to the random mutual trapping of individual dislocation lines with ongoing plastic deformation and is rather a characteristic of the *material*, i.e. the crystal structure, shear modulus, stacking fault energy,... This density can not be predicted by direct geometric arguments in contrast to the storage of the latter density  $\rho_{\text{GND}}$ , required in order to maintain continuity of a plastically inhomogeneously deforming body. Thus, in turn,  $\rho_{\text{GND}}$  is a characteristic of the *deformation geometry*, i.e. plastic curvature, and the *microstructure*, e.g. the arrangement and size of grains and phases.

So far the hardening (5.159) and dislocation density (5.160) relations are of rather phenomenological and isotropic character. In view of a more precise incorporation of the crystal structure, the extension of (5.159) to a slip system specific threshold reads

$$\tau_r^\alpha = c\mu b\sqrt{n^\alpha} \quad \text{with} \quad n^\alpha = \sum_{\beta} G^{\alpha\beta}\rho^\beta \quad (5.161)$$

see section 3.9 for a detailed discussion. Accordingly,  $n^\alpha$  is the effective obstacle density on slip system  $\alpha$  computed from all total densities  $\rho^\beta$ , i.e. all forest dislocation densities and the dislocation density on the same slip system. Thereby the relative contribution of the  $\beta$ -th dislocation density to  $n^\alpha$  depends on the interaction strength between the slip systems  $\alpha$  and  $\beta$  quantified through the interaction matrix  $G^{\alpha\beta}$  (e.g. BASSANI & WU [17]), see also section 3.9. Applying assumption (5.160), first adopted by ASHBY [12], to the slip system  $\beta$  (5.161) is rewritten as follows

$$\tau_r^\alpha = c\mu b \sqrt{\sum_{\beta} G^{\alpha\beta} (\rho_{\text{SSD}}^\beta + \rho_{\text{GND}}^\beta)} \quad (5.162)$$

Hence through (5.162) the characteristics of both, the SSD and the GND contribution to the obstacle density and thus further dislocation multiplication and resultant work hardening, are the same. This percipience of the *short range interaction* between individual SSDs and GNDs is well representative of the fact that the *real* individual dislocation is a microscopic line defect with physical characteristics independent of its *artificial* classification into SSD or GND. In contrast to the SSDs the collective action of the GNDs does not cancel, resulting in *long range* internal stresses. These are in many cases (STEINMANN [140], CERMELLI & GURTIN [26], SVENDSEN [145], EVERS ET AL. [38]) accounted for by the inclusion of a backstress measure into the formulation, resulting in a kinematic hardening behavior. However, since for now the concern is only with monotonic loading processes and isotropic hardening, this part of the hardening contribution will not be pursued any further. But it should be emphasized that the present theory does not by any means impede an extension to also include this hardening effect which is of relevance especially in cyclic tests.

To finally complete the hardening model, the respective relations for the SSD and GND density evaluations in (5.162) need to be specified. Here, the statistically stored dislocation density evolution is based on the following phenomenological constitutive law (GILLIS & GILMAN [48], ESSMANN & RAPP [37])

$$\dot{\rho}_{\text{SSD}}^\alpha := \lambda/b (1 - \rho_{\text{SSD}}^\alpha/\rho_{\text{SSD}}^{\text{sat}}) \dot{\gamma} \quad (5.163)$$

in terms of the saturation density  $\rho_{\text{SSD}}^{\text{sat}} := \lambda/y_c$  at which the rate of annihilation balances the rate of dislocation production. The coefficient  $\lambda$  characterizes the reciprocal mean free path between cross glide events and  $y_c$  the critical annihilation distance beneath which two dislocations of opposite sign cancel each other out. Solving the linear ordinary differential equation (5.163) for the SSD density on glide system  $\alpha$  gives

$$\rho_{\text{SSD}}^\alpha = \rho_{\text{SSD}}^{\text{sat}} [1 - (1 - \rho_{\text{SSD}}^{0,\alpha}/\rho_{\text{SSD}}^{\text{sat}}) \exp(-\gamma^\alpha/\gamma^{\text{sat}})] \quad (5.164)$$

where  $\gamma^{\text{sat}} := b\rho_{\text{SSD}}^{\text{sat}}/\lambda$  is the saturation slip strain and  $\rho_{\text{SSD}}^{0,\alpha}$  is the initial SSD density on system  $\alpha$ . According to these relations, only one scalar SSD density  $\rho_{\text{SSD}}^\alpha$  is considered for each slip system  $\alpha$  capturing mixed as well as pure screw and pure edge dislocation segments altogether. A more rigorous treatment based on internal variables which characterize the crystallographic dislocation density and evolve according to simple laws in dislocation mechanics, such as continuity of the dislocation line and conservation of the Burgers vector, was recently proposed by ARSENLIS & PARKS [7]. Now, the specific incorporation of the GND density into the present hardening model will finally be presented.

As explained in detail in the preceding sections the storage of GNDs is, in contrast to the SSD storage, directly related to the deformation geometry and thus implicitly depends on the gradients of the plastic deformation. In analogy to the SSD density, one scalar GND density  $\rho_{\text{GND}}^\alpha$  is specified for each slip system  $\alpha$  (of the e.g. 12 distinct ones in an fcc crystal) through the following assumption (recall the evaluations (5.157) and (5.158) of the dislocation tensor)

$$\begin{aligned} \rho_{\text{GND}}^\alpha &:= \frac{1}{b} |\mathbf{A}^\alpha| &= \sqrt{(\rho_{\text{GND}\perp}^\alpha)^2 + (\rho_{\text{GND}\odot}^\alpha)^2} \\ &= \frac{1}{b} \sqrt{(\nabla_{\mathbf{X}}\gamma^\alpha \cdot \mathbf{S}^\alpha)^2 + (\nabla_{\mathbf{X}}\gamma^\alpha \cdot \mathbf{T}^\alpha)^2} &= \frac{1}{b} |\mathbf{q}^\alpha| \end{aligned} \quad (5.165)$$

Thus within the proposed model, a density of geometrically necessary *mixed* dislocations  $\rho_{\text{GND}}^\alpha$  is computed separately for each slip system through the SRSS- (Square Root of a Sum of Squares) mean, i.e. a modified Root-Mean-Square, of the geometrically necessary edge  $\rho_{\text{GND}\perp}^\alpha$  and screw dislocations  $\rho_{\text{GND}\odot}^\alpha$  residing on the same slip system. Thereby, in contrast to the model of DAI & PARKS [35], only the projection  $\mathbf{q}^\alpha$  of the slip gradient  $\nabla_{\mathbf{X}}\gamma^\alpha$  onto the slip system contributes to this mixed density since a gradient perpendicular to the slip system is associated with a compatible deformation, see figure 5.23 for a visualization. Clearly through assumption (5.165), any information about a possible polarity of the stored edge or screw dislocation density is lost. Furthermore, since only one mixed dislocation density is considered per slip system, the fact that screw dislocations may cross slip is neglected. Consequently the same dislocation segment might produce a slip gradient on both slip systems in which it can reside. Thus through the present approach, this dislocation density would be picked up twice. Both of these consequences could be overcome by an extension of the crystallographic dislocation basis for both the SSDs and the GNDs to e.g. 12 edge and 6 screw dislocation densities for the case of an fcc crystal (KUBIN ET AL. [82]). Thereby also e.g. a possible mutual annihilation of GNDs and SSDs could be incorporated into the model. Such an extension might be included right away into the current model. Certainly its impact on the final results will, in the present context, however be negligible.

## 5.7. Micromechanically Motivated Strain Gradient Crystal Plasticity

The model of micromechanically motivated strain gradient crystal plasticity developed so far is summarized within table 5.1 or alternatively table 5.2. This summary is based on the constitutive framework of crystal plasticity as discussed in chapter 4 and the incompatibility analysis of the present chapter which led to the hardening relations proposed in the previous section. Thereby table 5.1 summarizes a model of crystal (visco-)plasticity which is especially applicable also in the rate independent setting with  $\tau_v^\alpha = 0 \forall \alpha$ . In contrast, the fully rate dependent crystal plasticity formulation summarized in table 5.2 is strictly speaking a model of crystal viscosity representative of the rate independent setting only in the limit case  $m = 0$ . Within this model,  $\tau_r^\alpha$  can be considered as the slip resistance if the slip rate on system  $\alpha$  is of the order of  $\dot{\gamma}_0$  throughout the deformation process. Both models are considered in the following numerical treatment. In both constitutive approaches an isotropic hardening response is adopted, governed by

**Table 5.1:** Constitutive model of strain gradient crystal (visco-)plasticity.

Macro-free energy	$\psi^{\text{macro}} = \hat{\psi}^e(\mathbf{F}^e)$	with $\mathbf{F}^e := \mathbf{F} \cdot \mathbf{F}^{p-1}$
Kirchhoff stresses	$\boldsymbol{\tau} = \mathbf{g}^{-1} \cdot \mathbf{P}^e \cdot \mathbf{F}^{eT}$	with $\mathbf{P}^e := \hat{\psi}_{,\mathbf{F}^e}^e$
Schmid stresses	$\tau^\alpha = -\mathbf{P}^e : \mathbf{F}_{,\gamma^\alpha}^e$	with $\mathbf{F}_{,\gamma^\alpha}^e := -\mathbf{F}^e \cdot \mathbf{S}^\alpha \otimes \mathbf{M}^\alpha$
Slip resistance	$\tau_r^\alpha = \hat{\tau}_r^\alpha(\gamma^1, \dots, \gamma^m, \nabla_{\mathbf{X}}\gamma^1, \dots, \nabla_{\mathbf{X}}\gamma^m)$	
Overstresses	$\tau_v^\alpha = \tau_{v0}(\dot{\gamma}^\alpha/\dot{\gamma}_0)^{1/\epsilon}$	
Flow criterion	$\Phi^\alpha = \tau^\alpha - \tau_r^\alpha - \tau_v^\alpha$	
Slip evolution	$\dot{\gamma}^\alpha \geq 0, \quad \Phi^\alpha \leq 0, \quad \dot{\gamma}^\alpha \Phi^\alpha = 0$	with $\gamma^\alpha(0) = 0$
Flow rule	$\dot{\mathbf{F}}^p \cdot \mathbf{F}^{p-1} = \sum_{\alpha=1}^m \dot{\gamma}^\alpha \mathbf{S}^\alpha \otimes \mathbf{M}^\alpha$	with $\mathbf{F}^p(0) = \mathbf{1}$

$$\begin{aligned} \tau_r^\alpha &= \hat{\tau}_r^\alpha(\gamma^1, \dots, \gamma^m, \nabla_{\mathbf{X}}\gamma^1, \dots, \nabla_{\mathbf{X}}\gamma^m) = c\mu b \sqrt{\sum_{\beta} G^{\alpha\beta} (\rho_{\text{SSD}}^\beta + \rho_{\text{GND}}^\beta)} \\ &\text{with } \rho_{\text{SSD}}^\beta = \rho_{\text{SSD}}^{\text{sat}} [1 - (1 - \rho_{\text{SSD}}^{0,\beta}/\rho_{\text{SSD}}^{\text{sat}}) \exp(-\gamma^\beta/\gamma^{\text{sat}})] \\ &\text{and } \rho_{\text{GND}}^\beta = 1/b \sqrt{(\nabla_{\mathbf{X}}\gamma^\beta \cdot \mathbf{S}^\beta)^2 + (\nabla_{\mathbf{X}}\gamma^\beta \cdot \mathbf{T}^\beta)^2} \end{aligned} \quad (5.166)$$

Therein the GND contribution is restricted to an increase in the forest density resulting in additional hardening. A possibly additional (kinematic) hardening contribution resulting from the residual stresses which arise in connection with the GND storage and the resulting incompatibilities is not considered at this point. As explained in connection with equation (5.136), such a further contribution to the constitutive behavior should be based on the symmetric part of Einstein's tensor. This would result in a constitutive dependence on second order derivatives of the plastic or equivalently elastic strains. A first simple extension in this respect is proposed in section 7.2.2.2. However, the specification of the precise form of this contribution requires further investigations. The kinematic hardening contribution proposed in EVERS ET AL. [38] relies on first order gradients of the GND density itself (i.e. second order derivatives of the plastic slip) and thus allows to also account for the fact that the GNDs are stored in arrays with finite dimensions. As stated already, here it is the goal to elaborate a micromechanically well founded model for the isotropic hardening contribution which gives a clear picture of the underlying mechanisms.

**Table 5.2:** Fully rate dependent strain gradient crystal plasticity model.

Macro-free energy	$\psi^{\text{macro}} = \hat{\psi}^e(\mathbf{F}^e)$	with $\mathbf{F}^e := \mathbf{F} \cdot \mathbf{F}^{p-1}$
Kirchhoff stresses	$\boldsymbol{\tau} = \mathbf{g}^{-1} \cdot \mathbf{P}^e \cdot \mathbf{F}^{eT}$	with $\mathbf{P}^e := \hat{\psi}_{,\mathbf{F}^e}^e$
Schmid stresses	$\tau^\alpha = -\mathbf{P}^e : \mathbf{F}_{,\gamma^\alpha}^e$	with $\mathbf{F}_{,\gamma^\alpha}^e := -\mathbf{F}^e \cdot \mathbf{S}^\alpha \otimes \mathbf{M}^\alpha$
Slip resistance	$\tau_r^\alpha = \hat{\tau}_r^\alpha(\gamma^1, \dots, \gamma^m, \nabla_{\mathbf{X}}\gamma^1, \dots, \nabla_{\mathbf{X}}\gamma^m)$	
Slip evolution	$\dot{\gamma}^\alpha = \dot{\gamma}_0 [ \tau^\alpha /\tau_r^\alpha]^{1/\epsilon} \text{sign}[\tau^\alpha]$	with $\gamma^\alpha(0) = 0$
Flow rule	$\dot{\mathbf{F}}^p \cdot \mathbf{F}^{p-1} = \sum_{\alpha=1}^m \dot{\gamma}^\alpha \mathbf{S}^\alpha \otimes \mathbf{M}^\alpha$	with $\mathbf{F}^p(0) = \mathbf{1}$

## 6. Numerical Implementation of Gradient Crystal Plasticity

According to the previous chapter, the *spatial distribution* of the plastic slips  $\gamma^\alpha$  is required in order to be able to compute the slip gradients and consequently the geometrically necessary dislocation density. In the following two main approaches are considered in this respect. Firstly, a *monolithic* fully implicit treatment of the model problem of strain gradient crystal plasticity will be considered. Thereby the plastic slips are introduced as *additional nodal degrees of freedom* besides the standard displacement degrees (see figure 6.1 a) for a simple visualization). Then within the fully rate dependent formulation (see e.g. table 5.2) the slip evolution is determined *globally* at the *node point level* instead of the standard *integration point level*. In turn, within the formulation of crystal (visco-) plasticity (see e.g. table 5.1) the Karush-Kuhn-Tucker loading/unloading conditions are enforced at the global node point level. Consequently these mixed formulations are denoted as *global formulations* within the following context. Secondly, the model problem of strain gradient crystal plasticity is treated on basis of an *operator split* where the spatial distribution of the plastic slips is computed by means of *interpolation algorithms* and the standard structure of the local boundary value problem is maintained (see figure 6.1 b) for a simple visualization). As will also be seen in the numerical examples in chapter 7, this results in a very effective approach denoted as *extended local formulation* within the subsequent developments. All these developments are derived for the geometrically non-linear setting and are validated by comparison with one another as well as with standard local formulations.

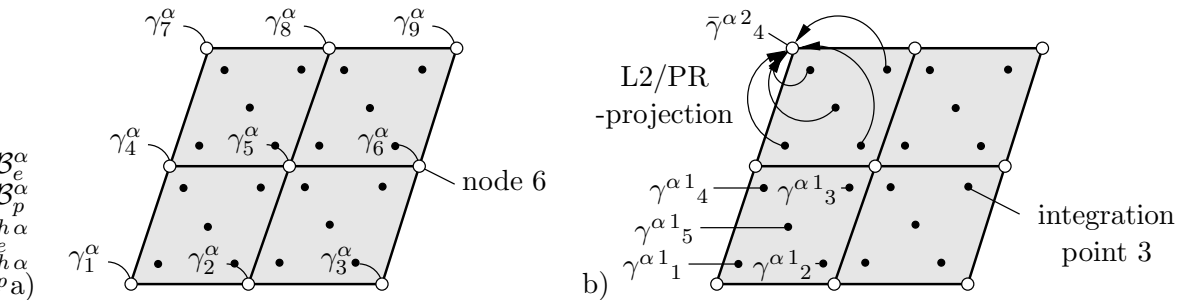


**Figure 6.1:** Numerical implementation of gradient plasticity for an element patch. a) Global formulation, b) extended local formulation based on a patch recovery (PR) or L2-projection.

A mixed formulation for elastoplasticity, however in a local context and at small strains, has been proposed by PINSKY [126]. Therein, additionally to the displacements the plastic parameter is discretized and in order to appropriately treat the plastic incompressibility constraint the mean stress field is approximated independently as well. This results in a three-field mixed formulation. Within the following a similar approach, however in the context of finite strain crystal plasticity, will be proposed where instead of the independent pressure approximation an enhanced strain method is adopted. Alternatively, SIMO ET AL. [137] proposed a complementary mixed formulation where the flow rule is enforced elementwise in a weak sense. An approach similar to the global formulation developed in the following has been proposed in the context of small strain phenomenological gradient plasticity by LIEBE & STEINMANN [86], or LIEBE [85], however with additional boundary conditions. Finally, within the context of dislocation density based strain gradient crystal plasticity, EVERS ET AL. [38] proposed a formulation where the GND densities are chosen as additional nodal degrees of freedom. An approach similar to the extended

local formulation developed below has been applied by MENZEL ET AL. [91] for single slip plasticity in the context of material forces.

### 6.1. Global Formulation for Fully Rate Dependent Gradient Plasticity

Within this section the global solution algorithm for the model problem of fully rate dependent strain gradient crystal plasticity will be developed. This model problem is summarized in table 5.2 together with the constitutive relations (5.166) and (A.1)-(A.3).

**6.1.1. Strong Form of the Coupled Problem.** In order to solve the problem of fully rate dependent gradient crystal plasticity in a *global* finite element context, both the deformation field  $\boldsymbol{\varphi} = \hat{\boldsymbol{\varphi}}(\mathbf{X})$  and the plastic slips  $\gamma^\alpha = [\hat{\gamma}^\alpha(\mathbf{X})]^{(\alpha=1,\dots,m)}$  are considered as *primary variables* parametrized in terms of the Lagrangian placements  $\mathbf{X}$ . These fields are determined on a *global level* throughout the solution domain by solving simultaneously the *equilibrium subproblem* and the *slip evolution equations*. Thereby the usual boundary conditions for the deformation field  $\boldsymbol{\varphi}$  and the tractions  $\mathbf{t}$  are prescribed on  $\partial\mathcal{B}_\varphi$  and on  $\varphi(\partial\mathcal{B}_T)$ , respectively. For the plastic slips, additional boundary conditions are not prescribed since at this point the structure of the local boundary value problem (BVP) should be maintained (i.e. the plastic slips might, in a purely local context, be condensed out again, see e.g section 6.2.6) and the only goal of this formulation is to provide for the spatial slip distribution. This might as well be interpreted as an implicit prescription of corresponding boundary conditions over the whole boundary within the *evolution subproblem*. Nevertheless, this formulation allows as well to artificially enforce boundary conditions for the plastic slips in the sense  $\gamma^\alpha = \hat{\gamma}^\alpha$  on  $\partial\mathcal{B}_\gamma$  e.g. at the surface of a thin film in section 7.1.1. The strong form of the coupled problem outlined so far is summarized in table 6.1. Thereby the equilibrium subproblem is given by the quasistatic balance of linear momentum (see equation (2.45)) and the evolution subproblem is specified by the evolution equation for the plastic slips (equation (4.27)).

**Table 6.1:** Strong form for coupled fully rate dependent plasticity.

Equilibrium subproblem
$\operatorname{div}[J^{-1} \boldsymbol{\tau}] + J^{-1} \rho_o \mathbf{b} = \mathbf{0} \quad \text{in} \quad \mathcal{S}$
$\boldsymbol{\varphi} = \bar{\boldsymbol{\varphi}} \quad \text{on} \quad \partial\mathcal{B}_\varphi$
$\mathbf{t} := \boldsymbol{\tau} \cdot \mathbf{n} = \bar{\mathbf{t}} \quad \text{on} \quad \varphi(\partial\mathcal{B}_T)$
Evolution subproblem
$\dot{\gamma}^\alpha - \dot{\gamma}_0 [ \tau^\alpha / \tau_r^\alpha ]^{1/\epsilon} \operatorname{sign}[\tau^\alpha] = \mathbf{0} \quad \text{in} \quad \mathcal{B}$

**6.1.2. Temporal Discretization and Weak Form of the Coupled Problem.** Considering a typical time increment  $[t_n, t_{n+1}]$  and an implicit backward Euler integration scheme, the temporal discretization of the strong form of the evolution subproblem reads

$$\gamma^\alpha - \gamma_n^\alpha - \dot{\gamma}_0 \Delta t [|\tau^\alpha|/|\tau_r^\alpha|]^{1/\epsilon} \operatorname{sign}[\tau^\alpha] = 0 \quad \forall \alpha = 1, \dots, m \quad (6.1)$$

where the indices indicating quantities evaluated at time  $t_{n+1}$  have been dropped. According to this notation the representation of the equilibrium subproblem remains unchanged and is thus not repeated here.

**Table 6.2:** Weak form for coupled fully rate dependent plasticity.

Equilibrium subproblem

$$\hat{G}_\varphi(\varphi, \gamma^\alpha, \delta\varphi) := \int_{\mathcal{B}} \nabla_{\mathbf{x}} \delta\varphi : \boldsymbol{\tau} dV - \int_{\mathcal{B}} \delta\varphi \cdot \mathbf{b} \rho_0 dV - \int_{\partial\mathcal{B}_T} \delta\varphi \cdot \bar{\mathbf{T}} dA = 0$$

and  $\varphi = \bar{\varphi}$  on  $\partial\mathcal{B}_\varphi$ 

Evolution subproblem

$$\hat{G}_{\gamma^\alpha}(\varphi, \gamma^\alpha, \delta\gamma^\alpha) := \int_{\mathcal{B}} \delta\gamma^\alpha \left[ \gamma^\alpha - \gamma_n^\alpha - \dot{\gamma}_0 \Delta t [|\tau^\alpha| / \tau_r^\alpha]^{1/\epsilon} \text{sign}[\tau^\alpha] \right] dV = 0$$

The weak form of the time discrete strong form is obtained through application of a standard Galerkin procedure. Thereby first the quasistatic balance of linear momentum is tested with a field of virtual displacements  $\delta\varphi$ , with  $\delta\varphi = \mathbf{0}$  on  $\varphi(\partial\mathcal{B}_\varphi)$ , which gives along with the divergence theorem and the stress boundary condition the weak form of the equilibrium subproblem, see table 6.2. (Note  $J^{-1} \boldsymbol{\tau} \cdot \mathbf{n} da = \boldsymbol{\tau} \mathbf{F}^{-T} \cdot \mathbf{N} dA = \mathbf{P} \cdot \mathbf{N} dA =: \mathbf{T} dA$ ). Similarly the slip evolution equation is tested with a field of virtual slips  $\delta\gamma^\alpha$  resulting for the coupled formulation in the expression  $\hat{G}_{\gamma^\alpha}(\varphi, \gamma^\alpha, \delta\gamma^\alpha) \forall \alpha = 1, \dots, m$ .

**6.1.3. Algorithmic Linearization for Monolithic Solution Procedure.** In view of a monolithic iterative solution of this system of coupled nonlinear equations, by means of a Newton-Raphson scheme the variational functionals  $\hat{G}_\varphi(\varphi, \gamma^\alpha, \delta\varphi)$  and  $\hat{G}_{\gamma^\alpha}(\varphi, \gamma^\alpha, \delta\gamma^\alpha)$  are now linearized with respect to the primary variables  $\varphi$  and  $\gamma^\alpha$ . The linearizations  $\text{Lin}\hat{G}_\varphi(\varphi, \gamma^\alpha, \delta\varphi, \Delta\varphi, \Delta\gamma^\beta)$  and  $\text{Lin}\hat{G}_{\gamma^\alpha}(\varphi, \gamma^\alpha, \delta\gamma^\alpha, \Delta\varphi, \Delta\gamma^\beta)$  are given in table 6.3 in terms of the algorithmic sensitivities (see chapter C in the Appendix for more details)

$$\begin{aligned} \Delta_\varphi[\nabla_{\mathbf{x}} \delta\varphi] &= -\nabla_{\mathbf{x}} \delta\varphi \cdot \nabla_{\mathbf{x}} \Delta\varphi \\ \Delta_\varphi[\boldsymbol{\tau}] &= \mathfrak{e}^e : \text{sym}[\nabla_{\mathbf{x}} \Delta\varphi] + \nabla_{\mathbf{x}} \Delta\varphi \cdot \boldsymbol{\tau} + \boldsymbol{\tau} \cdot \nabla_{\mathbf{x}}^T \Delta\varphi \\ \Delta_\varphi[\tau^\alpha] &= \mu \text{dev}[\mathbf{s}^\alpha \otimes \mathbf{m}^\alpha + \mathbf{s}^\alpha \otimes \mathbf{m}^\alpha] : \nabla_{\mathbf{x}} \Delta\varphi &=: \boldsymbol{\Gamma}_D^\alpha : \nabla_{\mathbf{x}} \Delta\varphi \\ \Delta_{\gamma^\beta}[\boldsymbol{\tau}] &= \mu \text{dev}[\tilde{\mathbf{F}}_{,\gamma^\beta}^e \cdot \tilde{\mathbf{F}}^{eT} + \tilde{\mathbf{F}}^e \cdot \tilde{\mathbf{F}}_{,\gamma^\beta}^{eT}] \Delta\gamma^\beta &=: \mathbf{D}_\Gamma^\beta \Delta\gamma^\beta \\ \Delta_{\gamma^\beta}[\tau^\alpha] &= \mu \{ (\tilde{\mathbf{F}}_{,\gamma^\beta}^e \cdot \mathbf{S}^\alpha) \cdot (\tilde{\mathbf{F}}^e \cdot \mathbf{M}^\alpha) + (\tilde{\mathbf{F}}^e \cdot \mathbf{S}^\alpha) \cdot (\tilde{\mathbf{F}}_{,\gamma^\beta}^e \cdot \mathbf{M}^\alpha) \} \Delta\gamma^\beta &=: \boldsymbol{\Gamma}_\Gamma^{\alpha\beta} \Delta\gamma^\beta \\ \Delta_{\gamma^\beta}[\tau_r^\alpha] &= c_\rho^\alpha \sum_{\omega=1}^m G^{\alpha\omega} (B^{\omega\beta} \Delta\gamma^\beta + \mathbf{E}^{\omega\beta} \cdot \nabla_{\mathbf{x}} \Delta\gamma^\beta) \end{aligned} \quad (6.2)$$

and with the definitions

$$\begin{aligned} c_\tau^\alpha &:= \tau^\alpha / \tau_r^\alpha \\ c_\rho^\alpha &:= (c\mu b)^2 / (2\tau_r^\alpha) \\ c_\gamma^\alpha &:= -\dot{\gamma}_0 \Delta t / (\epsilon \tau_r^\alpha) [|\tau^\alpha| / \tau_r^\alpha]^{(1-\epsilon)/\epsilon} \\ B^{\omega\beta} &:= 1/\gamma^{\text{sat}} (\rho_{\text{SSD}}^{\text{sat}} - \rho_{\text{SSD}}^{0,\omega}) \exp(-\gamma^\omega / \gamma^{\text{sat}}) \delta^{\omega\beta} \\ \mathbf{E}^{\omega\beta} &:= 1/(b^2 \rho_{\text{GND}}^\omega) \{ (\nabla_{\mathbf{x}} \gamma^\omega \cdot \mathbf{S}^\omega) \mathbf{S}^\omega + (\nabla_{\mathbf{x}} \gamma^\omega \cdot \mathbf{M}^\omega) \mathbf{M}^\omega \} \delta^{\omega\beta} \end{aligned} \quad (6.3)$$

Carefully note that the sensitivity  $\Delta_\varphi[\boldsymbol{\tau}]$  contains only the elastic part of the moduli. Furthermore, for the sake of a compact notation the incremental slip parameters determined

**Table 6.3:** Linearized form for monolithic solution procedure.

---

Equilibrium subproblem

$$\begin{aligned} \text{Lin } G_\varphi &:= \int_{\mathcal{B}} \Delta_\varphi[\nabla_{\mathbf{x}}\delta\varphi]:\boldsymbol{\tau} \, dV + \int_{\mathcal{B}} \nabla_{\mathbf{x}}\delta\varphi:\Delta_\varphi[\boldsymbol{\tau}] \, dV + \int_{\mathcal{B}} \nabla_{\mathbf{x}}\delta\varphi:\left(\sum_{\beta=1}^m \Delta_{\gamma^\beta}[\boldsymbol{\tau}]\right) \, dV \\ &+ G_\varphi = 0 \end{aligned}$$

Evolution subproblem

$$\begin{aligned} \text{Lin } G_{\gamma^\alpha} &:= \int_{\mathcal{B}} \delta\gamma^\alpha c_\gamma^\alpha \Delta_\varphi[\boldsymbol{\tau}^\alpha] \, dV \\ &+ \int_{\mathcal{B}} \delta\gamma^\alpha \sum_{\beta=1}^m [\delta^{\alpha\beta} \Delta\gamma^\beta + c_\gamma^\alpha (\Delta_{\gamma^\beta}[\boldsymbol{\tau}^\alpha] - c_\tau^\alpha \Delta_{\gamma^\beta}[\boldsymbol{\tau}_r^\alpha])] \, dV + G_{\gamma^\alpha} = 0 \end{aligned}$$


---

from the linearized form will be denoted by  $\Delta\gamma^\alpha$  within this chapter, i.e. the notation  $\Delta\Delta\gamma^\alpha$  of chapter 4 is abridged by  $\Delta\gamma^\alpha$ . Here, no abbreviation is introduced for  $\gamma^\alpha - \gamma_n^\alpha$ .

**6.1.4. Finite Element Discretization of the Coupled Problem.** In order to solve the set of coupled linearized equations of table 6.3 in a finite element context, the following interpolations are introduced within the element domain  $\mathcal{B}^e$

$$\begin{aligned} \boldsymbol{\varphi}^h &= \mathbf{X} + \sum_{I=1}^{n_{en}} N^I \mathbf{d}^I, & \delta\boldsymbol{\varphi}^h &= \sum_{I=1}^{n_{en}} N^I \delta\mathbf{d}^I, & \Delta\boldsymbol{\varphi}^h &= \sum_{I=1}^{n_{en}} N^I \Delta\mathbf{d}^I \\ \gamma^{h\alpha} &= \sum_{I=1}^{n_{en}} \mathcal{N}^I \gamma^{\alpha I}, & \delta\gamma^{h\alpha} &= \sum_{I=1}^{n_{en}} \mathcal{N}^I \delta\gamma^{\alpha I}, & \Delta\gamma^{h\alpha} &= \sum_{I=1}^{n_{en}} \mathcal{N}^I \Delta\gamma^{\alpha I} \end{aligned} \quad (6.4)$$

in terms of the nodal values  $\{\mathbf{d}^I, \delta\mathbf{d}^I, \Delta\mathbf{d}^I\}$  and  $\{\gamma^{\alpha I}, \delta\gamma^{\alpha I}, \Delta\gamma^{\alpha I}\}$  of the actual, virtual and incremental displacements and plastic slips. (For the sake of a compact notation the slip variables might as well be collected in corresponding vectors, however in view of the considerations in section 6.2 this will not be adopted here). Furthermore, in (6.4) an isoparametric interpolation has been chosen in terms of the shape functions  $N^I = \hat{N}^I(\boldsymbol{\xi})$  for the displacement and  $\mathcal{N}^I = \hat{\mathcal{N}}^I(\boldsymbol{\xi})$  for the slip interpolation, respectively. Nevertheless, throughout the numerical examples presented in chapter 7 generally the same interpolation order is used for the displacements and the slips, i.e.  $N^I = \mathcal{N}^I$ . The material gradient of the shape functions

$$\nabla_{\mathbf{X}} N^I = (\nabla_{\boldsymbol{\xi}} N^I) \cdot \mathbf{J}^{-1} \quad \text{and} \quad \nabla_{\mathbf{X}} \mathcal{N}^I = (\nabla_{\boldsymbol{\xi}} \mathcal{N}^I) \cdot \mathbf{J}^{-1} \quad (6.5)$$

is computed in terms of the coordinates  $\boldsymbol{\xi}$  of the parameter space and the Jacobian  $\mathbf{J}$  of the isoparametric map. The spatial gradients of the shape functions are computed with (6.5) and the discrete deformation gradient  $\mathbf{F}^h$  as follows

$$\begin{aligned} \nabla_{\mathbf{x}} N^I &= \nabla_{\mathbf{X}} N^I \cdot \nabla_{\mathbf{x}} \mathbf{X} = (\nabla_{\mathbf{X}} N^I) \cdot \mathbf{F}^{h-1} \\ \nabla_{\mathbf{x}} \mathcal{N}^I &= \nabla_{\mathbf{X}} \mathcal{N}^I \cdot \nabla_{\mathbf{x}} \mathbf{X} = (\nabla_{\mathbf{X}} \mathcal{N}^I) \cdot \mathbf{F}^{h-1} \quad \text{with} \quad \mathbf{F}^h = \mathbf{1} + \sum_{I=1}^{n_{en}} \mathbf{d}^I \otimes \nabla_{\mathbf{X}} N^I \end{aligned} \quad (6.6)$$

In index notation the spatial gradients will be denoted by  $N_{,j}^I$  or  $\mathcal{N}_{,j}^I$  and the material gradients by  $N_{,L}^I$  or  $\mathcal{N}_{,L}^I$ , respectively.  $\mathbf{F}^h$  serves as the fundamental kinematic variable for the computation of the stresses and the sensitivities (6.2).

Insertion of the finite element interpolations and the sensitivities (6.2) into the linearized form of table 6.3 finally results in a global system of fully coupled linear equations summarized in matrix format in table 6.4. The global arrays in table 6.4 are assembled from

**Table 6.4:** Coupled system of discretized linear equations.

$$\begin{bmatrix} \mathbf{K}_{DD} & \mathbf{K}_{D\Gamma}^\beta \\ \mathbf{K}_{\Gamma D}^\alpha & \mathbf{K}_{\Gamma\Gamma}^{\alpha\beta} \end{bmatrix} \begin{bmatrix} \Delta \mathbf{D} \\ \Delta \Gamma^\beta \end{bmatrix} = \begin{bmatrix} -\mathbf{F}_D^{\text{int}} + \mathbf{F}_D^{\text{ext}} \\ -\mathbf{F}_\Gamma^\alpha \end{bmatrix} \quad \text{for } \alpha, \beta = 1, \dots, m$$

the element arrays in the sense

$$\begin{aligned} \mathbf{K}_{DD} &:= \mathbf{A}_{e=1}^{n_{ele}} \mathbf{k}_{dd}^e, & \mathbf{K}_{D\Gamma}^\beta &:= \mathbf{A}_{e=1}^{n_{ele}} \mathbf{k}_{d\gamma}^{e\beta}, & \mathbf{K}_{\Gamma D}^\alpha &:= \mathbf{A}_{e=1}^{n_{ele}} \mathbf{k}_{\gamma d}^{e\alpha}, & \mathbf{K}_{\Gamma\Gamma}^{\alpha\beta} &:= \mathbf{A}_{e=1}^{n_{ele}} \mathbf{k}_{\gamma\gamma}^{e\alpha\beta}, \\ \Delta \mathbf{D} &:= \mathbf{A}_{e=1}^{n_{ele}} \Delta \mathbf{d}^e, & \Delta \Gamma^\beta &:= \mathbf{A}_{e=1}^{n_{ele}} \Delta \gamma^{e\beta}, & \mathbf{F}_D^{\text{int}} &:= \mathbf{A}_{e=1}^{n_{ele}} \mathbf{f}_d^{\text{int}e}, & \mathbf{F}_\Gamma^\alpha &:= \mathbf{A}_{e=1}^{n_{ele}} \mathbf{f}_\gamma^{e\alpha} \end{aligned} \quad (6.7)$$

Thereby the element residua and the element stiffness matrices are given by

$$\begin{aligned} [f_d^{\text{int}e}]_i^I &= \int_{\mathcal{B}^e} \sum_j N_{,j}^I [\tau_{ij}] dV \\ [f_\gamma^{e\alpha}]^I &= \int_{\mathcal{B}^e} \mathcal{N}^I \left[ c_{G_\gamma}^\alpha + \sum_J \{ \gamma^{\alpha J} - \gamma_n^{\alpha J} \} \mathcal{N}^J \right] dV \\ [k_{dd}^e]_{ik}^{JJ} &= \int_{\mathcal{B}^e} \sum_{j,l} N_{,j}^I \left[ \mathfrak{c}_{ijkl}^e + \tau_{lj} \delta_{ik} \right] N_{,l}^J dV \\ [k_{d\gamma}^{e\beta}]_i^{JJ} &= \int_{\mathcal{B}^e} \sum_j N_{,j}^I [D_{\Gamma ij}^\beta] \mathcal{N}^J dV \\ [k_{\gamma d}^{e\alpha}]_i^{JJ} &= \int_{\mathcal{B}^e} \sum_j \mathcal{N}^I [c_\gamma^\alpha \Gamma_{D ij}^\alpha] N_{,j}^J dV \\ [k_{\gamma\gamma}^{e\alpha\beta}]^{JJ} &= \int_{\mathcal{B}^e} \mathcal{N}^I \left[ \delta^{\alpha\beta} + c_\gamma^\alpha \Gamma_\Gamma^{\alpha\beta} - c_\gamma^\alpha c_\tau^\alpha c_\rho^\alpha \sum_{\omega=1}^m G^{\alpha\omega} B^{\omega\beta} \right] \mathcal{N}^J dV \\ &\quad + \int_{\mathcal{B}^e} \sum_L \mathcal{N}^I \left[ -c_\gamma^\alpha c_\tau^\alpha c_\rho^\alpha \sum_{\omega=1}^m G^{\alpha\omega} E_L^{\omega\beta} \right] \mathcal{N}_{,L}^J dV \end{aligned} \quad (6.8)$$

with the definition  $c_{G_\gamma}^\alpha := -\dot{\gamma}_0 \Delta t [|\tau^\alpha| / \tau_r^\alpha]^{1/\epsilon} \text{sign}[\tau^\alpha]$ .

Then, within the Newton-Raphson iteration, the global solutions for the nodal displacements and the plastic slips are updated via

$$\begin{aligned} \mathbf{D} &\Leftarrow \mathbf{D} + \Delta \mathbf{D} \\ \Gamma^\alpha &\Leftarrow \Gamma^\alpha + \Delta \Gamma^\alpha \end{aligned} \quad (6.9)$$

Within the numerical implementation of the outlined global formulation a bilinear interpolation has been chosen for both the displacements as well as the plastic slips. In order to improve the performance of the displacement part within bending dominated problems or in connection with localization phenomena, the mixed formulation considered so far

**Table 6.5:** Strong form for coupled crystal (visco-)plasticity.

---

Equilibrium subproblem	$\operatorname{div}[J^{-1} \boldsymbol{\tau}] + J^{-1} \rho_0 \mathbf{b} = \mathbf{0} \quad \text{in } \mathcal{S}$ $\boldsymbol{\varphi} = \bar{\boldsymbol{\varphi}} \quad \text{on } \partial \mathcal{B}_\varphi$ $\mathbf{t} := \boldsymbol{\tau} \cdot \mathbf{n} = \bar{\mathbf{t}} \quad \text{on } \varphi(\partial \mathcal{B}_T)$
Evolution subproblem	$\Phi^\alpha = \tau^\alpha - \tau_r^\alpha - \tau_v^\alpha \leq 0, \dot{\gamma}^\alpha \geq 0, \dot{\gamma}^\alpha \Phi^\alpha = 0 \quad \text{in } \mathcal{B}$

---

has been supplemented by an enhanced formulation. For more details in this respect refer to chapter D in the Appendix and to SIMO & ARMERO [138]. Furthermore note that the resulting global iteration matrix is generally unsymmetric. Only in the special case of single slip crystal plasticity the resulting system matrix is symmetric.

The developed global algorithm for fully rate dependent gradient crystal plasticity has been applied to the model problem of a constrained strip in simple shear in section 7.1.

## 6.2. Global Formulation for Gradient Crystal Viscoplasticity

Within this section the global solution algorithm of strain gradient crystal (visco-) plasticity will be developed. Through this formulation the case of fully rate independent plasticity may be recovered, in contrast to the previous formulation, not only in the limit case. This results in a distinction between purely elastic and elastoplastic loading branches. However, the algorithmic formulation, turns out to be much more difficult. The model problem of strain gradient crystal (visco-)plasticity is summarized in table 5.1 together with the constitutive relations (5.166) and (A.1)-(A.3).

**6.2.1. Strong Form of the Coupled Problem.** In this formulation the deformation field  $\boldsymbol{\varphi} = \hat{\boldsymbol{\varphi}}(\mathbf{X})$  and the plastic slips  $\gamma^\alpha = [\hat{\gamma}^\alpha(\mathbf{X})]^{(\alpha=1, \dots, m)}$  are again considered as primary variables. Here, again additional boundary conditions are generally not prescribed for the plastic slips, see the discussion in section 6.1.1. The strong form of the coupled problem is summarized in table 6.5. Thereby the evolution subproblem is now specified by the *Karush-Kuhn-Tucker loading/unloading conditions* (4.19). The complementary restrictions  $\dot{\gamma}^\alpha \Phi^\alpha = 0$  might as well be represented by a decomposition of the total solution domain  $\mathcal{B}$  into inactive elastic subdomains  $\mathcal{B}_e^\alpha$  and active elastoplastic subdomains  $\mathcal{B}_p^\alpha$  for each slip system  $\alpha$  according to (see figure 6.2 a) for a visualization)

$$\mathcal{B} = \mathcal{B}_e^\alpha \cup \mathcal{B}_p^\alpha \quad \text{and} \quad \mathcal{B}_e^\alpha \cap \mathcal{B}_p^\alpha = \emptyset \quad \forall \alpha = 1, \dots, m \quad (6.10)$$

with  $\mathcal{B}_e^\alpha = \{\mathbf{x} \in \mathcal{B} \mid \Phi^\alpha \leq 0, \dot{\gamma}^\alpha = 0\}$  and  $\mathcal{B}_p^\alpha = \{\mathbf{x} \in \mathcal{B} \mid \Phi^\alpha = 0, \dot{\gamma}^\alpha > 0\}$

**6.2.2. Temporal Discretization and Weak Form of the Coupled Problem.** The temporal integration of the strong form of the coupled problem is performed for a typical time step  $[t_n, t_{n+1}]$  by an implicit backward Euler scheme. Dropping the indices of all quantities evaluated at  $t_{n+1}$ , the time discrete evolution subproblem reads

$$\Phi^\alpha = \tau^\alpha - \tau_r^\alpha - \tau_v^\alpha \leq 0, \quad \gamma^\alpha - \gamma_n^\alpha \geq 0, \quad (\gamma^\alpha - \gamma_n^\alpha) \Phi^\alpha = 0 \quad \forall \alpha = 1, \dots, m \quad (6.11)$$



**Figure 6.2:** Decomposition of the solution domain into purely elastic and elastoplastic parts.

The time discrete form of the equilibrium subproblem is again obtained in a straightforward manner and thus not repeated here.

Applying a Galerkin procedure, the weak form of the time discrete strong form is obtained as follows. Testing the quasistatic balance of linear momentum with a field of virtual displacements  $\delta\varphi$ , with  $\delta\varphi = \mathbf{0}$  on  $\varphi(\partial\mathcal{B}_\varphi)$ , gives together with the stress boundary conditions the weak form of the equilibrium subproblem  $G_\varphi = \hat{G}_\varphi(\varphi, \gamma^\alpha, \delta\varphi)$ . Furthermore, the primary restrictions  $\Phi^\alpha \leq 0$  are tested with a field of virtual plastic slips  $\delta\gamma^\alpha > 0$  and the dual restrictions are tested by the virtual fields  $\delta\Phi^\alpha > 0$  resulting in the functionals  $G_{\gamma^\alpha} = \hat{G}_{\gamma^\alpha}(\varphi, \gamma^\alpha, \delta\gamma^\alpha)$  and  $G_{\Phi^\alpha} = \hat{G}_{\Phi^\alpha}(\varphi, \gamma^\alpha, \delta\Phi^\alpha)$ , respectively. The algorithmic

**Table 6.6:** Weak form for coupled crystal (visco-)plasticity.

Equilibrium subproblem
$\hat{G}_\varphi(\varphi, \gamma^\alpha, \delta\varphi) := \int_{\mathcal{B}} \nabla_{\mathbf{x}} \delta\varphi : \boldsymbol{\tau} dV - \int_{\mathcal{B}} \delta\varphi \cdot \mathbf{b} \rho_0 dV - \int_{\partial\mathcal{B}_T} \delta\varphi \cdot \bar{\mathbf{T}} dA = 0$ <p style="text-align: right;">and <math>\varphi = \bar{\varphi}</math> on <math>\partial\mathcal{B}_\varphi</math></p>
Evolution subproblem
$\hat{G}_{\gamma^\alpha}(\varphi, \gamma^\alpha, \delta\gamma^\alpha) := \int_{\mathcal{B}} \delta\gamma^\alpha [\tau^\alpha - \tau_r^\alpha - \tau_v^\alpha] dV \leq 0$
$\hat{G}_{\Phi^\alpha}(\varphi, \gamma^\alpha, \delta\Phi^\alpha) := \int_{\mathcal{B}} \delta\Phi^\alpha [\gamma^\alpha - \gamma_n^\alpha] dV \geq 0$

complementary restrictions  $G_{\gamma^\alpha} G_{\Phi^\alpha} = 0$  might again be represented by subdividing the solution domain in analogy to (6.10) into parts  $\mathcal{B}_e$  and  $\mathcal{B}_p$  currently subject to purely elastic and elastoplastic loading, respectively. Thus the weak form of the coupled problem is given in table 6.6 together with the following decomposition of the solution domain

$$\begin{aligned} \mathcal{B} &= \mathcal{B}_e^\alpha \cup \mathcal{B}_p^\alpha \quad \text{and} \quad \mathcal{B}_e^\alpha \cap \mathcal{B}_p^\alpha = \emptyset \quad \forall \quad \alpha = 1, \dots, m \\ \text{with } \mathcal{B}_e^\alpha &= \{ \mathbf{x} \in \mathcal{B} \mid G_{\gamma^\alpha} \leq 0, G_{\Phi^\alpha} = 0 \forall \delta\gamma^\alpha, \delta\Phi^\alpha > 0 \} \\ \mathcal{B}_p^\alpha &= \{ \mathbf{x} \in \mathcal{B} \mid G_{\gamma^\alpha} = 0, G_{\Phi^\alpha} > 0 \forall \delta\gamma^\alpha, \delta\Phi^\alpha > 0 \} \end{aligned} \quad (6.12)$$

**6.2.3. Algorithmic Linearization for Monolithic Solution Procedure.** For a frozen decomposition (6.12), the set of coupled nonlinear equations specified in table 6.6 is solved by means of a Newton-Raphson scheme. This bases on a linearization of the variational functionals  $\hat{G}_\varphi(\varphi, \gamma^\alpha, \delta\varphi)$ ,  $\hat{G}_{\gamma^\alpha}(\varphi, \gamma^\alpha, \delta\gamma^\alpha)$  and  $\hat{G}_{\Phi^\alpha}(\varphi, \gamma^\alpha, \delta\Phi^\alpha)$  with respect to the

**Table 6.7:** Linearized form for monolithic solution procedure.

---

Equilibrium subproblem

$$\begin{aligned} \text{Lin } G_\varphi &:= \int_{\mathcal{B}} \Delta_\varphi[\nabla_{\mathbf{x}}\delta\varphi]:\boldsymbol{\tau} \, dV + \int_{\mathcal{B}} \nabla_{\mathbf{x}}\delta\varphi:\Delta_\varphi[\boldsymbol{\tau}] \, dV + \int_{\mathcal{B}} \nabla_{\mathbf{x}}\delta\varphi:\left(\sum_{\beta=1}^m \Delta_{\gamma^\beta}[\boldsymbol{\tau}]\right) \, dV \\ &+ G_\varphi = 0 \end{aligned}$$

Evolution subproblem

$$\begin{aligned} \text{Lin } G_{\gamma^\alpha} &:= \int_{\mathcal{B}} \delta\gamma^\alpha \Delta_\varphi[\boldsymbol{\tau}^\alpha] \, dV + \int_{\mathcal{B}} \delta\gamma^\alpha \sum_{\beta=1}^m \Delta_{\gamma^\beta}[\boldsymbol{\tau}^\alpha - \boldsymbol{\tau}_r^\alpha - \boldsymbol{\tau}_v^\alpha] \, dV + G_{\gamma^\alpha} \leq 0 \\ \text{Lin } G_{\Phi^\alpha} &:= \int_{\mathcal{B}} \delta\Phi^\alpha \sum_{\beta=1}^m \delta^{\alpha\beta} \Delta_{\gamma^\beta} \, dV + G_{\Phi^\alpha} \geq 0 \end{aligned}$$


---

primary variables  $\varphi$  and  $\gamma^\alpha$ . The corresponding linearizations  $\text{Lin}\hat{G}_\varphi(\varphi, \gamma^\alpha, \delta\varphi, \Delta\varphi, \Delta\gamma^\alpha)$ ,  $\text{Lin}\hat{G}_{\gamma^\alpha}(\varphi, \gamma^\alpha, \delta\gamma^\alpha, \Delta\varphi, \Delta\gamma^\alpha)$  and  $\text{Lin}\hat{G}_{\Phi^\alpha}(\varphi, \gamma^\alpha, \delta\Phi^\alpha, \Delta\gamma^\alpha)$  are specified in table 6.7. The required sensitivities have already been specified in (6.2) together with the definitions (6.3)<sub>2,4,5</sub> and the remaining sensitivity

$$\Delta_{\gamma^\beta}[\boldsymbol{\tau}_v^\alpha] = \tau_{v0}/(\epsilon\dot{\gamma}_0\Delta t)\{(\gamma^\alpha - \gamma_n^\alpha)/(\dot{\gamma}_0\Delta t)\}^{(1-\epsilon)/\epsilon}\delta^{\alpha\beta}\Delta\gamma^\beta =: C^{\alpha\beta}\Delta\gamma^\beta \quad (6.13)$$

Thereby it should be carefully noted again that the sensitivity  $\Delta_\varphi[\boldsymbol{\tau}]$  contains only the elastic part of the moduli. The isochoric plastic softening part of the moduli of the standard purely local formulation is here contained in the sensitivities  $\boldsymbol{\Gamma}_D^\alpha$ ,  $\boldsymbol{D}_\Gamma^\beta$  and  $\Gamma_\Gamma^{\alpha\beta}$ , see section 6.2.6.

**6.2.4. Finite Element Discretization of the Coupled Problem.** Next the finite element discretization of the linearized form of the coupled problem in table 6.7 together with the decomposition (6.12) will be derived. This bases on the interpolations for the actual, virtual and incremental deformation map and the plastic slips as already specified in (6.4) in terms of the shapes  $N^I$  and  $\mathcal{N}^I$ , respectively. For the discretization of the virtual field  $\delta\Phi^\alpha$ , the same interpolation as for the plastic slips is chosen, i.e.  $\delta\Phi^{h\alpha} = \sum_{I=1}^{n_{en}} \mathcal{N}^I \delta\Phi^{\alpha I}$  in terms of the nodal values  $\delta\Phi^{\alpha I}$ . However, throughout the numerical examples in chapter 7 the same interpolation has been chosen for the deformation field and the plastic slips, i.e.  $N^I = \mathcal{N}^I$ . The material and spatial gradients of the shape functions and consequently the primary, virtual and incremental fields are again obtained in complete analogy to (6.5) and (6.6).

Before discretizing the linearized forms of table 6.7 for the solution domain  $\mathcal{B}$ , the specific decomposition of  $\mathcal{B}$  into active plastic and purely elastic parts  $\mathcal{B}_e^\alpha$  and  $\mathcal{B}_p^\alpha$  is required as a key ingredient. To this end, an *active set*  $\mathcal{A}^I$  is introduced at each node  $I$  containing all currently active slip systems  $\alpha$  at this node, i.e.  $\mathcal{A}^I := \{\alpha \mid \Gamma^{\alpha I} - \Gamma_n^{\alpha I} > 0\}$ . Thereby  $\Gamma^{\alpha I} = \mathbf{A}_{e=1}^{n_{ele}} \gamma^{e\alpha I}$ , see also (6.7). The determination of the active sets  $\mathcal{A}^I$  will be treated in detail in section 6.2.5. During the global Newton-Raphson iteration the active sets are assumed to be known, i.e. the decomposition (6.12) of the solution domain  $\mathcal{B}$  is given and

**Table 6.8:** Coupled system of discretized linear equations.

---


$$\begin{aligned} \sum_J [\mathbf{K}_{DD}]^{IJ} \Delta \mathbf{D}^J + \sum_J \sum_{\beta \in \mathcal{A}^J} [\mathbf{K}_{D\Gamma}^\beta]^{IJ} \Delta \Gamma^{\beta J} &= -[\mathbf{F}_D^{\text{int}} - \mathbf{F}_D^{\text{ext}}]^I \\ \sum_J [\mathbf{K}_{\Gamma D}^\alpha]^{IJ} \Delta \mathbf{D}^J + \sum_J \sum_{\beta \in \mathcal{A}^J} [K_{\Gamma\Gamma}^{\alpha\beta}]^{IJ} \Delta \Gamma^{\beta J} &= -[F_\Gamma^\alpha]^I \quad \forall \alpha \in \mathcal{A}^I \text{ at node } I \end{aligned}$$


---

reads in its discretized format (see figure 6.2 b) for a visualization)

$$\begin{aligned} \mathcal{B}^h &= \mathcal{B}_e^{h\alpha} \cup \mathcal{B}_p^{h\alpha} \quad \text{and} \quad \mathcal{B}_e^{h\alpha} \cap \mathcal{B}_p^{h\alpha} = \emptyset \quad \forall \alpha = 1, \dots, m \\ \text{with } \mathcal{B}_e^{h\alpha} &= \{I \in \mathcal{B}^h \mid F_\Gamma^{\alpha I} \leq 0, F_\Phi^{\alpha I} = 0 \forall \delta\gamma^\alpha, \delta\Phi^\alpha > 0\} \\ \mathcal{B}_p^{h\alpha} &= \{I \in \mathcal{B}^h \mid F_\Gamma^{\alpha I} = 0, F_\Phi^{\alpha I} > 0 \forall \delta\gamma^\alpha, \delta\Phi^\alpha > 0\} \end{aligned} \quad (6.14)$$

where  $F_\Gamma^{\alpha I}$  and  $F_\Phi^{\alpha I}$  are specified below. The decomposition (6.14) is equivalently represented by the active sets  $\mathcal{A}^I$  and corresponds to the discretized form  $F_\Gamma^{\alpha I} F_\Phi^{\alpha I} = 0$ ,  $\forall \alpha = 1, \dots, m$  and  $\forall I$  of the algorithmic complementary condition  $G_{\gamma^\alpha} G_{\Phi^\alpha} = 0$ .

Based on the assumed interpolations for the actual, virtual and incremental fields and the given nodal active sets  $\mathcal{A}^I$ , the discretization of the linearized weak forms  $\text{Lin}G_\varphi$  and  $\text{Lin}G_{\gamma^\alpha}$  results in the global system of fully coupled linear equations summarized in table 6.8. Thereby the global arrays are assembled from the corresponding element arrays according to (6.7) in terms of the element residua and the element stiffness matrices

$$\begin{aligned} [f_d^{\text{int}e}]_i^I &= \int_{\mathcal{B}^e} \sum_j N_j^I [\tau_{ij}] dV \\ [f_\gamma^{e\alpha}]^I &= \int_{\mathcal{B}^e} \mathcal{N}^I [\Phi^\alpha] dV \\ [k_{dd}^e]_{ik}^{IJ} &= \int_{\mathcal{B}^e} \sum_{j,l} N_j^I [\mathfrak{c}_{ijkl}^e + \tau_{lj} \delta_{ik}] N_l^J dV \\ [k_{d\gamma}^{e\beta}]_i^{IJ} &= \int_{\mathcal{B}^e} \sum_j N_j^I [D_{\Gamma ij}^\beta] \mathcal{N}^J dV \\ [k_{\gamma d}^{e\alpha}]_i^{IJ} &= \int_{\mathcal{B}^e} \sum_j \mathcal{N}^I [\Gamma_D^{\alpha ij}] N_j^J dV \\ [k_{\gamma\gamma}^{e\alpha\beta}]^{IJ} &= \int_{\mathcal{B}^e} \mathcal{N}^I \left[ \Gamma_\Gamma^{\alpha\beta} - C^{\alpha\beta} - c_\rho^\alpha \sum_{\omega \in \mathcal{A}^I} G^{\alpha\omega} B^{\omega\beta} \right] \mathcal{N}^J dV \\ &\quad + \int_{\mathcal{B}^e} \sum_L \mathcal{N}^I \left[ -c_\rho^\alpha \sum_{\omega \in \mathcal{A}^I} G^{\alpha\omega} E_L^{\omega\beta} \right] \mathcal{N}_{,L}^J dV \end{aligned} \quad (6.15)$$

Within a typical Newton-Raphson step, solution of (6.15) gives the updated nodal displacements and plastic slips via

$$\begin{aligned} \mathbf{D}^I &\Leftarrow \mathbf{D}^I + \Delta \mathbf{D}^I \\ \Gamma^{\alpha I} &\Leftarrow \Gamma^{\alpha I} + \Delta \Gamma^{\alpha I} \quad \forall \alpha \in \mathcal{A}^I \end{aligned} \quad (6.16)$$

A convenient way to incorporate the dual restriction  $G_{\Phi^\alpha} \geq 0$  into the global solution algorithm is obtained as follows. Instead of discretizing the linearized form  $\text{Lin}G_{\Phi^\alpha}$ , the dual restriction itself is directly discretized which results in the nodal residual expressions

$$G_{\Phi^\alpha}^{hI} := \sum_J [M_{\Phi\Gamma}^\alpha]^{IJ} (\Gamma^{\alpha J} - \Gamma_n^{\alpha J}) \geq 0 \quad \text{with} \quad [M_{\Phi\Gamma}^\alpha]^{IJ} = \mathbf{A} \int_{\mathcal{B}^e} \mathcal{N}^I \mathcal{N}^J dV \quad (6.17)$$

An approximate solution of (6.17) can be based on a diagonalization of  $[M_{\Phi\Gamma}^\alpha]^{IJ}$  which is equivalent to checking at each global node  $I$  the restriction

$$\Gamma^{\alpha I} - \Gamma_n^{\alpha I} \geq 0 \quad (6.18)$$

This is accounted for within the active set search in (6.22).

The outlined global formulation has been implemented based on bilinear or alternatively quadratic interpolations for both the displacements as well as the plastic slips. For the bilinear interpolations the displacement part was again implemented within the context of an enhanced formulation. For further details in this respect refer to chapter D in the Appendix and to SIMO & ARMERO [138].

**6.2.5. Active Set Search.** Finally, the active set search will be discussed as a key ingredient of the global solution algorithm. The following considerations are in line with the active set update strategy outlined within the context of the local stress update algorithm in section 4.2.5. Within the discretized setting at each node  $I$  the set of all possible slip systems  $\mathcal{S}^I := \{1, \dots, m\}$  is separated into a *working set*  $\mathcal{W}^I$  containing the slip systems subjected to active equality constraints

$$\mathcal{W}^I := \{\alpha \mid \Gamma^{\alpha I} - \Gamma_n^{\alpha I} = 0\} \quad \text{with} \quad \alpha \in \mathcal{S}^I \quad (6.19)$$

and an *active set*  $\mathcal{A}^I$  containing all currently active slip systems

$$\mathcal{A}^I := \mathcal{S}^I \setminus \mathcal{W}^I \quad (6.20)$$

Then at the beginning of each time step the actual active set is initialized with the one at the end of the last time step  $\mathcal{A} = \mathcal{A}_n$  and an improved solution point is computed via the Newton-Raphson update (6.16). If at any node  $I$  some violations of (6.18) occur in the sense  $\Gamma^{\alpha I} - \Gamma_n^{\alpha I} < 0$  for  $\alpha \in \mathcal{A}^I$ , the most violated system (index  $\alpha^-$ ) is identified and a corresponding scaling parameter  $\xi$  is computed

$$\alpha^- := \arg[\xi] \quad \text{and} \quad \xi := \min_{\substack{\alpha \in \mathcal{A}^I \\ \wedge \Gamma^{\alpha I} - \Gamma_n^{\alpha I} < 0}} \left( 1 - \frac{\Gamma^{\alpha I} - \Gamma_n^{\alpha I}}{\Delta\Gamma^{\alpha I}} \right) \quad (6.21)$$

Subsequently all slip parameters  $\Gamma^{\alpha I}$  at this node are scaled by

$$\Gamma^{\alpha I} \leftarrow \Gamma^{\alpha I} - (1 - \xi)\Delta\Gamma^{\alpha I} \quad \forall \quad \alpha \in \mathcal{A}^I \quad (6.22)$$

such that they are admissible in the sense of (6.18). Thereby  $\Gamma^{\alpha^- I} = \Gamma_n^{\alpha^- I}$  holds for the initially most violated system  $\alpha^-$ . Whether system  $\alpha^-$  needs to be removed from the active set  $\mathcal{A}^I$  or not is decided based on the sensitivity  $\Delta W^I$  in the solution point (6.22)

$$\Delta W^I := \sum_{\alpha \in \mathcal{A}^I} [F_\Gamma^\alpha]^I (\Gamma^{\alpha I} - \Gamma_n^{\alpha I}) > 0 \quad (6.23)$$

For  $\Delta W^I < 0$ , the most violated system  $\alpha^-$  is removed from the active set by the *system dropping update*

$$\mathcal{A}^I \Leftarrow \{\mathcal{A}^I \setminus (\alpha^- \in \mathcal{A}^I)\} \quad (6.24)$$

and a further global iteration loop is launched. Upon convergence of the global Newton iteration the primary restrictions  $[F_\Gamma^\alpha]^I \leq 0$  are checked at each node  $I$ . If some violation in the sense  $[F_\Gamma^\alpha]^I > 0$  for one of the currently non-active systems, i.e.  $\alpha \in \mathcal{S}^I \setminus \mathcal{A}^I$  occurs, the most violated system  $\alpha^+$  is identified through

$$\alpha^+ := \arg \left[ \max_{\substack{\alpha \in \mathcal{S}^I \setminus \mathcal{A}^I \\ \wedge [F_\Gamma^\alpha]^I > 0}} ([F_\Gamma^\alpha]^I) \right] \quad (6.25)$$

and consequently added to the active set by the *system adding update*

$$\mathcal{A}^I \Leftarrow \{\mathcal{A}^I \cup (\alpha^+ \in \mathcal{S}^I \setminus \mathcal{A}^I)\} \quad (6.26)$$

Subsequently a new global iteration loop is started and if finally upon convergence further active set updates (6.26) are not required, the minimizing solution is found and the global iteration is terminated. The complete coupled solution algorithm of global crystal (visco-)plasticity is summarized in table 6.9. An application of this algorithm within the analysis of a heterogeneous composite and in the bending analysis of a homogeneous single-crystalline beam is presented in section 7.2.

**6.2.6. Comparison of Discrete Global and Standard Local Formulation.** In the following, it will be shown that for a *purely local model of crystal (visco-)plasticity* (i.e. no slip gradients enter the model) the discrete settings of both the standard local as well as the global formulation are equivalent. Recall first the global system of discretized linear equations of the standard formulation

$$\begin{aligned} \sum_J \sum_k [K_{DD}]_{ik}^{IJ} \Delta D_k^J &= -[F_D^{\text{int}} - F_D^{\text{ext}}]^I \\ \text{with } [K_{DD}]_{ik}^{IJ} &= \mathbf{A}_{e=1}^{n_{ele}} \int_{B^e} \sum_{j,l} N_{.j}^I [\mathbf{c}_{ijkl}^{ep} + \tau_{lj} \delta_{ik}] N_{.l}^J dV \end{aligned} \quad (6.27)$$

in terms of the Eulerian elastoplastic tangent moduli  $\mathbf{c}^{ep}$  consisting of an elastic part and a plastic softening part (see section A.3 in the Appendix)

$$\mathbf{c}^{ep} = \mathbf{c}^e + \sum_{\alpha, \beta \in \mathcal{A}} H^{\alpha\beta-1} \mu \operatorname{dev}[\tilde{\mathbf{F}}_{,\gamma\hat{\alpha}}^e \cdot \tilde{\mathbf{F}}^{eT} + \tilde{\mathbf{F}}^e \cdot \tilde{\mathbf{F}}_{,\gamma\hat{\alpha}}^{eT}] \otimes \mu \operatorname{dev}[\mathbf{s}^\alpha \otimes \mathbf{m}^\alpha + \mathbf{m}^\alpha \otimes \mathbf{s}^\alpha] \quad (6.28)$$

The sensitivity  $H^{\alpha\beta} := -[\Phi^\alpha]_{,\gamma\beta}$  is derived in section A.2 in the Appendix and might be rewritten in terms of the definitions (6.2)<sub>5,6</sub>, (6.3)<sub>2,4</sub> and (6.13) as follows

$$-H^{\alpha\beta} = \Gamma_\Gamma^{\alpha\beta} - C^{\alpha\beta} - c_\rho^\alpha \sum_{\omega \in \mathcal{A}} G^{\alpha\omega} B^{\omega\beta} \quad (6.29)$$

Thus together with the definitions (6.2)<sub>3,4</sub> the elastoplastic moduli are given by

$$\mathbf{c}^{ep} = \mathbf{c}^e + \sum_{\alpha, \beta \in \mathcal{A}} H^{\alpha\beta-1} \mathbf{D}_\Gamma^\alpha \otimes \Gamma_D^\beta \quad (6.30)$$

**Table 6.9:** Coupled global solution algorithm of crystal (visco-)plasticity.

- 
1. Boundary Conditions:  $\mathbf{u} = \bar{\mathbf{u}}$  on  $\partial\mathcal{B}_u$ ,  $\mathbf{T} = \bar{\mathbf{T}}$  on  $\partial\mathcal{B}_T$   
Initialization:  $\{\mathbf{D}^I = \mathbf{D}_n^I, \Gamma^{\alpha I} = \Gamma_n^{\alpha I} \forall \alpha \in \mathcal{S}, \mathcal{A}^I = \mathcal{A}_n^I\} \quad \forall I = 1, \dots, n_{\text{node}}$
  2. Assemble and solve system of coupled linear equations of table 6.8
  3. Convergence check: If  $(\sqrt{\sum_I \sum_{\alpha \in \mathcal{A}^I} ([F_\Gamma^\alpha]^I)^2 + \sum_I ([\mathbf{F}_D^{\text{int}}]^I + \mathbf{F}_D^{\text{ext}}]^I)^2} \leq \text{tol})$  go to 7
  4. Newton update:  $\{\mathbf{D}^I \leftarrow \mathbf{D}^I + \Delta\mathbf{D}^I, \Gamma^{\alpha I} \leftarrow \Gamma^{\alpha I} + \Delta\Gamma^{\alpha I}\} \quad \forall I = 1, \dots, n_{\text{node}}, \alpha \in \mathcal{A}^I$
  5. System scaling/dropping update  $\forall I = 1, \dots, n_{\text{node}}$ : If  $\Gamma^{\alpha I} - \Gamma_n^{\alpha I} < 0$  for any  $\alpha \in \mathcal{A}^I$ 
    - identify most violated system  $\alpha^- := \arg[\xi]$  with  $\xi := \min_{\alpha \in \mathcal{A}^I} \left(1 - \frac{(\Gamma^{\alpha I} - \Gamma_n^{\alpha I})}{\Delta\Gamma^{\alpha I}}\right)$
    - perform scaling update  $\Gamma^{\alpha I} \leftarrow \Gamma^{\alpha I} - (1 - \xi)\Delta\Gamma^{\alpha I} \quad \forall \alpha \in \mathcal{A}^I$
    - If  $\Delta W^I := \sum_{\alpha \in \mathcal{A}^I} [F_\Gamma^\alpha]^I (\Gamma^{\alpha I} - \Gamma_n^{\alpha I}) > 0$  drop system  $\alpha^-$ ,  $\mathcal{A}^I \leftarrow \{\mathcal{A}^I \setminus (\alpha^- \in \mathcal{A}^I)\}$
  6. Go to 2
  7. System adding update, set  $c_{\mathcal{A}} = \text{false}$ ;  $\forall I = 1, \dots, n_{\text{node}}$ : If  $[F_\Gamma^\alpha]^I > 0$  for any  $\alpha \in \mathcal{S} \setminus \mathcal{A}^I$ 
    - identify most violated system  $\alpha^+ := \arg[\max_{\alpha \in \mathcal{S} \setminus \mathcal{A}^I} ([F_\Gamma^\alpha]^I)]$
    - add system  $\alpha^+$  to active set  $\mathcal{A}^I \leftarrow \{\mathcal{A}^I \cup (\alpha^+ \in \mathcal{S} \setminus \mathcal{A}^I)\}$
    - set  $c_{\mathcal{A}} = \text{true}$
  8. If  $c_{\mathcal{A}} = \text{true}$  go to 2
- 

Turning next to the global formulation the corresponding system of equations summarized in table 6.8 can be rewritten by condensing the algorithmic slip increments  $\Delta\Gamma^{\beta J}$  out

$$\sum_k \sum_J [\tilde{K}_{DD}]_{ik}^{IJ} \Delta D_k^J = -[F_D^{\text{int}} - F_D^{\text{ext}}]_i^I + \sum_{J,K} \sum_{\alpha, \beta \in \mathcal{A}^I} [K_{D\Gamma}^\alpha]_i^{IJ} [K_{\Gamma\Gamma}^{\alpha\beta}]^{JK-1} [F_\Gamma^\beta]^K \quad (6.31)$$

with  $[\tilde{K}_{DD}]_{ik}^{IJ} = [K_{DD}]_{ik}^{IJ} - \sum_{K,L} \sum_{\alpha, \beta \in \mathcal{A}^I} [K_{D\Gamma}^\alpha]_i^{IK} [K_{\Gamma\Gamma}^{\alpha\beta}]^{KL-1} [K_{\Gamma D}^\beta]_k^{LJ}$

Carefully note that  $[K_{DD}]_{ik}^{IJ}$  in (6.31)<sub>2</sub> contains only the purely elastic contribution of the moduli in contrast to  $[K_{DD}]_{ik}^{IJ}$  in (6.27)<sub>2</sub>. If the flow criterion is satisfied locally for each  $\alpha \in \mathcal{A}$ , this induces  $[F_\Gamma^\alpha]^K = 0$  at each node  $K$  as well and thus the right hand sides of (6.31)<sub>1</sub> and (6.27)<sub>1</sub> are equivalent. Finally insertion of (6.15)<sub>3-6</sub> into (6.31)<sub>2</sub> gives

$$[\tilde{K}_{DD}]_{ik}^{IJ} = \mathbf{A}_{e=1}^{n_{\text{ele}}} \int_{\mathcal{B}^e} \sum_{j,l} N_{,j}^I \left\{ \mathfrak{e}_{ijkl}^e + \tau_{lj} \delta_{ik} \right. \\ \left. - \sum_{K,L} \sum_{\alpha, \beta \in \mathcal{A}^I} D_{\Gamma ij}^\alpha \mathcal{N}^K \left( \mathcal{N}^K \left[ \Gamma_\Gamma^{\alpha\beta} - C^{\alpha\beta} - c_\rho^\alpha \sum_{\omega \in \mathcal{A}^I} G^{\alpha\omega} B^{\omega\beta} \right] \mathcal{N}^L \right)^{-1} \mathcal{N}^L \Gamma_{Dkl}^\beta \right\} N_{,l}^J dV \quad (6.32)$$

and thus  $[\tilde{K}_{DD}]_{ik}^{IJ}$  can be rewritten as

$$[\tilde{K}_{DD}]_{ik}^{IJ} = \mathbf{A}_{e=1}^{n_{\text{ele}}} \int_{\mathcal{B}^e} \sum_{j,l} N_{,j}^I \left\{ \mathfrak{e}_{ijkl}^e + \sum_{\alpha, \beta \in \mathcal{A}^I} H^{\alpha\beta-1} D_{\Gamma ij}^\alpha \Gamma_{Dkl}^\beta + \tau_{lj} \delta_{ik} \right\} N_{,l}^J dV \quad (6.33)$$

Consequently the condensed stiffness terms (6.33) of the global formulation are equivalent to the stiffness matrices of the standard formulation (6.27)<sub>2</sub>. These comprise in both cases of a geometric term and the elastoplastic tangent moduli  $\mathfrak{c}^{ep}$ .

### 6.3. Extended Local Formulation for Gradient Crystal Plasticity

The global formulation of crystal plasticity developed in the preceding sections is rather costly since it requires for example up to  $2 \times 12$  additional nodal degrees of freedom in a full multislip fcc crystal plasticity model. Furthermore the continuously changing nodal active sets induce varying dimensions of the global system of equations. This involves a non-standard implementation of the equation solver. These drawbacks of the global formulation motivate the development of a more efficient approach which will rely on an extension of the standard local formulation. Within this *extended local formulation*, the slip gradient computation will be based on a smoothing procedure. Thus the model problem of strain gradient crystal plasticity as summarized in tables 5.1 and 5.2 is now treated within an extended setting of the local formulation considered in chapter 4. The slip gradients and thus the GND-densities are accounted for in an explicit manner in the sense of an operator split where their specific values are computed in a postprocessing step. Within this postprocessing step, the local integration point solutions for the plastic slips  $\Gamma^{\alpha h}$  are projected to the nodes of the finite element mesh. Thereby the global field  $\Gamma^{\alpha h}$  contains the slip values  $\gamma_l^\alpha$  in each integration point  $l$  of the finite element discretization. Subsequently the values of the slip gradients  $\nabla_{\mathbf{X}}\Gamma^\alpha$  are computed based on the projected nodal values  $\bar{\Gamma}^\alpha$  and the finite element shape functions  $\mathbf{N}$  as follows

$$\nabla_{\mathbf{X}}\Gamma^\alpha = \nabla_{\mathbf{X}}\mathbf{N}\cdot\bar{\Gamma}^\alpha \quad (6.34)$$

Here, the slip gradients in each integration point  $\nabla_{\mathbf{X}}\gamma_l^\alpha$  are again collectively represented by  $\nabla_{\mathbf{X}}\Gamma^\alpha$ . With the slip gradients at hand the local material response can be determined for each integration point. Thereby the most efficient solution procedure is based on an explicit update of the GND density and the standard stress update algorithm as discussed in chapter 4. This is also conceptually visualized in figure 6.3. The key ingredient of this formulation is the *smoothing algorithm*. Within the following, two alternative projection methods will be briefly discussed, a  $L_2$ -projection and a *patch recovery*.

**6.3.1. The  $L_2$ -Projection.** The starting point in the development of this projection method is to demand that the difference between the continuous smoothed solutions  $\Gamma^{\alpha*}$  and the computed values of the finite element solution  $\Gamma^{\alpha h}$  has to vanish

$$\Gamma^{\alpha*} - \Gamma^{\alpha h} = \mathbf{0} \quad (6.35)$$

Therein the continuous smoothed solutions  $\Gamma^{\alpha*}$  are determined from the projected nodal values  $\bar{\Gamma}^\alpha$  with the finite element shape functions  $\mathbf{N}$

$$\Gamma^{\alpha*} = \mathbf{N}\cdot\bar{\Gamma}^\alpha \quad (6.36)$$

Satisfying (6.35) in a weak sense within the solution domain  $\mathcal{B}$ , the corresponding weak form is obtained with the test functions  $\delta\Gamma^{\alpha*} = \mathbf{N}\cdot\delta\bar{\Gamma}^\alpha$  as follows

$$\int_{\mathcal{B}} \delta\Gamma^{\alpha*}\cdot(\Gamma^{\alpha*} - \Gamma^{\alpha h}) dV \stackrel{(6.36)}{=} \delta\bar{\Gamma}^{\alpha T}\cdot \int_{\mathcal{B}} \mathbf{N}^T\cdot(\mathbf{N}\cdot\bar{\Gamma}^\alpha - \Gamma^{\alpha h}) dV = 0 \quad (6.37)$$

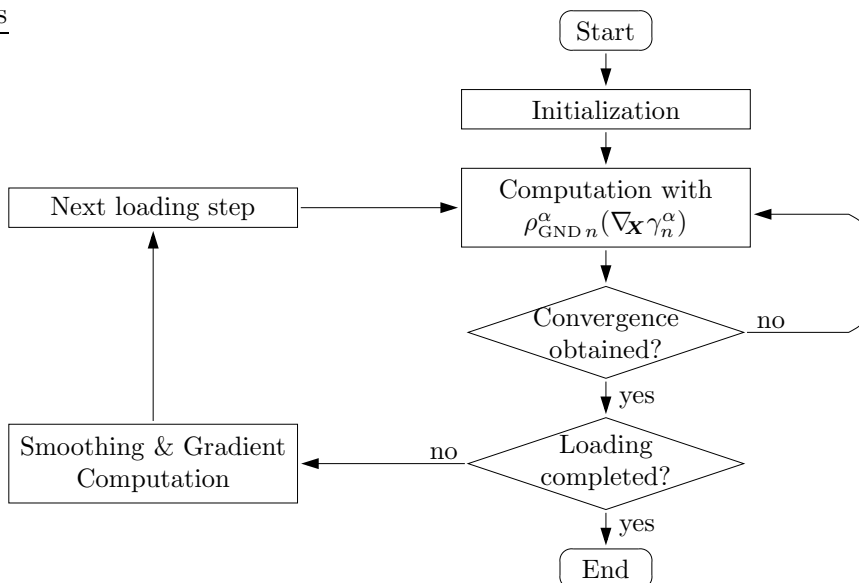


**Figure 6.3:** Solution procedure for extended local formulation.

which has to be met for arbitrary  $\delta\bar{\Gamma}^\alpha$ . Consequently (6.37) can be solved for the projected nodal plastic slips  $\bar{\Gamma}^\alpha$  through the following system of equations

$$\int_{\mathcal{B}} \mathbf{N}^T \cdot \mathbf{N} dV \cdot \bar{\Gamma}^\alpha = \int_{\mathcal{B}} \mathbf{N}^T \cdot \Gamma^{\alpha h} dV \quad \Rightarrow \quad \bar{\Gamma}^\alpha = \underbrace{\left[ \int_{\mathcal{B}} \mathbf{N}^T \cdot \mathbf{N} dV \right]}_{\mathbf{M}^{-1}}^{-1} \cdot \int_{\mathcal{B}} \mathbf{N}^T \cdot \Gamma^{\alpha h} dV \quad (6.38)$$

This global system of equations is most efficiently solved approximately by diagonalising the matrix  $\mathbf{M}$  in the sense of a lumped matrix  $\mathbf{M}_L$  (ZIENKIEWICZ & TAYLOR [160]). Thus the inversion of  $\mathbf{M}_L$  is straightforward. In this case the  $L_2$ -projection is of superior efficiency and gives very good results for linear and bilinear elements. However for higher order elements, e.g. quadratic triangles, this procedure is not applicable. In this case the smoothing algorithm will be based on the patch recovery discussed in the next section. (6.37) might, instead of the strong form (6.35), as well be motivated by the following *least square fit* or minimization problem for  $\bar{\Gamma}^\alpha$

$$\begin{aligned} \Pi = \hat{\Pi}(\bar{\Gamma}^\alpha) &= \frac{1}{2} \int_{\mathcal{B}} (\Gamma^{\alpha*} - \Gamma^{\alpha h})^T \cdot (\Gamma^{\alpha*} - \Gamma^{\alpha h}) dV \\ &= \frac{1}{2} \int_{\mathcal{B}} (\mathbf{N} \cdot \bar{\Gamma}^\alpha - \Gamma^{\alpha h})^T \cdot (\mathbf{N} \cdot \bar{\Gamma}^\alpha - \Gamma^{\alpha h}) dV \rightarrow \min \end{aligned} \quad (6.39)$$

which obviously is equivalent to (6.37)

**6.3.2. The Patch Recovery.** In the  $L_2$ -projection, an optimal smoothed solution  $\Gamma^{\alpha*}$  is determined for the whole solution domain  $\mathcal{B}$  through (6.39) at once which results in the global system of equations (6.38). In turn, within the patch recovery (ZIENKIEWICZ & ZHU [159], ZIENKIEWICZ & TAYLOR [160]) the projection of the integration point solutions  $\Gamma^{\alpha h}$  to the nodes is performed consecutively for each node on its own based on the respective surrounding element patch  $\mathcal{B}_p$ . When all nodal projections  $\bar{\Gamma}^\alpha$  have been determined, the smoothed solution  $\Gamma^{\alpha*}$  for the whole solution domain  $\mathcal{B}$  is again obtained

by use of the finite element shape functions, i.e.

$$\mathbf{\Gamma}^{\alpha*} = \mathbf{N} \cdot \bar{\mathbf{\Gamma}}^{\alpha} \quad (6.40)$$

The nodal projections  $\bar{\mathbf{\Gamma}}^{\alpha I}$  for node  $I$  are determined as follows. First an interpolation polynomial  $\tilde{\Gamma}^{\alpha I}$  of order  $p$  is constructed within the domain  $\mathcal{B}_p^I$  of the element patch comprised of all elements containing node  $I$ . For the 2-dimensional case it reads

$$\tilde{\Gamma}^{\alpha I}(\mathbf{X}) = \mathbf{p}(\mathbf{X}) \cdot \mathbf{a}^{\alpha I} \quad \forall \quad \mathbf{X} \in \mathcal{B}_p^I \quad \text{with} \quad \mathbf{p}(\mathbf{X}) = [1 \ X \ Y \ \dots \ X^p \ Y^p] \quad (6.41)$$

The coefficients  $\mathbf{a}^{\alpha I}$  are determined by the following least square fit of the interpolation  $\tilde{\Gamma}^{\alpha I}$  to the computed integration point solutions  $\gamma_l^\alpha$  within the element patch

$$\begin{aligned} \Pi = \hat{\Pi}(\mathbf{a}^{\alpha I}) &= \frac{1}{2} \sum_{l=1}^{n_I} (\tilde{\Gamma}^{\alpha I} - \gamma_l^\alpha)^2 \\ &= \frac{1}{2} \sum_{l=1}^{n_I} (\mathbf{p}(\mathbf{X}_l) \cdot \mathbf{a}^{\alpha I} - \gamma_l^\alpha)^2 \rightarrow \min \end{aligned} \quad (6.42)$$

in correspondence with (6.39) where  $\mathbf{\Gamma}^{\alpha h}$  collectively represents all  $\gamma_l^\alpha$ . The necessary condition for the solution of (6.42) then provides the basis for the determination of the coefficients  $\mathbf{a}^{\alpha I}$

$$\frac{\partial \hat{\Pi}(\mathbf{a}^{\alpha I})}{\partial \mathbf{a}^{\alpha I}} = \underbrace{\sum_{l=1}^{n_I} [\mathbf{p}(\mathbf{X}_l) \otimes \mathbf{p}(\mathbf{X}_l)]}_{\mathbf{A}^I} \mathbf{a}^{\alpha I} - \underbrace{\sum_{l=1}^{n_I} [\mathbf{p}(\mathbf{X}_l) \gamma_l^\alpha]}_{\mathbf{b}^{\alpha I}} = 0 \quad (6.43)$$

Solving (6.43) for the unknown coefficients gives  $\mathbf{a}^{\alpha I} = [\mathbf{A}^I]^{-1} \cdot \mathbf{b}^{\alpha I}$ . Now, with the known coefficients  $\mathbf{a}^{\alpha I}$ , the smoothed nodal projections  $\bar{\mathbf{\Gamma}}^{\alpha I}$  for node  $I$  are finally obtained by evaluation of (6.41) at  $\mathbf{X}_I$

$$\bar{\mathbf{\Gamma}}^{\alpha I} = \tilde{\Gamma}^{\alpha I}(\mathbf{X}_I) = \mathbf{p}(\mathbf{X}_I) \cdot \mathbf{a}^{\alpha I} \quad (6.44)$$

As pointed out by (ZIENKIEWICZ & ZHU [159]) it is noteworthy that

- (i)  $\mathbf{p}$  and especially also  $\mathbf{A}^I$  need to be evaluated only once for each element patch and remain unchanged for the computation of the coefficients  $\mathbf{a}^{\alpha I}$  for each component  $\alpha$  according to (6.43)
- (ii) it is important to avoid an ill-conditioning of the matrix  $\mathbf{A}^I$  by using normalized coordinates  $\tilde{\mathbf{X}}$ , e.g.  $\tilde{X}_l = X_l - \frac{1}{n_I} \sum_{i=1}^{n_I} X_i$  and  $\tilde{Y}_l = Y_l - \frac{1}{n_I} \sum_{i=1}^{n_I} Y_i$
- (iii) for an internal node in higher order elements it is convenient to use the average obtained from the recovery processes of all patches containing this node
- (iv) if the polynomial is of the same order  $p$  as the shape functions of the finite element interpolation, the ideal convergence properties at the sampling points also carry over to the smoothed solution  $\tilde{\mathbf{\Gamma}}^\alpha$ . Thus  $p$  should be picked in accordance with order of the finite element approximation.



## 7. Numerical Examples for Gradient Crystal Plasticity

In this chapter the modeling capabilities of the previously developed approach to gradient crystal plasticity and the corresponding algorithmic formulations will be tested for several example problems.

### 7.1. Numerical Example for Fully Rate Dependent Gradient Plasticity

As a first example the developments for the case of fully rate dependent crystal plasticity will be tested for the model problem of constraint simple shear of an infinitely wide strip under plane strain conditions.

**7.1.1. Constrained Shear of a Strip in Double Slip.** This model problem has recently been considered by many authors. For example SHU ET AL. [136] employed this example in order to compare the predictions of discrete dislocation simulations of VAN DER GIESSEN & NEEDLEMAN [154] with the ones of the nonlocal plasticity theory by FLECK & HUTCHINSON [40]. Furthermore, this model problem has been used to validate phenomenological gradient crystal plasticity formulations in SVENDSEN & REESE [146] and LIEBE [85] or dislocation density based gradient crystal plasticity models in EVERS ET AL. [38] and ARSENLIS ET AL. [8].

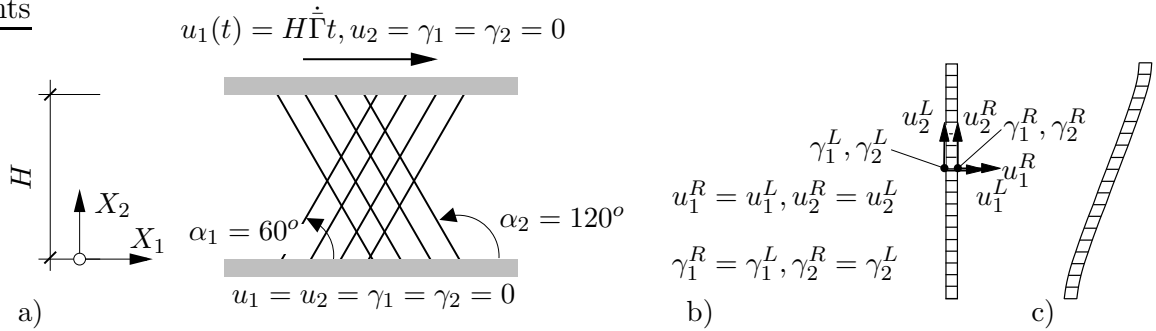


**Figure 7.1:** Simple shear of an infinitely wide strip. a) Geometry, boundary conditions and slip system orientations, b) exemplary finite element discretization and periodic boundary conditions, c) deformed configuration for  $H = 20\mu\text{m}$  at  $\bar{\Gamma} = 3\%$  (scaled by a factor 10).

The geometry of this boundary value problem is depicted in figure 7.1 a). Thereby an infinitely wide strip (represented by periodic boundary conditions) of varying height  $H$  is subjected to simple shear under plane strain conditions with a shear rate of  $\dot{\bar{\Gamma}} = 0.006 \text{ s}^{-1}$ . The plastic deformation, i.e. the plastic slips  $\Gamma^\alpha$ , are constrained to zero along the horizontal boundaries at the top and the bottom of the strip. Thus the boundary conditions are specified as follows (with time  $t$ )

$$\begin{aligned} u_1 &= 0, & u_2 &= 0, & \Gamma^\alpha &= 0 & \text{along } X_2 &= 0, \\ u_1(t) &= H\dot{\bar{\Gamma}}t, & u_2 &= 0, & \Gamma^\alpha &= 0 & \text{along } X_2 &= H \end{aligned} \quad (7.1)$$

The „micro-clamped” boundary conditions for the plastic deformations invoke an inhomogeneous plastic deformation state with corresponding strain gradients, see figure 7.1 c). This model problem is believed to be representative of the conditions found at the grain boundaries in polycrystals, the surface of a thin film or the interfaces in a composite material. In accordance with the literature, the strip consists of a homogeneous single crystalline material. Thereby the following investigations are restricted to *Asaro’s*

**Table 7.1:** Material parameters of copper adopted in constrained shear test.

Bulk modulus	$\kappa$	=	141176.0	MPa
Shear modulus	$\mu$	=	54135.0	MPa
Burgers vector length	$b$	=	0.256	nm
Reference plastic strain rate	$\dot{\gamma}_0$	=	0.001	s <sup>-1</sup>
Rate sensitivity exponent	$m$	=	0.12	—
Strength parameter	$c$	=	0.3	—
Initial SSD density	$\rho_{\text{SSD}}^{0,\alpha}$	=	$5.0 \times 10^{12}$	[m <sup>-2</sup> ]
Saturated SSD density	$\rho_{\text{SSD}}^{\text{sat}}$	=	$1.0 \times 10^{15}$	[m <sup>-2</sup> ]
Saturation slip strain	$\gamma^{\text{sat}}$	=	1.0	—

*planar double slip model* (ASARO [9]) where two in-plane slip systems with a relative orientation of  $60^\circ$  are considered. The size-effects for this arrangement are much more evident than for a single slip system which has as well been investigated in the present context but is not reported on in the sequel. As visualized in figure 7.1 a) the two slip systems are oriented initially at  $\alpha_1 = 60^\circ$  and  $\alpha_2 = 120^\circ$ , respectively. Furthermore the material is considered to be elastically isotropic with the material parameters specified in table 7.1 and representative of single crystalline copper. Thereby, in accordance with the literature, only self hardening is considered, i.e.  $G^{\alpha\beta} = \delta^{\alpha\beta}$ . The height  $H$  of the strip is varied between  $20\mu\text{m}$  and  $1000\mu\text{m}$  where the response for  $H = 1000\mu\text{m}$  turns out to be almost identical with the purely local one (i.e. no consideration of plastic slip gradients). For each height of the strip  $H$  finite element discretizations of  $1 \times 20$ ,  $1 \times 50$ ,  $1 \times 80$  and  $1 \times 100$  4-noded quadratic elements are investigated (quadrilateral isoparametric elements with bilinear shape functions for the displacements and the plastic slips and an enhanced formulation for the displacement part, see section 6.1.4 and section D in the Appendix for details). Unless stated otherwise the results presented in the following correspond to the discretization with  $1 \times 50$  elements. However, for the loading conditions, the material parameters and the dicretizations investigated in the present context, no mesh size dependence is observed, see also below.

To start the discussion of the results consider first the normalized shear profiles  $F_{12}/\bar{\Gamma}$

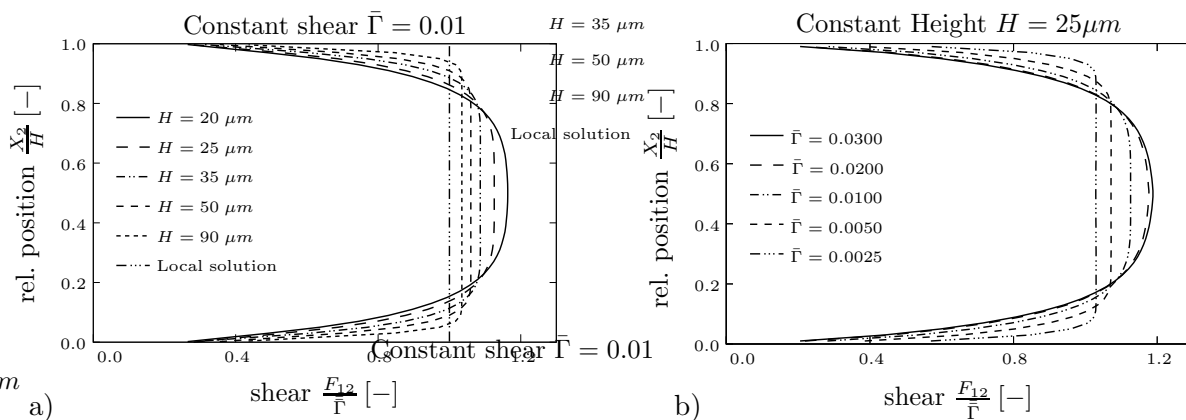


**Figure 7.2:** Boundary layer in constraint simple shear. a) Normalized shear profile for various heights  $H$  at a constant shear of  $\bar{\Gamma} = 0.01$ , b) Evolution of the shear profile with increasing shear deformation  $\bar{\Gamma}$  for a constant strip height of  $H = 25\mu\text{m}$ .

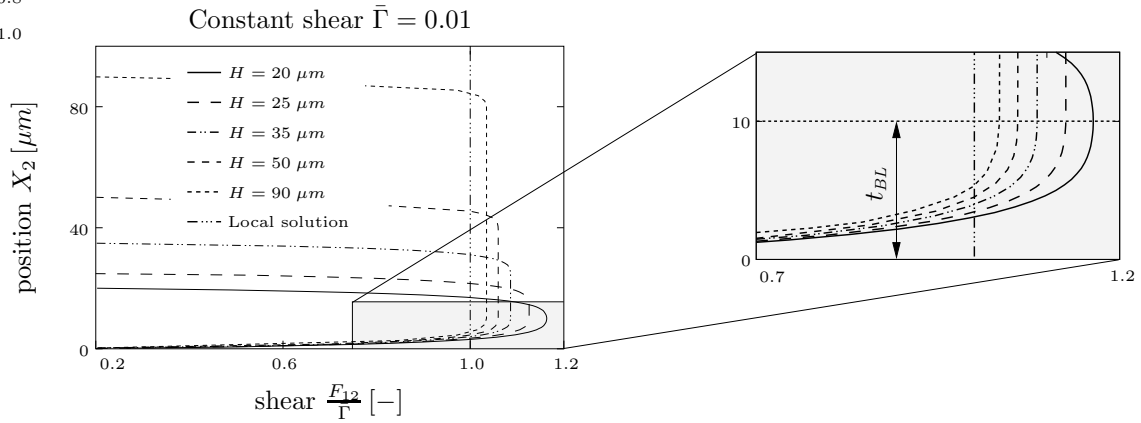


**Figure 7.3:** Absolute boundary layer thickness  $t_{BL}$  at an applied shear of  $\bar{\Gamma} = 0.01$ .

along the relative strip height  $X_2/H$  in figure 7.2. Clearly in the case of a homogeneous deformation without any gradient influence the shear deformation gradient  $F_{12}$  is constant and equivalent to the overall applied macroscopic shear  $\bar{\Gamma}$  throughout the strip height, i.e.  $F_{12}/\bar{\Gamma} = 1.0$ , see figure 7.2 a). This is the case for a purely local theory or equivalently a strip of infinite height,  $H \rightarrow \infty$ . Now, if strips of decreasing height  $H$  are considered the deformation inhomogeneity increases due to the growing influence of the boundary conditions for the plastic deformation at  $X_2 = 0$  and  $X_2 = H$ . Consequently  $F_{12}$  is a function of  $X_2$  and pronounced boundary layers with reduced shear deformation develop. This is visualized in figure 7.2 a) where the same normalized shear profile  $F_{12}/\bar{\Gamma}$  is plotted for various heights  $H$  and an applied macroscopic shear of  $\bar{\Gamma} = 0.01$ . With decreasing height the boundary layer develops over an increasing fraction of the strip height. Thereby the *absolute boundary layer thickness*  $t_{BL}$  is the same for all strip heights  $H$  and obtains a value of approximately  $t_{BL} \approx 10\mu m$  at an overall deformation level of  $\bar{\Gamma} = 0.01$ . This is obvious from the enlarged part of the diagram in figure 7.3 where the normalized shear profile is plotted with respect to the absolute strip height  $H$  at an applied macroscopic shear  $\bar{\Gamma} = 0.01$ . Consequently, for a strip height below  $20\mu m$  the boundary layer extends over the entire strip height.

Now if the deformation level is increased, the absolute boundary layer thickness increases as well until it extends over the full (more precisely 1/2 the) strip height. This is visualized

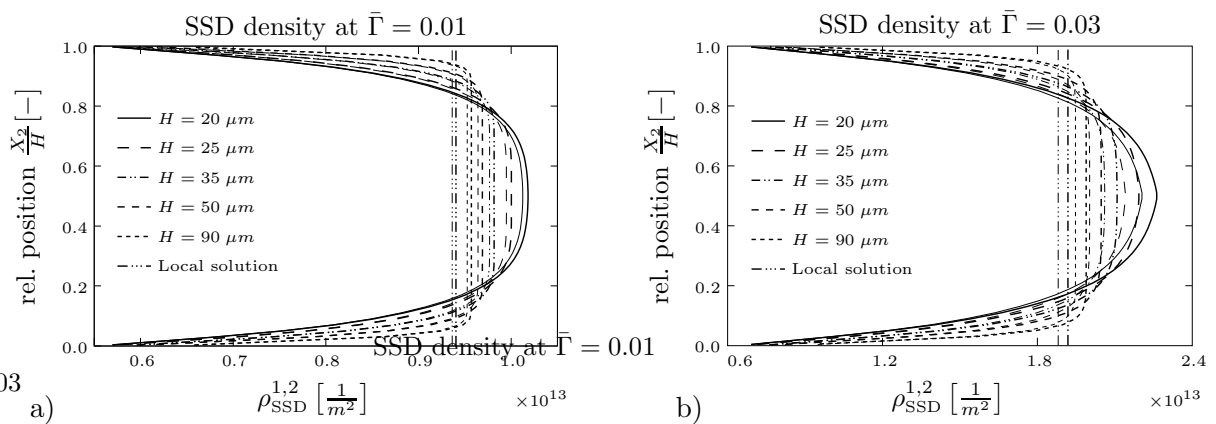


**Figure 7.4:** Distribution of the SSD density  $\rho_{SSD}$  along the dimensionless strip height. Thick lines indicate the density  $\rho_{SSD}^1$  on system 1 and thin lines the density  $\rho_{SSD}^2$  on system 2, respectively. a)  $\rho_{SSD}$  profile at a constant applied shear  $\bar{\Gamma} = 0.01$  and b)  $\bar{\Gamma} = 0.03$ .

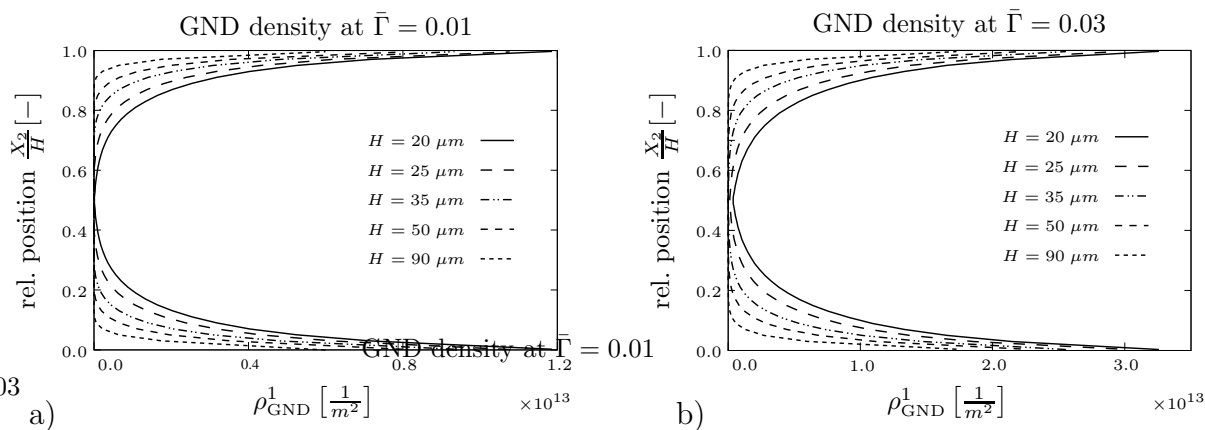


**Figure 7.5:** Distribution of the GND density  $\rho_{\text{GND}}^1$  of system 1 along the dimensionless strip height. The GND density distribution of system 2 is essentially identical and thus not visualized. a)  $\rho_{\text{GND}}^1$  profile at a constant applied shear of  $\bar{\Gamma} = 0.01$  and b) at  $\bar{\Gamma} = 0.03$ .

in figure 7.2 b) for a constant strip height of  $H = 25\mu\text{m}$  and an increase of the deformation level up to  $\bar{\Gamma} = 0.03$ . A plot in analogy to figure 7.1 at the final deformation level of  $\bar{\Gamma} = 0.03$  reveals an absolute boundary layer thickness of approximately  $t_{BL} = 14\mu\text{m}$  at this deformation level. Such a thickening of the boundary layer with increasing deformation is also consistent with the findings of SHU ET AL. [136], SVENDSEN & REESE [146] and EVERS ET AL. [38] but is not observed in an analysis which employs the nonlocal strain gradient crystal plasticity formulation of SHU & FLECK [135].

Turning next to the dislocation densities, consider first the distribution of the statistically stored dislocation density  $\rho_{\text{SSD}}$  along the dimensionless strip height  $X_2/H$  in figure 7.4. Clearly the SSD density in any material point is directly related to the shear deformation in this point which is also revealed by comparing the  $\rho_{\text{SSD}}$  profile in figure 7.4 a) with the shear profile in figure 7.2 a). Since the plastic slip is constrained at the horizontal boundaries at  $X_2 = 0$  and  $X_2 = H$ , the SSD density remains constant and equal to the initial density  $\rho_{\text{SSD}}^\alpha = \rho_{\text{SSD}}^{0,\alpha}$  at these boundaries throughout the deformation process. With increasing deformation the SSD density grows as well towards the middle of the strip (see figure 7.4 b)) which results in work hardening in the overall stress response, see below.

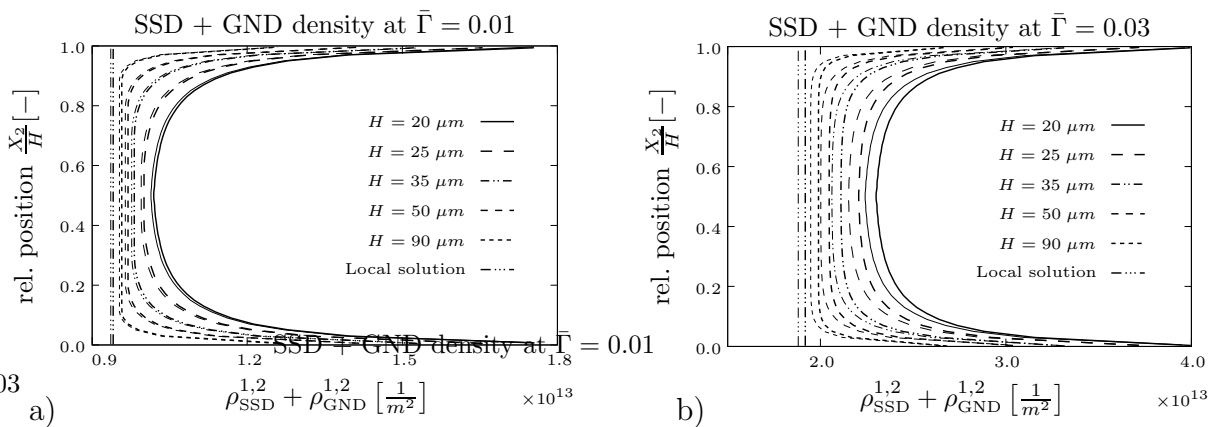


**Figure 7.6:** Combined SSD and GND density distributions. Thick lines indicate the density distributions on system 1 and thin lines on system 2, respectively. a)  $\rho_{\text{SSD}}^\alpha + \rho_{\text{GND}}^\alpha$  for an applied macroscopic shear of  $\bar{\Gamma} = 0.01$  and b)  $\bar{\Gamma} = 0.03$ .

As explained in detail in the preceding chapters deformation inhomogeneities, or equivalently the resulting slip gradients, induce the storage of geometrically necessary dislocations. Thus according to the previous observations a significant storage of such dislocations is to be expected in connection with the strongly inhomogeneous plastic deformations occurring in the present model problem. The visualization of the GND density profiles in figures 7.5 a) and b) reveals the storage of a significant GND density within the boundary layers. Thereby the density increases with the slip gradients towards the horizontal boundaries of the strip. This is in agreement with the findings of the discrete dislocation simulations in SHU ET AL. [136]. For sufficiently small strip heights with strong deformation inhomogeneities the maximum GND density exceeds the SSD density and thus induces additional hardening. In contrast to the SSD density, the GND density concentrates near the horizontal boundaries at  $X_2 = 0$  and  $X_2 = H$  and vanishes towards the middle of the strip where the deformations are (almost) homogeneous.

The combined profiles of the SSD and GND densities are visualized in figures 7.6 a) and b) again for the applied shear levels  $\bar{\Gamma} = 0.01$  and  $\bar{\Gamma} = 0.03$ . Obviously the maximum values of the GND densities significantly exceed the corresponding maxima of the SSD densities and thus govern the shape of the combined SSD+GND density profiles. This is in contrast to the results of EVERS ET AL. [38] where the SSD density exceeds the GND density by one order of magnitude and thus the SSD density governs the overall dislocation density profile. However, the results of the present analysis are for the respective strip sizes qualitatively as well as quantitatively in good agreement with the theoretical observations of ASHBY [12] and FLECK ET AL [42] documented in figure 5.3. The present relation between the SSD densities and the GND densities clearly explains the size effect which is observed in the overall stress response and is discussed below. The specimens of smaller size induce stronger deformation inhomogeneities and thus higher GND densities which result in increased hardening and thus a size effect.

Finally, the size dependence of the overall stress response will be discussed in detail. The macroscopic shear stress  $\bar{\tau}_{12}$  is plotted over the applied macroscopic shear  $\bar{\Gamma}$  in figure 7.7 a) for various strip heights  $H$ . Since the plastic slip remains zero throughout the elastic range and no further gradient effects are included in the description of the elastic material behavior, the response up to the initial yield point is identical for all strip heights analyzed. With the onset of plastic deformation a significant size effect is observable

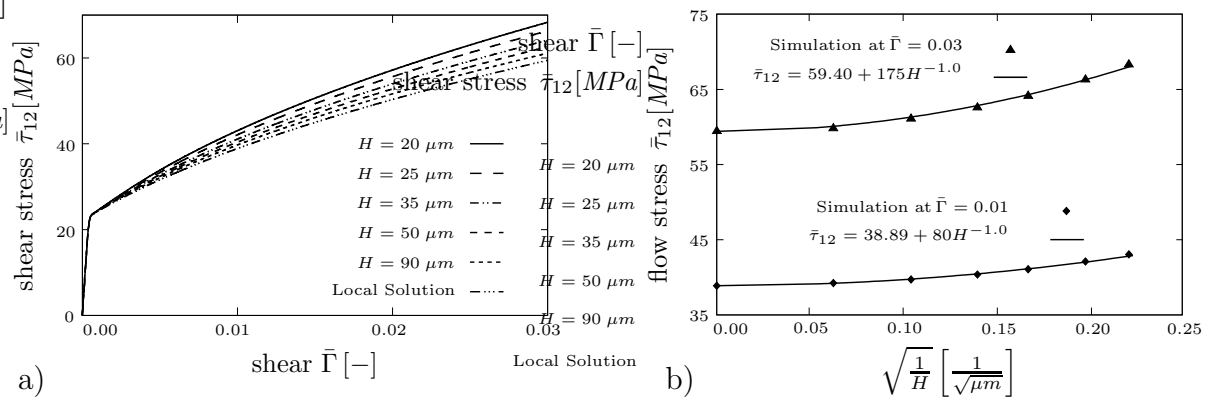


**Figure 7.7:** Size dependence of the macroscopic stress response. a) Shear stress  $\bar{\tau}_{12}$  vs. applied shear  $\bar{\Gamma}$  for various heights  $H$ . b) Flow ( $\hat{=}$  shear) stress vs. Hall-Petch ratio  $\sqrt{1/H}$  in current simulation (dots) and extended Hall-Petch fit (solid lines) at  $\bar{\Gamma} = 0.01$  and  $\bar{\Gamma} = 0.03$ .

where the smaller strip heights exhibit a stiffer response. As discussed previously, this size effect is due to the higher GND densities in the smaller specimens which display stronger deformation inhomogeneities. Thereby the only length scale which enters the present model besides the specimen dimensions (here the height  $H$ ) is the Burgers vector length  $b$  which in turn is a material parameter amenable through measurement within the real material under consideration (e.g. from the literature for copper  $b = 0.256 \text{ nm}$ ). The slightly nonlinear stress response is due to the chosen parameters for the SSD evolution.

As discussed in connection with relation (5.4) a size dependence of the yield strength is generally described through the so-called *Hall-Petch relation*. Since the goal of this work is to describe size effects due to developing plastic deformation inhomogeneities, the initial yield strength remains unaffected by the present formulation. Consequently the size effects observed in figure 7.7 a) will now be analyzed in the context of an *extended Hall-Petch relation* according to equation (5.5). To this end the  $\bar{\tau}_{12}$  components of the macroscopic stress responses are interpreted as macroscopic deformation dependent *flow stresses*. These flow stresses are plotted for each strip height over the corresponding *Hall-Petch ratios*  $1/\sqrt{H}$  as points in figure 7.7 b) for the macroscopic shear levels  $\bar{\Gamma} = 0.01$  and  $\bar{\Gamma} = 0.03$ . Recalling the extended Hall-Petch relation (5.5), it reads in the present context

$$\bar{\tau}_{12} = \bar{\tau}_{120}(\bar{\Gamma}) + k(\bar{\Gamma})H^{-n} \quad (7.2)$$

where  $\bar{\tau}_{120}(\bar{\Gamma})$  is the macroscopic flow stress of a homogeneously deforming single crystal, i.e. a strip of infinite height  $H$ , at the macroscopic shear level  $\bar{\Gamma}$ . A fit of the extended Hall-Petch relation (7.2) to the numerically obtained values of the present example is presented in figure 7.7 b) and gives at the respective shear levels the following relations

$$\begin{aligned} \bar{\Gamma} = 0.01 : \bar{\tau}_{12} &= 38.89 + 80H^{-1.0} \quad [MPa] \\ \bar{\Gamma} = 0.03 : \bar{\tau}_{12} &= 59.40 + 175H^{-1.0} \quad [MPa] \end{aligned} \quad (7.3)$$

where  $H$  has to be specified in  $\mu\text{m}$ . Thus the corresponding *Hall-Petch exponent* is  $n = 1.0$  and the *Hall-Petch slope* increases from  $k(\bar{\Gamma} = 0.01) = 80$  to  $k(\bar{\Gamma} = 0.03) = 175$  in the present analysis. Qualitatively similar, slightly nonlinear, Hall-Petch relations have also been observed for the predictions obtained through the nonlocal theory of SHU & FLECK [135] in SHU ET AL. [136] and through the dislocation density based gradient plasticity theory of EVERS ET AL. [38].

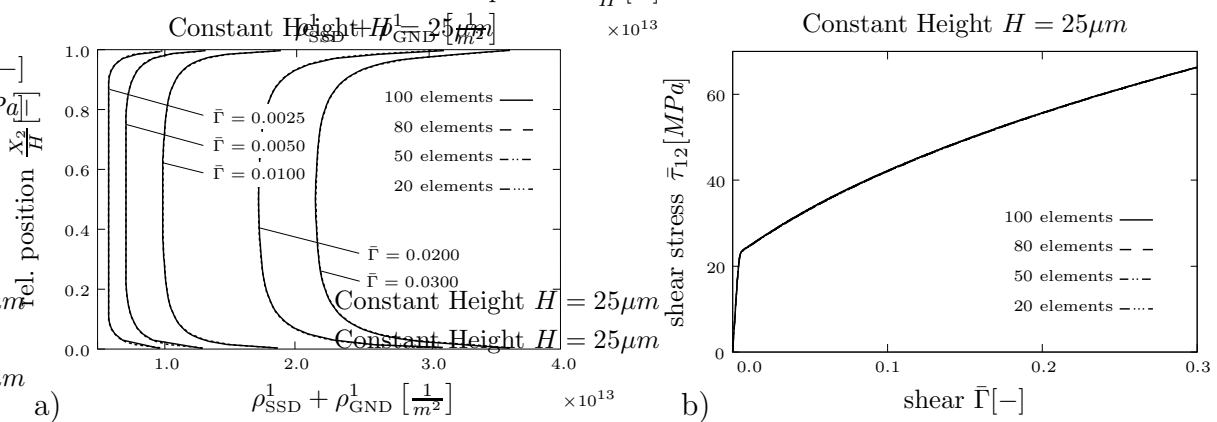


**Figure 7.8:** Mesh independence of the results for  $H = 25\mu\text{m}$ . a) Objectivity with respect to the discretization for combined SSD+GND density evolution of slip system 1, b) mesh independence of shear stress versus applied shear response.

Finally the mesh size dependence will be analyzed. In this respect the results for the combined  $\rho_{\text{SSD}}^1 + \rho_{\text{GND}}^1$  evolution of slip system 1 obtained for a discretization with  $1 \times 20, 1 \times 50, 1 \times 80$  and with  $1 \times 100$  elements are first compared in figure 7.8 a). Obviously the results obtained for all discretizations are almost identical for all analyzed deformation levels  $\bar{\Gamma}$ . The same observation is made for the macroscopic stress response in figure 7.8 b). Therein the results for the macroscopic shear stress response  $\bar{\tau}_{12}$  of a strip of height  $H = 25\mu\text{m}$  are compared again for discretizations with  $1 \times 20, 1 \times 50, 1 \times 80$  and  $1 \times 100$  elements. The resulting shear stress versus applied shear curves are identical. This holds also for the other heights  $H$  analyzed in this example. Thus it can be concluded that the results presented previously are independent of the chosen discretization.

## 7.2. Numerical Examples for Gradient Crystal Viscoplasticity

After demonstrating the performance of the algorithmic developments for the fully rate dependent setting in the previous section, the corresponding formulations for the case of gradient crystal (visco-)plasticity will be tested next. This includes also the fully rate independent setting.

### 7.2.1. Comparison of Global and Standard Local Plasticity Formulation.

In order to validate the global formulation of crystal (visco-)plasticity as outlined in section 6.2 and its numerical implementation, a comparison with results obtained by the standard local formulation will be presented for two tests in the following. Thereby the considerations are first restricted to the purely local setting, i.e. no slip gradients are taken into account, and to the fully rate independent case. On the theoretical side a comparison between the global and the standard local crystal plasticity formulations has been given in section 6.2.6.

**7.2.1.1. Comparison for a Homogeneous Simple Shear Test.** First both formulations are tested for a homogeneous model problem. Therefore a homogeneous simple shear test under plane strain conditions is performed for both the global as well as the standard local formulation. The general setup of this simple problem is visualized in figure 7.9 a). Thereby considerations in this and the following example are restricted to single slip with an initial slip system orientation  $\alpha$ . Combinations of two or more slip systems will be considered in the subsequent examples. The material parameters are again chosen according to table 7.1. However, since no rate dependence is included in the present analysis, the

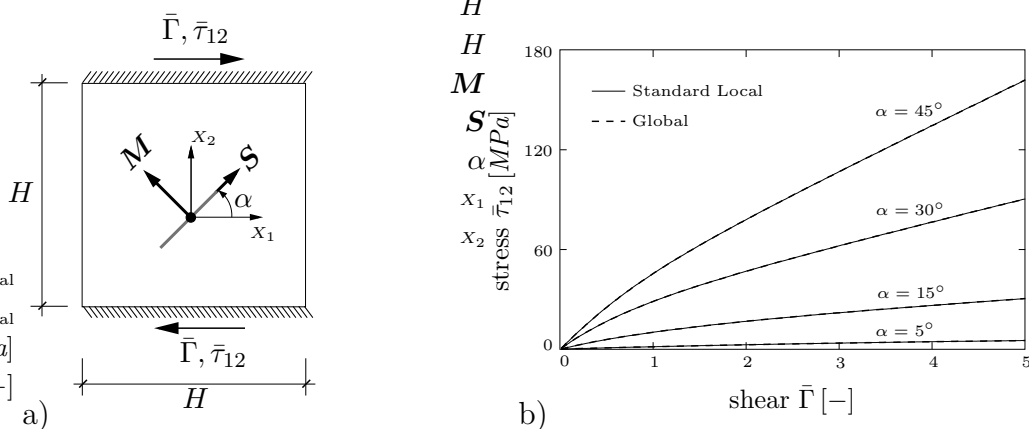


**Figure 7.9:** Homogeneous simple shear. a) test setup, b) evolution of Kirchhoff stress  $\bar{\tau}_{12}$ .

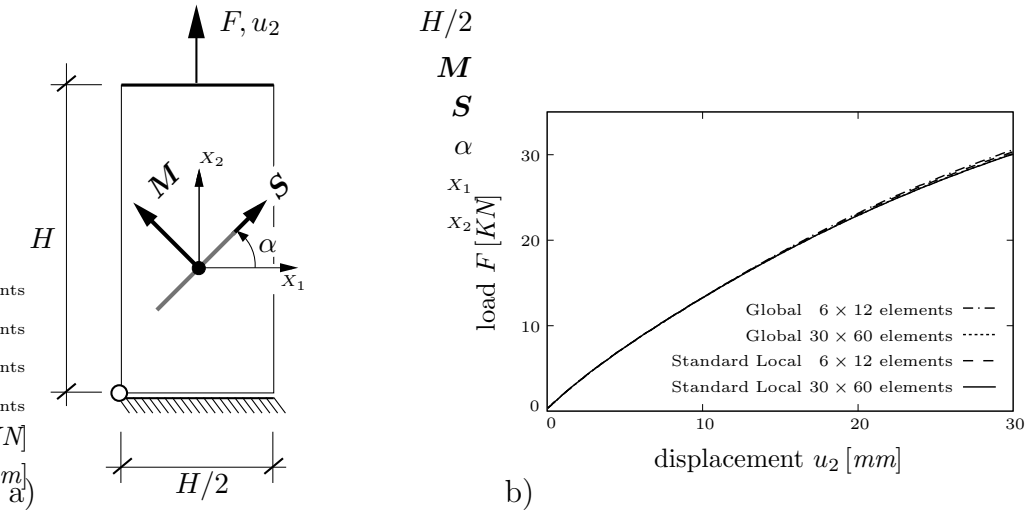


**Figure 7.10:** Tension test. a) test setup, b) Load displacement curves.

corresponding rate sensitivity parameters  $\dot{\gamma}_0$  and  $m$  are not used in the present context. Within the numerical treatment a discretization of  $5 \times 5$  four-noded elements has been chosen where again an enhanced formulation for the displacements has been employed in both the global as well as the standard local formulation. The simple shear test is performed for varying slip system angles of  $\alpha = 5^\circ, 15^\circ, 30^\circ$  and  $\alpha = 45^\circ$  and up to a total shear deformation of  $\bar{\Gamma} = 5$  [–], i.e.  $u_1 = 5H$ . The resulting macroscopic shear stress  $\bar{\tau}_{12}$  versus macroscopic shear  $\bar{\Gamma}$  responses are depicted in figure 7.9 b) for all investigated angles  $\alpha$  and both the global as well as the standard local formulation. Obviously the results for both formulations coincide. As to be expected, the stress as well as the plastic slip distributions are in both cases absolutely homogeneous throughout the solution domain.

**7.2.1.2. Comparison for an Inhomogeneous Tension Test.** As a second example, the results of both formulations are now compared for an inhomogeneous tension test. The basic test setup is visualized in figure 7.10 a). Again a single slip system with an initial orientation of  $\alpha = 45^\circ$  is considered under plane strain conditions. The specimen dimensions are chosen to be  $16$  [mm]  $\times$   $32$  [mm] but are of no further interest since only

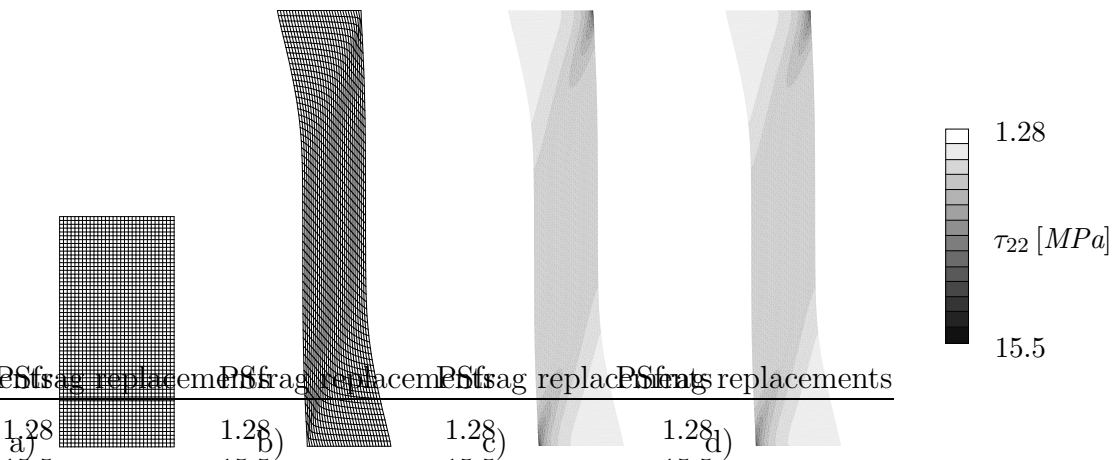


**Figure 7.11:** Tension test. a) discretization with  $30 \times 60$  elements, b) deformed mesh for  $u_2 = 30$  mm.  $\tau_{22}$  distributions for  $u_2 = 30$  mm, c) global and d) standard local formulation.

a purely local description without any gradient influence is chosen for now. Furthermore in the present analysis a simple linear hardening response is assumed with a hardening modulus of  $h = 1000 [MPa]$  and an initial slip resistance  $\tau_{r0} = 10 [MPa]$ . Bulk and shear modulus are again given by  $\kappa = 141176.0 [MPa]$  and  $54135.0 [MPa]$ . The specimen is elongated by  $30[mm]$  in  $X_2$  direction which results in the load displacement relations shown in figure 7.10 b). Thereby two discretizations have been investigated. A rather coarse discretization with  $6 \times 12$  four-noded elements and a finer discretization with  $30 \times 60$  elements as visualized in figure 7.11 a). Again an enhanced strain formulation is employed in both the global as well as the standard local formulation. As can be seen in figure 7.10 b) the description with both approaches results again in the same macroscopic response for each chosen discretization. Both formulations display a negligible mesh dependence where the coarser discretizations result in a slightly stiffer response. Also, the plastic slip and stress distributions obtained through either formulation are almost identical which is visualized exemplary for the  $\tau_{22}$  stress component in figures 7.11 c) and d).

**7.2.2. Shear Test for a Composite Material.** In the previous two examples the global formulation of crystal (visco-)plasticity was validated within a *purely local* context. The goal in the following examples is to employ this approach in the context of the *gradient* crystal (visco-)plasticity formulation developed in section 6.2 in order to describe *gradient* or *size effects* in *plastically inhomogeneously deforming crystals*. Thereby the *extended local* formulations developed in section 6.3 will also be used in view of an efficient inclusion of these effects. The extended local approaches are validated by comparison with the global formulation of gradient crystal (visco-)plasticity.

As a first example, macroscopic shearing of a composite material will be analyzed. This model problem was introduced in the context of discrete dislocation simulations by CLEVERINGA ET AL. [27]. Thereby a two-dimensional model composite with stiff elastic inclusions in a single crystalline matrix is subjected to macroscopic simple shear under plain strain conditions. The crystalline material is characterized by a single slip system which is horizontally aligned and parallel to the overall shear direction, see figure 7.12 for a visualization. The periodic composite material is modeled by one unit cell of height  $H$  and width  $W = \sqrt{3}H$  which contains in total two particles of size  $0.3H \times 0.6H$ , one particle being located in the center of the cell. According to CLEVERINGA ET AL. [27]

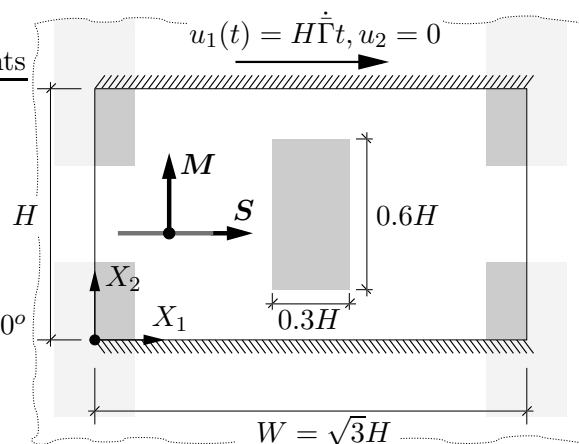


**Figure 7.12:** Unit cell of a model composite material investigated with current gradient plasticity model and by CLEVERINGA ET AL. [27]. Slip direction  $\mathbf{S}$ , slip plane normal  $\mathbf{M}$ .

the vertical displacements are constrained along the horizontal boundaries of the unit cell which results in the following prescribed boundary conditions

$$u_1(t) = H\dot{\bar{\Gamma}}t, \quad u_2(t) = 0, \quad \text{along } X_2 = 0 \text{ and } X_2 = H \quad (7.4)$$

where  $\dot{\bar{\Gamma}}$  is the applied macroscopic shear rate. Periodic displacement boundary conditions are imposed along the vertical boundaries at  $X_1 = 0$  and  $X_1 = \sqrt{3}H$ . The geometry and the boundary conditions represent the ones specified by CLEVERINGA ET AL. [27] for the so-called morphology (iii) (except that their particle height is  $0.588H$  instead of  $0.6H$ ) which allows for a comparison with their results. Thus a more reasonable implementation of periodic boundary conditions (instead of  $u_2(t) = 0$ ) also along the horizontal boundaries at  $X_2 = 0$  and  $X_2 = H$  is not adopted here since this induces a significantly softer overall response. The overall stress strain response is described in terms of the average shear stress  $\bar{\sigma}_{12}$  required to sustain the deformation. This stress is computed for example along the horizontal boundary at  $X_2 = H$  through the discrete analogon to

$$\bar{\tau}_{12} = \frac{1}{W} \int_0^W \tau_{12}(X_1, X_2 = H) dX_1 \quad (7.5)$$

evaluated in terms of the nodal reactions. Unless stated otherwise, a finite element discretization of  $102 \times 60$  quadrilaterals is used where again an enhanced strain formulation is employed in both the global and the extended local formulations. The unit cell is deformed up to a maximal shear deformation of  $\bar{\Gamma} = 0.01$ , see figure 7.13 for a visualization. Therein the displacements are magnified by a factor 10 and additionally the periodic boundary conditions for the plastic slips are visualized for the global formulation. Note that for a convenient implementation within the global formulation, two slip parameters  $\gamma_+$  and  $\gamma_-$  are introduced at each node, one for the positive ( $+\mathbf{S}$ ) and one for the negative ( $-\mathbf{S}$ ) slip direction.

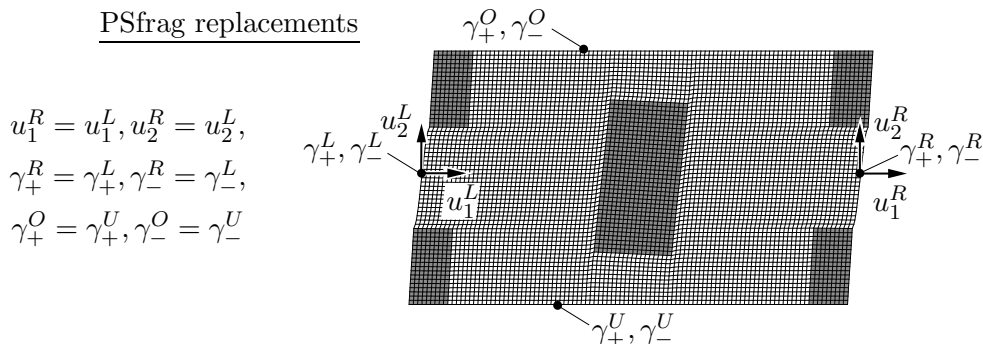


**Figure 7.13:** Finite element discretization of the unit cell using  $102 \times 60$  quadrilaterals, deformed configuration and periodic BCs (the displacements are magnified by a factor 10).

**7.2.2.1. Comparison of Global and Extended Local Formulations.** To start, the results obtained through a simulation employing the global formulation of gradient crystal plasticity are compared with the ones obtained through the extended local formulations of gradient crystal plasticity. Thereby the results obtained through the extended local formulations are almost identical whether the smoothing algorithm is based on a  $L_2$ -projection (see section 6.3.1) or a patch recovery (see section 6.3.2). Consequently, the following only reports on the results obtained through the global formulation and through the extended local formulation combined with a patch recovery (denoted as *Local+PR* in

**Table 7.2:** Material parameters for aluminum matrix with elastic inclusions.

<u>Matrix</u>			
Bulk modulus	$\kappa_M$	=	68600.0 MPa
Shear modulus	$\mu_M$	=	26300.0 MPa
Burgers vector length	$b$	=	0.286 nm
Strength parameter	$c$	=	0.3
Initial SSD density	$\rho_{\text{SSD}}^0$	=	$5.0 \times 10^{12}$ [ $m^{-2}$ ]
Saturated SSD density	$\rho_{\text{SSD}}^{\text{sat}}$	=	$1.0 \times 10^{15}$ [ $m^{-2}$ ]
Saturation slip strain	$\gamma^{\text{sat}}$	=	1.0
<u>Inclusions</u>			
Bulk modulus	$\kappa_I$	=	227300.0 MPa
Shear modulus	$\mu_I$	=	192300.0 MPa

the sequel). Besides the periodic boundary conditions visualized in figure 7.13, the plastic slips are constrained to zero along the particle-matrix interfaces within the global solution procedure. This is accounted for within the smoothing algorithm of the extended local formulation as well. Thereby the interpolated slip variables are also enforced to vanish along these interfaces.

The bulk and shear moduli are adopted from CLEVERINGA ET AL.[27] and BITTENCOURT ET AL.[21] and are representative of an aluminum matrix with silicon-carbide particles. The corresponding Burgers vector for aluminum is  $b = 0.286$  [nm]. Thus the only parameters which remain to be chosen are the saturation slip strain  $\gamma^{\text{sat}}$  and the initial and the saturation SSD densities  $\rho_{\text{SSD}}^0$  and  $\rho_{\text{SSD}}^{\text{sat}}$ . The material parameters adopted in this preliminary comparative analysis are summarized in table 7.2.

Considering first a unit cell of infinite height  $H$ , the comparison of the slip contours in figure 7.14 shows a reasonable agreement. In both cases the plastic slip concentrates in bands near the particle-matrix interfaces. However, the plastic slip localizes in sharper bands within the local formulation especially in the horizontal bands between the particles (Note that for  $H \rightarrow \infty$  slip gradients do not play any role).

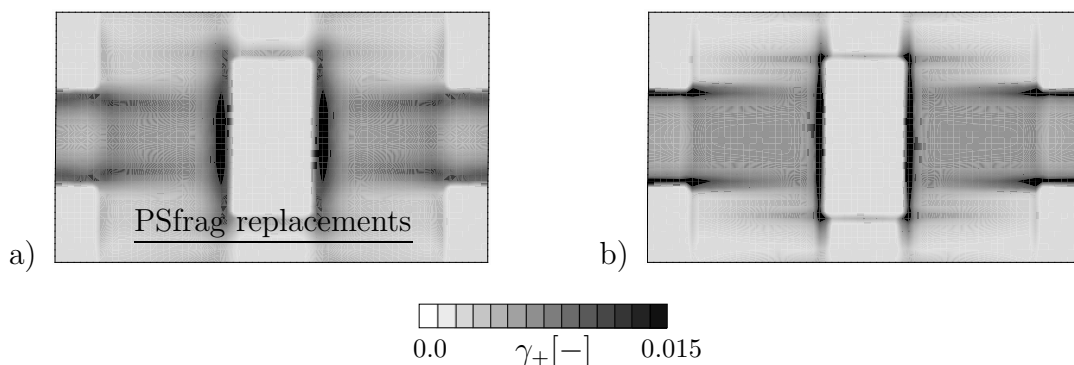


**Figure 7.14:** Contours of plastic slip  $\gamma_+$  at macroscopic shear level  $\bar{\Gamma} = 0.01$  and for  $H \rightarrow \infty$ . Slip contour obtained through a) global formulation and b) extended local formulation.

Turning next to the GND density contours for  $H = 8\mu m$  in figure 7.15 shows a good qualitative and quantitative agreement. According to the theoretical developments in chapter

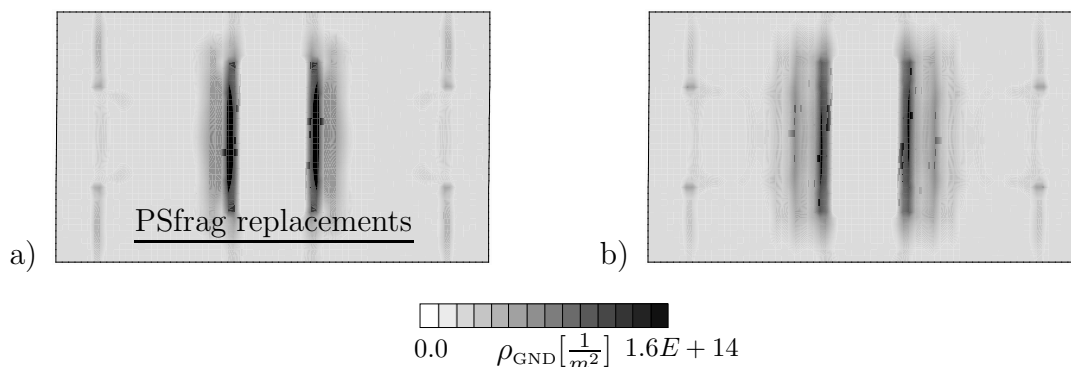


**Figure 7.15:** Contours of GND density  $\rho_{\text{GND}}$  at  $\bar{\Gamma} = 0.01$  and for  $H = 8\mu\text{m}$ . Contour obtained through a) global and b) extended local formulation of gradient crystal plasticity.

5, slip gradients perpendicular to the slip plane do not induce a storage of geometrically necessary dislocations which is also obvious from figure 7.15. Comparing the results of figure 7.15 with the microstress distributions in BITTENCOURT ET AL.[21] also shows a good qualitative agreement.

In view of a more precise comparison of the results for the slip and GND density distributions, a horizontal cut at  $X_2 = H/2$  through the respective contours at a macroscopic shear level of  $\bar{\Gamma} = 0.004$  is visualized in figure 7.16. The overall agreement of the results of both formulations is rather good, especially in regions of smooth gradient distributions. The localization of the plastic slip is however slightly more pronounced in the extended local formulation, see figure 7.16 a). This in turn results in higher slip gradients and thus increased peak values of the GND density, see figure 7.16 b).

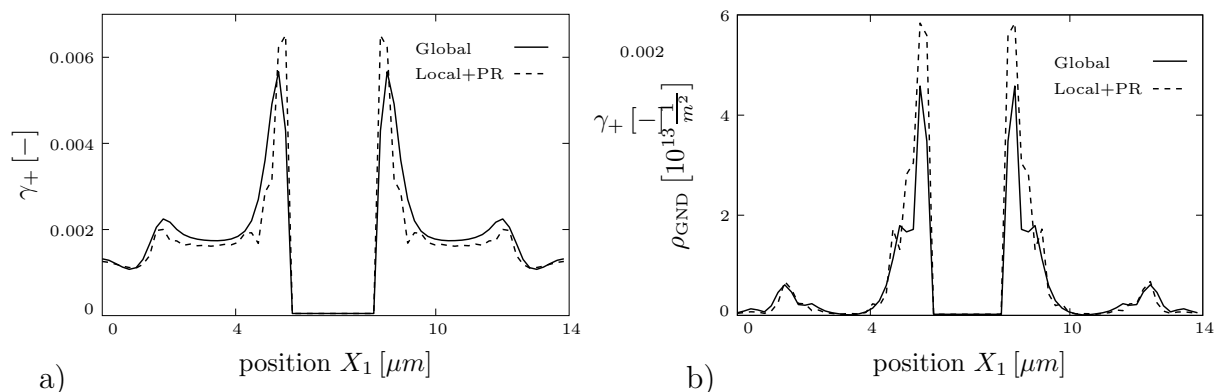


**Figure 7.16:** Cross sections through the slip and GND density contours at  $X_2 = H/2$  and  $\bar{\Gamma} = 0.004$  for  $H = 8\mu\text{m}$ . Comparison of a) slip profiles  $\gamma_+$  and b)  $\rho_{\text{GND}}$  profiles obtained through global and extended local (Local+PR) formulation of gradient crystal plasticity.

The overall response of the composite material in terms of macroscopic shear stress  $\bar{\sigma}_{12}$  versus macroscopic shear  $\bar{\Gamma}$  is given in figure 7.17 a). Obviously the responses obtained through both formulations are in quite good agreement for the local setup, i.e.  $H \rightarrow \infty$ , where the slip gradients are of no influence. As expected, the material response displays in both cases a significant size effect for decreasing heights  $H$  due to the plastically inhomogeneous deformations and the corresponding storage of geometrically necessary dislocations. However the size effect is more pronounced in the global formulation which shows a stiffer response as presented in figure 7.17 for a height of  $H = 8\mu\text{m}$ . This is due to

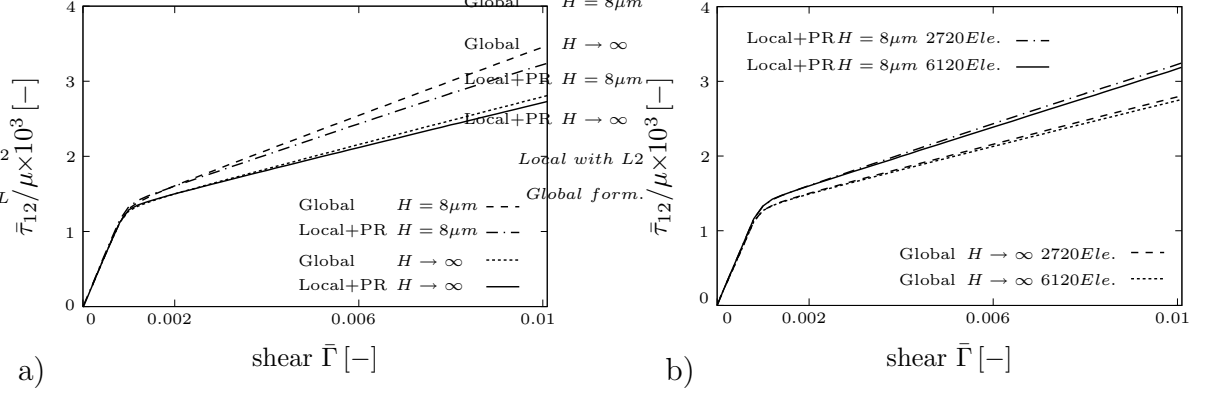


**Figure 7.17:** Overall shear stress  $\bar{\tau}_{12}$  versus shear strain  $\bar{\Gamma}$  response for the composite material. a) Size effect and comparison for the global and the extended local (Local+PR) formulation, b) mesh sensitivity for discretizations with  $68 \times 40$  and  $102 \times 60$  elements.

the sharper localization in the vicinity of the particles in the extended local formulation which reduces the overall influence of the incompatibilities. Finally, the mesh sensitivity is analyzed for both formulations in figure 7.17 b). Obviously for the chosen discretizations the mesh density has only a minor influence on the overall result.

**7.2.2.2. Comparison with Discrete Dislocation Plasticity Predictions.** In the following the extended local formulation will be employed in order to prove that the present formulations are capable of recovering the discrete dislocation plasticity predictions of CLEVERINGA ET AL.[27] and CLEVERINGA ET AL.[29]. According to the previous investigations, it is clear that these predictions can then similarly be recovered by the global formulation as well. Since the hardening relations in the present model are restricted to isotropic contributions, only monotonic loading processes are considered within this analysis. However, upon unloading kinematic effects and residual stresses are also present in the actual treatment due to the structural heterogeneities.

The bulk and shear moduli as well as the Burgers vector remain unchanged, see table 7.2, and are adopted according to the specifications in CLEVERINGA ET AL.[27] and BITTENCOURT ET AL.[21]. The only parameters to be fitted to the results of the discrete dislocation plasticity predictions are the saturation slip strain  $\gamma^{\text{sat}}$ , the initial and the saturation SSD densities  $\rho_{\text{SSD}}^0$  and  $\rho_{\text{SSD}}^{\text{sat}}$  and the unit cell height  $H$ . Thereby the first three

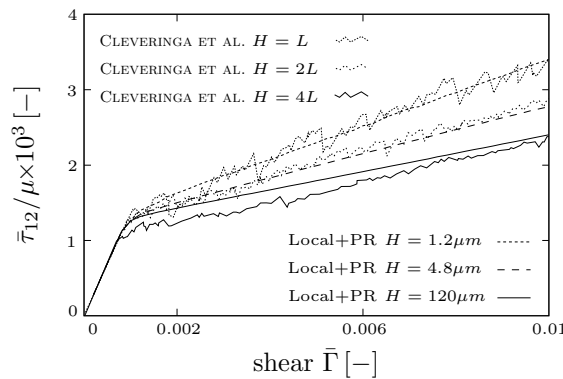


**Figure 7.18:** Comparison between discrete dislocation plasticity predictions of CLEVERINGA ET AL.[29] (where the *material length*  $L$  is chosen as  $L = 1\mu m$ ) and simulation results obtained with the extended local formulation of gradient crystal plasticity.

parameters govern the underlying SSD density evolution and thus the local response with  $H \rightarrow \infty$ . A reasonable fit to the discrete dislocation plasticity predictions is found for  $\gamma^{\text{sat}} = 5 [-]$ ,  $\rho_{\text{SSD}}^0 = 4.8 \times 10^{13} m^{-2}$  and  $\rho_{\text{SSD}}^{\text{sat}} = 1.0 \times 10^{15} m^{-2}$ . The size effect predicted by the discrete dislocation plasticity simulations is recovered in the present analysis by specifying the unit cell height  $H$  accordingly. Note that besides the Burgers vector length  $b$ , which is a material constant given by  $b = 0.286nm$  for aluminum, no further *internal* length scale is included in the present model. According to the representation in figure 7.18, the discrete dislocation plasticity predictions can be recovered by the cell sizes  $H = 120\mu m$ , which is equivalent to the solution for  $H \rightarrow \infty$  and thus corresponds to the local solution,  $H = 4.8\mu m$  and  $H = 1.2\mu m$ .

The identification obtained in figure 7.18 proves the modeling capabilities of the present formulation. However, the specific size effect predicted by the present approach differs from the one obtained through the discrete dislocation plasticity simulations. The size effect predicted by the latter formulation correlates to the cell sizes  $H = 4\mu m$ ,  $H = 2\mu m$  and  $H = 1\mu m$  which implies the relation  $4 : 2 : 1$  for the cell heights. In turn, the results of the present approach induce the relation  $100 : 4 : 1$  which induces an extended Hall-Petch relation different from the one predicted by the discrete dislocation plasticity simulations. In order to pick up the relation predicted by the reference solution, the present model might be extended by an additional *isotropic* hardening contribution which induces the following extension for the slip resistance

$$\tau_r^\alpha := c\mu b \sqrt{\sum_\beta G^{\alpha\beta} (\rho_{\text{SSD}}^\beta + \rho_{\text{GND}}^\beta)} + \mu l^2 \sqrt{\bar{\mathbf{G}}^\alpha : \bar{\mathbf{G}}^\alpha} \quad (7.6)$$

in terms of the *incompatibility measure*  $\bar{\mathbf{G}}^\alpha = \mathbf{F}^{p\alpha} \cdot \mathbf{G}^\alpha \cdot \mathbf{F}^{pT\alpha}$  and an additional *internal length scale*  $l$ . The length scale is introduced for dimensional reasons and the incompatibility measure  $\bar{G}^{\alpha\bar{M}\bar{N}}$  is obtained through a push forward of the symmetric incompatibility tensor  $G^{\alpha MN} = G^{\alpha(MN)}$  to the intermediate configuration  $\bar{\mathbf{B}}$ . Thereby  $G^{\alpha MN}$  and thus  $\bar{G}^{\alpha\bar{M}\bar{N}}$  is associated with residual stresses related to the incompatibility induced dislocation storage through the Lagrangian analogon to (5.136). Here it is convenient to employ a definition of the Cartan geometry over the Lagrangian configuration since in this case the computation of  $G^{MN}$  bases directly on gradients of  $\mathbf{F}^{p\alpha}$  and thus the slip gradients in analogy to the previous considerations. Furthermore, within this preliminary approach, *separate single slip* is assumed such that an incompatibility measure  $G^{\alpha MN}$  is computed separately for each slip system (in the present context only single slip is considered any-

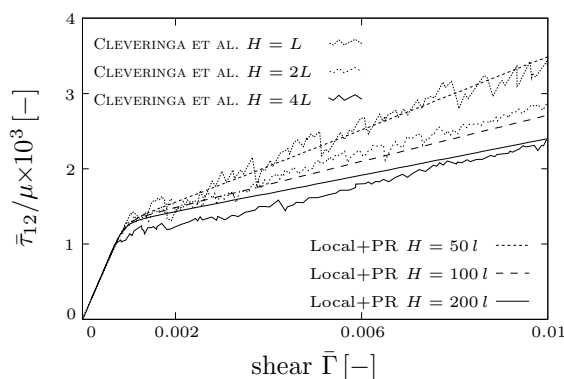


**Figure 7.19:** Comparison of the size effect predicted on basis of the extended hardening relation (7.6) with the discrete dislocation plasticity predictions of CLEVERINGA ET AL. [29].

way). As explained in detail for a definition of the Cartan geometry over the Eulerian configuration in section 5.5.4, equations (5.131)-(5.133),  $G^{\alpha MN}$  is the second order contravariant curvature contribution related to the Riemannian part  $\mathcal{G}_{BC}^A$  of the connection  $\Gamma_{BC}^A = F^{p-1A}{}_{\bar{A}} F^{p\bar{A}}{}_{C,B}$ . Consequently the extended hardening relation (7.6) bases on second order gradients of  $\mathbf{F}^{p\alpha}$  and thus second order slip gradients  $\nabla_{\mathbf{X}\mathbf{X}}\gamma^\alpha$ . Therefore quadratic triangles are employed within the numerical implementation. The simulations are then performed in complete analogy to the previous considerations for a discretization with 1492 quadratic triangular elements. A reasonable agreement with the discrete dislocation plasticity predictions is found for a length scale  $l = 0.8\mu\text{m}$ , see figure 7.19 for a visualization. Finally, through this extension the relation 4 : 2 : 1 predicted by the discrete dislocation simulations for the corresponding cell heights is also picked up by the present formulation. However, the specific form of the proposed extension (7.6) has only a preliminary character and raises many open questions, such as the physical interpretation of the additional length scale  $l$  or the inclusion of the incompatibility measure  $G^{MN}$  in an isotropic manner or rather as a backstress contribution. Nevertheless, these questions will not be further investigated in this work.

**7.2.3. Bending Test for a Single Crystal.** As a second example in the context of gradient crystal (visco-)plasticity, pure bending of a single crystal under plane strain conditions will be considered. Thereby a comparison of the simulation results for the global and the extended local formulations of gradient crystal plasticity will also be given. In view of a convenient prescription of the bending mode and in order to reduce spurious influences of the boundary conditions, the bending test is implemented within an *inhomogeneous driver setup*.

**7.2.3.1. Inhomogeneous Deformation Driver.** The following *inhomogeneous deformation driver* is developed in view of an unified testing method for higher order material models subjected to inhomogeneous deformation modes. Thereby a deformation mode is prescribed macroscopically, i.e. uniformly for the entire solution domain. The overall response of the specimen to this prescribed deformation mode is then obtained by *super-*

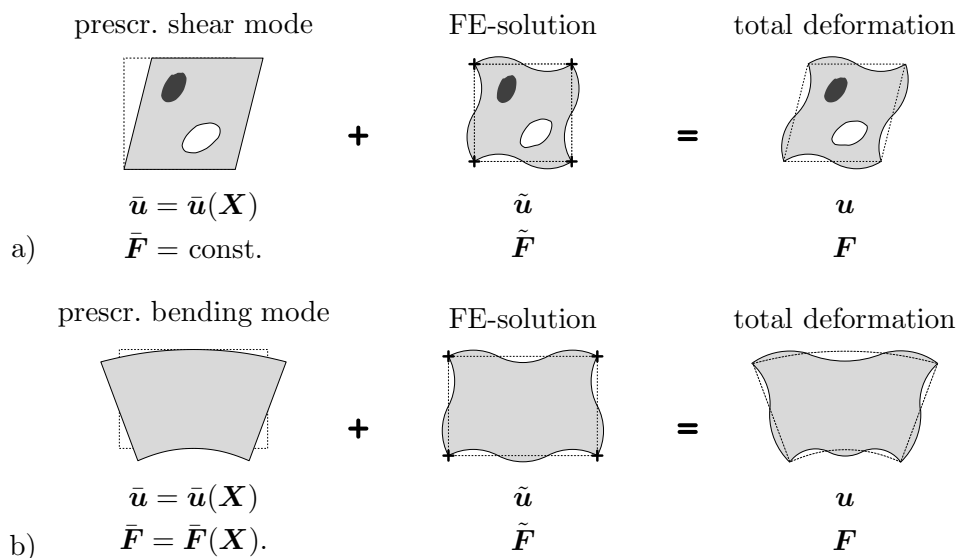


**Figure 7.20:** Inhomogeneous deformation driver. Superposition of prescribed displacements  $\bar{\mathbf{u}}$  with fluctuations  $\tilde{\mathbf{u}}$  computed for  $\bar{\mathbf{u}}$  gives total displacements  $\mathbf{u}$ . Prescribed a) *homogeneous* mode for *inhomogeneous* material, b) *inhomogeneous* mode for *homogeneous* material.

position of the prescribed displacement field  $\bar{\mathbf{u}}$  and the fluctuation field  $\tilde{\mathbf{u}}$  which develops throughout the solution domain as a response to the local stress fields, see figure 7.20 for a visualization. Thereby various boundary conditions might be specified for the fluctuation field  $\tilde{\mathbf{u}}$  depending on the desired overall deformation mode.

Regarding the numerical implementation of such driver tests, the deformation gradient  $\bar{\mathbf{F}}$  is prescribed directly on the element level and remains constant throughout the global iteration for the actual loading step. Hence, the discrete elementwise deformation gradient  $\mathbf{F}^h$  is extended as follows

$$\mathbf{F}^h = \bar{\mathbf{F}}(\mathbf{X}^h) + \sum_{I=1}^{n_{en}} \tilde{\mathbf{d}}^I \otimes \nabla_{\mathbf{X}} N^I \quad (7.7)$$

in terms of the nodal values of the fluctuation field  $\tilde{\mathbf{d}}^I$  and the material gradients  $\nabla_{\mathbf{X}} N^I$  of the finite element shape functions. Otherwise the standard finite element structure is completely retained. Thus, throughout the standard global iteration procedure the fluctuation field  $\tilde{\mathbf{u}}$  and thus the corresponding gradient  $\tilde{\mathbf{F}}$  is determined for a prescribed  $\bar{\mathbf{F}}$ . Upon global convergence the total displacement field is obtained by superposition, i.e.  $\mathbf{u} = \bar{\mathbf{u}} + \tilde{\mathbf{u}}$ . Thereafter, the next loading step is simply launched by imposing an advanced prescribed deformation gradient  $\bar{\mathbf{F}}$  on the element level. The implementation of this driver is thus very simple since the modifications of the standard structures are restricted to the prescription of  $\bar{\mathbf{F}}$  and the superposition of the (fluctuation) solution with  $\bar{\mathbf{u}}$ . Thereby it is also possible to prescribe very complex inhomogeneous deformation modes in a unified and very convenient manner.

**7.2.3.2. Bending Test for a Single Crystal in Double Slip.** The inhomogeneous deformation driver will now be employed within a pure bending test of a homogeneous single crystal in double slip. The basic test setup is visualized in figure 7.21. Thereby a compatible bending mode (SOKOLNIKOFF [139]) is prescribed as follows

$$\bar{\mathbf{u}}(\mathbf{X}) = c/H \cdot \begin{bmatrix} -X_1 X_2 \\ \frac{1}{2}(X_1^2 + \nu X_2^2) \\ 0 \end{bmatrix}, \quad \bar{\mathbf{F}}(\mathbf{X}) = \mathbf{1} + c/H \cdot \begin{bmatrix} -X_2 & -X_1 & 0 \\ X_1 & \nu X_2 & 0 \\ 0 & 0 & 0 \end{bmatrix} \quad (7.8)$$

in terms of the dimensionless *loading parameter*  $c$ , the specimen height  $H$  and Poisson's ratio  $\nu$ . This bending mode represents an inhomogeneous compatible ( $\text{Curl } \bar{\mathbf{F}} \equiv 0$ ) deformation mode. In order to obtain pure bending with no resulting normal forces and to prevent rigid body motions, the following boundary conditions are prescribed for the

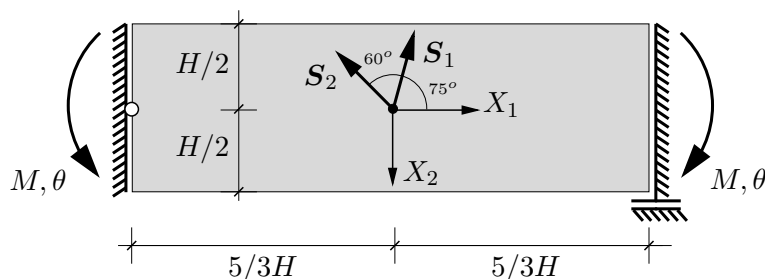


**Figure 7.21:** Pure bending of a single crystal. Setup for double slip with boundary conditions for the determination of the fluctuation field within the inhomogeneous driver test.

**Table 7.3:** Parameters used in pure bending test of a single crystal.

Bulk modulus	$\kappa$	=	68600.0	<i>MPa</i>
Shear modulus	$\mu$	=	26300.0	<i>MPa</i>
Poisson's ratio	$\nu$	=	0.33	–
Burgers vector length	$b$	=	0.286	<i>nm</i>
Strength parameter	$c$	=	0.3	–
Initial SSD density	$\rho_{\text{SSD}}^0$	=	$6.0 \times 10^{13}$	$[m^{-2}]$
Saturated SSD density	$\rho_{\text{SSD}}^{\text{sat}}$	=	$1.0 \times 10^{15}$	$[m^{-2}]$
Saturation slip strain	$\gamma^{\text{sat}}$	=	0.5	–

fluctuation field  $\tilde{\mathbf{u}}$

$$\begin{aligned} \tilde{u}_1(X_1 = -5/3H, X_2) &= 0, & \tilde{u}_1(X_1 = 5/3H, X_2) &= \text{const.} \\ \tilde{u}_2(X_1 = -5/3H, X_2 = 0) &= 0, & & \end{aligned} \quad (7.9)$$

These boundary conditions are also visualized in figure 7.21. (Explanatory note: through the prescription of the bending mode (7.8) in combination with the boundary conditions for the fluctuations (7.9), in total only the end rotations  $\theta$  at  $X_1 = \pm 5/3h$  are prescribed.) Furthermore, note that within the global formulation no boundary conditions are imposed for the plastic slips in the present example.

The specimen of the dimensions  $10/3H \times H$  is characterized by two slip systems with a relative orientation of  $60^\circ$  representative of Asaro's planar double slip model (ASARO [9]). Thereby slip system 1 is oriented at  $75^\circ$  with respect to the  $X_1$ -axis. The overall response of the homogeneous single crystal to the prescribed bending mode is described in terms of the applied rotation angle  $\theta$  and the work-conjugate bending moment  $M$ . For the given specimen dimensions the rotation angle follows at a given *load level*  $c$  from (7.8)<sub>1</sub> as

$$\theta = \hat{\theta}(c) = \arctan \left[ \frac{60c}{36 - 100c - 9\nu c} \right] \quad (7.10)$$

The bending moment is computed e.g. along the vertical boundary at  $X_1 = 5/3H$  through the discrete form corresponding to

$$M = \int_{-H/2}^{H/2} X_2 \sigma_{11}(X_1 = 5/3H, X_2) dX_2 \quad (7.11)$$

Unless stated otherwise, the specimen is discretized by  $100 \times 30$  quadrilaterals and deformed in the context of the inhomogeneous driver up to a maximal rotation angle of

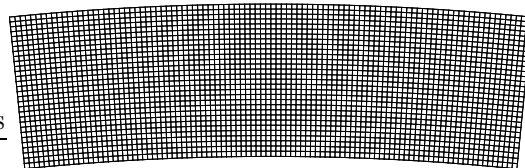


**Figure 7.22:** Finite element discretization of the homogeneous single crystal using  $100 \times 30$  quadrilaterals, deformed configuration at an imposed rotation of  $\theta = 6^\circ$ .

$\theta = 6^\circ$ , see figure 7.22 for a visualization. The material parameters used in the present analysis are representative of aluminum and are summarized in table 7.3. In the following the capabilities of the present approach to predict size effects and the storage of GNDs under inhomogeneous deformations are again investigated. Therefore the specimen dimensions are varied between  $H \rightarrow \infty$  and  $H = 6\mu\text{m}$ .

To start, the  $\sigma_{11}$  contour obtained for a chosen specimen height of  $H = 6\mu\text{m}$  through the global formulation of gradient crystal plasticity is compared with the corresponding contour obtained through the extended local formulation of gradient crystal plasticity in figure 7.23. Thereby an  $L_2$ -projection has been employed in the smoothing algorithm for the determination of the projected nodal slips within the extended local formulation. This is indicated by the notation *Local+L<sub>2</sub>* in the following. As discussed also in more detail in the next subsection, the results obtained through the Local+L<sub>2</sub> formulation are almost identical to the ones obtained through an extended local formulation combined with a patch recovery. Regarding the stress distributions shown in figure 7.23, the results obtained through the extended local formulation are in a good qualitative as well as quantitative agreement with the results of the global formulation. A very slight influence of the boundary conditions is only visible within the results of the global formulation in figure 7.23 a). Otherwise the stress profiles fully recover a pure bending mode.

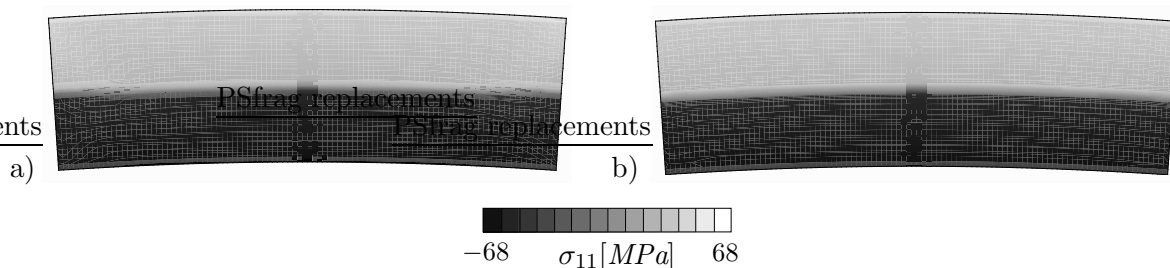


**Figure 7.23:** Stress contours at an imposed rotation of  $\theta = 4^\circ$  for  $H = 6\mu\text{m}$ .  $\sigma_{11}$  profile obtained through a) global and b) extended local formulation of gradient crystal plasticity.

Turning next to the GND density distributions, the comparison in figure 7.24 also reveals a good qualitative as well as quantitative agreement of the results of both formulations. Thereby the effective GND density  $\bar{\rho}_{\text{GND}}$  is visualized in figures 7.24 a) and b) where

$$\bar{\rho}_{\text{GND}} = \sqrt{\sum_{\alpha} [\rho_{\text{GND}}^{\alpha}]^2} \quad (7.12)$$

with  $\alpha = 1, 2$  for the present double slip case. Note that in the present formulation the GND densities do not possess any polarity. Obviously a non-vanishing GND density

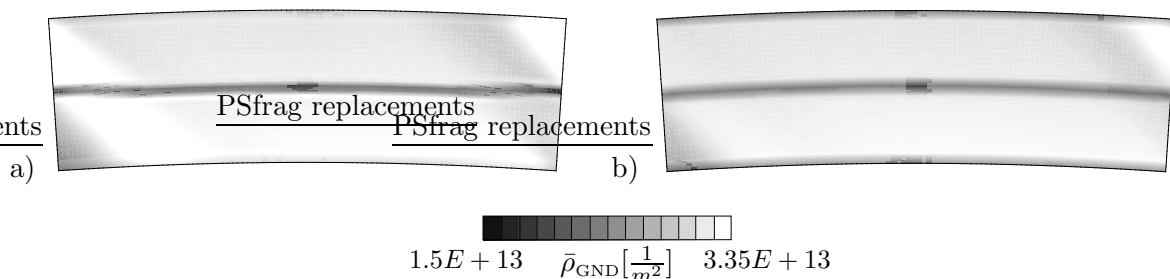


**Figure 7.24:**  $\bar{\rho}_{\text{GND}}$  contours at an imposed rotation of  $\theta = 4^\circ$  for  $H = 6\mu\text{m}$ .  $\bar{\rho}_{\text{GND}}$  profile obtained through a) global and b) extended local formulation for double slip.

develops over the full specimen height, specifically also on the neutral axis. In contrast to the composite material of the preceding example, the specimen in the present analysis is absolutely homogeneous. Here the incompatibilities and the corresponding GND storage are induced directly by the a priori inhomogeneous (but compatible) total deformation state. For comparison: following NYE [119], see also equation (5.1), the GND density stored in connection with a corresponding stress free lattice curvature  $\kappa$  is given by  $\rho_{\text{GND}} = \kappa/b$ . For an imposed end rotation of  $\theta = 4^\circ$  and the actual parameters  $H = 6\mu\text{m}$  and  $b = 0.286\text{nm}$ , the resulting GND density is obtained as  $\rho_{\text{GND}}(\theta = 4^\circ, H = 6\mu\text{m}) = 4\pi/(300Hb) = 2.4410E + 13 \frac{1}{\text{m}^2}$ . This is well within the range specified in figure 7.24 and thus very close to the average effective GND density for the specimen as a whole obtained through the present analysis.

Next, the capability of the present model to predict size effects shall be investigated. Clearly such size effects are expected since the incompatibility induced GND storage induces additional hardening as discussed in detail in chapter 5. In this respect, various specimen dimensions are again investigated while all remaining parameters are kept constant. The overall response of the specimen to the prescribed bending mode is plotted in figure 7.25 in terms of the resulting bending moment against the imposed end rotation  $\theta$  for the heights  $H \rightarrow \infty, H = 12\mu\text{m}$  and  $H = 6\mu\text{m}$ . Obviously a significant size effect is again captured by the present approach. Thereby the reference moment  $M_{\text{ref}}$  in figure 7.25 corresponds the resulting moment at the onset of plastic slip in the purely local description, i.e. for  $H \rightarrow \infty$ . Furthermore, the comparison of the overall response obtained through the global formulation with the corresponding results of the extended local formulation reveals a very good agreement, see figure 7.25 for a visualization. Therein both formulations predict for each height ( $H \rightarrow \infty, H = 12\mu\text{m}$  and  $H = 6\mu\text{m}$ ) an almost identical response. Thus it is highly favourable to employ the extended local formulation within the numerical treatment of gradient crystal plasticity due to its superior efficiency.

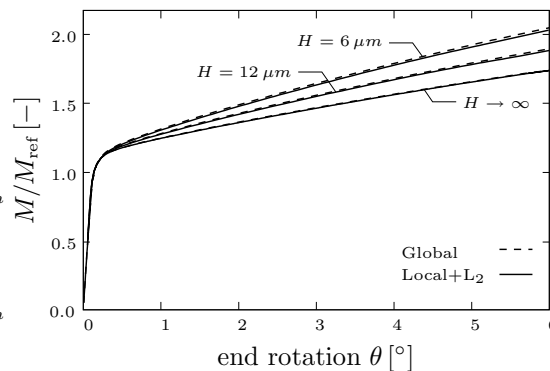


**Figure 7.25:** Overall response of the double slip single crystal to bending in terms of the resulting bending moment  $M$  versus the imposed end rotation  $\theta$ . Size effect and comparison of the results for the global and the extended local (Local+L<sub>2</sub>) formulation

**7.2.3.3. Bending Test for a FCC Single Crystal.** Finally the same analysis will be carried out for a full multislip *fcc single crystal*. Thus in the following the same bending mode and boundary conditions as in the setup for the double slip case will be imposed on a fcc single crystal. Thereby the parameters of table 7.3 are also adopted in the following. However, for the multislip case now the full slip system interaction according to section 3.9

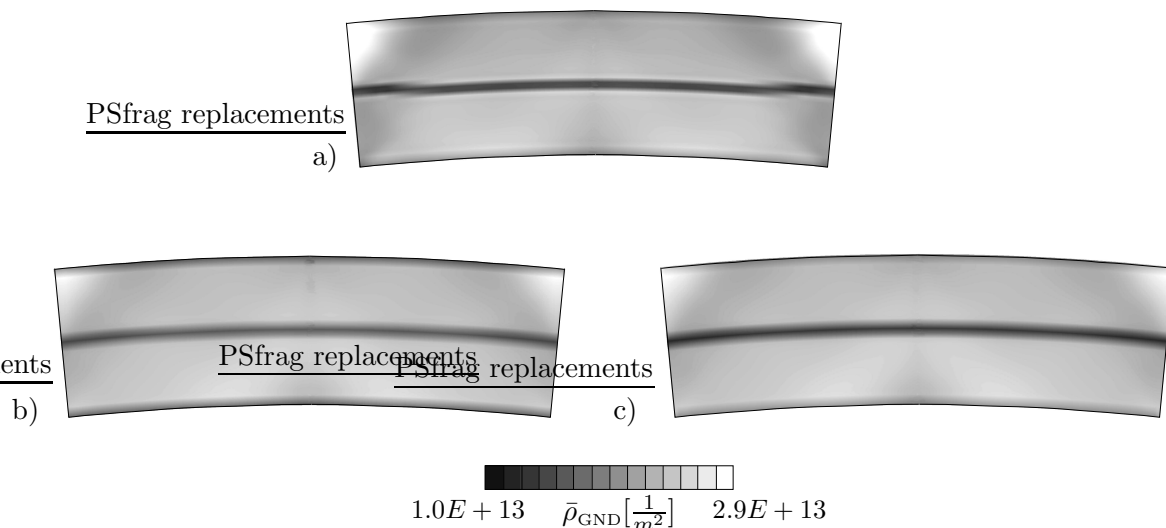


**Figure 7.26:**  $\bar{\rho}_{\text{GND}}$  contours at an imposed rotation of  $\theta = 6^\circ$  for  $H = 12\mu\text{m}$ .  $\bar{\rho}_{\text{GND}}$  profile obtained through a) global, b) Local+ $L_2$  and c) Local+PR formulation for a full fcc crystal.

will be considered within the hardening relations. Therefore the full *strength interaction matrix*  $G^{\alpha\beta}$  specified in figure 3.20 b) is employed in the hardening relations. For the present case of an aluminum single crystal, the *strength interaction coefficients* are adopted from ARSENLIS & PARKS [7]. Thus the coefficients characteristic of the interactions specified in table 3.3 are specified through  $G_1 = 0.3$ ,  $G_2 = 0.16$ ,  $G_3 = 0.22$ ,  $G_4 = 0.38$  and  $G_5 = 0.45$ . Furthermore the initial orientation of the single crystal is specified through the following Euler angles ( $0^\circ/0^\circ/0^\circ$ ). In view of an analysis of the predicted size effects, the specimen height is again varied between  $H \rightarrow \infty$  and  $H = 6\mu\text{m}$ .

As a first result, the effective GND density contours are considered in figure 7.26 for an imposed end rotation of  $\theta = 6^\circ$  and a specimen height of  $H = 12\mu\text{m}$ . Therein the results obtained through all three developed formulations of gradient crystal (visco-)plasticity are visualized. Comparing the results obtained by the extended local formulations either based on a  $L_2$ -projection (figure 7.26 b)) or a patch recovery (figure 7.26 c)) reveals a good agreement. The global formulation (figure 7.26 a)) also gives qualitatively as well as quantitatively similar results. Following Nye's considerations, the resulting GND density for an imposed end rotation of  $\theta = 6^\circ$  and the actual parameters  $H = 12\mu\text{m}$  and  $b = 0.286\text{nm}$  is obtained as  $\rho_{\text{GND}}(\theta = 6^\circ, H = 12\mu\text{m}) = \pi/(50Hb) = 1.8308E+13 \frac{1}{m^2}$ . This is again well within the range specified in figure 7.26 and thus very close to the average effective GND density for the specimen as a whole predicted by the present analysis.

Turning to the overall response in terms of the resulting bending moment plotted against the imposed end rotation in figure 7.27 a) reveals again a significant size effect. As expected, the smallest specimen of dimensions  $20 \times 6\mu\text{m} \times \mu\text{m}$  gives the stiffest response due to the highest stored GND density. Comparing the responses predicted by the global formulation with the ones predicted by the extended local formulations in figure 7.27 a) shows that all three approaches give almost identical results for all investigated specimen heights  $H$ . However, the extended local formulations are of superior efficiency since they require no additional nodal degrees of freedom and thus greatly reduce the numerical costs in comparison to the global formulation. Within the latter formulation up to 24 additional nodal degrees of freedom are introduced for a full fcc crystal. In the present

example this results in a total of 81406 nodal degrees of freedom for the chosen discretization with  $100 \times 30$  elements. In turn the extended local formulations require only 6262 nodal degrees of freedom at the additional costs of the smoothing procedure. Thus the extended local formulations significantly reduce the numerical costs while they are of sufficient accuracy.

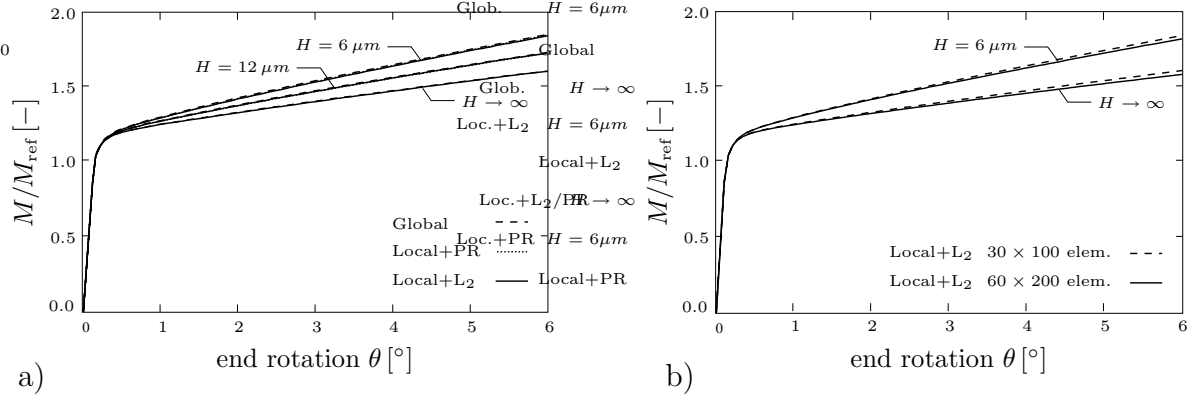


**Figure 7.27:** Overall response of the full fcc single crystal to the prescribed bending mode. a) Size effect and comparison of the global and the extended local (Local+L<sub>2</sub> and Local+PR) formulations, b) mesh sensitivity for discretizations with  $30 \times 100$  and  $60 \times 200$  elements.

Finally the mesh sensitivity is analyzed in figure 7.27 b). Thereby besides the discretization with 3000 elements a discretization with 12000 elements is investigated and the considerations are restricted to the extended local formulation combined with a L<sub>2</sub>-projection. Obviously for both heights considered ( $H \rightarrow \infty$  and  $H = 6 \mu\text{m}$ ) the chosen discretization is only of minor influence.

**7.2.4. Tension Test for an FCC Polycrystal.** As a last example the developed formulation of finite strain gradient crystal (visco-)plasticity will be tested for an aluminum polycrystal subjected to uniaxial tension under plane strain conditions. Here the capability of the present approach to predict size effects shall again be investigated. This includes also a comparison with experimental data taken from HONEYCOMBE [63]. The same test data has also been used by DAI & PARKS [35] to validate the predictions of their scale dependent constitutive model for planar double slip. Furthermore EVERS ET AL. [39] also investigated a polycrystal in tension under plane stress conditions in order to simulate size dependent material behavior.

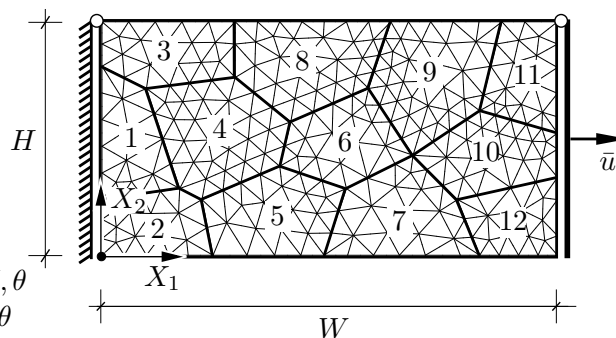


**Figure 7.28:** Tension test of an aluminum polycrystal with 12 arbitrary oriented grains, boundary conditions and discretization with 472 quadratic triangles.

**Table 7.4:** Initial lattice orientations of the fcc crystal grains.

Grain #	Euler angles	Grain #	Euler angles
1	( 99.47°/ 359.85°/ 1.23°)	7	( 189.75°/ 0.15°/ 129.78°)
2	( 0.13°/ 269.01°/ 90.16°)	8	( 209.85°/ 179.81°/ 91.14°)
3	( 179.82°/ 329.71°/ 1.43°)	9	( 279.96°/ 339.98°/ 79.86°)
4	( 224.75°/ 89.34°/ 9.87°)	10	( 39.97°/ 1.01°/ 9.78°)
5	( 0.21°/ 209.78°/ 89.21°)	11	( 109.82°/ 92.32°/ 9.43°)
6	( 1.86°/ 88.12°/ 178.65°)	12	( 2.04°/ 271.10°/ 10.53°)

The test setup for the present analysis is visualized in figure 7.28. The fcc polycrystal of dimensions  $W \times H$ , with  $W = 41/21H$ , is subjected to uniaxial tension with a prescribed displacement  $\bar{u}$  at the right boundary, thus the boundary conditions read

$$\begin{aligned} u_1(t, X_1 = 0, X_2) &= 0, & u_2(t, X_1 = 0, X_2 = H) &= 0, \\ u_1(t, X_1 = W, X_2) &= \bar{u}(t), & u_2(t, X_1 = W, X_2 = H) &= 0 \end{aligned} \quad (7.13)$$

In view of a description of the overall response of the specimen to the imposed tensile straining, the resulting nominal stress  $\bar{P}_{11}$  is computed through the discrete form of

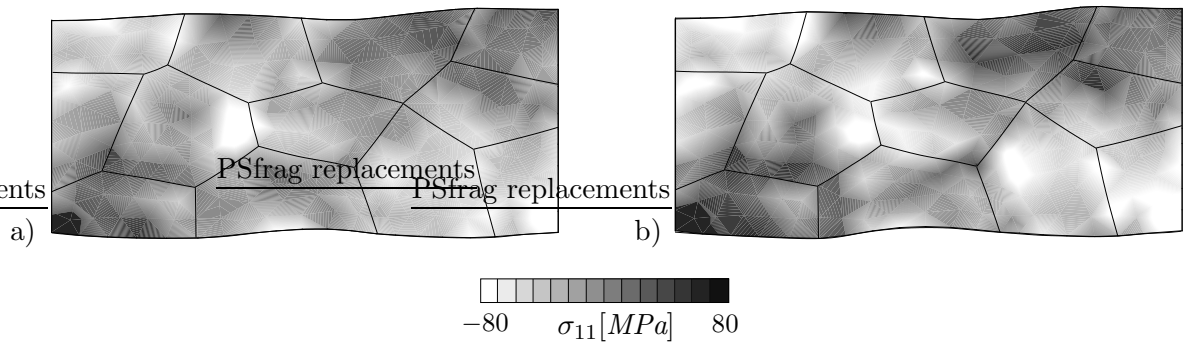
$$\bar{P}_{11} = \frac{1}{H} \int_0^H P_{11}(X_1 = W, X_2) dX_2 \quad (7.14)$$

evaluated in terms of the nodal reactions.

The polycrystalline aluminum specimen consists of 12 single crystal grains. The initial crystallographic orientations of the grains are chosen arbitrarily and are reported upon in table 7.5. Except for the crystallographic orientations, the remaining material parameters are chosen to be identical for all 12 grains. In view of a comparison of the results obtained through the present analysis with the experimental data of HONEYCOMBE [63], the bulk and shear moduli as well as the Burgers vector are chosen to be representative of aluminum. The initial and saturated SSD density and the saturation slip strain specified in

**Table 7.5:** Parameters used in tension test of an aluminum polycrystal.

Bulk modulus	$\kappa$	=	75500.0	<i>MPa</i>
Shear modulus	$\mu$	=	25500.0	<i>MPa</i>
Burgers vector length	$b$	=	0.286	<i>nm</i>
Strength parameter	$c$	=	0.3	–
Initial SSD density	$\rho_{\text{SSD}}^{0, \alpha}$	=	$1.0 \times 10^{10}$	$[m^{-2}]$
Saturated SSD density	$\rho_{\text{SSD}}^{\text{sat}}$	=	$6.0 \times 10^{13}$	$[m^{-2}]$
Saturation slip strain	$\gamma^{\text{sat}}$	=	0.1	–
Interaction coefficient	$G_1$	=	0.30	–
–”–	$G_2$	=	0.16	–
–”–	$G_3$	=	0.22	–
–”–	$G_4$	=	0.38	–
–”–	$G_5$	=	0.45	–



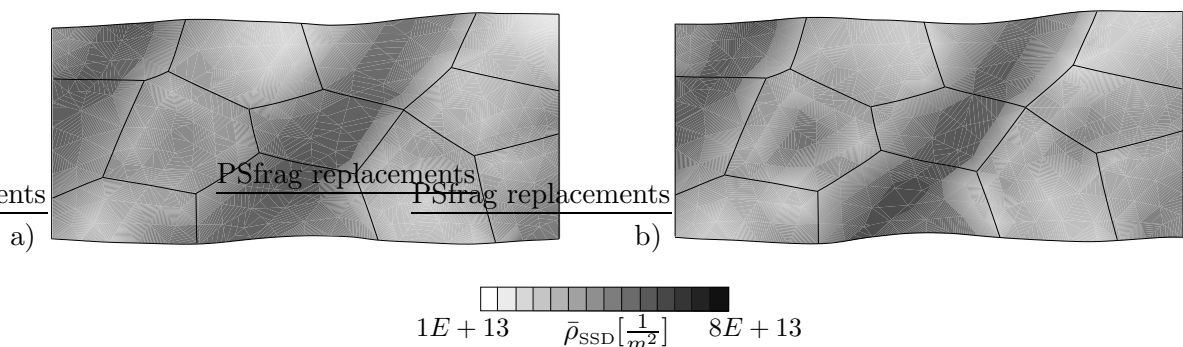
**Figure 7.29:** Stress state in the fcc polycrystal at a total deformation of  $\bar{\epsilon} = 8\%$ .  $\sigma_{11}$  stress contours for a)  $H = 1240 \mu m$  and b)  $H = 84 \mu m$ .

table 7.5 are obtained through fitting the simulation data to the test data for an average grain size of  $\bar{d} = 500 \mu m$ , see below. The slip system interaction strength is governed by the strength interaction coefficients  $G_i$  which are again adopted from ARSENLIS & PARKS [7] for aluminum (here a specification of the piercing densities is disregarded).

For the numerical simulation the fcc polycrystal is discretized with 472 quadratic triangles with 6 nodes per element which results in a total of 1003 nodes. In view of an efficient treatment of this example problem, the extended local formulation combined with a patch recovery within the smoothing algorithm for the slip projection is employed throughout the present investigation. The specimen is deformed up to a total deformation of 8% which, for the chosen parameters, results in the inhomogeneous stress state visualized in figure 7.29. In order to already gain an insight into the effect of the specimen dimensions on the response of the polycrystal, the results for two heights  $H$  are compared. According to figures 7.29 a) and 7.29 b), the  $\sigma_{11}$  stress contours for  $H = 1240 \mu m$  and  $H = 84 \mu m$  do not differ significantly.

Also, the comparison of the effective SSD density contours in figures 7.30 a) and 7.30 b) reveals no significant differences. In the smaller specimen the SSD density is slightly increased and the SSDs accumulate stronger towards the center of the grains. The effective SSD density  $\bar{\rho}_{SSD}$  is computed in analogy to (7.12).

Now, the comparison of the effective GND densities in figure 7.31 reveals a significant difference. On the one hand the GND density stored in the larger specimen is negligible, especially in comparison to the SSD density, while on the other hand a significant amount



**Figure 7.30:** Comparison of the effective SSD density distributions at  $\bar{\epsilon} = 8\%$ . a)  $\bar{\rho}_{SSD}$  contours for  $H = 1240 \mu m$  and b)  $\bar{\rho}_{SSD}$  contours for  $H = 84 \mu m$ .

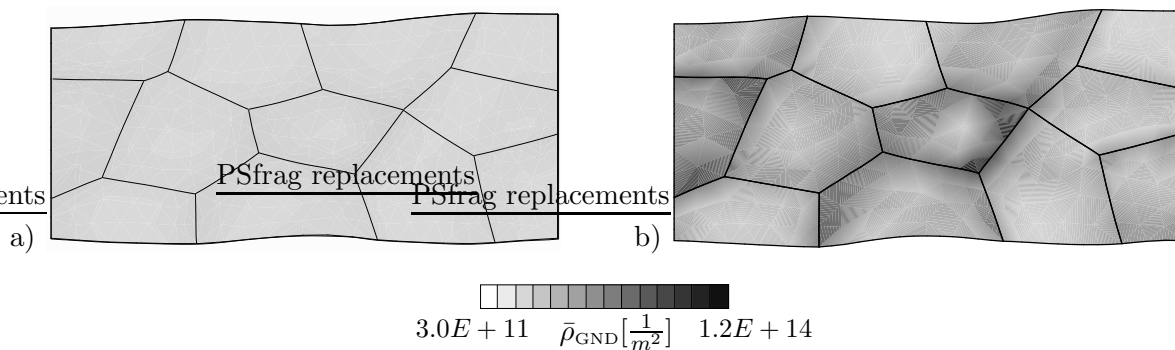


**Figure 7.31:** Comparison of the effective GND density distributions at  $\bar{\epsilon} = 8\%$ . a)  $\bar{\rho}_{\text{GND}}$  contours for  $H = 1240\mu\text{m}$  and b)  $\bar{\rho}_{\text{GND}}$  contours for  $H = 84\mu\text{m}$ .

of GNDs is stored in the smaller specimen. Clearly the GND storage is induced by the incompatibility of the plastic deformation of neighbouring grains. Thereby the plastic slip gradients in the smaller sized specimen are much higher since the inhomogeneities occur over a smaller distance which in turn results in an increased GND density. For the specimen of height  $H = 84\mu\text{m}$ , the GNDs concentrate at the grain boundaries and significantly exceed the level of the effective SSD density.

Clearly the increased GND storage for the smaller specimen will also induce a size effect in the overall response since the GND density supplements to the SSD density and thus induces additional hardening. The size effect predicted in this manner through the present formulation shall finally be compared with the *experimental observations for pure aluminum* of HONEYCOMBE [63]. Therefore the parameters  $\rho_{\text{SSD}}^{0,\alpha}$ ,  $\rho_{\text{SSD}}^{\text{sat}}$  and  $\gamma^{\text{sat}}$  are first fitted only to the experimental test data for the largest specimen with a grain size of  $\bar{d} = 500\mu\text{m}$ . The test data is directly adopted from HONEYCOMBE [63], p. 238, see the bullets in figure 7.32 a) where also the corresponding fit for  $\bar{d} = 500\mu\text{m}$  is visualized. The obtained material parameters are specified in table 7.5. (Also the previously presented simulation results are based on these values.) In the present example a relation between the investigated specimen dimensions  $H \times W$  and the average grain size  $\bar{d}$  can be established as follows. The total area occupied by the specimen depicted in figure 7.28 is given by  $A = W \times H = 41/21H \times H$ . Hence the average grain size  $\bar{d}$  can be computed from the area occupied by one out of 12 grains as

$$A_{\text{grain}} = \frac{A}{12} = \frac{41}{252}H^2 \quad \Rightarrow \quad \bar{d} = \sqrt{\frac{41}{252}}H \approx 0.403H \quad (7.15)$$

With this relation at hand, the size effect predicted through the present model can now be compared with the experimental observations. In the experiment grain sizes of  $\bar{d} = 500\mu\text{m}$ ,  $240\mu\text{m}$  and  $88\mu\text{m}$  down to  $34\mu\text{m}$  have been investigated. In turn, in the numerical simulation specimen heights of  $H = 1240\mu\text{m}$ ,  $H = 315\mu\text{m}$  and  $H = 137\mu\text{m}$  down to  $H = 84\mu\text{m}$  have been analyzed. These dimensions correspond to the average grain sizes  $\bar{d} = 500\mu\text{m}$ ,  $127\mu\text{m}$ ,  $55\mu\text{m}$  and  $\bar{d} = 34\mu\text{m}$ . The resulting size effect predicted through the present model is reported upon in figure 7.32 a) along with the experimentally observed size effect. Obviously the experimental observations can be recovered quite well by the actual approach, especially for the grain sizes  $\bar{d} = 500\mu\text{m}$  and  $\bar{d} = 34\mu\text{m}$ . A comparison between the investigated and the measured responses for the intermediate grain sizes reveals some difference in the observed size effects, i.e. a difference in the corresponding Hall-Petch exponents. In this respect, the extended Hall-Petch relations are

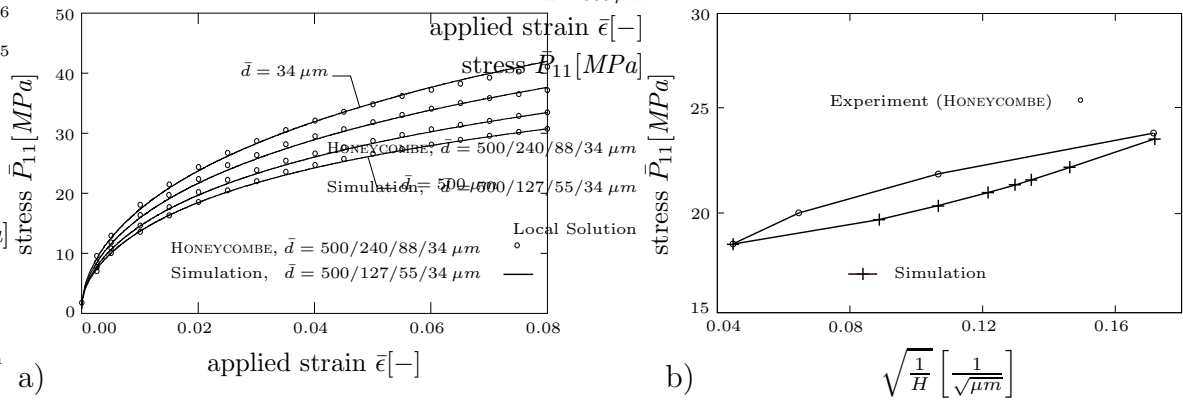


**Figure 7.32:** Size dependence in the response of a pure aluminum polycrystal under tension. Comparison between the simulation results and the experimental measurements of HONEYCOMBE [63]. a) Overall response in terms of normal stress  $\bar{P}_{11}$  versus applied strain  $\bar{\epsilon}$ . b) extended Hall-Petch relations at  $\bar{\epsilon} = 2\%$ .

plotted at an applied strain level of  $\bar{\epsilon} = 2\%$  in figure 7.32 b) for both the experiment and the simulation. The experiment reveals a Hall-Petch exponent of  $n < 0.5$  while the present approach predicts an exponent of  $n > 0.5$  close to  $n = 1$ . Thereby it is worthy to mention that within the numerical simulations for the smaller specimen dimensions, *no* further material parameters than the ones already specified for  $\bar{d} = 500 \mu m$  had to be adopted.

Here it should be noted again that the size effect in the present model results only from the incompatibility induced GND storage. Thereby the present formulation of strain gradient crystal plasticity requires no additional material parameters, especially no additional *internal length scale*. The only length scale included in the model is represented by the Burgers vector which has a clear physical interpretation and is inherent to the investigated material, i.e. a priori defined and amenable through measurement. Thus the obtained agreement with the experimental observations is quite remarkable since the size effect recovered by the present analysis is a direct outcome of the simulation for varying absolute specimen dimensions which are identical to the real specimen dimensions. This especially includes also the fact that the predicted size effect is not scalable through an additional phenomenological length scale. These observations can be directly attributed to the micromechanical motivation of the present model and its mathematical foundation on the matter of incompatibility. Possible future extensions should concern a Hall-Petch like size dependence of the initial flow stress, e.g. through an a priori misorientation induced dislocation storage at the grain boundaries, or a residual stress based kinematic hardening contribution which accounts for the fact that the GND arrays extend over a nonzero width.



## 8. Incremental Stability of Microheterogeneous Materials

In the following instability phenomena in microheterogeneous standard dissipative solids and associated size-dependencies of classical micro-to-macro transitions will be investigated. The underlying basis of the subsequent developments is an incremental variational formulation as briefly outlined for the model problem of finite strain crystal plasticity in chapter 4. With the incremental description of the response of standard dissipative materials at hand, existence results of finite strain elasticity can be extended to finite strain inelasticity. This allows for the development of stability criteria for the analysis of structural (e.g. buckling) and material (e.g. localization) instability phenomena on the micro- and macro-scale as well as their interactions. It is shown that in the non-convex regime induced by structural micro-instabilities, the minimization problem of homogenization needs to be enveloped by an additional minimization with respect to the size of the representative volume element. Therewith size dependencies of classical micro-to-macro transitions in the postcritical non-convex regime are eliminated. In contrast to the length scale dependencies analyzed in the previous chapters, such size dependencies are nonphysical and result from the specific choice of the representative volume element size which is, in classical homogenization approaches, unrestricted by possibly occurring instabilities.

This chapter is organized as follows. After a brief introduction into the homogenization analysis, its limitations and the resulting motivation for further developments, the incremental variational formulation of homogenization will be discussed in section 8.2. Thereafter, in section 8.3, stability criteria will be developed and the effect of the representative volume element size will be discussed. This leads to the development of a non-convex homogenization approach for standard dissipative materials. Finally, in section 8.4, the performance of the presented concepts will be demonstrated for two numerical examples.

### 8.1. Introduction

*Microheterogeneous* materials can be described in a very efficient manner through average-type *homogenization* procedures. The underlying classical assumption of such approaches is that the overall *macroscopic* behavior of a (periodic) composite can be described in terms of two separate scales as visualized in figure 8.1 (see HILL [58, 60], WILLIS [156], HASHIN [54], SUQUET [144], NEMAT-NASSER & HORI [117], PONTE CASTAÑEDA & SUQUET [127] or MIEHE ET AL. [104] among others for an overview over this methodology). In

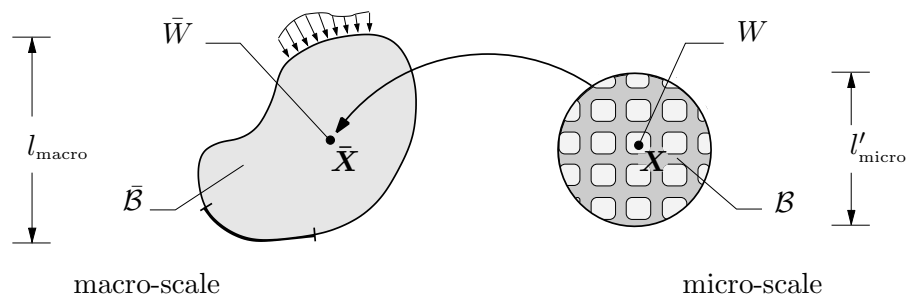


**Figure 8.1:** Micro-to-macro transition for standard dissipative materials. Attached to each macroscopic point  $\bar{\mathbf{X}} \in \bar{\mathcal{B}}$  is a micro-structure  $\mathcal{B} \subset \mathcal{R}^3$  representative of the microheterogeneous standard dissipative material. The macroscopic stress potential  $\bar{W}$  is obtained through a minimization principle from the microscopic stress potential  $W$ .

order to avoid significant influences of boundary layer effects and to justify a neglect of body and inertial forces with respect to the contact forces on the boundary of a typical micro-structure the characteristic dimensions of both scales should differ by more than an order of magnitude, i.e.  $l'_{\text{micro}} \ll l_{\text{macro}}$  (in the global form of the balance of linear momentum  $\int_{\partial V} \mathbf{t} dA + \int_B \rho_0(\mathbf{b} - \ddot{\boldsymbol{\varphi}}) = \mathbf{0}$  the influence of the contact forces scales with  $l'^2_{\text{micro}}$  while the one of the inertial and body forces scales with  $l'^3_{\text{micro}}$  which is thus negligible for  $l'_{\text{micro}}/l_{\text{macro}} \rightarrow 0$ ). The periodicity of the microheterogeneities allows to describe the micro-structure through a *representative volume element (RVE)*. Based on the RVE macroscopic quantities are obtained through averaging principles from their microscopic counterparts and in turn the microscopic deformation state  $\mathbf{F}$  is driven by the macroscopic deformation gradient  $\bar{\mathbf{F}}$  which is constant throughout the micro-structure (see MICHEL ET AL. [93], MOULINEC & SUQUET [113], MIEHE ET AL. [104, 109, 107], KOUZNETSOVA [74] for the development of numerical homogenization methods).

In the case of *instabilities* on the macro- or micro-scale such as e.g. buckling phenomena, classical homogenization procedures hit their limitations. The goal of this chapter is the development of an extended homogenization formulation for standard dissipative materials which is also valid within the non-convex postcritical regime. This includes the development of stability criteria for a loss of *structural* and *material stability* on the micro- and the macro-scale as well as their mutual interaction. As will be seen later, the specific choice of the RVE induces an undesired *size dependency* within the non-convex regime which is eliminated within the presented extension of the homogenization procedure.

The following developments are concerned with the class of so-called *standard dissipative materials*, where the response is governed by the *energy storage function*  $\psi = \hat{\psi}(\mathbf{F}, \mathcal{I})$  and a *dissipation function*  $\phi = \hat{\phi}(\dot{\mathcal{I}}, \mathcal{I})$ . This class of materials is representative of a wide range of models in finite elasticity, elastoplasticity, viscoplasticity or damage mechanics. The development of the homogenization procedure for standard dissipative materials in general and the subsequent extension to the non-convex regime in particular rely on an incremental variational formulation of inelasticity (MIEHE [97, 98], MIEHE ET AL. [103], MIEHE & SCHOTTE [101], also ORTIZ & REPETTO [121]). Thereby the incremental variational formulation bases on the incremental stress potential introduced already in chapter 4.

## 8.2. Incremental Homogenization Analysis in Finite Inelasticity

Before starting with the stability analysis of microheterogeneous standard dissipative materials and the development of an approach to the non-convex homogenization analysis, the homogenization analysis in finite inelasticity will be briefly reviewed in the following.

**8.2.1. Microscopic Incremental Variational Formulation of Inelasticity.** As a starting point the definition of an *incremental stress potential function* proposed in MIEHE [97] and MIEHE ET AL. [103] for generalized standard dissipative materials is briefly reiterated (see also section 4.2.3). For the actual time increment  $[t_n, t_{n+1}]$ , the local (microscopic) material response can be characterized by the incremental stress potential function  $W$  defined through the variational problem

$$W(\mathbf{F}_{n+1}) = \inf_{\mathcal{I} \in \mathcal{G}} \int_{t_n}^{t_{n+1}} [\dot{\psi} + \phi] dt \quad \text{with} \quad \mathcal{I}(t_n) = \mathcal{I}_n \quad (8.1)$$

which defines an optimal path of the internal variables  $\mathcal{I}(t)$  within the time step under consideration. As shown in MIEHE ET AL. [103], the variational formulation (8.1) is a consistent approximation of Biot's normal dissipative evolution equation

$$\partial_{\mathcal{I}}\psi(\mathbf{F}, \mathcal{I}) + \partial_{\dot{\mathcal{I}}}\phi(\dot{\mathcal{I}}, \mathcal{I}) = 0 \quad \text{with} \quad \mathcal{I}(0) = \mathcal{I}_0 \quad (8.2)$$

for the internal variables  $\mathcal{I}$ . The algorithmic solution of the minimization problem (8.1) bases on the functional

$$\hat{W}(\mathbf{F}_{n+1}, \mathcal{I}_{n+1}) = [\psi(\mathbf{F}, \mathcal{I})]_{t_n}^{t_{n+1}} + \int_{t_n}^{t_{n+1}} \phi(\dot{\mathcal{I}}, \mathcal{I}) dt \quad (8.3)$$

along with the necessary condition  $\hat{W}_{,\mathcal{I}} = \mathbf{0}$  which implies an integration algorithm for the internal variables  $\mathcal{I}$ . A specification to finite strain crystal plasticity and the development of the corresponding algorithmic formulation was given in section 4.2. The function  $W$  serves as a potential for the determination of the micro-stresses  $\mathbf{P}_{n+1}$  and the micro-moduli  $\mathcal{A}_{n+1}^{cp}$  at a local point  $\mathbf{X} \in \mathcal{B}$  of the heterogeneous micro-structure through quasi-hyperelastic function evaluation in the sense

$$\mathbf{P}_{n+1} = \partial_{\mathbf{F}}W(\mathbf{F}_{n+1}) \quad \text{and} \quad \mathcal{A}_{n+1} = \partial_{\mathbf{F}\mathbf{F}}^2W(\mathbf{F}_{n+1}) \quad (8.4)$$

**8.2.2. Fluctuation Field on Heterogeneous Micro-structures.** Within the context of a deformation driven homogenization approach the internal variables on the micro-scale are determined for given micro-deformation  $\mathbf{F}$  through the minimization problem (8.1). Subsequently the actual micro-stress state is derived from (8.4). The micro-deformation itself is assumed to be driven by a prescribed macro-deformation  $\bar{\mathbf{F}}$ . Consequently the deformation map of a heterogeneous micro-structure  $\varphi(\mathbf{X}, t)$  comprises of a linear part  $\bar{\mathbf{F}}(t)\mathbf{X}$  and a superimposed fine-scale fluctuation field  $\mathbf{w} : \mathcal{B} \times \mathcal{R}_+ \rightarrow \mathcal{R}^3$

$$\varphi(\mathbf{X}, t) = \bar{\mathbf{F}}(t) \cdot \mathbf{X} + \mathbf{w}(\mathbf{X}, t) \quad (8.5)$$

which results in the decomposition of the micro-deformation gradient locally at  $\mathbf{X} \in \mathcal{B}$

$$\mathbf{F}(\mathbf{X}, t) = \bar{\mathbf{F}}(t) + \nabla \mathbf{w}(\mathbf{X}, t) \quad (8.6)$$

Following HILL [60], the macro-deformation  $\bar{\mathbf{F}}$  is assumed to be governed by surface data of the microscopic deformation field

$$\bar{\mathbf{F}}(t) = \frac{1}{|\mathcal{V}|} \int_{\partial\mathcal{V}} \varphi(\mathbf{X}, t) \otimes \mathbf{N}(\mathbf{X}) dA \quad (8.7)$$

where volume of the micro-structure  $\mathcal{V} = \mathcal{B} \cup \mathcal{H}$  consists of a solid part  $\mathcal{B}$  and holes  $\mathcal{H}$ .  $\mathbf{N}$  denotes the outward normal of the micro-structure at  $\mathbf{X} \in \partial\mathcal{V}$ . Insertion of the decomposition (8.5) into (8.7) results, after application of the integral theorem, in the constraint for the fluctuation field  $\mathbf{w}$

$$\frac{1}{|\mathcal{V}|} \int_{\partial\mathcal{V}} \mathbf{w}(\mathbf{X}, t) \otimes \mathbf{N}(\mathbf{X}) dA = \mathbf{0} \quad (8.8)$$

which is satisfied for the *non-trivial* assumption of a *periodic superimposed fluctuation field* on  $\partial\mathcal{V}$ , i.e.

$$\mathbf{w}^+(\mathbf{X}) = \mathbf{w}^-(\mathbf{X}) \quad \text{with} \quad \mathbf{N}^+ = -\mathbf{N}^- \quad \text{on} \quad \partial\mathcal{V} \quad (8.9)$$

This implies the decomposition of the boundary into two parts  $\partial\mathcal{V} = \partial\mathcal{V}^+ \cup \partial\mathcal{V}^-$  with the respective outward normals  $\mathbf{N}^+ = -\mathbf{N}^-$  at two associated points  $\mathbf{X}^- \in \partial\mathcal{V}^-$  and  $\mathbf{X}^+ \in \partial\mathcal{V}^+$ , see figure 8.2 for a visualization. Alternatively, the constraint (8.8) can be satisfied for *homogeneous deformations on the boundary*  $\partial\mathcal{V}$  with  $\mathbf{w} = \mathbf{0}$  on  $\partial\mathcal{V}$  or *homogeneous stresses on the boundary*  $\partial\mathcal{V}$  with  $\mathbf{t}(\mathbf{X}, t, \mathbf{N}) = \bar{\mathbf{P}}(\bar{\mathbf{X}}, t) \cdot \mathbf{N}(\mathbf{X})$  on  $\partial\mathcal{V}$ , see MIEHE ET AL. [104, 109, 103, 101] for a detailed discussion of these boundary conditions. However, in the following the considerations will be restricted to periodic boundary conditions as given by (8.8).

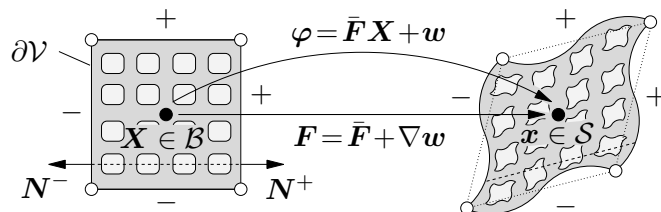


**Figure 8.2:** Deformation of a micro-structure. The micro-deformation is driven by the local deformation gradient  $\bar{\mathbf{F}}$  in the corresponding macroscopic point  $\bar{\mathbf{X}}$ . On the micro-scale a superimposed fluctuation field  $\mathbf{w}$  develops due to heterogeneities or developing instabilities.

**8.2.3. Incremental Variational Formulation of Homogenization.** For given micro-deformation  $\mathbf{F}$ , the stress state on the micro-scale is governed by the microscopic incremental stress potential  $W$  through the quasi-hyperelastic function evaluation (8.4). This analogy to finite elasticity motivates the following incremental variational formulation of the homogenization problem for standard dissipative materials. The fine-scale fluctuation field  $\mathbf{w}_{n+1}$  is determined at time  $t_{n+1}$  through the *principle of minimum average incremental energy* proposed in MIEHE [97] as an extension of the so-called *average variational principle* of nonlinear elasticity discussed by MÜLLER [114] and PONTE CASTAÑEDA & SUQUET [127]

$$\bar{W}(\bar{\mathbf{F}}_{n+1}, \bar{\mathbf{X}}) = \inf_{\mathbf{w}_{n+1} \in \mathcal{W}^\#} \frac{1}{|\mathcal{V}|} \int_{\mathcal{B}} W(\bar{\mathbf{F}}_{n+1} + \nabla \mathbf{w}_{n+1}, \mathbf{X}) dV \quad (8.10)$$

where the fluctuations  $\mathbf{w}_{n+1}$  are subject to the boundary conditions (8.9), i.e.

$$\mathbf{w}_{n+1} \in \mathcal{W}^\# := \{\mathbf{w} \in \mathcal{W}^{1,p}(\mathcal{B}) \mid \mathbf{w}^+ = \mathbf{w}^- \text{ on } \partial\mathcal{V}\} \quad (8.11)$$

(or in general also either the homogeneous deformation or the homogeneous stress boundary conditions on  $\partial\mathcal{V}$ ). The minimization problem (8.10) is considered as the *key homogenization condition* which provides for the determination of the fine-scale fluctuation field  $\mathbf{w}$ , the homogenized incremental stress potential  $\bar{W}$  on the macro-scale and thus in complete analogy to (8.4) through quasi-hyperelastic function evaluation the macro-stresses  $\bar{\mathbf{P}}_{n+1}$  and the macro-moduli  $\bar{\mathbf{A}}_{n+1}$

$$\bar{\mathbf{P}}_{n+1} = \partial_{\bar{\mathbf{F}}} \bar{W}(\bar{\mathbf{F}}_{n+1}) \quad \text{and} \quad \bar{\mathbf{A}}_{n+1} = \partial_{\bar{\mathbf{F}}\bar{\mathbf{F}}}^2 \bar{W}(\bar{\mathbf{F}}_{n+1}) \quad (8.12)$$

In view of an approximative solution of the minimization problem of homogenization (8.10) by a finite element method, the fluctuation field and its gradient are discretized by

$$\mathbf{w}_{n+1}^h(\mathbf{X}) = \mathbf{N}_e(\mathbf{X}) \cdot \mathbf{d}_{n+1}^e \quad \text{and} \quad \nabla \mathbf{w}_{n+1}^h = \mathbf{B}_e(\mathbf{X}) \cdot \mathbf{d}_{n+1}^e \quad \text{in } \mathcal{B}^e \quad (8.13)$$

**Table 8.1:** Discretization of incremental variational problem of homogenization.

Macro-scale	<p>I. Boundary Conditions: <math>\bar{\mathbf{u}} = \bar{\mathbf{u}}^{\text{prescr}}</math> on <math>\partial\bar{\mathcal{B}}_{\bar{\mathbf{u}}}</math>, <math>\bar{\mathbf{T}} = \bar{\mathbf{T}}^{\text{prescr}}</math> on <math>\partial\bar{\mathcal{B}}_{\bar{\mathbf{T}}}</math>.</p> <p>II. Solve microscopic homogenization problem in each macro-(integration) point <math>\bar{\mathbf{X}}</math>:</p> <div style="border: 1px solid black; padding: 5px; margin: 5px 0;"> <p style="text-align: center;">Micro-scale</p> <ol style="list-style-type: none"> <li>1. Given Database <math>\{\bar{\mathbf{F}}, \mathbf{d}_n\}</math>. Initialize nodal displacements <math>\mathbf{d}_{n+1} = \mathbf{d}_n</math>.</li> <li>2. Evaluate derivatives of minimization function <math>\bar{W}^h(\bar{\mathbf{F}}_{n+1}, \mathbf{d}_{n+1})</math>:           <math display="block">\bar{W}_{,\mathbf{d}}^h = \frac{1}{ \mathcal{V} } \mathbf{A}_{e=1}^{n_{ele}} \int_{\mathcal{B}^e} \mathbf{B}_e^T \cdot \mathbf{P}_{n+1} dV, \quad \bar{W}_{,\mathbf{d}\mathbf{d}}^h = \frac{1}{ \mathcal{V} } \mathbf{A}_{e=1}^{n_{ele}} \int_{\mathcal{B}^e} \mathbf{B}_e^T \cdot \mathcal{A}_{n+1} \cdot \mathbf{B}_e dV,</math> <math display="block">\bar{W}_{,\bar{\mathbf{F}}}^h = \frac{1}{ \mathcal{V} } \mathbf{A}_{e=1}^{n_{ele}} \int_{\mathcal{B}^e} \mathbf{P}_{n+1} dV, \quad \bar{W}_{,\bar{\mathbf{F}}\bar{\mathbf{F}}}^h = \frac{1}{ \mathcal{V} } \mathbf{A}_{e=1}^{n_{ele}} \int_{\mathcal{B}^e} \mathcal{A}_{n+1} dV,</math> <math display="block">\bar{W}_{,\mathbf{d}\bar{\mathbf{F}}}^h = \frac{1}{ \mathcal{V} } \mathbf{A}_{e=1}^{n_{ele}} \int_{\mathcal{B}^e} \mathbf{B}_e^T \cdot \mathcal{A}_{n+1} dV.</math> </li> <li>3. Convergence check: If <math>(\ \bar{W}_{,\mathbf{d}}^h\  \leq \text{tol})</math> go to 5.</li> <li>4. Newton update of nodal displacements <math>\mathbf{d}_{n+1} \leftarrow \mathbf{d}_{n+1} - [\bar{W}_{,\mathbf{d}\mathbf{d}}^h]^{-1} [\bar{W}_{,\mathbf{d}}^h]</math>, go to 2.</li> <li>5. Nominal macro-stresses and macro-moduli:           <math display="block">\bar{\mathbf{P}}_{n+1}(\bar{\mathbf{X}}) = \bar{W}_{,\bar{\mathbf{F}}}^h \quad \text{and} \quad \bar{\mathcal{A}}_{n+1}(\bar{\mathbf{X}}) = \bar{W}_{,\bar{\mathbf{F}}\bar{\mathbf{F}}}^h - [\bar{W}_{,\bar{\mathbf{F}}\mathbf{d}}^h] [\bar{W}_{,\mathbf{d}\mathbf{d}}^h]^{-1} [\bar{W}_{,\mathbf{d}\bar{\mathbf{F}}}^h]</math> </li> </ol> </div> <p>III. Evaluate derivatives of macroscopic incremental potential energy <math>\bar{\Pi}(\bar{\mathbf{d}}_{n+1})</math>:           <math display="block">\bar{\Pi}_{,\bar{\mathbf{d}}}^h = \mathbf{A}_{e=1}^{n_{ele}} \int_{\bar{\mathcal{B}}^e} \left[ \bar{\mathbf{B}}_e^T \cdot \bar{\mathbf{P}}_{n+1}(\bar{\mathbf{X}}) - \bar{\mathbf{N}}_e^T \cdot \bar{\boldsymbol{\gamma}}_{n+1} \right] d\bar{V} - \mathbf{A}_{e=1}^{n_{ele}} \int_{\partial\bar{\mathcal{B}}_{\bar{\mathbf{t}}}} \bar{\mathbf{N}}_e^T \cdot \bar{\mathbf{t}}_{n+1} d\bar{A}</math> <math display="block">\bar{\Pi}_{,\bar{\mathbf{d}}\bar{\mathbf{d}}}^h = \mathbf{A}_{e=1}^{n_{ele}} \int_{\bar{\mathcal{B}}^e} \bar{\mathbf{B}}_e^T \cdot \bar{\mathcal{A}}_{n+1}(\bar{\mathbf{X}}) \cdot \bar{\mathbf{B}}_e d\bar{V}</math> </p> <p>IV. Convergence check: if <math>(\ \bar{\Pi}_{,\bar{\mathbf{d}}}^h\  \leq \text{tol})</math> EXIT.</p> <p>V. Newton update of nodal displacements <math>\bar{\mathbf{d}} \leftarrow \bar{\mathbf{d}} - [\bar{\Pi}_{,\bar{\mathbf{d}}\bar{\mathbf{d}}}^h]^{-1} [\bar{\Pi}_{,\bar{\mathbf{d}}}^h]</math>, go to II.</p>
-------------	--

within the element domain  $\mathcal{B}^e \subset \mathcal{B}$  in terms of the matrix of shape functions  $\mathbf{N}_e$ , the associated gradient matrix  $\mathbf{B}_e$  and the nodal fluctuation vector  $\mathbf{d}_e$ . Thus the spatial discretization of (8.10) defines the function

$$\bar{W}^h(\bar{\mathbf{F}}_{n+1}, \mathbf{d}_{n+1}) = \frac{1}{|\mathcal{V}|} \mathbf{A}_{e=1}^{n_{ele}} \int_{\mathcal{B}^e} W(\bar{\mathbf{F}}_{n+1} + \mathbf{B}_e \cdot \mathbf{d}_{n+1}^e) dV \quad (8.14)$$

in terms of the finite element assembly operator  $\mathbf{A}_{e=1}^{n_{ele}}$  for  $n_{ele}$  elements. Minimization of the function (8.14) with respect to the nodal fluctuations  $\mathbf{d}_{n+1} = \mathbf{A}_{e=1}^{n_{ele}} \mathbf{d}_{n+1}^e$  gives the discretized form of the variational principle (8.10). The necessary condition of this minimization problem reads

$$\bar{W}_{,\mathbf{d}}^h = \mathbf{0} \quad (8.15)$$

This defines a nonlinear system of equations for the determination of the nodal fluctuations  $\mathbf{d}_{n+1}$  which can be solved e.g. by a Newton-Raphson method. The resulting algorithm for the solution of the minimization problem of homogenization (8.10) is included in the overall algorithm for the computational treatment of the micro-to-macro transition of table 8.1.

**8.2.4. Macroscopic Incremental Variational Formulation of Inelasticity.** Finally in view of a solution of the boundary value problem on the macro-scale (see figure 8.1 for an illustration), consider the following potential function  $\bar{\Pi}$  defined in terms of the homogenized incremental stress potential  $\bar{W}$  at the right boundary of a typical time increment  $[t_n, t_{n+1}]$  through

$$\bar{\Pi}(\bar{\varphi}_{n+1}) = \int_{\bar{\mathcal{B}}} \bar{W}(\bar{\mathbf{F}}_{n+1}) d\bar{V} - [\bar{\Pi}_{\text{ext}}(\bar{\varphi}_{n+1}) - \bar{\Pi}_{\text{ext}}(\bar{\varphi}_n)] \quad (8.16)$$

which depends on the actual macroscopic deformation map  $\bar{\varphi}_{n+1}$ .  $\bar{\Pi}_{\text{ext}}$  is the external load potential due to the body forces  $\bar{\mathbf{b}}(\bar{\mathbf{X}}, t)$  in  $\bar{\mathcal{B}}$  and the surface tractions  $\bar{\mathbf{t}}(\bar{\mathbf{X}}, t)$  on  $\partial\bar{\mathcal{B}}_{\bar{\mathbf{t}}}$  and evaluated by  $\bar{\Pi}_{\text{ext}}(\bar{\varphi}) = \int_{\bar{\mathcal{B}}} \bar{\varphi} \cdot \bar{\mathbf{b}} \rho_0 d\bar{V} + \int_{\partial\bar{\mathcal{B}}_{\bar{\mathbf{t}}}} \bar{\varphi} \cdot \bar{\mathbf{t}} dA$ . Crucial for the formulation of this potential function is the possibility to define the incremental stress potential function  $\bar{W}$ . If the constitutive description of the material is restricted to one single scale, i.e. the material response is assumed to be homogeneous over all scales, the stress potential function  $\bar{W}$  is directly defined through (8.1). If, however, possible microheterogeneities are resolved through a homogenization analysis, the homogenized stress potential  $\bar{W}$  is determined by (8.10). Now with the functional  $\bar{\Pi}$  at hand, the actual deformation map is determined by a *principle of minimum potential energy* in the sense

$$\bar{\Pi}(\bar{\varphi}_{n+1}^*) = \inf_{\bar{\varphi}_{n+1} \in \bar{\mathcal{W}}} \bar{\Pi}(\bar{\varphi}_{n+1}) \quad (8.17)$$

which minimizes the functional (8.16) for an admissible macro-deformation map  $\bar{\varphi}_{n+1} \in \bar{\mathcal{W}} := \{\bar{\varphi}_{n+1} \in \mathcal{W}^{1,p}(\bar{\mathcal{B}}) \mid \bar{\varphi}_{n+1} = \bar{\varphi}_{n+1}^{\text{prescr}}$  on  $\partial\bar{\mathcal{B}}_{\bar{\varphi}}\}$ . This minimization principle for standard dissipative materials represents an analogon to the *principle of minimum potential energy* in finite elasticity. The solution of (8.17) can be determined in a straightforward manner through discretization in the context of a displacement-type finite element formulation with the following discretizations for the displacements and their gradients

$$\bar{\mathbf{d}}_{n+1}^h(\bar{\mathbf{X}}) = \bar{\mathbf{N}}_e(\bar{\mathbf{X}}) \cdot \bar{\mathbf{d}}_{n+1}^e \quad \text{and} \quad \nabla \bar{\mathbf{d}}_{n+1}^h = \bar{\mathbf{B}}_e(\bar{\mathbf{X}}) \cdot \bar{\mathbf{d}}_{n+1}^e \quad \text{in} \quad \bar{\mathcal{B}}^e \quad (8.18)$$

Based on these interpolations the discrete necessary conditions of the minimization problem (8.17) read

$$\bar{\Pi}_{,\bar{\mathbf{d}}}^h = \mathbf{0} \quad (8.19)$$

This provides a system of nonlinear equations for the determination of the macroscopic nodal displacements  $\bar{\mathbf{d}}_{n+1} = \mathbf{A}_{e=1}^{\bar{n}_{ele}} \bar{\mathbf{d}}_{n+1}^e$ . The corresponding macroscopic solution algorithm is summarized in table 8.1 together with its microscopic counterpart.

### 8.3. Non-Convex Homogenization for Standard Dissipative Materials

After discussing the incremental variational formulation of the homogenization problem in the preceding sections, criteria for a stability analysis will now be introduced. These stability criteria are mainly an extension of the corresponding criteria of finite strain elasticity, as discussed in MIEHE ET AL. [108], to the general case of standard dissipative materials. This extension crucially relies on the introduced incremental variational setting of inelasticity. Recent developments in the mathematical theory for the existence of sufficiently stable minimizers in incremental finite strain elastoplasticity can be found in MIELKE & MÜLLER [110]. Finally, the development of a homogenization approach for the postcritical non-convex regime will be presented and the interaction between instabilities on the micro- and the macro-scale will be discussed.

**8.3.1. Stability Analysis of Inelastic Microheterogeneous Solids.** Micro-instabilities significantly alter the macroscopic material behavior. For example, micro-buckling of stiff fibers leads to a considerable softening in the macro-response accompanied by localized discontinuities on the macro-scale. In order to gain more insight into such instability phenomena, *material* and *structural instability criteria* will be introduced on the micro- and macro-scale in the following.

**8.3.1.1. Stability Analysis in Macroscopic Finite Inelasticity.** To begin with the instability analysis on the macro-scale, recall the incremental macroscopic boundary value problem in its *direct variational form*

$$\bar{\Pi}(\bar{\varphi}_{n+1}^*) = \inf_{\bar{\varphi}_{n+1} \in \bar{\mathcal{W}}} \bar{\Pi}(\bar{\varphi}_{n+1}) = \inf_{\bar{\varphi}_{n+1} \in \bar{\mathcal{W}}} \left\{ \int_{\bar{\mathcal{B}}} \bar{W}(\bar{\mathbf{F}}_{n+1}) d\bar{V} - [\bar{\Pi}_{\text{ext}}(\bar{\varphi}_{n+1}) - \bar{\Pi}_{\text{ext}}(\bar{\varphi}_n)] \right\} \quad (8.20)$$

A solution  $\bar{\varphi}_{n+1}^*$  of the direct problem exists if the functional  $\bar{\Pi}$  is (i) *coerciv* and (ii) *sequentially weakly lower semicontinuous*, (*s.w.l.s.*) (TONELLI [150], DACOROGNA [34], NGUYEN [118]). Thereby *coercivity* demands

$$\bar{\Pi}(\bar{\varphi}_{n+1}) \geq \alpha \|\bar{\varphi}_{n+1}\| + \beta \quad \text{with} \quad \alpha \in \mathcal{R}^+, \beta \in \mathcal{R} \quad (8.21)$$

which ensures an infinitely increasing resistance of the material ( $\bar{\Pi} \rightarrow \infty$ ) to excessive deformations ( $\det[\mathbf{F}_{n+1}] \rightarrow 0^+$  or  $\|\mathbf{F}_{n+1}\| \rightarrow \infty$ ). Sequential weak lower semicontinuity of the functional  $\bar{\Pi}$  is expressed by the condition

$$\bar{\Pi}(\bar{\varphi}_{n+1}^*) \leq \lim_{N \rightarrow \infty} \left\{ \inf_{\bar{\varphi}_{n+1}^N} \bar{\Pi}(\bar{\varphi}_{n+1}^N) \right\} \quad \text{for} \quad \bar{\varphi}_{n+1}^N \rightharpoonup \bar{\varphi}_{n+1} \quad (8.22)$$

which demands that the value of the functional in the solution point  $\bar{\varphi}_{n+1}^*$  is always less or equal than the limit value for any series  $\bar{\varphi}_{n+1}^N$  weakly convergent to this solution point.

Several (*weak*) *convexity* properties of the integrand  $\bar{W}$  represent necessary conditions for the sequential weak lower semicontinuity of the functional  $\bar{\Pi}$ . These convexity conditions will be discussed in the following. Thereby the considerations will be restricted to the internal part  $\bar{\Pi}_{\text{int}} = \int_{\bar{\mathcal{B}}} \bar{W}(\bar{\mathbf{F}}_{n+1}) d\bar{V}$  without a loss of generality. Strictly speaking, Ball's theory as presented below is not applicable in the case of finite strain elastoplasticity. As discussed in detail in chapter 5, in this case generally neither the plastic part  $\mathbf{F}^p$  nor the elastic part  $\mathbf{F}^e$  is compatible and hence a gradient field. Consequently an additional incorporation of an incompatibility measure, e.g. the dislocation density tensor  $\mathbf{A}$ , into the constitutive relations is required. In this sense it has recently been shown by MIELKE & MÜLLER [110] that an extension of the stored energy function through an additional inclusion of a general *convex* dependence on the dislocation density tensor is sufficient to guarantee lower semicontinuity. However, this would, in the present context, require a *higher order homogenization analysis* (which in contrast to KOUZNETSOVA ET AL. [75] bases already on a non-classical formulation of the microscopic problem). Furthermore, an incorporation of corresponding concepts on the macro-scale would a priori regularize the development of material instabilities on that scale and thus limit the development of structural instabilities on the micro-scale. Since a key concern in the following is the investigation of an intimate connection between structural micro- and material macro-instabilities, the inclusion of such regularizing terms is not considered here.

**Convexity** of the macroscopic stress potential function  $\bar{W}$  is a *sufficient* but *not a necessary condition* for sequential weak lower semicontinuity of  $\bar{\Pi}_{\text{int}}$ .  $\bar{W}$  is *convex* if the convexity condition

$$\bar{W}(\bar{\mathbf{F}}_{n+1} + \xi \Delta \bar{\mathbf{F}}) \leq \bar{W}(\bar{\mathbf{F}}_{n+1}) + \xi [\bar{W}(\bar{\mathbf{F}}_{n+1} + \Delta \bar{\mathbf{F}}) - \bar{W}(\bar{\mathbf{F}}_{n+1})] \quad (8.23)$$

holds for arbitrary perturbations  $\Delta \bar{\mathbf{F}}$  of the actual deformation state  $\bar{\mathbf{F}}_{n+1}$  and  $0 < \xi < 1$ . Convexity of  $\bar{W}$  guarantees  $\bar{\Pi}_{\text{int}}$  to be s.w.l.s. but as shown by BALL [13], COLEMAN & NOLL [30] and HILL [57] and summarized in MARSDEN & HUGHES [90] this strong restriction constrains the material behavior in a nonphysical manner and is thus unacceptable. These nonphysical restrictions are briefly reiterated as follows. Since convexity implies uniqueness, global stability problems like buckling would be a priori excluded in the case of a convex  $\bar{W}$ . Furthermore, the convexity condition is incompatible with the principle of material frame invariance and precludes the limit  $\bar{W} \rightarrow \infty$  for  $\det[\bar{\mathbf{F}}] \rightarrow 0$ .

**Polyconvexity** is a less restrictive and, as shown by BALL [13], *sufficient condition* for sequential weak lower semicontinuity of  $\bar{\Pi}_{\text{int}}$ .  $\bar{W}$  is *polyconvex* if a *convex function*  $\bar{W}_{\text{poly}}$  with an extended list of arguments exists such that

$$\bar{W}(\bar{\mathbf{F}}_{n+1}) = \bar{W}_{\text{poly}}(\{\bar{\mathbf{F}}_{n+1}, \det[\bar{\mathbf{F}}_{n+1}] \bar{\mathbf{F}}_{n+1}^{-T}, \det[\bar{\mathbf{F}}_{n+1}]\}^T) \quad (8.24)$$

Thus the polyconvexity condition demands that the function  $\bar{W}_{\text{poly}}$  is convex with respect to each of its arguments  $\bar{\mathbf{F}}_{n+1}, \det[\bar{\mathbf{F}}_{n+1}] \bar{\mathbf{F}}_{n+1}^{-T} =: \text{cof}[\bar{\mathbf{F}}_{n+1}]$  and  $\det[\bar{\mathbf{F}}_{n+1}]$ . Unlike the convexity condition, the polyconvexity condition does not violate physical principles. However, since the macroscopic potential function  $\bar{W}$  is obtained as the solution of the minimization problem (8.10),  $\bar{W}$  is not a priori a constitutive function in the full range of  $\bar{\mathbf{F}}$ . Thus it is not possible to check the polyconvexity condition in the present context.

**Quasiconvexity** is a weaker convexity condition and was introduced by MORREY [112]. The quasiconvexity condition reads for an arbitrary part  $\bar{\Omega}$  of the inelastic solid

$$\frac{1}{|\bar{\Omega}|} \int_{\bar{\Omega}} \bar{W}(\bar{\mathbf{F}}_{n+1} + \nabla \bar{\mathbf{v}}(\bar{\mathbf{Y}})) d\bar{V} \geq \bar{W}(\bar{\mathbf{F}}_{n+1}) \quad (8.25)$$

with  $\bar{\mathbf{v}}(\bar{\mathbf{Y}}) \in W_0^{1,\infty}$  and  $\bar{\mathbf{Y}} \in \bar{\Omega}$ . Thus it demands that among all deformations with support on  $\partial \bar{\Omega}$  the homogeneous deformation  $\bar{\mathbf{F}}_{n+1}$  provides an absolute minimizer of the function  $\bar{W}$ . Consequently quasiconvexity of  $\bar{W}$  rules out internal buckling, the development of local fine-scale micro-structures or phase decompositions of a homogeneous local deformation state characterized by an internal (due to  $\bar{\mathbf{v}} = \mathbf{0}$  on  $\partial \bar{\Omega}$ ) fluctuation field  $\bar{\mathbf{v}}$ . Quasiconvexity plays a central role within existence theorems in the special case of finite strain elasticity. In this case it can be shown that, under certain growth conditions, quasiconvexity of the integrand guarantees as a *necessary* and *sufficient condition* (DACOROGNA [34]) s.w.l. semicontinuity of the internal energy functional. For general standard dissipative materials quasiconvexity of  $\bar{W}$  is a *necessary* but from the mathematical viewpoint due to the missing proof not yet sufficient *condition* for the existence of a minimizer in (8.20). Nevertheless, it can be expected that quasiconvexity represents as well in the present context the central criterion in the stability analysis of the homogenized material.

**Rank-1-convexity** is the weakest of the discussed convexity conditions and reads

$$\bar{W}(\bar{\mathbf{F}}_{n+1} + \xi \bar{\mathbf{p}} \otimes \bar{\mathbf{N}}) \leq \bar{W}(\bar{\mathbf{F}}_{n+1}) + \xi [\bar{W}(\bar{\mathbf{F}}_{n+1} + \bar{\mathbf{p}} \otimes \bar{\mathbf{N}}) - \bar{W}(\bar{\mathbf{F}}_{n+1})] \quad (8.26)$$

for  $0 < \xi < 1$ . Thus it describes *local material stability* against *rank-one perturbations*  $\Delta \bar{\mathbf{F}} = \bar{\mathbf{p}} \otimes \bar{\mathbf{N}}$  with arbitrary directions  $\bar{\mathbf{p}}$  and  $\bar{\mathbf{N}}$ . For a twice differentiable  $\bar{W}$  (8.26) implies the *infinitesimal rank-1-convexity* or *Hadarmard condition* (HADARMARD [52], TRUESDELL & NOLL [153])

$$(\bar{\mathbf{p}} \otimes \bar{\mathbf{N}}) : \bar{\mathcal{A}}_{n+1} : (\bar{\mathbf{p}} \otimes \bar{\mathbf{N}}) \geq 0 \quad \text{with} \quad \bar{\mathcal{A}}_{n+1} := \partial_{\bar{\mathbf{F}}}^2 \bar{W}(\bar{\mathbf{F}}_{n+1}, \bar{\mathbf{X}}) \quad (8.27)$$

where  $\bar{\mathcal{A}}_{n+1}$  denotes the consistent macroscopic tangent moduli. An alternative representation of (8.27) reads

$$\bar{\mathbf{p}} \cdot (\bar{\mathbf{Q}}_{n+1} \cdot \bar{\mathbf{p}}) \geq 0 \quad \text{with} \quad [\bar{\mathbf{Q}}_{n+1}]_{ab} := [\bar{\mathcal{A}}_{n+1}]_a^{A B} \bar{N}_A \bar{N}_B \quad (8.28)$$

which demands *positive semidefiniteness* of the *acoustic tensor*  $\bar{\mathbf{Q}}$ . Positive semidefiniteness of the acoustic tensor guarantees that the Euler equations  $\text{DIV}[\bar{W}_{,\bar{\mathbf{F}}}] + \rho_0 \bar{\mathbf{b}} = \mathbf{0}$  of the macroscopic problem (8.17) are *strictly elliptic*. (Within the wave theory strict ellipticity ensures real wave propagation speeds.) If rank-1-convexity is not a priori known an *accompanying algorithmic control for rank-1-convexity* in any macroscopic point  $\bar{\mathbf{X}}$  can be based on the alternative criterion  $\det[\bar{\mathbf{Q}}_{n+1}(\bar{\mathbf{N}})] \geq 0$ . Thus if for any direction  $\bar{\mathbf{N}}$  a violation in the sense  $\det[\bar{\mathbf{Q}}_{n+1}(\bar{\mathbf{N}})] \leq 0$  occurs, strict rank-1-convexity of  $\bar{W}$  is lost, i.e.

$$\min_{\|\bar{\mathbf{N}}\|=1} \{ \det[\bar{\mathbf{Q}}_{n+1}] \} \begin{cases} > 0 & \text{for strictly infinit. Rank-1-convex } \bar{W}(\bar{\mathbf{F}}_{n+1}) \\ \leq 0 & \text{for not strictly infinit. Rank-1-convex } \bar{W}(\bar{\mathbf{F}}_{n+1}) \end{cases} \quad (8.29)$$

A computational treatment of this check is outlined for 2D problems in MIEHE & SCHRÖDER [105]. The occurrence of material instabilities in the sense of (8.29) induces a failure of ellipticity and consequently the development of jump discontinuities of the macroscopic deformation gradient along a singular surface with normal direction  $\bar{\mathbf{N}}$ . The Eulerian vector  $\bar{\mathbf{p}}$  characterizes the kind of jump discontinuity.

The four convexity conditions (8.23)-(8.26) of the homogenized incremental stress potential  $\bar{W}$  are related by

$$\text{convexity} \Rightarrow \text{polyconvexity} \Rightarrow \text{quasiconvexity} \Rightarrow \text{rank-1-convexity}$$

where the stronger condition always induces the weaker convexity condition. The inverse relationships are not generally valid. While convexity implies stability of the actual energetic state  $\bar{W}(\bar{\mathbf{F}}_{n+1})$  with respect to *arbitrary perturbations*  $\Delta \bar{\mathbf{F}}$ , polyconvexity requires stability for *(combined) changes of line-, surface and volume elements* through  $\Delta \bar{\mathbf{F}}$ ,  $\text{cof}[\Delta \bar{\mathbf{F}}]$  and  $\det[\Delta \bar{\mathbf{F}}]$ . Quasiconvexity demands stability with respect to *internal fluctuations*  $\Delta \bar{\mathbf{F}} = \nabla \bar{\mathbf{v}}$  with support on the surface ( $\bar{\mathbf{v}} = \mathbf{0}$  on  $\partial \bar{\Omega}$ ) and rank-1-convexity demands local material stability against the development of *first order laminates* characterized by  $\Delta \bar{\mathbf{F}} = \bar{\mathbf{p}} \otimes \bar{\mathbf{N}}$ . As pointed out earlier, quasiconvexity is considered as the key condition in the analysis of local material stability. A loss of rank-1-convexity implies a loss of quasiconvexity and thus the existence of a sufficiently regular minimizer for the direct problem (8.20) is no longer guaranteed.

For materials being initially homogeneous over all scales, a loss of material stability indicates the development of fine-scale deformation inhomogeneities. In turn, for a priori microheterogeneous solids material instabilities on the superior homogeneous scale are induced by structural instabilities on the micro-scale. This interaction between structural and material instabilities on the micro- and macro-scale is considered in section 8.3.3.

Finally, the criterion for a *local structural stability* analysis on the macro-scale will be discussed. Therefore the energy state in the *actual equilibrium configuration*  $\bar{\varphi}_{n+1}^*$  is compared with the energy state in an *arbitrary configuration*  $\bar{\varphi}_{n+1}^* + \delta\bar{\varphi}$  in the *infinitesimal neighborhood* of  $\bar{\varphi}_{n+1}^*$ . Accordingly, structural instabilities of the macro-structure like buckling occur if the *local or infinitesimal structural stability condition*

$$\bar{\Pi}(\bar{\varphi}_{n+1}^*) - \bar{\Pi}(\bar{\varphi}_{n+1}^* + \delta\bar{\varphi}) = \frac{1}{2} \int_{\bar{B}} \nabla \delta\bar{\varphi} : \bar{\mathcal{A}}_{n+1} : \nabla \delta\bar{\varphi} d\bar{V} > 0 \quad (8.30)$$

is violated. Thus the criterion states that any kinematically admissible *infinitesimal perturbation*  $\delta\bar{\varphi}$  of the equilibrium state  $\bar{\varphi}_{n+1}^*$  results in an increase in energy. The discrete counterpart to (8.30) reads in the actual solution point  $\bar{\mathbf{d}}_{n+1}^*$

$$\bar{\Pi}^h(\bar{\mathbf{d}}_{n+1}^*) - \bar{\Pi}^h(\bar{\mathbf{d}}_{n+1}^* + \delta\bar{\mathbf{d}}) = \frac{1}{2} \delta\bar{\mathbf{d}}^T \cdot [\bar{\Pi}_{,\bar{\mathbf{d}}\bar{\mathbf{d}}}^h(\bar{\mathbf{d}}_{n+1}^*)] \cdot \delta\bar{\mathbf{d}} \quad (8.31)$$

which demands *positive definiteness of the tangential stiffness matrix*  $\bar{\Pi}_{,\bar{\mathbf{d}}\bar{\mathbf{d}}}^h(\bar{\mathbf{d}}_{n+1}^*)$  of the discretized macro-structure defined in step III in table 8.1. Possible *equilibrium path following methods* are in complete analogy to the ones discussed in connection with the structural instability analysis on the micro-scale in the following subsection 8.3.1.2. In the present macroscopic analysis these methods base on a parametrization of the external loads in terms of a load parameter  $\bar{\lambda} \in \mathcal{R}$  for example in the form

$$\bar{\lambda} \mapsto \rho_0 \bar{\mathbf{b}}_{\bar{\lambda}} := \rho_0 \bar{\lambda} \bar{\mathbf{b}} \quad \text{and} \quad \bar{\lambda} \mapsto \bar{\mathbf{t}}_{\bar{\lambda}} := \bar{\lambda} \bar{\mathbf{t}} \quad (8.32)$$

**8.3.1.2. Stability Analysis in Microscopic Finite Inelasticity.** The *direct variational form* of the homogenization problem is given by (8.10). In analogy to the previous considerations sufficiently regular minimizers  $\mathbf{w} \in \mathcal{W}^\#$  exist if the potential function  $\bar{W}$  is (i) *coerciv* and (ii) *s.w.l.s.*

**Convexity** of the microscopic stress potential function  $W$  demands

$$W(\mathbf{F}_{n+1} + \xi \Delta \mathbf{F}) \leq W(\mathbf{F}_{n+1}) + \xi [W(\mathbf{F}_{n+1} + \Delta \mathbf{F}) - W(\mathbf{F}_{n+1})] \quad (8.33)$$

for  $0 < \xi < 1$  and arbitrary perturbations  $\Delta \mathbf{F} = \nabla \mathbf{v}$  of the actual microscopic equilibrium configuration  $\mathbf{F}_{n+1} = \bar{\mathbf{F}}_{n+1} + \nabla \mathbf{w}_{n+1}$  where  $\mathbf{v}$  satisfies the essential boundary conditions (8.11). Convexity of  $W$  guarantees  $\bar{W}$  to be s.w.l.s.. However, as pointed out above convexity of  $W$  is a too restrictive condition and hence physically unacceptable.

**Polyconvexity** of  $W$  is a less restrictive and in connection with coercivity sufficient condition for the existence of minimizers  $\mathbf{w}_{n+1}$  in (8.10).  $W$  is polyconvex if a convex function  $W_{\text{poly}}$  with an extended list of arguments exists such that

$$W(\mathbf{F}_{n+1}) = W_{\text{poly}}(\{\mathbf{F}_{n+1}, \text{cof}[\mathbf{F}_{n+1}], \det[\mathbf{F}_{n+1}]\}^T) \quad (8.34)$$

Hence the polyconvexity condition demands that the function  $W_{\text{poly}}$  is convex with respect to each of its arguments  $\mathbf{F}_{n+1}$ ,  $\text{cof}[\mathbf{F}_{n+1}]$  and  $\det[\mathbf{F}_{n+1}]$ . However, since the incremental stress potential function  $W$  is obtained as the solution of the minimization problem (8.1),  $W$  is not a priori a constitutive function in the full range of  $\mathbf{F}$ . Consequently, it is not possible to directly check the polyconvexity condition in the present context.

**Quasiconvexity** of the microscopic stress potential  $W$  is, in analogy to the previous discussion, considered as the *key criterion for local material stability of the incremental*

response of standard dissipative solids. For a loss of quasiconvexity of  $W$  on the micro-scale the existence of sufficiently regular minimizers of (8.10) can no longer be guaranteed. Vice versa, a quasiconvex  $W$  ensures from an engineering viewpoint in connection with certain growth conditions a sufficiently stable solution. The quasiconvexity condition

$$\frac{1}{|\Omega|} \int_{\Omega} W(\mathbf{F}_{n+1} + \nabla \mathbf{v}(\mathbf{Y})) dV \geq W(\mathbf{F}_{n+1}) \quad (8.35)$$

demands stability of the actual micro-deformation state  $\mathbf{F}_{n+1} = \bar{\mathbf{F}}_{n+1} + \nabla \mathbf{w}_{n+1}$  with respect to fluctuations  $\mathbf{v}(\mathbf{Y})$  at  $\mathbf{Y} \in \Omega$  with support on  $\partial\Omega$  where  $\Omega$  is an arbitrarily chosen part of the standard dissipative solid. Hence (8.35) rules out internal buckling, the development of local fine-scale micro-structures on the micro-level and phase decompositions of an initially homogeneous deformation state.

**Rank-1-convexity** can be considered as a close approximation of the quasiconvexity condition and reads in its incremental format

$$(\mathbf{p} \otimes \mathbf{N}) : \mathcal{A}_{n+1} : (\mathbf{p} \otimes \mathbf{N}) \geq 0 \quad \text{with} \quad \mathcal{A}_{n+1} := \partial_{\mathbf{F}\mathbf{F}}^2 W(\mathbf{F}_{n+1}, \mathbf{X}) \quad (8.36)$$

which demands positive semidefiniteness of the microscopic acoustic tensor  $[Q_{n+1}]_{ab} := [\mathcal{A}_{n+1}]_a^A b^B N_A N_B$  for arbitrary unit vectors  $\mathbf{N}$ . A loss of rank-1-convexity implies a loss of quasiconvexity and thus the existence of sufficiently regular minimizers of the homogenization problem is no longer guaranteed. However, in the remainder of this chapter the local material response on the micro-scale is considered to be sufficiently stable. (According to MIELKE & MÜLLER [110] and as discussed in section 8.3.1.1, this might a priori be guaranteed through the inclusion of a convex dependence of the micro-energy storage function on the dislocation density tensor  $\mathbf{A}$  as a regularizing contribution.)

Finally, the *local structural stability analysis* on the micro-scale will be considered. Therefore the functional  $\bar{W}$  is evaluated for the actual equilibrium fluctuation field  $\mathbf{w}$  and a fluctuation field  $\mathbf{w} + \delta\mathbf{w}$  in the infinitesimal neighborhood of the equilibrium state. The fluctuation field  $\mathbf{w}$  is *locally stable* if the infinitesimal structural stability criterion

$$\bar{W}(\bar{\mathbf{F}}_{n+1}, \mathbf{w}_{n+1} + \delta\mathbf{w}) - \bar{W}(\bar{\mathbf{F}}_{n+1}, \mathbf{w}_{n+1}) = \frac{1}{2} \frac{1}{|\mathcal{V}|} \int_{\mathcal{B}} \nabla \delta\mathbf{w} : \mathcal{A}_{n+1} : \nabla \delta\mathbf{w} dV > 0 \quad (8.37)$$

is satisfied. Hence any kinematically admissible infinitesimal perturbation  $\delta\mathbf{w}$  of the equilibrium state results in an increase of the energetic state. The discrete counterpart of (8.37) reads in the actual solution point  $\mathbf{d}_{n+1}$

$$\bar{W}^h(\bar{\mathbf{F}}_{n+1}, \mathbf{d}_{n+1} + \delta\mathbf{d}) - \bar{W}^h(\bar{\mathbf{F}}_{n+1}, \mathbf{d}_{n+1}) = \frac{1}{2} \delta\mathbf{d}^T \cdot [\bar{W}_{,\mathbf{d}\mathbf{d}}^h(\bar{\mathbf{F}}_{n+1}, \mathbf{d}_{n+1})] \cdot \delta\mathbf{d} > 0 \quad (8.38)$$

which demands positive definiteness of the tangential stiffness matrix  $\bar{W}_{,\mathbf{d}\mathbf{d}}^h$  of the discretized micro-structure specified in table 8.1, step II/2.

The detection of *limit* and *bifurcation points* can be based on *equilibrium path following methods* as outlined for example in WRIGGERS ET AL. [157]. In the present context such a method might be based on a parametrization of the loading of the micro-structure in terms of a loading parameter  $\lambda \in \mathcal{R}$  through  $\lambda \mapsto \{\bar{\mathbf{F}}_{\lambda}\}_{n+1} := \lambda \bar{\mathbf{F}}_{n+1}$ . This induces a dependence of the discrete homogenized stress potential (8.14) on  $\lambda$ . Starting from some initial point, the loading is advanced along the equilibrium path in the space  $\mathcal{R}^{m+1}$  of the

discrete fluctuations  $\mathbf{d}_{n+1} \in \mathcal{R}^m$  and the loading parameter  $\lambda$ . This path is parametrized by the arclength  $s \in \mathcal{R}$

$$s \mapsto \begin{cases} \{\mathbf{d}_s\}_{n+1} \\ \lambda_s \end{cases} \quad (8.39)$$

where the position on the equilibrium path is updated in finite increments  $\Delta s$  through  $s \leftarrow s + \Delta s$ . In each increment, the eigenvalue problem

$$\delta \mathbf{d}_s^T \cdot [\bar{W}_{,\mathbf{d}\mathbf{d}}^h(\{\mathbf{d}_s\}_{n+1}, \lambda_s)] \cdot \delta \mathbf{d}_s = \mu_s \delta \mathbf{d}_s^T \cdot \delta \mathbf{d}_s \quad (8.40)$$

induced by the stability criterion (8.38) is solved for the minimum spectrum of eigenvalues  $\mu_s$ . The stability of the discrete fluctuation state  $\{\mathbf{d}_s\}_{n+1}$  at the position  $s$  of the equilibrium path can be characterized by the sign of the eigenvalues  $\mu_s$ , i.e.

$$\min[\mu_s] \begin{cases} > 0 & \text{for a locally stable fluctuation state } \{\mathbf{d}_s\}_{n+1} \\ \leq 0 & \text{for a locally unstable fluctuation state } \{\mathbf{d}_s\}_{n+1} \end{cases} \quad (8.41)$$

Based on the buckling mode  $\delta \mathbf{d}_s$  obtained as an eigenvector of (8.40) associated with a critical eigenvalue, a differentiation of the type of structural instability may be based on

$$\delta \mathbf{d}_s^T \bar{W}_{,\mathbf{d}\lambda}^h(\{\mathbf{d}_s\}_{n+1}, \lambda_s) \begin{cases} = 0 & \text{for a simple bifurcation point} \\ \neq 0 & \text{for a limit point} \end{cases} \quad (8.42)$$

At a bifurcation point, the deformation may switch from the primary equilibrium path into a secondary equilibrium path. This branch switch may numerically be triggered by a perturbation  $\{\mathbf{d}_s\}_{n+1} \leftarrow \{\mathbf{d}_s\}_{n+1} + \epsilon \delta \mathbf{d}_s / \|\delta \mathbf{d}_s\|$  of the current displacement vector by the buckling mode  $\delta \mathbf{d}_s$  scaled with a small perturbation parameter  $\epsilon$ .

**8.3.2. Size of the Representative Micro-structure.** Structural instabilities on the micro-scale raise the fundamental problem to specify the relevant size of the micro-structure which catches the energy minimizing failure mode. This is alternatively expressed by a loss of ellipticity of the homogenization functional. To this end, consider first the specification of the micro-structure  $\mathcal{V}$  representative of a periodic composite as an *ensemble of  $n_c$  generic cells  $\mathcal{C}$*  according to

$$\mathcal{V}(n_c) := \bigcup_{k=1}^{n_c} \mathcal{C}_k \quad \text{with} \quad n_c = 1, 8, 27, 64 \quad (8.43)$$

for three-dimensional and  $n_c = 1, 4, 9, 16, \dots$  for two-dimensional problems. A visualization of (8.43) is given in figure 8.3. If stability problems like buckling modes occur on the micro-scale of the periodic composite, the representative volume element  $\mathcal{V}$  must comprise of a critical number of unit cells  $n_c$  in order to capture the relevant micro-buckling modes. The wavelengths of the buckling modes are not a priori known and may completely change during the deformation process. As a consequence, the critical ensemble size  $n_c$  is a priori unknown as well. Thus  $n_c$  must be considered as an unknown in the analysis of periodic composites at finite strains when stability modes on the micro-structure may occur. This is considered to be a fundamental difficulty of the homogenization theory at large strains.

The determination of the critical ensemble size  $n_c$  bases on fundamental investigations by MÜLLER [114] on non-convex integral functionals employing the notion of  $\Gamma$ -convergence.

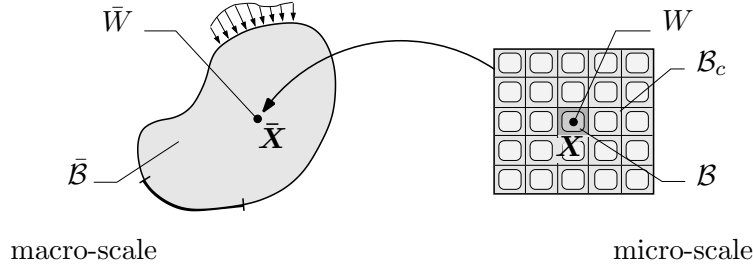


**Figure 8.3:** Assembly of the representative micro-structure from generic cells in a periodic composite. The combination of  $n_c$  generic cells  $\mathcal{B} \subseteq \mathcal{B}_c$  gives the critical micro-structure  $\mathcal{B}_c$  which catches the energy minimizing failure mode.

As shown by MÜLLER [114], GEYMONAT ET AL. [47] and MIEHE ET AL. [108] for problems of finite elasticity, the size  $\mathcal{V}(n_c)$  of the representative micro-structure follows from a minimization process that envelopes the minimization problem for the determination of the current fluctuation field. Accordingly the macroscopic incremental stress potential is determined based on the microscopic incremental stress potential by the expression

$$\bar{W}(\bar{\mathbf{F}}_{n+1}, \bar{\mathbf{X}}) = \inf_{n_c} \left\{ \inf_{\mathbf{w}_{n+1} \in \mathcal{W}^\#} \frac{1}{|\mathcal{V}(n_c)|} \int_{\mathcal{B}(n_c)} W(\bar{\mathbf{F}}_{n+1} + \nabla \mathbf{w}_{n+1}, \mathbf{X}) dV \right\} \quad (8.44)$$

where the fluctuation field  $\mathbf{w}_{n+1}$  satisfies the periodicity condition (8.11). The minimization problem (8.44) represents the *key homogenization condition in the postcritical non-convex regime*. It determines the fluctuation field  $\mathbf{w}_{n+1}$  and the size  $n_c$  of the representative volume. Thus a *nonphysical dependence* of the homogenized material response in general or of the possibly developing failure modes in particular *upon the size of the representative micro-structure* is excluded through (8.44). Such a size dependence in the material response is highly undesirable unlike the *physically well-founded size effects* observed in connection with *plastically inhomogeneous deformations*, i.e. incompatibilities of the intermediate configuration, as discussed in the preceding chapters.

**8.3.3. Micro-Macro-Interaction of Instability Phenomena.** Finally the interaction between structural instability phenomena on the micro-scale and material instabilities on the macro-scale shall be investigated. TRIANTAFYLIDIS & MAKER [151] showed that a long wave-length micro-instability in a layered composite induces a loss of rank-one convexity of the homogenized moduli on the macro-scale. A generalization of the connection between microscopic and macroscopic instability phenomena for all nonlinear elastic periodic micro-structures is given in GEYMONAT ET AL. [47].

Following essentially the considerations in MIEHE ET AL. [108], the connection between structural instabilities on the micro-scale and material instabilities on the macro-scale can be established as follows. Comparing (8.37) and (8.30) for a locally stable macroscopic material response, one expects

$$\frac{1}{2|\mathcal{V}|} \int_{\mathcal{B}(n_c)} (\delta \bar{\mathbf{F}} + \nabla \delta \mathbf{w}) : \mathcal{A}_{n+1} : (\delta \bar{\mathbf{F}} + \nabla \delta \mathbf{w}) dV \stackrel{!}{=} \frac{1}{2} \delta \bar{\mathbf{F}} : \bar{\mathcal{A}}_{n+1} : \delta \bar{\mathbf{F}} > 0 \quad (8.45)$$

with  $\mathcal{A}_{n+1} = \partial_{\mathbf{F}\mathbf{F}}^2 W(\bar{\mathbf{F}}_{n+1} + \nabla \mathbf{w}_{n+1})$  and  $\bar{\mathcal{A}}_{n+1} = \partial_{\bar{\mathbf{F}}\bar{\mathbf{F}}}^2 \bar{W}(\bar{\mathbf{F}}_{n+1})$ . A typical assumption for the macroscopic stability mode  $\delta \bar{\mathbf{F}}$  in the case of a macroscopic localization is the Maxwell form  $\delta \bar{\mathbf{F}} = \bar{\mathbf{m}} \otimes \bar{\mathbf{M}}$ . Inserting this ansatz into (8.45), the right-hand side reads

$$\frac{1}{2} \delta \bar{\mathbf{F}} : \bar{\mathcal{A}}_{n+1} : \delta \bar{\mathbf{F}} = \frac{1}{2} (\bar{\mathbf{m}} \otimes \bar{\mathbf{M}}) : \bar{\mathcal{A}}_{n+1} : (\bar{\mathbf{m}} \otimes \bar{\mathbf{M}}) > 0 \quad (8.46)$$

which represents the macroscopic condition (8.27) of *strict* infinitesimal rank–one convexity. In the *critical case of a loss of macroscopic rank-one convexity* this expression becomes zero. Then for the critical case (8.45) implies the quadratic incremental minimization problem

$$\inf_{\delta \mathbf{w} \in \mathcal{V}^\#} \frac{1}{2|\mathcal{V}|} \int_{\mathcal{B}(n_c)} (\bar{\mathbf{m}} \otimes \bar{\mathbf{M}} + \nabla \delta \mathbf{w}) : \mathcal{A}_{n+1} : (\bar{\mathbf{m}} \otimes \bar{\mathbf{M}} + \nabla \delta \mathbf{w}) dV = 0 \quad (8.47)$$

where  $\delta \mathbf{w}$  satisfies the periodic boundary conditions (8.11). The associated Euler–Lagrange equation reads

$$\text{Div}[\mathcal{A}_{n+1} : (\bar{\mathbf{m}} \otimes \bar{\mathbf{M}} + \nabla \delta \mathbf{w})] = \mathbf{0}. \quad (8.48)$$

The solution  $\delta \bar{\mathbf{F}} + \nabla \delta \mathbf{w} = \bar{\mathbf{m}} \otimes \bar{\mathbf{M}} + \nabla \delta \mathbf{w}$  of (8.48) is denoted as *shear deformation* modulated by the periodic contribution  $\delta \mathbf{w}$ . It represents a bifurcation mode on the micro–scale that leads to a loss of rank–one convexity of the macroscopic moduli. Hence a loss of ellipticity for the homogenized material corresponds to an onset of long wavelength bifurcation modes on the micro–scale. Consequently a microscopic instability problem associated with (8.48) can be detected by a loss of strict ellipticity associated with the homogenized moduli  $\bar{\mathcal{A}}_{n+1}$ . Note that equations (8.45) and (8.47) hold only for the relevant micro–structure  $\mathcal{B}(n_c)$  and hence the above mentioned connection between micro– and macro–instabilities is only valid for the relevant micro–structure of size  $n_c$ .

#### 8.4. Numerical Examples

In order to reduce the complexity in the following numerical examples, the material response of the micro–constituents will be restricted to *purely phenomenological isotropic elastoplasticity* at finite strains. The constitutive model is developed in terms of a plastic metric formulation within the framework of a logarithmic strain space. Therein the key point is the following additive decomposition of the elastic strain measure  $\mathbf{E}^e$

$$\mathbf{E}^e := \mathbf{E} - \mathbf{E}^p \quad \text{with} \quad \mathbf{E} := \frac{1}{2} \ln[\mathbf{C}] = \frac{1}{2} \ln[\mathbf{F}^T \cdot \mathbf{g} \cdot \mathbf{F}] \quad (8.49)$$

in terms of the *logarithmic Lagrangian total strains* or *Hencky strains*  $\mathbf{E}$  and the *logarithmic Lagrangian plastic strains*  $\mathbf{E}^p$  which can be related to a so-called *plastic metric*  $\tilde{\mathbf{G}}^p \in \text{Sym}_+(3)$  through  $\mathbf{E}^p := \frac{1}{2} \ln[\tilde{\mathbf{G}}^p]$ . The plastic strains together with some additional hardening variables (here  $A$ ) constitute the internal variables  $\mathcal{I}$ . Based on the decomposition (8.49)<sub>1</sub>, the constitutive model is subsequently formulated solely within the logarithmic strain space. In the following, the material response of the micro–constituents is governed by the free energy function

$$\psi = \frac{1}{2} \|\mathbf{E}^e\|_{\mathbb{E}}^2 + \psi^p(A) \quad \text{with} \quad \|\mathbf{E}^e\|_{\mathbb{E}} := \sqrt{\mathbf{E}^e : \mathbb{E} : \mathbf{E}^e} \quad (8.50)$$

where the nonlinear isotropic hardening contribution is given by

$$\psi^p = \frac{1}{2} h A^2 + (y_\infty - y_0) \left( A + \frac{1}{\omega} \exp[-\omega A] \right) \quad (8.51)$$

and by the Von Mises type yield criterion function

$$\phi = \|\mathcal{I}\|_{\mathbb{P}} - \sqrt{2/3} (y_0 - B) \leq 0 \quad \text{with} \quad \|\mathcal{I}\|_{\mathbb{P}} := \sqrt{\mathcal{I} : \mathbb{P} : \mathcal{I}} \quad (8.52)$$

in terms of the logarithmic stresses  $\mathbf{T} := \mathbb{E}:\mathbf{E}^e$ , the internal forces  $B := -hA - (y_\infty - y_0)(1 - \exp[-\omega A])$  and the fourth-order deviatoric projection tensor  $\mathbb{P} := \mathbb{I} - \frac{1}{3}\mathbf{1} \otimes \mathbf{1}$ . Restricting the considerations to elastic isotropy, the fourth-order elasticity tensor reads

$$\mathbb{E} := \left(\kappa - \frac{2}{3}\mu\right)\mathbf{1} \otimes \mathbf{1} + 2\mu\mathbb{I} \quad (8.53)$$

Here it is important to note that the resulting isotropic Hookean quadratic free energy function is not polyconvex in the full range of elastic strains. While the compressive range is not restricted, elastic tensile stretches have to be limited to moderately large values. A detailed investigation which results in a limitation of the principal stretches for incompressible materials can be found in BRUHNS ET AL. [23] or is also deducible from the stress-stretch relations presented in MIEHE & LAMBRECHT [100]. However, the elastic deformations induced in the following model problems always obey these limitations. For a detailed discussion of the constitutive and the algorithmic modeling in the logarithmic strain space refer to MIEHE ET AL. [99].

**8.4.1. Buckling Analysis of a Fiber Reinforced Micro-Structure.** A key point in the analysis of instability phenomena on the micro-scale is the determination of the proper size of the representative micro-structure. According to the previous considerations, the relevant size of the micro-structure is determined from the criterion (8.44). In other words, the problem is to find the proper size  $n_c$  of the representative micro-structure  $\mathcal{B}(n_c)$  which catches the energy minimizing buckling mode, see figure 8.4 for a visualization. Within the

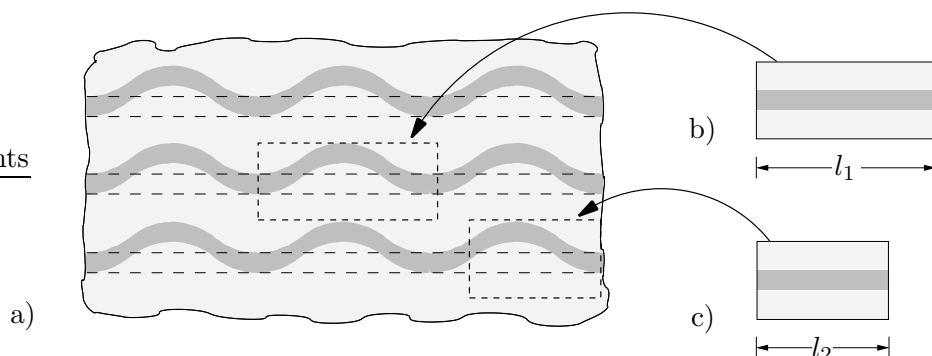


**Figure 8.4:** The problem of finding the relevant size  $l$  of the micro-structure for a fiber-reinforced material. Micro-structure b) has the relevant size. Micro-structure c) is not able to catch the energy minimizing buckling mode with periodic boundary conditions.

following example in Section 8.4.1.1 the relevant size of the micro-structure is determined for a fiber reinforced material consisting of purely elastic constituents. Then in Section 8.4.1.2 the same procedure is employed in order to determine the relevant size of the micro-structure for an elastic-plastic material.

**8.4.1.1. Buckling Analysis of a Purely Elastic Micro-Structure.** In the following a purely elastic periodic heterogeneous material is considered consisting of a soft matrix material surrounding horizontally aligned stiff fibers. The constituents are assumed to be governed by the elastic part of the isotropic stored micro-energy function (8.50). The volume fraction of the fibers is 20 %. Bulk and shear moduli of the soft matrix material are  $\kappa_m = 164.2 \text{ kN/mm}^2$  and  $\mu_m = 80.2 \text{ kN/mm}^2$ , respectively. The material parameters of the stiff fibers are set to  $\kappa_f = 100\kappa_m$  and  $\mu_f = 100\mu_m$ . The deformation of the micro-structure is driven by the macroscopic deformation gradient  $\bar{\mathbf{F}}_{n+1}$  which takes for the

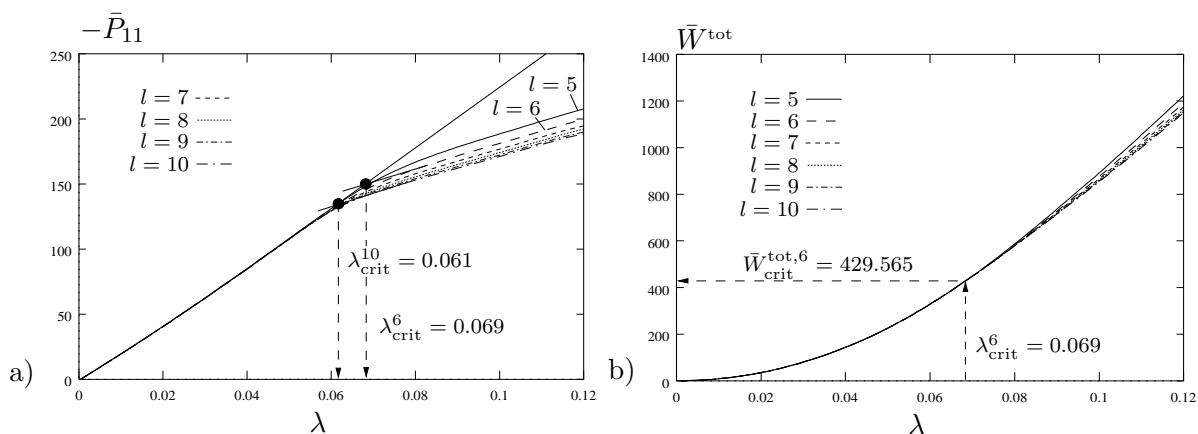


**Figure 8.5:** Determination of the bifurcation point and the respective accumulated energy, purely elastic case. a) Macroscopic first Piola-Kichhoff stress component  $\bar{P}_{11}$ , and b) accumulated macroscopic energy  $\bar{W}^{\text{tot}}$  versus  $\lambda$  for different lengths  $l$  of the micro-structure.

present case of a horizontal compression the following format

$$\bar{\mathbf{F}}_{n+1} = \text{diag}[1 - \lambda, 1, 1] \quad \text{with} \quad \lambda > 0 \quad (8.54)$$

Here  $\lambda$  denotes the compression parameter. For this macroscopic deformation mode two failure modes may occur on the micro-scale. The stiff fibers can either buckle in- or out-of-phase. As the out-of-phase buckling mode is related to a higher energy level in the subsequent investigations, only the relevant in-phase mode is considered to determine the number  $n_c$ , i.e. the size of the micro-structure, which induces an infimum in (8.44) for this mode. For the periodic structure under consideration the number  $n_c$  is thoroughly specified by the length  $l$  of the micro-structure. In view of a determination of the relevant size of the micro-structure, the stress potential  $\bar{W}$  has to be evaluated at the instability point for varying lengths  $l$  in a way similar to that outlined in MIEHE ET AL. [108].

In order to perform a finite element simulation of the problem at hand, the micro-structures of different sizes are discretized with mixed MINI-type triangular elements as conceptually outlined in CROUZEIX & RAVIART [32]. These mixed triangles provide in addition to the two degrees of freedom for the displacements at each node an additional

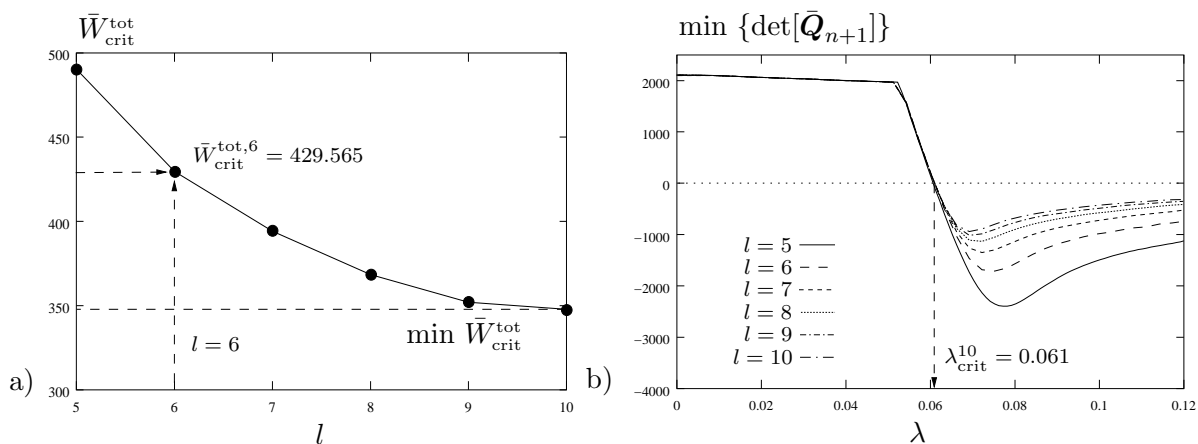


**Figure 8.6:** Determination of the relevant size of the micro-structure and macroscopic material instability, purely elastic case. a)  $\bar{W}^{\text{tot}}$  at the bifurcation point versus  $l$ , b) determinant of macroscopic acoustic tensor versus  $\lambda$  for different lengths  $l$  of the micro-structure.

degree of freedom for the pressure. The employment of unstructured meshes a priori induces imperfections within the mesh. In order to keep the influence of this random effect on the attained buckling mode low, a geometric imperfection is prescribed, i.e. a downward eccentricity of  $f = l/1000$ , of the stiff fibers at  $l/2$ . Six micro-structures with a constant height of  $h = 1$  and lengths  $l = 5, 6, 7, 8, 9$  and  $l = 10$  are investigated. Figure 8.5 a) shows the dependence of the homogenized first Piola-Kirchhoff stress component  $\bar{P}_{11}$  on the compression parameter  $\lambda$  for different lengths  $l$ . Obviously the homogenized material response significantly softens at a compression parameter of roughly  $\lambda = 0.06$ . This is due to the buckling of the stiff fibers on the micro-scale. Because of the prescribed imperfections, no explicit bifurcation point can be detected in the load displacement curve. Hence, approximate bifurcation points are determined by means of a backward extrapolation as indicated in figure 8.5 a) for the sizes  $l = 6$  and  $l = 10$ . Now for each length  $l$  the value of the accumulated macroscopic energy  $\bar{W}_{\text{crit}}^{\text{tot}}$  at the approximate bifurcation points  $\lambda_{\text{crit}}$  is determined from figure 8.5 b) in order to obtain the relevant size  $l$  of the micro-structure. Note that due to illustrative reasons the accumulated energy  $\bar{W}^{\text{tot}}$ , as defined in (8.55) below (with  $A_{n+1} = 0$  for the purely elastic case), is plotted in figures 8.5 b) and 8.6 a). In contrast to the incremental stress potential  $\bar{W}(\bar{\mathbf{F}}_{n+1})$ , the accumulated energy is invariant with respect to the chosen time increment (see also the explanations below). Next, the values of  $\bar{W}^{\text{tot}}$  at the instability point are plotted versus the respective length  $l$  in figure 8.6 a). From there it is obvious that the relevant micro-structure has to be of sufficient length  $l$  in order to originate an infimum in (8.44) and thus describe the real material properties with an adequate accuracy.

As outlined in Section 8.3.3, structural instability phenomena on the micro-scale entail a loss of infinitesimal rank-one convexity on the macro-scale and hence can be encountered by an analysis of the determinant of the macroscopic acoustic tensor, inducing the relationship shown in figure 8.6 b). From there one observes that macroscopic material instabilities occur at a compression parameter of  $\lambda_{\text{crit}}^{10} = 0.061$ . Figure 8.5 a) indicates that the relevant micro-structure of size  $l = 10$  exhibits a structural instability on the micro-scale at the same compression parameter of  $\lambda_{\text{crit}}^{10} = 0.061$ . Thus the existence of a connection between the onset of macroscopic material instabilities and the occurrence

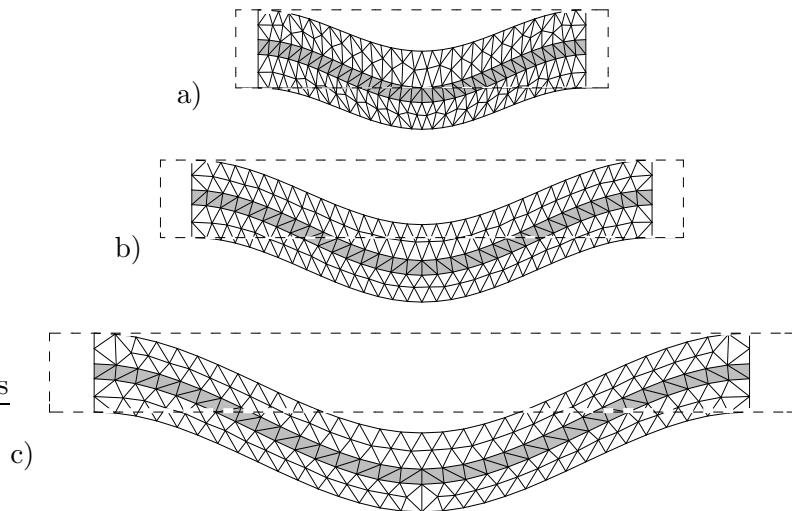


**Figure 8.7:** Postcritical microscopic buckling modes for compression parameter  $\lambda = 0.12$  and different micro-structure lengths  $l$  of a)  $l = 5$ , b)  $l = 7$  and c)  $l = 10$ , purely elastic case.

of microscopic structural instabilities is verified for the relevant micro-structure  $\mathcal{B}(n_c)$ . Figure 8.7 visualizes postcritical buckling modes for the micro-structures of lengths  $l = 5$ ,  $l = 7$ , and  $l = 10$  at a compression parameter of  $\lambda = 0.12$ , respectively. Carefully note again that the micro-structure length  $l$  just specifies the size  $n_c$  of the micro-structure. The physical specimen dimensions and the length scale associated with the microheterogeneities (e.g. the fiber distance) are kept constant throughout the present investigation.

**8.4.1.2. Buckling Analysis of an Elastic-Plastic Micro-Structure.** The analysis of the previous section is now applied for a periodic heterogeneous material consisting of an elastic-plastic matrix material surrounding purely elastic stiff fibers. The elastic behavior of the constituents is again governed by the elastic part of  $\psi$  in (8.50). The material response of the elastic-plastic matrix material is governed by the von Mises plasticity-model with coupled linear-nonlinear hardening as outlined at the beginning of this section. The material parameters of the matrix material are:  $\kappa_m = 164.2 \text{ kN/mm}^2$ ,  $\mu_m = 80.2 \text{ kN/mm}^2$ , flow stress  $y_0 = 0.45 \text{ kN/mm}^2$ , saturation stress  $y_\infty = 0.715 \text{ kN/mm}^2$ , linear hardening parameter  $h = 0.129 \text{ kN/mm}^2$  and saturation parameter  $\omega = 16.93 [-]$ . Bulk and shear moduli of the purely elastic fibers are  $\kappa_f = 100\kappa_m$  and  $\mu_f = 100\mu_m$ , and their volume fraction is 20 %. The same horizontal compression mode  $\bar{\mathbf{F}}_{n+1}$  as in the preceding section is applied and the same discretizations of the six micro-structures are used. The goal is to determine the number  $n_c$ , i.e. the relevant size of the micro-structure, for the governing in-phase buckling mode. Figure 8.8 a) depicts the undeformed con-

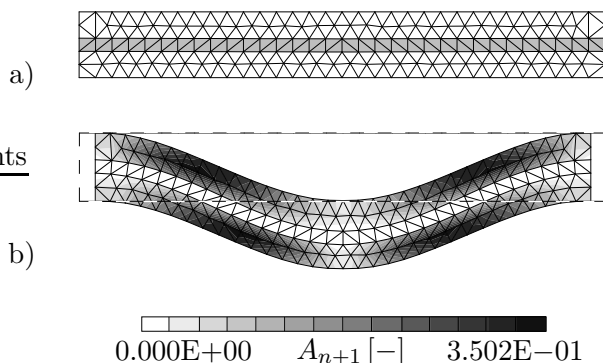


**Figure 8.8:** Micro-structure of length  $l = 8$ . a) Initial configuration. b) Deformed mesh and equivalent plastic strains  $A_{n+1}$  at  $\lambda = 0.06$ .

figuration of the micro-structure of length  $l = 8$ . Figure 8.8 b) visualizes the deformed mesh and the distribution of the equivalent plastic strains on the micro-scale for a horizontal compression of 6%. Figure 8.9 a) shows the dependence of the first Piola-Kirchhoff stress component  $\bar{P}_{11}$  on the compression parameter  $\lambda$  for different lengths  $l$ . From this load displacement curve the respective compression parameters  $\lambda_{\text{crit}}$  at the approximate bifurcation points are again determined by the above mentioned backward extrapolation. Then from figure 8.9 b) the values of the accumulated macroscopic energy  $\bar{W}_{\text{crit}}^{\text{tot}}$  at the particular instability points are determined. Again note that due to illustrative reasons in figure 8.9 b) the accumulated energy

$$\bar{W}^{\text{tot}} = \frac{1}{|\mathcal{V}|} \int_{\mathcal{B}} \{\psi_{n+1} + y_0 A_{n+1}\} dV \quad (8.55)$$

is plotted which, in contrast to the incremental stress potential  $\bar{W}(\bar{\mathbf{F}}_{n+1})$ , is invariant with respect to the chosen time increment. In (8.55)  $\psi_{n+1}$  denotes the micro-energy (8.50)

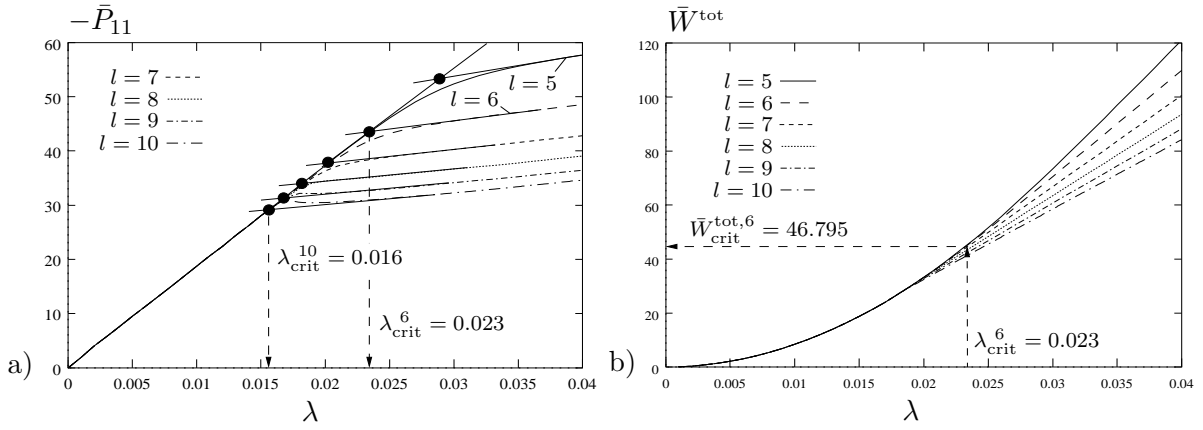


**Figure 8.9:** Determination of the bifurcation point and the respective accumulated energy, elastic-plastic case. a) Macroscopic first Piola-Kichhoff stress component  $P_{11}$ , and b) accumulated macroscopic energy  $\bar{W}^{\text{tot}}$  versus  $\lambda$  for different lengths  $l$  of the micro-structure.

at the end  $t_{n+1}$  of the respective time-step and  $y_0 A_{n+1}$  results from the evaluation of the dissipation. Clearly the accumulated energy obtains identical values up to the relevant bifurcation point for all sizes of the micro-structure. Within the postcritical regime the incremental stress potential and consequently also the accumulated energy are both overestimated in an identical manner for micro-structures which do not possess the correct dimensions in the sense of (8.44). Thus an analysis of  $\bar{W}^{\text{tot}}$  or  $\bar{W}$  results in identical observations. Finally the values of the accumulated energy at the instability point are plotted versus the respective length  $l$  giving the relationship shown in figure 8.10 a). From there one observes that the relevant micro-structure has to be of sufficient length  $l$  in order to originate an infimum in (8.44) and thus describe the real material properties with an adequate accuracy.

Again the relationship between the onset of macroscopic material instabilities and the occurrence of microscopic structural instability phenomena can be proven by application of an acoustic tensor analysis inducing the relationship shown in figure 8.10 b). The loss of infinitesimal rank-one convexity on the macro-scale is characterized by a zero-crossing of  $\min\{\det[\bar{Q}_{n+1}]\}$ . Thus from figure 8.10 b) one observes that the onset of

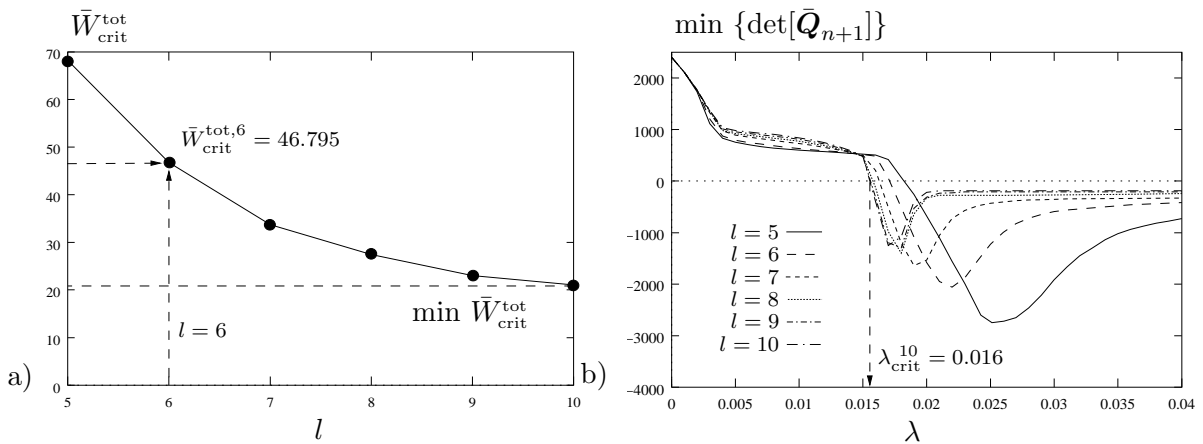


**Figure 8.10:** Determination of the relevant size of the micro-structure and macroscopic material instability, elastic-plastic case. a)  $\bar{W}^{\text{tot}}$  at the bifurcation point versus  $l$ , b) determinant of macroscopic acoustic tensor versus  $\lambda$  for different lengths  $l$  of the micro-structure.

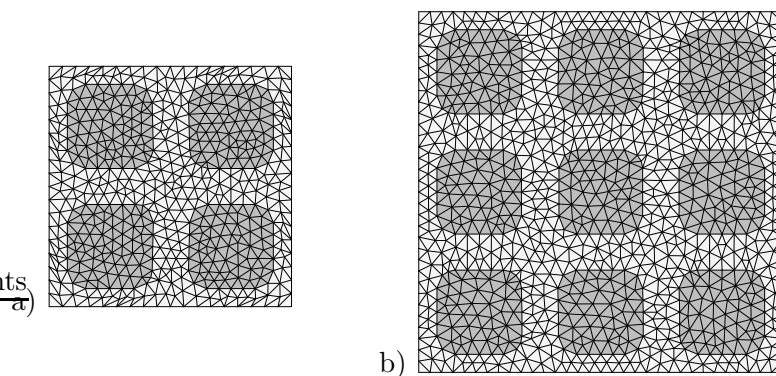


**Figure 8.11:** Initial configurations of discretized micro-structures. Micro-structure consisting of a)  $n_c = 4$  and b)  $n_c = 9$  generic cells  $\mathcal{C}$ .

macroscopic material instabilities for the relevant micro-structure of size  $l = 10$  occurs at the same compression parameter of  $\lambda_{\text{crit}}^{10} = 0.016$  as the microscopic structural instability characterized by the bifurcation point in figure 8.9 a).

**8.4.2. Buckling Analysis of a Cellular Micro-Structure.** Within the following example the procedure outlined in section 8.4.1 is now employed in order to determine the relevant size  $n_c$  of the micro-structure for a cellular material consisting of a stiff elastic matrix and soft inclusions as depicted in figure 8.11. First, in section 8.4.2.1 a purely elastic material is considered, subsequently in section 8.4.2.2 a material consisting of a purely elastic matrix and elastic-plastic inclusions is analyzed. In order to determine the relevant size of the micro-structure again, the number  $n_c$  of generic cells  $\mathcal{C}$  building up the micro-structure  $\mathcal{B}(n_c)$  is varied and the respective value of the accumulated energy  $\bar{W}_{\text{crit}}^{\text{tot}}$  is evaluated at the instability points. Here the generic cell  $\mathcal{C}$  consists of a single inclusion surrounded by stiff matrix material. The micro-structure which induces the least value of the accumulated energy  $\bar{W}^{\text{tot}}$  at the instability point then indicates the relevant micro-structural size  $n_c$  and hence is to be used within an analysis employing micro-to-macro transitions for the heterogeneous material at hand subject to the present loading.

**8.4.2.1. Buckling Analysis of a Purely Elastic Micro-Structure.** In the following the focus is put on a purely elastic periodic heterogeneous material consisting of a stiff matrix material surrounding soft inclusions. The constituents are again governed by the elastic part of the isotropic stored micro-energy function (8.50). The volume fraction of the soft inclusions is 70 %, their bulk and shear moduli are  $\kappa_i = 164.2 \text{ kN/mm}^2$  and

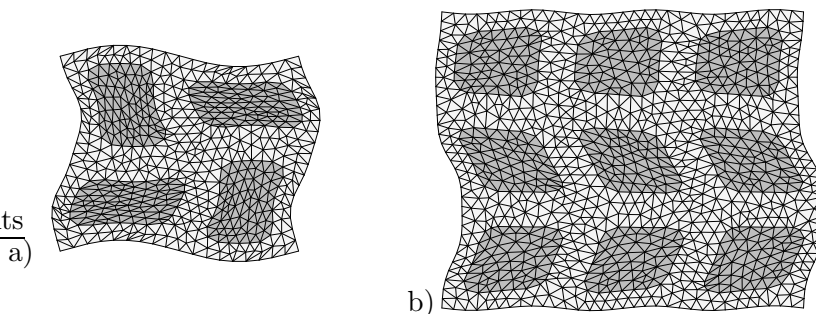


**Figure 8.12:** Postcritical microscopic higher order buckling modes for a compression parameter of  $\lambda = 0.15$  and sizes a)  $n_c = 4$  and b)  $n_c = 9$ .

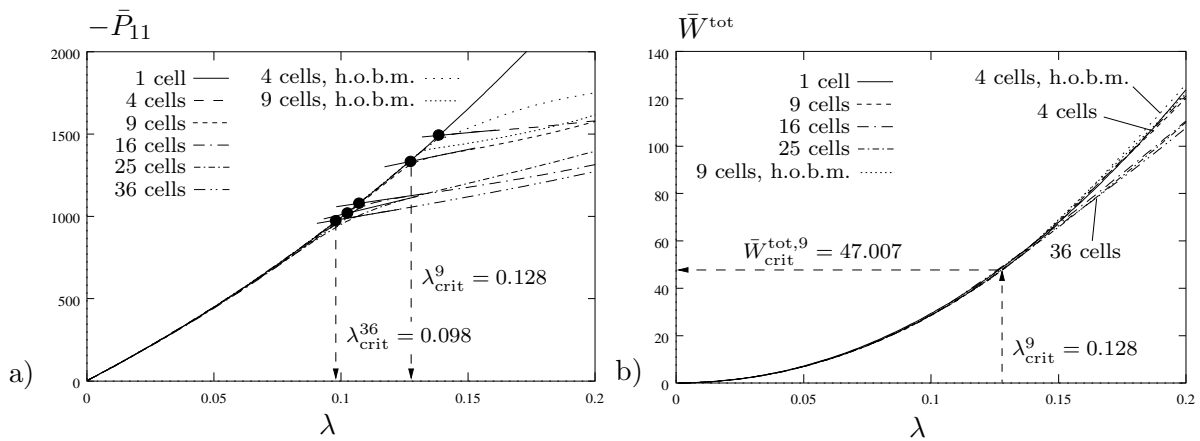


**Figure 8.13:** Determination of the bifurcation point and the respective accumulated energy, purely elastic case. a) Macroscopic first Piola-Kichhoff stress component  $\bar{P}_{11}$ , and b) accumulated macroscopic energy  $\bar{W}^{tot}$  versus  $\lambda$  for different sizes  $n_c$  of the micro-structure.

$\mu_i = 80.2 \text{ kN/mm}^2$ , respectively. The material parameters of the stiff matrix material are set to  $\kappa_m = 100\kappa_i$  and  $\mu_m = 100\mu_i$ . The macroscopic deformation mode is a vertical compression driving the deformation of the micro-structure. The macroscopic deformation gradient  $\bar{\mathbf{F}}_{n+1}$  takes the following format

$$\bar{\mathbf{F}}_{n+1} = \text{diag}[1, 1 - \lambda, 1] \quad \text{with } \lambda > 0 \quad (8.56)$$

Here  $\lambda$  denotes the compression parameter. In order to determine the relevant micro-structural size corresponding to this deformation mode, the number of generic cells which are used to build up the micro-structure needs to be varied. Here, a generic cell consists of a quadrilateral domain with dimensions  $1 \times 1$  containing one single inclusion. In the following investigations 6 quadratic micro-structures  $\mathcal{B}(n_c)$  consisting of  $n_c = 1, 4, 9, 16, 25$  or  $n_c = 36$  generic cells are considered. In order to perform a finite element simulation of the problem at hand, the micro-structures of different sizes are discretized again with mixed linear triangles. The micro-buckling modes are triggered by prescribing a small geometric imperfection, i.e. a horizontal eccentricity of either the central inclusion ( $n_c = 1, 9, 25$ ) or the central cross-over point of the matrix ( $n_c = 4, 16, 36$ ). Due to the macroscopic deformation mode (8.56), various buckling modes might occur on the micro-scale. The

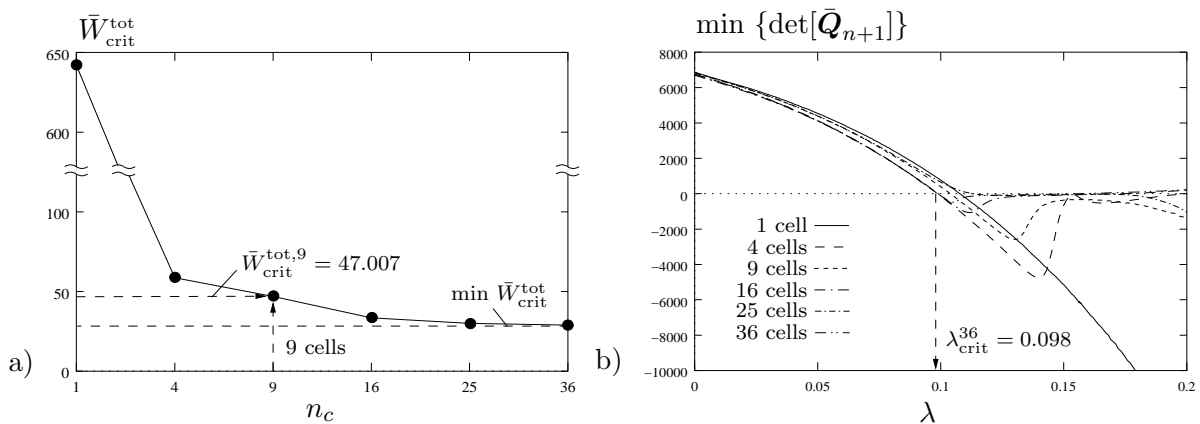


**Figure 8.14:** Determination of the relevant size of the micro-structure and macroscopic material instability, purely elastic case. a)  $\bar{W}^{tot}$  at the bifurcation point versus  $n_c$ , b) determinant of macroscopic acoustic tensor versus  $\lambda$  for different sizes  $n_c$  of the micro-structure.

1st-order buckling modes for the current purely elastic case are similar to the ones depicted in figures 8.17 and 8.18. Figure 8.12 shows higher order buckling modes (h.o.b.m.) for the micro-structures of size  $n_c = 4$  and  $n_c = 9$ , respectively (note that these buckling modes were triggered by different imperfections). Figure 8.13 a) shows the dependence of the homogenized first Piola-Kirchhoff stress component  $\bar{P}_{11}$  on the compression parameter  $\lambda$  for different sizes  $n_c$ . From there the respective instability points  $\lambda_{\text{crit}}$  are determined by means of the indicated backward extrapolation. Obviously the higher order buckling modes occur at higher values of the compression parameter  $\lambda$  than the corresponding 1st-order buckling modes. On the other hand, it is apparent from figure 8.13 b) that the higher order buckling modes are related to a higher energy level. Thus in the subsequent investigations only the relevant 1st-order buckling modes are considered. Now, in order to specify the relevant size of the micro-structure  $n_c$ , the value of the accumulated macroscopic energy  $\bar{W}_{\text{crit}}^{\text{tot}}$  at the approximate bifurcation points  $\lambda_{\text{crit}}$  is determined for each size from figure 8.13 b) as indicated for the size  $n_c = 9$ . The values of  $\bar{W}^{\text{tot}}$  are then plotted versus the respective size  $n_c$  giving the relationship shown in figure 8.14 a). From there it is obvious that the relevant micro-structure has to be of sufficient size  $n_c$  in order to originate an infimum in (8.44) and thus describe the real material properties with an adequate accuracy.

Finally, in order to show the relationship between structural instability phenomena on the micro-scale and the onset of material instabilities on the macro-scale, an analysis of the macroscopic acoustic tensor is performed, inducing the relationship shown in figure 8.14 b). From there one observes that the relevant micro-structure of size  $n_c = 36$  exhibits an onset of macroscopic material instabilities at a compression parameter of  $\lambda_{\text{crit}}^{36} = 0.098$  which coincides with the instability point indicated in figure 8.13 a). Thus the existence of the above mentioned connection is verified for the relevant micro-structure  $\mathcal{B}(n_c)$ .

**8.4.2.2. Buckling Analysis of an Elastic-Plastic Micro-Structure.** The analysis of the previous section is now employed for a periodic heterogeneous material consisting of a purely elastic matrix material surrounding elastic-plastic soft inclusions. The elastic behavior of the constituents is governed again by the corresponding part of the storage function (8.50). The material behavior of the elastic-plastic inclusions is governed by the von Mises plasticity-model with coupled linear-nonlinear hardening as out-

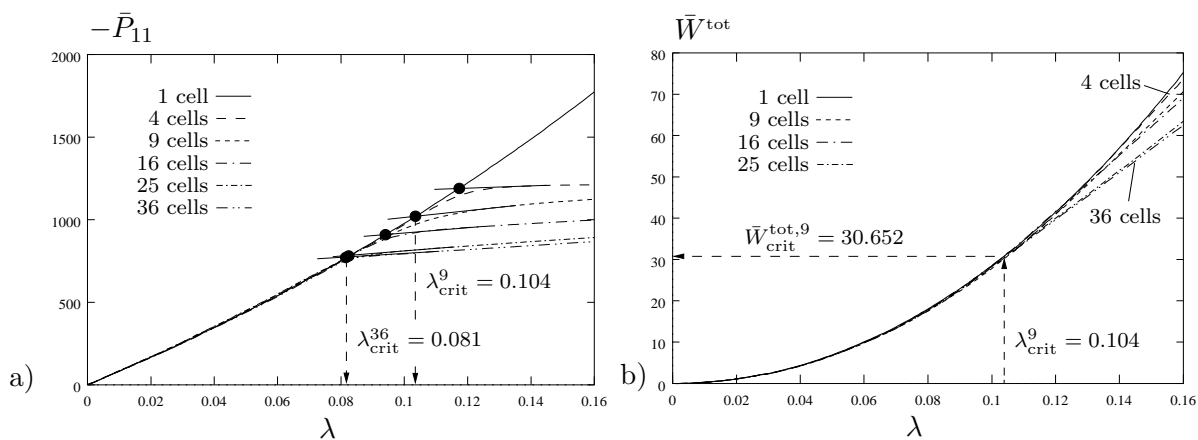


**Figure 8.15:** Determination of the bifurcation point and the respective accumulated energy, elastic-plastic case. a) Macroscopic first Piola-Kirchhoff stress component  $\bar{P}_{11}$ , and b) accumulated macroscopic energy  $\bar{W}^{\text{tot}}$  versus  $\lambda$  for different sizes  $n_c$  of the micro-structure.

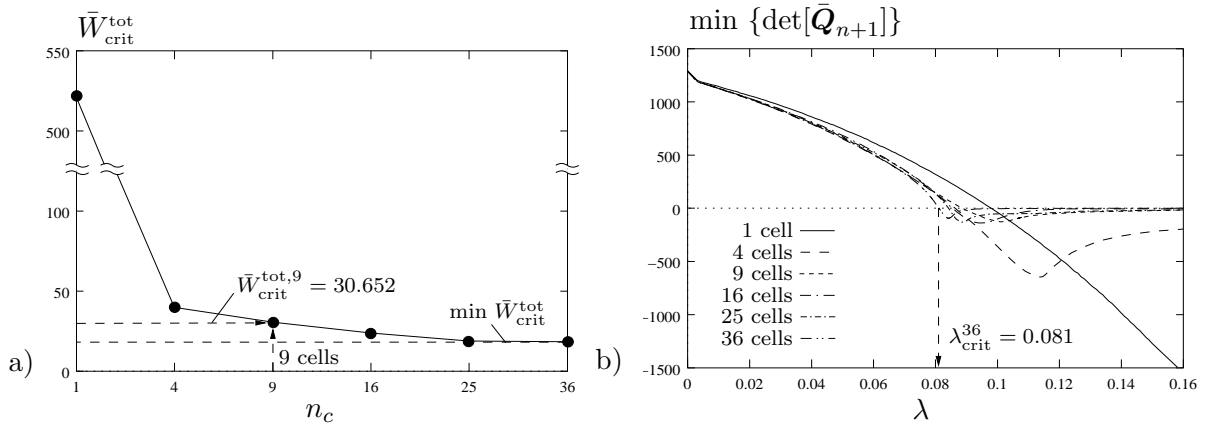


**Figure 8.16:** Determination of the relevant size of the micro-structure and macroscopic material instability, elastic-plastic case. a)  $\bar{W}_{crit}^{tot}$  at the bifurcation point versus  $n_c$ , b) determinant of macroscopic acoustic tensor versus  $\lambda$  for different sizes  $n_c$  of the micro-structure.

lined at the beginning of this section. The material parameters of the soft inclusions are:  $\kappa_i = 164.2 \text{ kN/mm}^2$ ,  $\mu_i = 80.2 \text{ kN/mm}^2$ , flow stress  $y_0 = 0.45 \text{ kN/mm}^2$ , saturation stress  $y_\infty = 0.715 \text{ kN/mm}^2$ , linear hardening parameter  $h = 0.129 \text{ kN/mm}^2$  and saturation parameter  $\omega = 16.93 [-]$ . Bulk and shear moduli of the purely elastic matrix material are  $\kappa_m = 100\kappa_i$  and  $\mu_m = 100\mu_i$ . The volume fraction of the inclusions is 70 %. Again a vertical compression mode  $\bar{F}_{n+1}$  as described by (8.56) is applied and the six micro-structures are discretized by mixed triangles. Figure 8.15 a) shows the dependence of the first Piola-Kirchhoff stress component  $\bar{P}_{11}$  on the compression parameter  $\lambda$  for different sizes  $n_c$ . From this load displacement curve the respective compression parameters  $\lambda_{crit}$  at the approximate bifurcation points are again determined by means of the above mentioned backward extrapolation. In a next step from figure 8.15 b), the values of the accumulated macroscopic energy  $\bar{W}_{crit}^{tot}$  at the particular instability points are determined and subsequently plotted versus the respective size  $n_c$  in figure 8.16 a). From there one observes that the relevant micro-structure has to be of sufficient size  $n_c \geq 36$ .

Again the relationship between the onset of macroscopic material instabilities and the occurrence of microscopic structural instability phenomena can be proven by application of an acoustic tensor analysis inducing the relationship shown in figure 8.16 b). The loss of infinitesimal rank-one convexity on the macro-scale is characterized by a zero-crossing of  $\min\{\det[\bar{Q}_{n+1}]\}$ . Thus from figure 8.16 b) one observes that the onset of

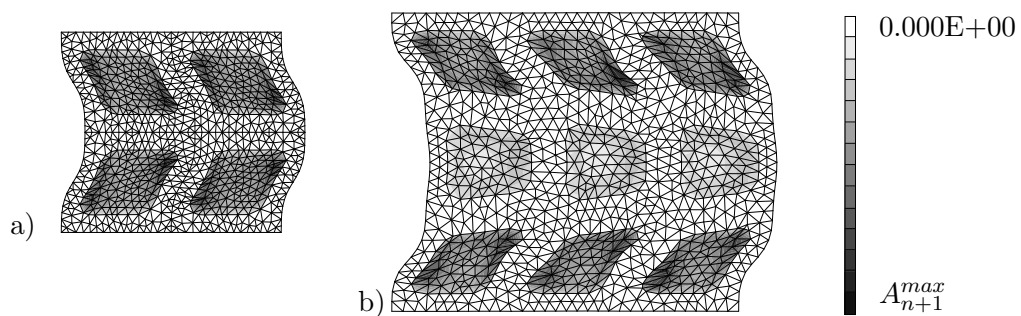


**Figure 8.17:** Postcritical microscopic 1st-order buckling modes and respective distributions of the equivalent plastic strains  $A_{n+1}$  for a compression parameter of  $\lambda = 0.15$ . a)  $n_c = 4$  and  $A_{n+1}^{max} = 9.106E-01$ , b)  $n_c = 9$  and  $A_{n+1}^{max} = 9.501E-01$ .

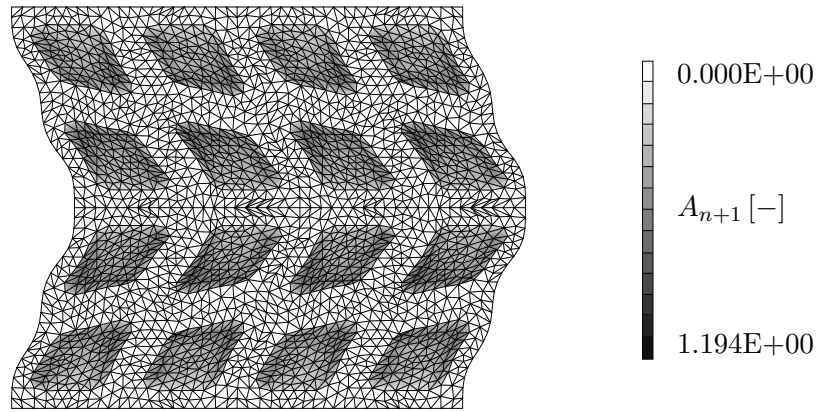


**Figure 8.18:** Postcritical microscopic 1st-order buckling mode and distribution of the equivalent plastic strains  $A_{n+1}$  for a micro-structure composed of  $n_c = 16$  generic cells,  $\lambda = 0.15$ .

macroscopic material instabilities for the relevant micro-structure of size  $n_c = 36$  occurs at the same compression parameter of  $\lambda_{\text{crit}}^{36} = 0.081$  as the microscopic structural instability characterized by the bifurcation point in figure 8.15 a). Figures 8.17 and 8.18 visualize some postcritical 1st-order buckling modes and the corresponding distributions of the equivalent plastic strains of the elastic-plastic micro-structures.

## 9. Conclusion

The general outline of this thesis is an investigation of size effects in nonhomogeneously deforming crystals and a non-convex homogenization analysis of instable microheterogeneous standard materials. The major focal points and achievements of this work are:

A detailed incompatibility analysis of continuously dislocated metal crystals. In a first more direct manner, the matter of incompatibility is approached with tools from calculus, i.e. the integrability conditions which demand path independence of line integrals on simply connected domains. Specified to multiplicative plasticity, this already allows for the definition of the dislocation density tensor as an incompatibility measure. Secondly the incompatibility analysis is approached from a differential geometric point of view. This defines the Cartan torsion and the Riemann-Christoffel curvature tensor as incompatibility measures of an affine and metric geometry. Based on these measures, the setting of finite strain crystal plasticity is interpreted as a Cartan geometry. The torsion measures the incompatibility and the vanishing curvature tensor provides the continuity equations for the dislocation density tensor and relates the dislocation storage to residual stresses.

An extensive discussion of the dislocation density tensor. The interpretation of the dislocation density tensor as a mapping provides a unified framework which includes various dislocation density tensors proposed in literature. Thereby the formal coincidence between the stress measures and the dislocation density tensors is also emphasized. Furthermore, a detailed crystallographic interpretation of the dislocation density tensor in terms of a slip gradient induced net dislocation storage is given. With these considerations, the incompatibility analysis and the given review of the formal distinction between SSDs and GNDs, a selfcontained picture of the underlying physics of nonhomogeneous deformations in metal crystals is developed in this work.

The development of a dislocation density based strain gradient crystal plasticity model for finite strains in the rate dependent as well as the rate independent setting. The model is equipped with a sound mathematical foundation on the matter of incompatibility and a strong micromechanical basis in terms of the storage of geometrically necessary dislocations. The model directly incorporates the dislocation density tensor and solely contains the Burgers vector length as an internal length scale with a precise physical significance for the isotropic hardening relation considered. Possible future extensions of the model might concern a residual stress based kinematic hardening contribution or a Hall-Petch like size dependence of the initial flow stress, e.g. through an a priori misorientation induced dislocation storage at the grain boundaries.

The elaboration of two alternative algorithmic formulations for the numerical treatment of finite strain gradient crystal plasticity. Both formulations are developed for the rate dependent as well as the rate independent case. The first (global) solution strategy bases on a mixed finite element formulation which directly provides the plastic slip distribution throughout the solution domain required for the gradient computation. This necessitates a non-standard nodal active set search for the rate independent case. Alternatively, in view of an efficient treatment, an extended local formulation is developed on basis of an operator split where the slip distribution is obtained through a smoothing algorithm.

A broad validation of the developed model of gradient plasticity and the algorithmic formulations. This includes the qualitative (and quantitative) comparison with discrete dislocation predictions, classical analytical predictions and other continuum models of

gradient crystal plasticity as well as the numerical replication of experimental observations. In addition, the alternative algorithmic formulations are compared with one another which also demonstrates the superior efficiency of the extended local formulation. These investigations reveal the modeling capabilities of the developed formulations. This covers the prediction of the expected size effects in the case of inhomogeneous elastic or plastic deformations and an associated GND density which exceeds the corresponding SSD density. The obtained Hall-Petch (like) exponents are at the upper limit of the experimental observations and are thus very well within the overall range of computational predictions.

The incremental non-convex homogenization analysis of microheterogeneous unstable inelastic solids at finite strains. To this end, incremental stability criteria for an analysis of structural and material instabilities on the micro- and the macroscale are developed. This relies on an extension of existence results for finite strain elasticity to finite strain inelasticity based on an incremental variational formulation for standard dissipative materials. In order to eliminate an undesired dependency of the homogenized material response upon the size of the representative microstructure in the non-convex postcritical regime, an extended homogenization principle is proposed. The underlying basis is the  $\Gamma$ -limit of heterogeneous micro-structures which states that the micro-structure is composed of an a priori unknown number of generic cells. The relevant micro-structure size catches the energy-minimizing buckling mode. The course of the homogenization procedure in the postcritical regime is demonstrated for some representative examples. These examples outline the complexity of the non-convex homogenization analysis. Thus it is highly desirable to avoid instability phenomena in the context of a homogenization analysis. However, if instabilities can not a priori be precluded, a tractable approach might, from an engineering viewpoint, as well be to directly employ a sufficiently large micro-structure.

## A. A Model Problem of Single Crystal Viscoplasticity

### A.1. Constitutive Functions

The model problem of single crystal plasticity considered throughout the main parts of this work bases on an isotropic elastic response governed by the lattice storage function

$$\hat{\psi}^e = \kappa(J^e - \ln J^e - 1) + \frac{1}{2}\mu(\tilde{\mathbf{b}}^e : \mathbf{g} - 3) = \hat{\psi}_{\text{vol}}^e + \hat{\psi}_{\text{iso}}^e \quad (\text{A.1})$$

in terms of the Eulerian elastic Finger tensor  $\tilde{\mathbf{b}}^e := \tilde{\mathbf{F}}^e \cdot \bar{\mathbf{G}}^{-1} \cdot \tilde{\mathbf{F}}^{eT}$ , the Jacobian  $J^e := \det[\mathbf{F}^e]$  and the unimodular part  $\tilde{\mathbf{F}}^e := J^{e-1/3} \mathbf{F}^e$  of the elastic deformation map and the metric  $\bar{\mathbf{G}}$  of the intermediate and  $\mathbf{g}$  of the current configuration. Furthermore,  $\kappa$  and  $\mu$  are the bulk and shear modulus, respectively.

As a second constitutive function, the yield criterion function  $\Phi^\alpha$  is specified as follows

$$\Phi^\alpha = \tau^\alpha - \tau_r^\alpha - \tau_v^\alpha \quad (\text{A.2})$$

Assuming a Schmid type crystal behavior, the Schmid stresses  $\tau^\alpha = -\hat{\psi}_{,\gamma^\alpha}^e$  are derived on basis of (A.1) as

$$\tau^\alpha = \text{dev}[\bar{\Sigma}] : \mathbf{S}^\alpha \otimes \mathbf{M}^\alpha = \mu \text{dev}[\tilde{\mathbf{F}}^{eT} \cdot \tilde{\mathbf{F}}^e] : \mathbf{S}^\alpha \otimes \mathbf{M}^\alpha = \mu \mathbf{s}^\alpha \cdot \mathbf{m}^\alpha \quad (\text{A.3})$$

with  $\mathbf{s}^\alpha := \tilde{\mathbf{F}}^e \mathbf{S}^\alpha$  and  $\mathbf{m}^\alpha := \tilde{\mathbf{F}}^e \mathbf{M}^\alpha$ . Furthermore, in (A.2)  $\tau_v^\alpha$  denotes the viscous over-stresses, see e.g. (4.24). Finally, in view of a micromechanically based hardening response, the slip resistance  $\tau_r^\alpha$  is assumed to be governed by the relations (3.24) and (3.26)

$$\tau_r^\alpha = c\mu b\sqrt{n^\alpha} \quad \text{with} \quad n^\alpha = \sum_{\beta} G^{\alpha\beta} \rho^\beta \quad \text{and} \quad \rho^\beta = \rho^{\text{sat}} \left[ 1 - \left( 1 - \frac{\rho^{0,\beta}}{\rho^{\text{sat}}} \right) \exp\left(-\frac{\gamma^\beta}{\gamma^{\text{sat}}}\right) \right] \quad (\text{A.4})$$

in terms of the initial and saturated dislocation densities  $\rho^{0,\beta}$  and  $\rho^{\text{sat}}$ , the saturation slip strain  $\gamma^{\text{sat}}$ , a constant  $c$ , the Burgers vector length  $b$  and the interaction matrix  $G^{\alpha\beta}$

### A.2. Algorithmic Expressions of the Standard Formulation

As pointed out in (4.34) within the standard formulation, the determination of the plastic slips bases on the yield criterion function as a residual expression and its sensitivity with respect to the plastic slips defines the corresponding iteration matrix

$$r^\alpha := -\Phi^\alpha \quad \text{and} \quad H^{\alpha\beta} := -[\Phi^\alpha]_{,\gamma^\beta} = [-\tau^\alpha]_{,\gamma^\beta} + [\tau_r^\alpha]_{,\gamma^\beta} + [\tau_v^\alpha]_{,\gamma^\beta} \quad \forall (\alpha, \beta) \in \mathcal{A} \quad (\text{A.5})$$

The sensitivity of the Schmid stresses (A.3) with respect to the plastic slip is obtained as

$$\partial_{\gamma^\beta}[\tau^\alpha] = \mu \{ (\tilde{\mathbf{F}}^e_{,\gamma^\beta} \cdot \mathbf{S}^\alpha) \cdot (\tilde{\mathbf{F}}^e \cdot \mathbf{M}^\alpha) + (\tilde{\mathbf{F}}^e \cdot \mathbf{S}^\alpha) \cdot (\tilde{\mathbf{F}}^e_{,\gamma^\beta} \cdot \mathbf{M}^\alpha) \} \quad (\text{A.6})$$

in terms of the algorithmic sensitivities of the unimodular part of the elastic deformation map  $\tilde{\mathbf{F}}^e_{,\gamma^\beta}$ . The sensitivity of the slip resistance follows with (A.4) as

$$\partial_{\gamma^\beta}[\tau_r^\alpha] = \frac{(c\mu b)^2}{2\tau_r^\alpha} \sum_{\omega \in \mathcal{A}} G^{\alpha\omega} \frac{1}{\gamma^{\text{sat}}} (\rho^{\text{sat}} - \rho^{0,\omega}) \exp(-\gamma^\omega/\gamma^{\text{sat}}) \delta^{\omega\beta} \quad (\text{A.7})$$

And finally, the sensitivity of the viscous over-stresses with respect to  $\gamma^\beta$  reads

$$\partial_{\gamma^\beta}[\tau_v^\alpha] = \frac{\tau_{v0}}{\epsilon \dot{\gamma}_0 \Delta t} \left( \frac{\gamma^\alpha - \gamma_n^\alpha}{\dot{\gamma}_0 \Delta t} \right)^{(1-\epsilon)/\epsilon} \delta^{\alpha\beta} \quad (\text{A.8})$$

### A.3. Stresses and Consistent Tangent Moduli

According to (A.1), the Eulerian Kirchhoff stresses of the model under consideration can be split into a volumetric and an isochoric part

$$\boldsymbol{\tau} = 2 \hat{\psi}_{,\mathbf{g}}^e = p \mathbf{g}^{-1} + \mu \operatorname{dev}[\tilde{\mathbf{b}}^e] = \boldsymbol{\tau}_{\text{vol}} + \boldsymbol{\tau}_{\text{iso}} \quad \text{with} \quad p = \kappa (J^e - 1) \quad (\text{A.9})$$

where the standard result  $\partial_{\mathbf{g}} J^e = \frac{1}{2} J^e \mathbf{g}^{-1}$  has been used and the *deviator* of a tensor is defined as  $\operatorname{dev}[(\bullet)] := (\bullet) - \frac{1}{3} \operatorname{tr}[(\bullet)] \mathbf{g}^{-1}$  with  $\operatorname{tr}[(\bullet)] := \mathbf{g} : (\bullet)$ . Analogously, the consistent Eulerian elastic-plastic tangent moduli can be represented in terms of volumetric and isochoric elastic contributions and a purely volumetric plastic softening part

$$\mathbf{c}^{ep} = \mathbf{c}_{\text{vol}}^e + \mathbf{c}_{\text{iso}}^e - \mathbf{c}_{\text{iso}}^p \quad (\text{A.10})$$

where

$$\begin{aligned} \mathbf{c}_{\text{vol}}^e &:= 2 \partial_{\mathbf{g}} [p \mathbf{g}] &= \kappa J^e \mathbf{g}^{-1} \otimes \mathbf{g}^{-1} - 2p \mathbb{I}_{\mathbf{g}^{-1}} \\ \mathbf{c}_{\text{iso}}^e &:= 2 \partial_{\mathbf{g}} \boldsymbol{\tau}_{\text{iso}} |_{\gamma^\alpha} &= \frac{2}{3} \mu \operatorname{tr}[\tilde{\mathbf{b}}^e] (\mathbb{I}_{\mathbf{g}^{-1}} - \frac{1}{3} \mathbf{g}^{-1} \otimes \mathbf{g}^{-1}) - \frac{2}{3} \{ \mathbf{g}^{-1} \otimes \boldsymbol{\tau}_{\text{iso}} + \boldsymbol{\tau}_{\text{iso}} \otimes \mathbf{g}^{-1} \} \\ \mathbf{c}_{\text{iso}}^p &:= - \sum_{\alpha \in \mathcal{A}} \partial_{\gamma^\alpha} \boldsymbol{\tau}_{\text{iso}} \otimes 2 \partial_{\mathbf{g}} \gamma^\alpha \end{aligned} \quad (\text{A.11})$$

with  $\partial_{\mathbf{g}}[\mathbf{g}^{-1}] = -\mathbb{I}_{\mathbf{g}^{-1}}$ . The sensitivity of the isochoric part of the Kirchhoff stresses required in (A.11)<sub>3</sub> follows directly from (A.9) in terms of the algorithmic sensitivities  $\tilde{\mathbf{F}}_{,\gamma^{\hat{\alpha}}}^e$

$$\partial_{\gamma^\alpha} \boldsymbol{\tau}_{\text{iso}} = \mu \operatorname{dev}[\tilde{\mathbf{F}}_{,\gamma^{\hat{\alpha}}}^e \cdot \tilde{\mathbf{F}}^{eT} + \tilde{\mathbf{F}}^e \cdot \tilde{\mathbf{F}}_{,\gamma^{\hat{\alpha}}}^{eT}] \quad (\text{A.12})$$

Secondly, the sensitivity of the plastic slips with respect to the Eulerian metric is derived via the implicit function theorem, see (4.67)<sub>1</sub>, as

$$\begin{aligned} 2 \partial_{\mathbf{g}} \gamma^\alpha &= \sum_{\beta \in \mathcal{A}} H^{\alpha\beta-1} 2 \partial_{\mathbf{g}} \tau^\beta \\ \text{with } 2 \partial_{\mathbf{g}} \tau^\beta &= \mu \operatorname{dev}[\mathbf{s}^\alpha \otimes \mathbf{m}^\alpha + \mathbf{m}^\alpha \otimes \mathbf{s}^\alpha] \end{aligned} \quad (\text{A.13})$$

Thus the complete algorithmic elastic-plastic tangent moduli for the model problem under consideration reads

$$\begin{aligned} \mathbf{c}^{ep} &= \kappa J^e \mathbf{g}^{-1} \otimes \mathbf{g}^{-1} - 2p \mathbb{I}_{\mathbf{g}^{-1}} + \frac{2}{3} \mu \operatorname{tr}[\tilde{\mathbf{b}}^e] (\mathbb{I}_{\mathbf{g}^{-1}} - \frac{1}{3} \mathbf{g}^{-1} \otimes \mathbf{g}^{-1}) \\ &\quad - \frac{2}{3} \{ \mathbf{g}^{-1} \otimes \boldsymbol{\tau}_{\text{iso}} + \boldsymbol{\tau}_{\text{iso}} \otimes \mathbf{g}^{-1} \} \\ &\quad + \sum_{\alpha \in \mathcal{A}} \sum_{\beta \in \mathcal{A}} H^{\alpha\beta-1} \mu \operatorname{dev}[\tilde{\mathbf{F}}_{,\gamma^{\hat{\alpha}}}^e \cdot \tilde{\mathbf{F}}^{eT} + \tilde{\mathbf{F}}^e \cdot \tilde{\mathbf{F}}_{,\gamma^{\hat{\alpha}}}^{eT}] \otimes \mu \operatorname{dev}[\mathbf{s}^\alpha \otimes \mathbf{m}^\alpha + \mathbf{m}^\alpha \otimes \mathbf{s}^\alpha] \end{aligned} \quad (\text{A.14})$$

## B. The Curl Operator

### B.1. Definition of the Contravariant Lagrangian and Eulerian Curl Operators

This work employs the following definition of the *contravariant Lagrangian Curl operator* applied to a mixed variant second order Tensor  $\mathbf{T}$

$$\operatorname{Curl}^T \mathbf{T} := -\nabla_{\mathbf{X}} \mathbf{T} : \overset{3}{\mathbf{E}} \quad (\text{B.15})$$

in terms of the third order *Lagrangian fundamental tensor*  $\overset{3}{\mathbf{E}}$ .  $\overset{3}{\mathbf{E}}$  is defined with the standard *permutation symbol*  $\epsilon^{IJK}$  and the *volume*  $\sqrt{G}$  of the parallelepiped spanned by the general Lagrangian base system  $\mathbf{G}_I$  as (recall the definition of the Lagrangian covariant metric tensor  $\mathbf{G} = G_{IJ} \mathbf{G}^I \otimes \mathbf{G}^J = \mathbf{G}_I \cdot \mathbf{G}_J \mathbf{G}^I \otimes \mathbf{G}^J$ )

$$\overset{3}{\mathbf{E}} := \frac{1}{\sqrt{G}} \epsilon^{IJK} \mathbf{G}_I \otimes \mathbf{G}_J \otimes \mathbf{G}_K \quad \text{with} \quad G := \det|G_{IJ}| \quad (\text{B.16})$$

Analogously, the following definition of the *contravariant Eulerian curl operator* is used

$$\text{curl}^T \mathbf{T} := -\nabla_{\mathbf{x}} \mathbf{T} : \overset{3}{\mathbf{e}} \quad (\text{B.17})$$

Thereby the corresponding third order *Eulerian fundamental tensor*  $\overset{3}{\mathbf{e}}$  is defined in terms of the standard permutation symbol  $\epsilon^{ijk} = \epsilon^{IJK}$  and the parallelepiped volume  $\sqrt{g}$  spanned by the Eulerian base system  $\mathbf{g}_i$  (recall  $\mathbf{g} = g_{ij} \mathbf{g}^i \otimes \mathbf{g}^j = \mathbf{g}_i \cdot \mathbf{g}_j \mathbf{g}^i \otimes \mathbf{g}^j$ )

$$\overset{3}{\mathbf{e}} := \frac{1}{\sqrt{g}} \epsilon^{ijk} \mathbf{g}_i \otimes \mathbf{g}_j \otimes \mathbf{g}_k \quad \text{with} \quad g := \det|g_{ij}| \quad (\text{B.18})$$

This induces the following component representation with respect to a Cartesian coordinate system ( $\sqrt{G} = 1$ ) for the material Curl of the deformation gradient  $\mathbf{F}$

$$[\text{Curl} \mathbf{F}]^{Ca} = [\text{Curl}^T \mathbf{F}]^{aC} = -F^a_{A,B} \epsilon^{ABC} \quad (\text{B.19})$$

and similarly the component representation with respect to a Cartesian coordinate system ( $\sqrt{g} = 1$ ) for the spatial curl of the inverse deformation gradient  $\mathbf{F}^{-1}$  reads

$$[\text{curl} \mathbf{F}^{-1}]^{cA} = [\text{curl}^T \mathbf{F}^{-1}]^{Ac} = -F^{-1A}_{a,b} \epsilon^{abc} \quad (\text{B.20})$$

The component representations with respect to a general coordinate system follow directly by replacing  $\epsilon^{ABC}$  by  $\bar{\epsilon}^{ABC} = \epsilon^{ABC}/\sqrt{G}$  in (B.19) and  $\epsilon^{abc}$  by  $\bar{\epsilon}^{abc} = \epsilon^{abc}/\sqrt{g}$  in (B.20). Note that for some authors the Curl of  $\mathbf{T}$  is the transpose of the definition for the Curl operator employed in this work.

## B.2. Relation Between Eulerian and Lagrangian Curl Operator

In order to find a relation between the spatial curl of  $\mathbf{F}^{-1}$  and the material Curl of  $\mathbf{F}$ , the fundamental tensors  $\overset{3}{\mathbf{e}}$  and  $\overset{3}{\mathbf{E}}$  are related as follows

$$\overset{3}{\mathbf{e}} = \frac{1}{J} F^a_A F^b_B \left\{ \frac{1}{\sqrt{G}} \epsilon^{IJK} G^A_I G^B_J G^C_K \right\} F^c_C \mathbf{e}_a \otimes \mathbf{e}_b \otimes \mathbf{e}_c = \frac{1}{J} [\mathbf{F} \odot \mathbf{F}] : \overset{3}{\mathbf{E}} \cdot \mathbf{F}^T \quad (\text{B.21})$$

This follows e.g. in convective coordinates by insertion of  $\mathbf{g}_I = \mathbf{F} \mathbf{G}_I$ , (2.17), into (B.18) and with the definition of the Jacobian  $J$  (section 2.1.2). Here, the symbol  $\odot$  indicates a dyadic product in the sense of  $[\mathbf{F} \odot \mathbf{F}]^{ab}_{AB} = [\mathbf{F}]^a_A [\mathbf{F}]^b_B$ . Furthermore, the relation between the spatial gradient of  $\mathbf{F}^{-1}$  and the material gradient of  $\mathbf{F}$  follows from

$$\nabla_{X^C} (F^a_A F^{-1A}_b) = F^a_{A,C} F^{-1A}_b + F^a_A F^{-1A}_{b,c} F^c_C = 0 \quad (\text{B.22})$$

which implies in direct notation

$$-\nabla_{\mathbf{X}} \mathbf{F} = \mathbf{F} \cdot \nabla_{\mathbf{x}} \mathbf{F}^{-1} : [\mathbf{F} \odot \mathbf{F}] \quad (\text{B.23})$$

Now contraction of (B.23) with the material fundamental tensor  $\overset{3}{\mathbf{E}}$  gives with (B.21) and (B.17) the relation between the spatial curl of  $\mathbf{F}^{-1}$  and the material Curl of  $\mathbf{F}$

$$\text{Curl}^T \mathbf{F} = -J \mathbf{F} \cdot \text{curl}^T \mathbf{F}^{-1} \cdot \mathbf{F}^{-T} \quad (\text{B.24})$$

### B.3. The Curl Operator in the Intermediate Configuration

Based on the anholonomic derivative, see also section 5.5.2, equation (5.61),

$$\bar{\nabla}(\bullet) = \nabla_{\mathbf{X}}(\bullet) \cdot \mathbf{F}^{p-1} = \nabla_{\mathbf{x}}(\bullet) \cdot \mathbf{F}^e \quad (\text{B.25})$$

the contravariant Curl operator of the intermediate configuration applied to a mixed variant second order tensor  $\mathbf{T}$  is introduced in analogy to (B.15)

$$\overline{\text{Curl}}^T \mathbf{T} := -\bar{\nabla} \mathbf{T} : \overset{3}{\mathbf{E}} \quad (\text{B.26})$$

with the third order *fundamental tensor*  $\overset{3}{\mathbf{E}}$  of the intermediate configuration.  $\overset{3}{\mathbf{E}}$  is related to the Lagrangian and Eulerian fundamental tensors in analogy to (B.21) as follows

$$\overset{3}{\mathbf{E}} = \frac{1}{J^p} [\mathbf{F}^p \odot \mathbf{F}^p] : \overset{3}{\mathbf{E}} \cdot \mathbf{F}^{pT} = J^e [\mathbf{F}^{e-1} \odot \mathbf{F}^{e-1}] : \overset{3}{\mathbf{e}} \cdot \mathbf{F}^{e-T} \quad (\text{B.27})$$

With these relations at hand, the material Curl of  $\mathbf{F}^p$  can be related to the  $\overline{\text{Curl}}$  of  $\mathbf{F}^{p-1}$  in the intermediate configuration in analogy to (B.24) as follows

$$\text{Curl}^T \mathbf{F}^p = -J^p \mathbf{F}^p \cdot \overline{\text{Curl}}^T \mathbf{F}^{p-1} \cdot \mathbf{F}^{p-T} \quad (\text{B.28})$$

and the intermediate  $\overline{\text{Curl}}$  of  $\mathbf{F}^e$  can be expressed in terms of the spatial curl of  $\mathbf{F}^{e-1}$  by

$$\overline{\text{Curl}}^T \mathbf{F}^e = -J^e \mathbf{F}^e \cdot \text{curl}^T \mathbf{F}^{e-1} \cdot \mathbf{F}^{e-T} \quad (\text{B.29})$$

## C. Algorithmic Sensitivities

In the following, the algorithmic sensitivities required especially within the algorithmic linearizations in chapter 6 will be derived.

### C.1. Sensitivities with respect to the Total Deformation Field

**Linear increment**  $\Delta_{\varphi}[\nabla_{\mathbf{x}}\delta\varphi]$ : This linear increment might first be rewritten as follows

$$\Delta_{\varphi}[\nabla_{\mathbf{x}}\delta\varphi] = \Delta_{\varphi}[\nabla_{\mathbf{X}}(\delta\varphi) \cdot \mathbf{F}^{-1}] = \nabla_{\mathbf{X}}(\delta\varphi) \cdot \Delta_{\varphi}[\mathbf{F}^{-1}] = \nabla_{\mathbf{x}}(\delta\varphi) \cdot \mathbf{F} \cdot \Delta_{\varphi}[\mathbf{F}^{-1}] \quad (\text{C.30})$$

where  $\Delta_{\varphi}[\mathbf{F}^{-1}]$  follows from  $\Delta[\mathbf{F} \cdot \mathbf{F}^{-1}] = \mathbf{0}$ , i.e.

$$\begin{aligned} \Delta_{\varphi}[\mathbf{F}^{-1}] &= -\mathbf{F}^{-1} \cdot \Delta_{\varphi}[\mathbf{F}] \cdot \mathbf{F}^{-1} = -\mathbf{F}^{-1} \cdot \Delta_{\varphi}[\nabla_{\mathbf{X}}\varphi] \cdot \mathbf{F}^{-1} \\ &= -\mathbf{F}^{-1} \cdot \nabla_{\mathbf{X}}\Delta\varphi \cdot \mathbf{F}^{-1} = -\mathbf{F}^{-1} \cdot \nabla_{\mathbf{x}}\Delta\varphi \end{aligned} \quad (\text{C.31})$$

Insertion of (C.31) into (C.30) gives

$$\Delta_{\varphi}[\nabla_{\mathbf{x}}\delta\varphi] = -\nabla_{\mathbf{x}}\delta\varphi \nabla_{\mathbf{x}}\Delta\varphi \quad (\text{C.32})$$

**Linear increment**  $\Delta_{\varphi}[\boldsymbol{\tau}]$ : With (C.31), an objective stress increment of the Kirchhoff stresses can be computed in the sense of a Lie-derivative as follows

$$\mathcal{L}_{\Delta_{\varphi}}\boldsymbol{\tau} = \mathbf{F} \cdot \Delta_{\varphi}[\mathbf{S}] \cdot \mathbf{F}^T = \mathbf{F} \cdot \Delta_{\varphi}[\mathbf{F}^{-1} \cdot \boldsymbol{\tau} \cdot \mathbf{F}^{-T}] \cdot \mathbf{F}^T = \Delta_{\varphi}[\boldsymbol{\tau}] - \nabla_{\mathbf{x}}\Delta\varphi \cdot \boldsymbol{\tau} - \boldsymbol{\tau} \cdot \nabla_{\mathbf{x}}^T\Delta\varphi \quad (\text{C.33})$$

which denotes the Oldroyd-type incremental stress rate.  $\mathcal{L}_{\Delta\varphi}\boldsymbol{\tau}$  might on the other hand be derived from the constitutive equations, see e.g. equation (A.14), which defines the elastic-plastic tangent moduli

$$\mathcal{L}_{\Delta\varphi}\boldsymbol{\tau} = 2\partial_{\mathbf{g}}\boldsymbol{\tau} : \left(\frac{1}{2}\mathcal{L}_{\Delta\varphi}\mathbf{g}\right) = \mathfrak{c}^{ep} : \text{sym}[\nabla_{\mathbf{x}}\Delta\varphi] \quad \text{with} \quad \mathfrak{c}^{ep} := 2\partial_{\mathbf{g}}\boldsymbol{\tau} \quad (\text{C.34})$$

Consequently  $\Delta_{\varphi}[\boldsymbol{\tau}]$  can be computed as follows

$$\Delta_{\varphi}[\boldsymbol{\tau}] = c^{ep} : \text{sym}[\nabla_{\mathbf{x}}\Delta\varphi] + \nabla_{\mathbf{x}}\Delta\varphi \cdot \boldsymbol{\tau} + \boldsymbol{\tau} \cdot \nabla_{\mathbf{x}}^T \Delta\varphi \quad (\text{C.35})$$

**Linear increment  $\Delta_{\varphi}[\boldsymbol{\tau}^{\alpha}]$ :** With (A.3) the increment  $\Delta_{\varphi}[\boldsymbol{\tau}^{\alpha}]$  reads

$$\begin{aligned} \Delta_{\varphi}[\boldsymbol{\tau}^{\alpha}] &= \Delta_{\varphi}[\text{dev } \boldsymbol{\Sigma} : \mathbf{S}^{\alpha} \otimes \mathbf{M}^{\alpha}] \\ &= \mu (\mathbf{F}^{p-T} \cdot \Delta_{\varphi}[\tilde{\mathbf{F}}^T] \cdot \tilde{\mathbf{F}} \cdot \mathbf{F}^{p-1} + \mathbf{F}^{p-T} \cdot \tilde{\mathbf{F}}^T \cdot \Delta_{\varphi}[\tilde{\mathbf{F}}] \cdot \mathbf{F}^{p-1}) : \mathbf{S}^{\alpha} \otimes \mathbf{M}^{\alpha} \end{aligned} \quad (\text{C.36})$$

Therein  $\Delta_{\varphi}[\tilde{\mathbf{F}}^T]$  follows with  $\Delta_{\varphi}[J] = J(1 : \nabla_{\mathbf{x}}\Delta\varphi)$  and  $\Delta\mathbf{F} = \nabla_{\mathbf{x}}\Delta\varphi \cdot \mathbf{F}$  as

$$\Delta_{\varphi}[\tilde{\mathbf{F}}^T] = \Delta_{\varphi}(J^{-1/3}\mathbf{F}^T) = -1/3(1 : \nabla_{\mathbf{x}}\Delta\varphi) \cdot \tilde{\mathbf{F}}^T + \tilde{\mathbf{F}}^T \cdot \nabla_{\mathbf{x}}^T \Delta\varphi \quad (\text{C.37})$$

Finally insertion of (C.37) into (C.36) gives

$$\begin{aligned} \Delta_{\varphi}[\boldsymbol{\tau}^{\alpha}] &= \mu [-2/3(1 : \nabla_{\mathbf{x}}\Delta\varphi) \cdot \mathbf{1} + \nabla_{\mathbf{x}}^T \Delta\varphi + \nabla_{\mathbf{x}}\Delta\varphi] : \tilde{\mathbf{F}}^e \cdot \mathbf{S}^{\alpha} \otimes \mathbf{M}^{\alpha} \cdot \tilde{\mathbf{F}}^{eT} \\ &= \mu [-2/3(1 : \nabla_{\mathbf{x}}\Delta\varphi) \cdot \mathbf{1} + \nabla_{\mathbf{x}}^T \Delta\varphi + \nabla_{\mathbf{x}}\Delta\varphi] : \mathbf{s}^{\alpha} \otimes \mathbf{m}^{\alpha} \\ &= \mu [-2/3(1 \otimes 1) : \mathbf{s}^{\alpha} \otimes \mathbf{m}^{\alpha} + \mathbf{m}^{\alpha} \otimes \mathbf{s}^{\alpha} + \mathbf{m}^{\alpha} \otimes \mathbf{s}^{\alpha}] : \nabla_{\mathbf{x}}\Delta\varphi \\ &= \mu \text{dev}[\mathbf{s}^{\alpha} \otimes \mathbf{m}^{\alpha} + \mathbf{s}^{\alpha} \otimes \mathbf{m}^{\alpha}] : \nabla_{\mathbf{x}}\Delta\varphi \end{aligned} \quad (\text{C.38})$$

## C.2. Sensitivities with respect to the Plastic Slip

**Linear increment  $\Delta_{\gamma\beta}[\boldsymbol{\tau}]$ :** This sensitivity is derived in analogy to (A.12) in terms of the algorithmic sensitivity  $\tilde{\mathbf{F}}^e_{,\gamma\beta}$  (note:  $\Delta_{\gamma\beta}p = 0$ )

$$\Delta_{\gamma\beta}[\boldsymbol{\tau}] = \mu \text{dev}[\tilde{\mathbf{F}}^e_{,\gamma\beta} \cdot \tilde{\mathbf{F}}^{eT} + \tilde{\mathbf{F}}^e \cdot \tilde{\mathbf{F}}^e_{,\gamma\beta}] \Delta\gamma^{\beta} \quad (\text{C.39})$$

**Linear increment  $\Delta_{\gamma\beta}[\boldsymbol{\tau}^{\alpha}]$ :** This sensitivity follows from (A.3) in analogy to (A.6)

$$\Delta_{\gamma\beta}[\boldsymbol{\tau}^{\alpha}] = \mu \{ (\tilde{\mathbf{F}}^e_{,\gamma\beta} \cdot \mathbf{S}^{\alpha}) \cdot (\tilde{\mathbf{F}}^e \cdot \mathbf{M}^{\alpha}) + (\tilde{\mathbf{F}}^e \cdot \mathbf{S}^{\alpha}) \cdot (\tilde{\mathbf{F}}^e_{,\gamma\beta} \cdot \mathbf{M}^{\alpha}) \} \Delta\gamma^{\beta} \quad (\text{C.40})$$

**Linear increment  $\Delta_{\gamma\beta}[\boldsymbol{\tau}_r^{\alpha}]$ :** For the specific form (5.166) of the slip resistance  $\boldsymbol{\tau}_r^{\alpha}$ , this sensitivity is determined as follows

$$\Delta_{\gamma\beta}[\boldsymbol{\tau}_r^{\alpha}] = c_{\rho}^{\alpha} \sum_{\omega=1}^m G^{\alpha\omega} (\Delta_{\gamma\beta}[\rho_{\text{SSD}}^{\omega}] + \Delta_{\nabla_{\mathbf{X}}\gamma^{\beta}}[\rho_{\text{GND}}^{\omega}]) \quad (\text{C.41})$$

with the definition

$$c_{\rho}^{\alpha} := (c\mu b)^2 / (2\tau_r^{\alpha}) \quad (\text{C.42})$$

and the sensitivities

$$\begin{aligned} \Delta_{\gamma\beta}[\rho_{\text{SSD}}^{\omega}] &= \frac{1}{\gamma^{\text{sat}}} (\rho^{\text{sat}} - \rho^{0,\omega}) \exp(-\gamma^{\omega}/\gamma^{\text{sat}}) \delta^{\omega\beta} \Delta\gamma^{\beta} &=: B^{\omega\beta} \Delta\gamma^{\beta} \\ \Delta_{\nabla_{\mathbf{X}}\gamma^{\beta}}[\rho_{\text{GND}}^{\omega}] &= \frac{1}{b^2 \rho_{\text{GND}}^{\omega}} \{ (\nabla_{\mathbf{X}}\gamma^{\omega} \cdot \mathbf{S}^{\omega}) \mathbf{S}^{\omega} + (\nabla_{\mathbf{X}}\gamma^{\omega} \cdot \mathbf{M}^{\omega}) \mathbf{M}^{\omega} \} \delta^{\omega\beta} \nabla_{\mathbf{X}}\Delta\gamma^{\beta} &=: \mathbf{E}^{\omega\beta} \cdot \nabla_{\mathbf{X}}\Delta\gamma^{\beta} \end{aligned} \quad (\text{C.43})$$

Thus by insertion of (C.43) into (C.41) the sensitivity  $\Delta_{\gamma\beta}[\boldsymbol{\tau}_r^{\alpha}]$  can be written as

$$\Delta_{\gamma\beta}[\boldsymbol{\tau}_r^{\alpha}] = c_{\rho}^{\alpha} \sum_{\omega=1}^m G^{\alpha\omega} (B^{\omega\beta} \Delta\gamma^{\beta} + \mathbf{E}^{\omega\beta} \cdot \nabla_{\mathbf{X}}\Delta\gamma^{\beta}) \quad (\text{C.44})$$

## D. The Enhanced Strain Formulation

The global as well as the extended local formulations of gradient crystal plasticity considered in chapter 6 have been implemented within the context of an *enhanced strain* formulation. This was not explained in detail in chapters 6 in view of a compact notation. A brief outline of the corresponding implications will thus be given in this chapter. For more details see SIMO & ARMERO [138]. The central idea of such an *enhanced formulation* is to split the deformation gradient  $\mathbf{F}$  into the *standard deformation gradient*  $\mathbf{F}_C = \nabla_{\mathbf{x}}\varphi$  and an *enhanced displacement gradient*  $\mathbf{H}_E$

$$\mathbf{F} := \mathbf{F}_C + \mathbf{H}_E \quad \text{in } \mathcal{B} \quad (\text{D.45})$$

associated with the *actual (or compatible) deformation map*  $\varphi_C$  and an *enhanced displacement field*  $\mathbf{u}_E$  in the sense

$$\varphi := \varphi_C + \mathbf{u}_E \quad \text{in } \mathcal{B} \quad (\text{D.46})$$

The relation exploited in order to determine the enhanced displacement field is obtained as follows. Consider a three-field formulation of the Hu-Washizu type in terms of the deformation map, the deformation gradient and the stresses. Reparametrization in terms of (D.45) and variation renders three contributions to the weak form: the equilibrium equations which will be weakly satisfied, the stress identification being strongly satisfied, and the so-called *L<sub>2</sub>-orthogonality*

$$\int_{\mathcal{B}} \delta \mathbf{P} : \mathbf{H}_E dV = 0 \quad (\text{D.47})$$

Thus the corresponding Euler-Lagrange equation demands that for the continuum problem the enhanced displacement gradient  $\mathbf{H}_E$  vanishes in  $\mathcal{B}$ . If  $\mathcal{T}$  is the admissible space for  $\delta \mathbf{P}$  and  $\mathcal{H}$  contains all  $\mathbf{H}_E$ , then all admissible stresses  $\mathbf{P}$  are as well in  $\mathcal{T}$  and  $\mathbf{H}_E$  analogously contains all admissible  $\delta \mathbf{H}_E$ . Consequently, (D.47) may be rewritten as  $\int_{\mathcal{B}} \delta \mathbf{H}_E : \mathbf{P} dV = 0$ . Within the finite element formulation, interelement continuity is only required for  $\varphi_C$ . In view of a spatial, formulation the L<sub>2</sub>-orthogonality is written as

$$G_{\mathbf{u}_E}(\varphi_C, \gamma^\alpha, \mathbf{u}_E, \delta \mathbf{u}_E) := \int_{\mathcal{B}} \nabla_{\mathbf{x}} \delta \mathbf{u}_E : \boldsymbol{\tau} dV = 0 \quad (\text{D.48})$$

This equation will be included as a third relation into the weak form besides the equilibrium condition  $G_{\varphi_C}(\varphi_C, \gamma^\alpha, \mathbf{u}_E, \delta \varphi_C)$  and the slip evolution equations/KKT conditions  $G_{\gamma^\alpha}(\varphi_C, \gamma^\alpha, \mathbf{u}_E, \delta \gamma^\alpha)$ . This system of nonlinear equations will be solved within a Newton-Raphson scheme in line with the considerations in chapter 6. The corresponding developments will be outlined for  $G_{\varphi_C}$  and  $G_{\mathbf{u}_E}$  in the following. The derivations for the corresponding  $G_{\gamma^\alpha}$  are in complete analogy to the previous considerations and are consequently not considered here again.  $\text{Lin} \hat{G}_{\varphi_C}(\varphi_C, \gamma^\alpha, \mathbf{u}_E, \delta \varphi_C, \Delta \varphi_C, \Delta \mathbf{u}_E)$  and  $\text{Lin} \hat{G}_{\mathbf{u}_E}(\varphi_C, \gamma^\alpha, \mathbf{u}_E, \delta \mathbf{u}_E, \Delta \varphi_C, \Delta \mathbf{u}_E)$  read

$$\begin{aligned} \text{Lin} G_{\varphi_C} := & \int_{\mathcal{B}} \left( \nabla_{\mathbf{x}} \delta \varphi_C : \mathbb{c}^{ep} : \nabla_{\mathbf{x}} \Delta \varphi_C + \nabla_{\mathbf{x}} \delta \varphi_C : \mathbb{c}^{ep} : \nabla_{\mathbf{x}} \Delta \mathbf{u}_E \right. \\ & \left. + \nabla_{\mathbf{x}} \delta \varphi_C : [\nabla_{\mathbf{x}} \Delta \varphi_C \cdot \boldsymbol{\tau}] + \nabla_{\mathbf{x}} \delta \varphi_C : [\nabla_{\mathbf{x}} \Delta \mathbf{u}_E \cdot \boldsymbol{\tau}] \right) dV \\ & + \int_{\mathcal{B}} \boldsymbol{\tau} : \nabla_{\mathbf{x}} \delta \varphi_C dV + \int_{\mathcal{B}} \nabla_{\mathbf{x}} \delta \varphi_C : \left( \sum_{\beta=1}^m \Delta_{\gamma^\beta}[\boldsymbol{\tau}] \right) dV - \hat{G}_{\varphi_C^{ext}}(\delta \varphi_C) = 0 \end{aligned} \quad (\text{D.49})$$

$$\begin{aligned}
\text{Lin}G_{\mathbf{u}_E} &:= \int_{\mathcal{B}} \left( \nabla_{\mathbf{x}} \delta \mathbf{u}_E : \mathbf{c}^{ep} : \nabla_{\mathbf{x}} \Delta \boldsymbol{\varphi}_C + \nabla_{\mathbf{x}} \delta \mathbf{u}_E : \mathbf{c}^{ep} : \nabla_{\mathbf{x}} \Delta \mathbf{u}_E \right. \\
&\quad \left. + \nabla_{\mathbf{x}} \delta \mathbf{u}_E : [\nabla_{\mathbf{x}} \Delta \boldsymbol{\varphi}_C \cdot \boldsymbol{\tau}] + \nabla_{\mathbf{x}} \delta \mathbf{u}_E : [\nabla_{\mathbf{x}} \Delta \mathbf{u}_E \cdot \boldsymbol{\tau}] \right) dV \\
&\quad + \int_{\mathcal{B}} \boldsymbol{\tau} : \nabla_{\mathbf{x}} \delta \mathbf{u}_E dV + \int_{\mathcal{B}} \nabla_{\mathbf{x}} \delta \mathbf{u}_E : \left( \sum_{\beta=1}^m \Delta_{\gamma^\beta} [\boldsymbol{\tau}] \right) dV = 0
\end{aligned} \tag{D.50}$$

Within the finite element formulation, the virtual and incremental deformations are discretized in terms of the discrete compatible deformations and enhanced displacements

$$\boldsymbol{\varphi}^h = \boldsymbol{\varphi}_C^h + \mathbf{u}_E^h, \quad \delta \boldsymbol{\varphi}^h = \delta \boldsymbol{\varphi}_C^h + \delta \mathbf{u}_E^h, \quad \Delta \boldsymbol{\varphi}^h = \Delta \boldsymbol{\varphi}_C^h + \Delta \mathbf{u}_E^h \tag{D.51}$$

where the compatible parts are identical with the standard displacement interpolations, see chapter 6. The additional enhanced parts are in turn not required to be interelement continuous and can thus be considered as internal element degrees discretized as follows

$$\mathbf{u}_E^h = \sum_{f=1}^m M^f \mathbf{a}^f, \quad \delta \mathbf{u}_E^h = \sum_{f=1}^m M^f \delta \mathbf{a}^f, \quad \Delta \mathbf{u}_E^h = \sum_{f=1}^m M^f \Delta \mathbf{a}^f \tag{D.52}$$

where  $\{\mathbf{a}^f, \delta \mathbf{a}^f, \Delta \mathbf{a}^f\}$  denote actual, virtual and incremental internal element degrees associated with a fictive node  $e$ .  $M^f = \hat{M}^f(\boldsymbol{\xi})$  are the corresponding enhanced interpolation modes (e.g. for a quadrilateral in 2D  $\hat{M}^f(\boldsymbol{\xi}) = \frac{1}{2}(\xi_e^2 - 1)$ ,  $f = 1, 2$ ). The material gradients of these enhanced shapes are defined through  $\nabla_{\mathbf{X}} M^f := J_0 / J (\nabla_{\boldsymbol{\xi}} M^f) \cdot \mathbf{J}_0^{-1}$ .  $\mathbf{J}_0$  denotes the Jacobian of the isoparametric map  $\boldsymbol{\chi} := \boldsymbol{\xi} \rightarrow \mathbf{X}$  evaluated at  $\boldsymbol{\xi} = \mathbf{0}$  and  $J := \det[\mathbf{J}(\boldsymbol{\xi})]$  and  $J_0 := \det[\mathbf{J}_0]$  denote the Jacobian determinants evaluated at  $\boldsymbol{\xi}$  and the element center  $\boldsymbol{\xi} = \mathbf{0}$ . The spatial gradients of the shape functions are finally computed in terms of the enhanced discrete deformation gradient  $\mathbf{F}^h$  as follows

$$\begin{aligned}
\nabla_{\mathbf{x}} N^I &= (\nabla_{\mathbf{X}} N^I) \cdot \mathbf{F}^{h-1} & \text{with } \mathbf{F}^h &= \underbrace{\mathbf{1} + \sum_{I=1}^{n_{en}} \mathbf{d}^I \otimes \nabla_{\mathbf{X}} N^I}_{\text{compatible}} + \underbrace{\sum_{f=1}^m \mathbf{a}^f \otimes \nabla_{\mathbf{X}} M^f}_{\text{enhanced}} \\
\nabla_{\mathbf{x}} M^f &= (\nabla_{\mathbf{X}} M^f) \cdot \mathbf{F}^{h-1}
\end{aligned} \tag{D.53}$$

Thereby  $\mathbf{F}^h$  now consists of a compatible and an enhanced part. (Note that within the strain gradient crystal plasticity formulation of chapter 6, only material gradients of the plastic slips and thus the corresponding shapes are required.)

In the following, the full system of all three residual expressions of the enhanced global formulation of strain gradient crystal plasticity will be considered. Insertion of the discretizations into (D.49), (D.50) and the respective *enhanced forms* of the residual expressions  $G_{\gamma^\alpha}^h$  of chapter 6 results in the coupled system of linearized discrete element equations

$$\begin{bmatrix} \mathbf{k}_{dd}^e & \mathbf{k}_{d\gamma}^{e\beta} & \mathbf{k}_{da}^e \\ \mathbf{k}_{\gamma d}^{e\alpha} & \mathbf{k}_{\gamma\gamma}^{e\alpha\beta} & \mathbf{k}_{\gamma a}^{e\alpha} \\ \mathbf{k}_{ad}^e & \mathbf{k}_{a\gamma}^{e\beta} & \mathbf{k}_{aa}^e \end{bmatrix} \begin{bmatrix} \Delta \mathbf{d} \\ \Delta \gamma^\beta \\ \Delta \mathbf{a} \end{bmatrix} = \begin{bmatrix} -\mathbf{f}_d^{\text{int } e} + \mathbf{f}_d^{\text{ext } e} \\ -\mathbf{f}_\gamma^{e\alpha} \\ -\mathbf{f}_a^{\text{int } e} \end{bmatrix} \tag{D.54}$$

The element parameters  $\mathbf{a}$  are defined on the element domain. Thus their increments  $\Delta \mathbf{a}$  in (D.54) can be eliminated on the element level by static condensation based on the elimination equation

$$\Delta \mathbf{a} = [\mathbf{k}_{aa}^e]^{-1} \left( -\mathbf{f}_a^{\text{int } e} - [\mathbf{k}_{ad}^e \quad \mathbf{k}_{a\gamma}^{e\beta}] \begin{bmatrix} \Delta \mathbf{d} \\ \Delta \gamma^\beta \end{bmatrix} \right) \tag{D.55}$$

Insertion of (D.55) into (D.54) then results in the condensed elementwise equations

$$\tilde{\mathbf{K}}^e [\Delta \mathbf{d} \quad \Delta \gamma^\beta]^T = \tilde{\mathbf{F}}^e \quad (\text{D.56})$$

in terms of the condensed element tangent  $\tilde{\mathbf{K}}^e$  and residual  $\tilde{\mathbf{F}}^e$  which are given by

$$\begin{aligned} \tilde{\mathbf{K}}^e &:= \begin{bmatrix} \mathbf{k}_{dd}^e & \mathbf{k}_{d\gamma}^{e\beta} \\ \mathbf{k}_{\gamma d}^{e\alpha} & k_{\gamma\gamma}^{e\alpha\beta} \end{bmatrix} - \begin{bmatrix} \mathbf{k}_{da}^e \\ \mathbf{k}_{\gamma a}^{e\alpha} \end{bmatrix} [\mathbf{k}_{aa}^e]^{-1} [\mathbf{k}_{ad}^e \quad \mathbf{k}_{a\gamma}^{e\beta}] \\ \text{and } \tilde{\mathbf{F}}^e &:= \begin{bmatrix} -\mathbf{f}_d^{\text{int } e} + \mathbf{f}_d^{\text{ext } e} \\ -f_\gamma^{e\alpha} \end{bmatrix} + \begin{bmatrix} \mathbf{k}_{da}^e \\ \mathbf{k}_{\gamma a}^{e\alpha} \end{bmatrix} [\mathbf{k}_{aa}^e]^{-1} [\mathbf{f}_a^{\text{int } e}] \end{aligned} \quad (\text{D.57})$$

These condensed element tangent and residual arrays are assembled within each global Newton-Raphson iteration step. The consecutive global update then gives the improved displacement and slip increments. Finally, the update of the element parameters  $\mathbf{a}$  is performed elementwise through (D.55).

## References

- [1] ACHARYA, A.; BASSANI, J. L. [2000]: *Lattice incompatibility and a gradient theory of crystal plasticity*. Journal of the Mechanics and Physics of Solids, 48: 1565–1595.
- [2] ACHARYA, A.; BEAUDOIN, A. J. [2000]: *Grain-size effect in viscoplastic polycrystals at moderate strains*. Journal of the Mechanics and Physics of Solids, 48: 2213–2230.
- [3] ANTHONY, K. H. [1970]: *Die Reduktion von nichteuklidischen geometrischen Objekten in eine euklidische Form und physikalische Deutung der Reduktion durch Eigenspannungszustände in Kristallen*. Archive for Rational Mechanics and Analysis, 37: 161–180.
- [4] ANTHONY, K. H. [1970]: *Die Theorie der Disklinationen*. Archive for Rational Mechanics and Analysis, 39: 43–88.
- [5] ARMSTRONG, R.; CODD, I.; DOUTHWAITE, R. M.; PETCH, N. J. [1962]: *The plastic deformation of polycrystalline aggregates*. The Philosophical Magazine, 7: 45–58.
- [6] ARSENLIS, A.; PARKS, D. M. [1999]: *Crystallographic aspects of geometrically-necessary and statistically-stored dislocation density*. Acta Materialia, 47: 1597–1611.
- [7] ARSENLIS, A.; PARKS, D. M. [2002]: *Modeling the evolution of crystallographic dislocation density in crystal plasticity*. Journal of the Mechanics and Physics of Solids, 50: 1979–2009.
- [8] ARSENLIS, A.; PARKS, D. M.; BECKER, R.; BULATOV, V. V. [2004]: *On the evolution of crystallographic dislocation density in non-homogeneously deforming crystals*. Journal of the Mechanics and Physics of Solids, 52: 1213–1246.
- [9] ASARO, R. [1979]: *Geometrical effects in the inhomogeneous deformation of ductile single crystals*. Acta Metallurgica, 27: 445–453.
- [10] ASARO, R. [1983]: *Crystal plasticity*. Journal of Applied Mechanics, 50: 921–934.
- [11] ASARO, R. [1983]: *Micromechanics of crystals and polycrystals*. Advances in Applied Mechanics, 23: 1–115.
- [12] ASHBY, M. F. [1970]: *The deformation of plastically non-homogeneous materials*. The Philosophical Magazine A, 21: 399–424.
- [13] BALL, J. M. [1977]: *Convexity conditions and existence theorems in nonlinear elasticity*. Archive of Rational Mechanics and Analysis, 63: 337–403.
- [14] BASINSKI, S. J.; BASINSKI, Z. S. [1966]: *The nature of the cold worked state*. In *Recrystallization, Grain Growth and Textures*, Chapter 1, pp. 1–44. American Society for Metals, Metals Park, Ohio.
- [15] BASSANI, J. L. [1993]: *Plastic flow of crystals*. Advances in Applied Mechanics, 30: 191–258.
- [16] BASSANI, J. L. [2001]: *Incompatibility and a simple gradient theory of plasticity*. Journal of the Mechanics and Physics of Solids, 49: 1983–1996.
- [17] BASSANI, J. L.; WU, T. Y. [1991]: *Latent hardening in single crystals II. Analytical characterization and predictions*. Proceedings of the Royal Society London A, 435: 21–41.

- [18] BILBY, B. A. [1960]: *Continuous distributions of dislocations*, *Progress in Solid Mechanics 1*. North-Holland Publishing Company.
- [19] BILBY, B. A.; BULLOUGH, R.; SMITH, E. [1955]: *Continuous distributions of dislocations: a new application of the methods of non-Riemannian geometry*. Proceedings of the Royal Society London A, 231: 263–273.
- [20] BILBY, B. A.; SMITH, E. [1956]: *Continuous distributions of dislocations III*. Proceedings of the Royal Society London A, 236: 481–505.
- [21] BITTENCOURT, E.; NEEDLEMAN, A.; GURTIN, M. E.; VAN DER GIESSEN, E. [2003]: *A comparison of nonlocal continuum and discrete dislocation plasticity predictions*. Journal of the Mechanics and Physics of Solids, 51: 281–310.
- [22] BORJA, R. I.; WREN, J. R. [1993]: *Discrete micromechanics of elastoplastic crystals*. International Journal for Numerical Methods in Engineering, 36: 3815–3840.
- [23] BRUHNS, O. T.; XIAO, H.; MEYERS, A. [2001]: *Constitutive inequalities for an isotropic elastic strain-energy function based on Hencky's logarithmic strain tensor*. Proceedings of the the Royal Society of London, Series A, 457: 2207–2226.
- [24] CARTAN, É. [1923]: *Sur les variétés de connexion affine et la théorie de la relativité généralisée*. Annales scientifiques de l'École Normale Supérieure III, 40: 325–412.
- [25] CERMELLI, P.; GURTIN, M. E. [2001]: *On the characterization of geometrically necessary dislocations in finite plasticity*. Journal of the Mechanics and Physics of Solids, 49: 1539–1568.
- [26] CERMELLI, P.; GURTIN, M. E. [2002]: *Geometrically necessary dislocations in viscoplastic single crystals and bicrystals undergoing small deformations*. International Journal of Solids and Structures, 39: 6281–6309.
- [27] CLEVERINGA, H. H. M.; VAN DER GIESSEN, E.; NEEDLEMAN, A. [1997]: *Comparison of discrete dislocation and continuum plasticity predictions for a composite material*. Acta Materialia, 45: 3163–3179.
- [28] CLEVERINGA, H. H. M.; VAN DER GIESSEN, E.; NEEDLEMAN, A. [1999]: *A discrete dislocation analysis of bending*. International Journal of Plasticity, 15: 837–868.
- [29] CLEVERINGA, H. H. M.; VAN DER GIESSEN, E.; NEEDLEMAN, A. [1999]: *A discrete dislocation analysis of residual stresses in a composite material*. Philosophical Magazine A, 79: 493–920.
- [30] COLEMAN, B.; NOLL, W. [1959]: *On the thermostatics of continuous media*. Archive of Rational Mechanics and Analysis, 4: 97–128.
- [31] COTTRELL, A. H. [1964]: *The mechanical properties of matter*. New York: Wiley.
- [32] CROUZEIX, M.; RAVIART, P. A. [1973]: *Conforming and nonconforming finite element methods for solving the stationary stokes equations*. Revue Francaise D'Automatique D'Informatique et de Recherche Operationelle/Mathematical Modelling and Numerical Analysis, 7: 33–76.
- [33] CUITIÑO, A. M.; ORTIZ, M. [1992]: *Computational modelling of single crystals*. Modelling and Simulation in Materials Science and Engineering, 1: 225–263.
- [34] DACOROGNA, B. [1989]: *Direct methods in the calculus of variations*. Springer.

- [35] DAI, H.; PARKS, D. M. [1997]: *Geometrically-necessary dislocation density and scale-dependent crystal plasticity*. *Plasticity '97*, pp. 17–18.
- [36] ERINGEN, A. C. [1971]: *Continuum Physics, Volume I - Mathematics*. Academic Press.
- [37] ESSMANN, U.; RAPP, M. [1973]: *Slip in copper crystals following weak neutron bombardment*. *Acta Metallurgica*, 21: 1305–1317.
- [38] EVERS, L. P.; BREKELMANS, W. A. M.; GEERS, M. G. D. [2004]: *Non-local crystal plasticity model with intrinsic SSD and GND effects*. *Journal of the Mechanics and Physics of Solids*, 52: 2379–2401.
- [39] EVERS, L. P.; BREKELMANS, W. A. M.; GEERS, M. G. D. [2004]: *Scale dependent crystal plasticity framework with dislocation density and grain boundary effects*. *International Journal of Solids and Structures*, 41: 5209–5230.
- [40] FLECK, N. A.; HUTCHINSON, J. W. [1993]: *A phenomenological theory for strain gradient effects in plasticity*. *Journal of the Mechanics and Physics of Solids*, 41: 1825–1857.
- [41] FLECK, N. A.; HUTCHINSON, J. W. [1997]: *Strain gradient plasticity*. *Advances in Applied Mechanics*, 33: 295–362.
- [42] FLECK, N. A.; MÜLLER, G. M.; ASHBY, M. F.; HUTCHINSON, J. [1994]: *Strain gradient plasticity: theory and experiment*. *Acta Materialia*, 42: 475–487.
- [43] FRANCIOSI, P. [1983]: *Glide mechanisms in BCC crystals: an investigation of the case of  $\alpha$ -iron through multislip and latent hardening tests*. *Acta Metallurgica*, 31: 1331–1342.
- [44] FRANCIOSI, P.; BERVEILLER, M.; ZAOUI, A. [1980]: *Latent hardening in copper and aluminium single crystals*. *Acta Metallurgica*, 28: 273–283.
- [45] FRANCIOSI, P.; ZAOUI, A. [1982]: *Multislip in f.c.c. crystals: a theoretical approach compared with experimental data*. *Acta Metallurgica*, 30: 1627–1637.
- [46] FRANK, F. C. [1951]: *Crystal dislocations - Elementary concepts and definitions*. *The Philosophical Magazine*, 42: 809–819.
- [47] GEYMONAT, G.; MÜLLER, S.; TRIANTAFYLIDIS, N. [1993]: *Homogenization of nonlinearly elastic materials, microscopic bifurcation and macroscopic loss of rank-one convexity*. *Archive of Rational Mechanics and Analysis*, 122: 231–290.
- [48] GILLIS, P. P.; GILMAN, J. J. [1965]: *Dynamical dislocation theory of crystal plasticity II. Easy glide and strain hardening*. *Journal of Applied Physics*, 36: 3380–3386.
- [49] GÜNTHER, W. [1958]: *Zur Statik und Kinematik des Cosseratschen Kontinuums*. In *Abhandlungen der Braunschweigischen Wissenschaftlichen Gesellschaft*, pp. 195–213. Band X.
- [50] GURTIN, M. E. [2000]: *On the plasticity of single crystals: free energy, microforces, plastic-strain gradients*. *Journal of the Mechanics and Physics of Solids*, 48: 989–1036.
- [51] GURTIN, M. E. [2002]: *A gradient theory of single-crystal viscoplasticity that accounts for geometrically necessary dislocations*. *Journal of the Mechanics and Physics of Solids*, 50: 5–32.

- [52] HADARMARD, J. [1903]: *Leçons sur la propagation des ondes et les équations de l'hydrodynamique*. Hermann, Paris.
- [53] HALL, E. O. [1951]: *The deformation and aging of mild steel. Part III: discussion and results*. Proceedings of the Physical Society of London, 64: 747–753.
- [54] HASHIN, Z. [1983]: *Analysis of composite materials – a survey*. ASME Journal of Applied Mechanics, 50: 481–505.
- [55] HAUPT, P. [2000]: *Continuum mechanics and theory of materials*. Springer Verlag, Berlin.
- [56] HAVNER, K. S. [1992]: *Finite plastic deformation of crystalline solids*. Cambridge University Press, Cambridge.
- [57] HILL, R. [1957]: *On uniqueness and stability in the theory of finite elastic strain*. Journal of the Mechanics and Physics of Solids, 5: 229–241.
- [58] HILL, R. [1963]: *Elastic properties of reinforced solids: some theoretical principles*. Journal of the Mechanics and Physics of Solids, 11: 357–372.
- [59] HILL, R. [1966]: *Generalized constitutive relations for incremental deformation of metal crystals by multislip*. Journal of the Mechanics and Physics of Solids, 14: 95–102.
- [60] HILL, R. [1972]: *On constitutive macro-variables for heterogeneous solids at finite strain*. Proceedings of the the Royal Society of London, Series A, 326: 131–147.
- [61] HILL, R.; RICE, J. [1972]: *Constitutive analysis of elastic-plastic crystals at arbitrary strain*. Journal of the Mechanics and Physics of Solids, 20: 401–413.
- [62] HOLZAPFEL, G. A. [2000]: *Nonlinear solid mechanics*. John Wiley & Sons.
- [63] HONEYCOMBE, R. W. K. [1984]: *The plastic deformation of metals*. Edward Arnold, London, 2nd Edition.
- [64] HULL, D.; BACON, D. J. [1984]: *Introduction to dislocations*. Pergamon Press, Oxford.
- [65] HUTCHINSON, J. W. [1970]: *Elastic-plastic behaviour of polycrystalline metals and composites*. Proceedings of the the Royal Society of London, Series A, 319: 247–272.
- [66] HUTCHINSON, J. W. [1976]: *Bounds and self-consistent estimates for creep of polycrystalline materials*. Proceedings of the the Royal Society of London, Series A, 348: 101–127.
- [67] KLINGBEIL, E. [1989]: *Tensorrechnung für Ingenieure*. BI-Hochschultaschenbücher; Bd. 197.
- [68] KOCKS, U. F. [1966]: *A statistical theory of flow stress and work-hardening*. The Philosophical Magazine, 13: 541–566.
- [69] KOCKS, U. F. [1977]: *The theory of an obstacle-controlled yield strength – report after an international workshop*. Materials Science and Engineering, 27: 291–29.
- [70] KOITER, W. T. [1960]: *General theorems of elasto-plastic solids*, Progress in Solid Mechanics. I. N. Sneddon; R. Hill (editors), North Holland Publishing Company.
- [71] KONDO, K. [1952]: *On the geometrical and physical foundations of the theory of yielding*. Proceedings Japan National Congress of Applied Mechanics, 2: 41–47.

- [72] KONDO, K. [1955]: *Memoirs of the unifying study of the basic problems in engineering sciences by means of geometry*. Vol I, Tokyo, Gakujutsu Bunken Fukuyū-Kai.
- [73] KONDO, K. [1958]: *Memoirs of the unifying study of the basic problems in engineering sciences by means of geometry*. Vol II, Tokyo, Gakujutsu Bunken Fukuyū-Kai.
- [74] KOUZNETSOVA, V. [2002]: *Computational homogenization for the multi-scale analysis of multi-phase materials*. Ph.D. Thesis, Eindhoven University of Technology, Institute of Mechanics of Materials.
- [75] KOUZNETSOVA, V. G.; GEERS, M. G. D.; BREKELMANS, W. A. M. [2004]: *Multi-scale second-order computational homogenization of multi-phase materials: a nested finite element solution strategy*. *Computer Methods in Applied Mechanics and Engineering*, 193: 5525–5550.
- [76] KRÖNER, E. [1958]: *Kontinuumstheorie der Versetzungen und Eigenspannungen*. In COLLATZ, L.; LÖSCH, F. (Editors): *Ergebnisse der angewandten Mathematik*. Vol. 5, Springer.
- [77] KRÖNER, E. [1960]: *Allgemeine Kontinuumstheorie der Versetzungen und Eigenspannungen*. *Archive for Rational Mechanics and Analysis*, 4: 273–334.
- [78] KRÖNER, E. [1981]: *Differential geometry of defects in condensed systems of particles with only translational mobility*. *International Journal of Engineering Science*, 19: 1507–1515.
- [79] KRÖNER, E. [1992]: *The internal mechanical state of solids with defects*. *International Journal of Solids and Structures*, 29: 1849–1857.
- [80] KRÖNER, E.; SEEGER, A. [1959]: *Nicht-lineare Elastizitätstheorie der Versetzungen und Eigenspannungen*. *Archive for Rational Mechanics and Analysis*, 3: 97–119.
- [81] KRÖNER, E.; TEODOSIU, C. [1972]: *Lattice defect approach to plasticity and viscoplasticity*. In SAWZUK, A. (Editor): *Problems in Plasticity*. Nordhoff International Publishing.
- [82] KUBIN, L. P.; CANOVA, G.; CONDAT, M.; DEVINCRE, B.; PONTIKIS, V.; BRECHET, Y. [1992]: *Dislocation microstructures and plastic flow: a 3D simulation*. *Solid State Phenomena*, 23/24: 455–472.
- [83] LEE, E. H. [1969]: *Elastic-plastic deformation at finite strains*. *Journal of Applied Mechanics*, ASME, 36: 1–6.
- [84] LEVKOVITCH, V.; SIEVERT, R.; SVENDSEN, B. [2004]: *Application of extended crystal plasticity to the modeling of glide and kink bands and of crack opening in single crystals*. *Computational Materials Science*, 32: 426–434.
- [85] LIEBE, T. [2003]: *Theory and numerics of higher gradient inelastic material behaviour*. Ph.D. Thesis, Fachbereich Maschinenbau und Verfahrenstechnik, Universität Kaiserslautern, Advisors: P. Steinmann, Co-advisor: B. Svendsen, A. Benallal.
- [86] LIEBE, T.; STEINMANN, P. [2001]: *Theory and numerics of a thermomechanically consistent framework for geometrically linear gradient plasticity*. *International Journal for Numerical Methods in Engineering*, 51: 1437–1467.
- [87] LIN, T. H. [1971]: *Physical theory of plasticity*. *Advances in Applied Mechanics*, 11: 255–311.

- [88] MALVERN, L. E. [1969]: *Introduction to the mechanics of a continuous medium*. Prentice-Hall Inc., New Jersey.
- [89] MANDEL, J. [1972]: *Plasticité classique et viscoplasticité*. In *CISM Courses and Lectures, No. 97*. Springer.
- [90] MARSDEN, J. E.; HUGHES, T. J. R. [1983]: *Mathematical foundation of elasticity*. Dover Publications, Inc., New Jersey.
- [91] MENZEL, A.; DENZER, R.; STEINMANN, P. [2004]: *On the comparison of two approaches to compute material forces for inelastic materials. Application to single-slip crystal-plasticity*. *Computer Methods in Applied Mechanics and Engineering*, 193: 5411–5428.
- [92] MENZEL, A.; STEINMANN, P. [2000]: *On the continuum formulation of higher gradient plasticity for single and polycrystals*. *Journal of the Mechanics and Physics of Solids*, 48: 1777–1796.
- [93] MICHEL, J.; MOULINEC, H.; SUQUET, P. [2000]: *A computational method based on augmented lagrangians and fast fourier transforms for composites with high contrast*. *Computer Modeling in Engineering and Sciences*, 1: 79–88.
- [94] MIEHE, C. [1996]: *Exponential map algorithm for stress updates in anisotropic multiplicative elastoplasticity for single crystals*. *International Journal for Numerical Methods in Engineering*, 39: 3367–3390.
- [95] MIEHE, C. [1996]: *Multisurface thermoplasticity for single crystals at large strains in terms of eulerian vector updates*. *International Journal of Solids and Structures*, 33: 3103–3130.
- [96] MIEHE, C. [1999-2005]: *Geometrische Methoden der Nichtlinearen Kontinuumsmechanik und Kontinuumsthermodynamik*. Lecture Notes, Universität Stuttgart.
- [97] MIEHE, C. [2002]: *Strain-driven homogenization of inelastic microstructures and composites based on an incremental variational formulation*. *International Journal for Numerical Methods in Engineering*, 55: 1285–1322.
- [98] MIEHE, C. [2003]: *Computational micro-to-macro transitions for discretized microstructures of heterogeneous materials at finite strains based on the minimization of averaged incremental energy*. *Computer Methods in Applied Mechanics and Engineering*, 192: 559–591.
- [99] MIEHE, C.; APEL, N.; LAMBRECHT, M. [2002]: *Anisotropic additive plasticity in the logarithmic strain space. Modular kinematic formulation and implementation based on incremental minimization principles for standard materials*. *Computer Methods in Applied Mechanics and Engineering*, 191: 5383–5425.
- [100] MIEHE, C.; LAMBRECHT, M. [2001]: *Algorithms for computation of stresses and elasticity moduli in terms of Seth-Hill's family of generalized strain tensors*. *Communications in Numerical Methods in Engineering*, 17: 337–353.
- [101] MIEHE, C.; SCHOTTE, J. [2004]: *Anisotropic finite elastoplastic analysis of shells: simulation of earing in deep-drawing of single- and polycrystalline sheets by Taylor-type micro-to-macro transitions*. *Computer Methods in Applied Mechanics and Engineering*, 193: 25–57.

- [102] MIEHE, C.; SCHOTTE, J. [2004]: *Crystal plasticity and evolution of polycrystalline microstructure*. In STEIN, E.; BORST, R. DE ; HUGHES, J. R. (Editors): *Encyclopedia of Computational Mechanics*, Chapter 8, pp. 267–289. John Wiley & Sons.
- [103] MIEHE, C.; SCHOTTE, J.; LAMBRECHT, M. [2002]: *Homogenization of inelastic solid materials at finite strains based on incremental minimization principles. Application to the texture analysis of polycrystals*. *Journal of the Mechanics and Physics of Solids*, 50: 2123–2167.
- [104] MIEHE, C.; SCHOTTE, J.; SCHRÖDER, J. [1999]: *Computational micro-macro transitions and overall moduli in the analysis of polycrystals at large strains*. *Computational Materials Science*, 16: 372–382.
- [105] MIEHE, C.; SCHRÖDER, J. [1994]: *Post-critical discontinuous localization analysis of small-strain softening elastoplastic solids*. *Archive of Applied Mechanic*, 64: 267–285.
- [106] MIEHE, C.; SCHRÖDER, J. [2001]: *A comparative study of stress update algorithms for rate-independent and rate-dependent crystal plasticity*. *International Journal for Numerical Methods in Engineering*, 50: 273–298.
- [107] MIEHE, C.; SCHRÖDER, J.; BAYREUTHER, C. G. [2002]: *On the homogenization analysis of composite materials based on discretized fluctuations on the microstructure*. *Acta Mechanica*, 155: 1–16.
- [108] MIEHE, C.; SCHRÖDER, J.; BECKER, M. [2002]: *Computational homogenization analysis in finite elasticity. Material and structural instabilities on the micro- and macro-scales of periodic composites and their interaction*. *Computer Methods in Applied Mechanics and Engineering*, 191: 4971–5005.
- [109] MIEHE, C.; SCHRÖDER, J.; SCHOTTE, J. [1999]: *Computational homogenization analysis in finite plasticity. Simulation of texture development in polycrystalline materials*. *Computer Methods in Applied Mechanics and Engineering*, 171(3–4): 387–418.
- [110] MIELKE, A.; MÜLLER, S. [2005]: *Lower semi-continuity and existence of minimizers in incremental finite-strain elastoplasticity*. *Zeitschrift für angewandte Mathematik und Mechanik*, to appear.
- [111] MITCHELL, T. E. [1964]: *The deformation of metal crystals*. *Progress in Applied Materials Research*, 6: 119–156.
- [112] MORREY, C. B. [1952]: *Quasi-convexity and the lower semicontinuity of multiple integrals*. *Pacific Journal of Mathematics*, 2: 25–53.
- [113] MOULINEC, H.; SUQUET, P. [1994]: *A fast numerical method for computing the linear and nonlinear mechanical properties of composites*. *Comptes Rendus de l'Academie des Sciences II*, 318: 1417–1423.
- [114] MÜLLER, S. [1987]: *Homogenization of nonconvex integral functionals and cellular elastic materials*. *Archive of Rational Mechanics and Analysis*, 99: 189–212.
- [115] NABARRO, F. R. N.; BASINSKI, Z. S.; HOLT, D. B. [1964]: *The plasticity of pure single crystals*. *Advances in Physics*, 13: 193–269.
- [116] NEEDLEMAN, A.; ASARO, R. J.; LEMONDS, J.; PEIRCE, D. [1985]: *Finite element analysis of crystalline solids*. *Computer Methods in Applied Mechanics and Engineering*, 52: 689–708.

- [117] NEMAT-NASSER, S.; HORI, M. [1993]: *Micromechanics: Overall properties of heterogeneous materials*. In *North-Holland Series in: Applied Mathematics and Mechanics*. 37 Edition.
- [118] NGUYEN, Q. S. [2000]: *Stability and nonlinear solid mechanics*. John Wiley & Sons, Chichester.
- [119] NYE, J. F. [1953]: *Some geometrical relations in dislocated crystals*. *Acta Metallurgica*, 1: 153–162.
- [120] ORTIZ, M.; RADOVITZKY, R. A.; REPETTO, E. A. [2001]: *The computation of the exponential and logarithmic mappings and their first and second linearizations*. *International Journal for Numerical Methods in Engineering*, 52: 1431–1441.
- [121] ORTIZ, M.; REPETTO, E. A. [1999]: *Nonconvex energy minimization and dislocation structures in ductile single crystals*. *Journal of the Mechanics and Physics of Solids*, 47: 397–462.
- [122] ORTIZ, M.; REPETTO, E. A.; STAINIER, L. [2000]: *A theory of subgrain dislocation structures*. *Journal of the Mechanics and Physics of Solids*, 48: 2077–2114.
- [123] ORTIZ, M.; STAINIER, L. [1999]: *The variational formulation of viscoplastic constitutive updates*. *Computer Methods in Applied Mechanics and Engineering*, 171: 419–444.
- [124] PEIRCE, D.; ASARO, R.; NEEDLEMAN, A. [1982]: *An analysis of nonuniform and localized deformation in ductile single crystals*. *Acta Metallurgica*, 30: 1087–1119.
- [125] PETCH, N. J. [1953]: *The cleavage strength of polycrystals*. *Journal of the Iron and Steel Institute*, 174: 25–28.
- [126] PINSKY, P. [1986]: *A finite element formulation for elastoplasticity based on a three-field variational equation*. *Computer Methods in Applied Mechanics and Engineering*, 61: 41–60.
- [127] PONTE CASTAÑEDA, P.; SUQUET, P. [1998]: *Nonlinear composites*. *Advances in Applied Mechanics*, 34: 171–303.
- [128] RASHID, M. M.; NEMAT-NASSER, S. [1992]: *A constitutive algorithm for rate-dependent crystal plasticity*. *Computer Methods in Applied Mechanics and Engineering*, 94: 201–228.
- [129] RICE, J.R. [1971]: *Inelastic constitutive relations for solids: an internal-variable theory and its application to metal plasticity*. *Journal of the Mechanics and Physics of Solids*, 19: 433–455.
- [130] SCHMID, E.; BOAS, W. [1935]: *Kristallplastizität*. Springer.
- [131] SCHMIDT-BALDASSARI, M. [2003]: *Numerical concepts for rate-independent single crystal plasticity*. *Computer Methods in Applied Mechanics and Engineering*, 192: 1261–1280.
- [132] SCHOUTEN, J. A. [1954]: *Ricci-Calculus*. In: *Die Grundlehren der Mathematischen Wissenschaften in Einzeldarstellungen*, Band X, Springer, Second Edition.
- [133] SHIZAWA, K.; ZBIB, H. M. [1999]: *A thermodynamical theory of gradient elastoplasticity with dislocation density tensor. I: fundamentals*. *International Journal of Plasticity*, 15: 899–938.

- [134] SHU, J. Y.; FLECK, N. A. [1998]: *The prediction of a size effect in micro indentation*. International Journal of Solids and Structures, 35: 1363–1383.
- [135] SHU, J. Y.; FLECK, N. A. [1999]: *Strain gradient crystal plasticity: size-dependent deformation of bicrystals*. Journal of the Mechanics and Physics of Solids, 47: 297–324.
- [136] SHU, J. Y.; FLECK, N. A.; VAN DER GIESSEN, E.; NEEDLEMAN, A. [2001]: *Boundary layers in constrained plastic flow: comparison of nonlocal and discrete dislocation plasticity*. Journal of the Mechanics and Physics of Solids, 49: 1361–1395.
- [137] SIMO, J.; KENNEDY, J.; TAYLOR, R. [1989]: *Complementary mixed finite element formulations for elastoplasticity*. Computer Methods in Applied Mechanics and Engineering, 74: 177–206.
- [138] SIMO, J. C.; ARMERO, F. [1992]: *Geometrically non-linear enhanced strain mixed methods and the method of incompatible modes*. International Journal for Numerical Methods in Engineering, 33: 1413–1449.
- [139] SOKOLNIKOFF, I. S. [1956]: *Mathematical theory of elasticity*. McGraw-Hill.
- [140] STEINMANN, P. [1996]: *Views on multiplicative elastoplasticity and the continuum theory of dislocations*. International Journal of Engineering Science, 34: 1717–1735.
- [141] STEINMANN, P.; STEIN, E. [1996]: *On the numerical treatment and analysis of finite deformation ductile single crystal plasticity*. Computer Methods in Applied Mechanics and Engineering, 129: 235–254.
- [142] STELMASHENKO, A.; WALLS, A.; BROWN, L.; MILMAN, Y. [1993]: *Microindentation on  $w$  and  $mo$  oriented single crystals: an stm study*. Acta Metallurgica et Materialia, 41: 2855–2865.
- [143] STOLKEN, J.; EVANS, A. [1998]: *A microbend test method for measuring the plasticity length scale*. Acta Materialia, 46: 5109–5115.
- [144] SUQUET, P. M. [1987]: *Elements of homogenization for inelastic solid mechanics*. In SANCHEZ-PALENZIA, E.; ZAOU, A. (Editors): *Homogenization Techniques for Composite Materials*, Lecture Notes in Physics, Vol. 272. Springer, Berlin.
- [145] SVENDSEN, B. [2002]: *Continuum thermodynamic models for crystal plasticity including the effects of geometrically-necessary dislocations*. Journal of the Mechanics and Physics of Solids, 50: 1297–1329.
- [146] SVENDSEN, B.; REESE, S. [2003]: *Continuum thermodynamic modeling and simulation of additional hardening due to deformation incompatibility*. In MIEHE, C. (Editor): *Computational Mechanics of Solid Materials at Large Strains, Kluwer Series on Solid Mechanics and its Applications*, pp. 141–150, Vol. 108. Kluwer Academic Publishers, Dordrecht.
- [147] TAYLOR, G. I. [1934]: *The mechanism of plastic deformation of crystals. Part I + II*. Proceedings of the the Royal Society of London, Series A, 145: 362–404.
- [148] TAYLOR, G. I. [1938]: *Plastic strain in metals*. Journal of the Institute of Metals, 62: 307–324.

- [149] TEODOSIU, C. [1970]: *A dynamic theory of dislocations and its applications to the theory of the elastic-plastic continuum*, Fundamental Aspects of Dislocation Theory. National Bureau of Standards (U.S.) Special Publication, Vol., II, 837–876.
- [150] TONELLI, L. [1921]: *Fondamenti di calcolo delle variazioni*. Zanichelli, Bologna.
- [151] TRIANTAFYLIDIS, N.; MAKER, B. N. [1985]: *On the Comparison Between Microscopic and Macroscopic Instability Mechanisms in a Class of Fiber-Reinforced Composites*. Journal of Applied Mechanics, 52: 794–800.
- [152] TROOST, A. [1980]: *Einführung in die allgemeine Werkstoffkunde metallischer Werkstoffe I*. Bibliographisches Institut, Zürich.
- [153] TRUESDELL, C.; NOLL, W. [1965]: *The non-linear field theories of mechanics*. In FLÜGGE, S. (Editor): *Handbuch der Physik, Vol. III (3)*. Springer Verlag, Berlin.
- [154] VAN DER GIESSEN, E.; NEEDLEMAN, A. [1995]: *Discrete dislocation plasticity: a simple planar model*. Modelling and Simulation in Materials Science and Engineering, 3: 689–735.
- [155] WEBER, G.; ANAND, L. [1990]: *Finite deformation constitutive equations and a time integration procedure for isotropic, hyperelastic-viscoplastic solids*. Computer Methods in Applied Mechanics and Engineering, 79: 173–202.
- [156] WILLIS, J.R. [1981]: *Variational and related methods for the overall properties of composites*. Advances in Applied Mechanics, 21: 1–78.
- [157] WRIGGERS, P.; WAGNER, W.; MIEHE, C. [1988]: *A quadratically convergent procedure for the calculation of stability points in finite element analysis*. Computer Methods in Applied Mechanics and Engineering, 70: 329–347.
- [158] WU, T. Y.; BASSANI, J. L.; LAIRD, C. [1991]: *Latent hardening in single crystals I. Theory and Experiments*. Proceedings of the Royal Society London A, 435: 1–19.
- [159] ZIENKIEWICZ, O. C.; ZHU, J. Z. [1992]: *The superconvergent patch recovery and a posteriori error estimates*. International Journal for Numerical Methods in Engineering, 33: 1331–1364.
- [160] ZIENKIEWICZ, O. C.; TAYLOR, R. L. [1994]: *The finite element method, Vol. 1, Basic formulations and linear problems*. McGraw-Hill, London.

# Curriculum Vitae

## Personal Details

---

Name	Martin Becker
Date of Birth	May 15, 1976
Place of Birth	Reutlingen, Germany
Parents	Brita and Olaf Becker
Siblings	Karin Degler and Jan Becker

## School Education/Military Service

---

1982-1986	Elementary School: Köngen
1986-1995	Secondary School: „Robert-Bosch-Gymnasium Wendlingen“
July 1995	General Qualification for University Entrance („Abitur“)
1995-1996	Basic Military Service: „Panzerartilleriebataillon 285 Münsingen“

## University Education

---

1996-2001	Studies of Civil Engineering, Universität Stuttgart
1999-2000	Studies of Civil Engineering, University of Calgary, Canada
August 2001	Graduation as Diplom-Ingenieur

## Professional Occupation

---

Since 2001	Research Associate and Assistant Lecturer, Institute of Applied Mechanics (Civil Engineering), University of Stuttgart
------------	--



**In dieser Schriftenreihe bisher erschienene Berichte:**

- I-1(1996) *Theoretische und algorithmische Konzepte zur phänomenologischen Beschreibung anisotropen Materialverhaltens*, J. Schröder, Dissertation, 1996.
- I-2(1996) *Zur Theorie und Numerik finiter elastoplastischer Deformationen von Schalentragwerken*, B. Seifert, Dissertation, 1996.
- I-3(1996) *Zur Modellierung des künstlichen Infrarot-Dichroismus in Polymerfolien bei großen Verformungen*, J. Buhler, Dissertation, 1996.
- I-4(1998) *Verfahren zur Ermittlung der Erdbebenlasten mit Berücksichtigung des stochastischen Charakters des Bebens*, S. Zhang, Dissertation, 1998.
- I-5(1998) *Zur Beschreibung finiter Deformationen von Polymeren: Experimente, Modellbildung, Parameteridentifikation und Finite-Elemente-Formulierung*, J. Keck, Dissertation, 1998.
- I-6(1999) *Berechnungsverfahren instationär erregter Systeme im Frequenzbereich*, A. Jaworek, Dissertation, 1999.
- I-7(2000) *Homogenisierungsmethoden der nichtlinearen Kontinuumsmechanik unter Beachtung von Stabilitätsproblemen*, J. Schröder, Habilitation, 2000.
- I-8(2002) *Theorie und Numerik von Materialinstabilitäten elastoplastischer Festkörper auf der Grundlage inkrementeller Variationsformulierungen*, M. Lambrecht, Dissertation, 2002.
- I-9(2002) *Mikromechanisch motivierte Modelle zur Beschreibung finiter Deformationen gummiartiger Polymere: physikalische Modellbildung und numerische Simulation*, F. Lulei, Dissertation, 2002.
- I-10(2003) *Adaptive Finite-Elemente-Berechnungen der nichtlinearen Festkörpermechanik bei kleinen und großen Verzerrungen*, A. Koch, Dissertation, 2003.
- I-11(2003) *Theorie und Numerik der Parameteridentifikation von Materialmodellen der finiten Elastizität und Inelastizität auf der Grundlage optischer Feldmeßmethoden*, G. Scheday, Dissertation, 2003.
- I-12(2004) *Approaches to the Description of Anisotropic Material Behaviour at Finite Elastic and Plastic Deformations, Theory and Numerics*, N. Apel, Dissertation, 2004.
- I-13(2004) *Temperaturabhängige Beschreibung visko-elasto-plastischer Deformationen kurzglasfaserverstärkter Thermoplaste: Modellbildung, Numerik und Experimente*, S. Rieger, Dissertation, 2004.
- I-14(2005) *Zur Parameteridentifikation komplexer Materialmodelle auf der Basis realer und virtueller Testdaten*, A. Rieger, Dissertation, 2005.
- I-15(2005) *Viskoelastisches Verhalten von Elastomeren bei finiten Verzerrungen: Experimente, Modellierung und Simulationen*, H. Zecha, Dissertation, 2005.

- I-16(2005) *Mehrskalenmodelle in der Festkörpermechanik und Kopplung von Mehrgitter- methoden mit Homogenisierungsverfahren*, C.G. Bayreuther, Dissertation, 2005.
- I-17(2005) *Static and Dynamic Homogenization Analyses of Discrete Granular and Atomistic Structures on Different Time and Length Scales*, J. Dettmar, Dissertation, 2005.
- I-18(2006) *Incompatibility and Instability Based Size Effects in Crystals and Composites at Finite Elastoplastic Strains*, M. Becker, Dissertation, 2006.

